# Trace Metal Biogeochemical Cycling and Fluxes in the eastern South Atlantic

## Dissertation

vorgelegt von

**Te Liu**

Zur Erlangung des akademischen Grades eines Doktors der

Naturwissenschaften

**– Dr. rer. nat –**

an der Mathematisch-Naturwissenschaftlichen Fakultät der Christian-Albrechts-Universität zu Kiel
Kiel, 2023

1. Gutachter: Prof. Eric P. Achterberg

2. Gutachter: Dr. Florian Scholz

Tag der mündlichen Prüfung: 20.07.2023

# Abstract

Concentrations of trace metals (TMs) in the ocean provide important information that allows assessment of ocean productivity, carbon sequestration, Earth's history and future climate. Studying the biogeochemical cycles of TMs in the ocean is nowadays often part of the investigations of ocean processes including biological assimilation and remineralization, large-scale ocean circulation, ocean-boundary exchange, sedimentary records and ocean deoxygenation. Some TMs are bio-essential micronutrients for phytoplankton, including cadmium (Cd), cobalt (Co), copper (Co), iron (Fe), manganese (Mn), nickel (Ni) and Zinc (Zn), whereas some can be toxic at high concentrations such as Cu and lead (Pb). Some TMs are sensitive to seawater oxygen conditions (Fe, Co and Mn). Other TMs can act as tracers of ocean circulation (Cd and Ni), supply and scavenging (aluminum (Al)) and anthropogenic contamination (Pb). The study of multiple TMs simultaneously is a powerful tool to gain process insights into the ocean system. We performed a detailed investigation into TM distributions across the Benguela Upwelling System (BUS), Congo River margin (Congo shelf and offshore Congo plume) and eastern South Atlantic as part of the GEOTRACES GA08 cruise. Our objective was to asses TM sources, fluxes and internal cycling.

Within the BUS, dissolved TMs (dTMs) showed contrasting behaviors and can be categorized into two groups of nutrient-type (dCo, dNi and dCu) and redox sensitive type (dFe, dCo and dMn) elements. The distributions of nutrient-type TMs are driven by intense remineralization across the Namibian shelf and Antarctic-derived waters in the open eastern South Atlantic. Shelf sediments constituted a dominant source of redox-sensitive TMs to both coastal waters and the open eastern South Atlantic compared to other inputs, such as atmospheric deposition. The shelf edge played a key role concerning off-shelf transfer of dFe and dCo as their off-shelf fluxes from the subsurface (200-500 m) were considerably larger than those in the upper 200 m. Under future conditions with more intense ocean deoxygenation, benthic fluxes of dFe, dCo and dMn could increase further, potentially contributing to a shift towards more extensive regional limitation of primary production by fixed nitrogen availability rather than Fe or Co.

Enhanced surface TM concentrations across the Congo shelf indicate a "missing" source other than mixing between Congo River water and coastal seawater. Analysis of TMs in rainwater shows a significant supply of TM from wet deposition (rainfall), thus explaining the discrepancy in TMs budget across the Congo shelf and in the offshore Congo plume identified in prior work. Concentrations of Zn, Pb, Cd and Cu in rainwater indicate an anthropogenic source, which can be related to an abundance of gas flaring sites along the western African coast. Our results show TM fluxes in the Congo plume are augmented by rainfall, which results in an apparently smaller removal rate of Fe (~50%) compared to the typical removal rate (90-99%) for river and seawater mixing. Increased stability of dFe by organic matter complexing and(or) continuous photo-reduction in rain droplets could be efficient mechanisms facilitating distal transport of dFe alongside substantial lateral TM fluxes in the offshore Congo plume.

In the open eastern South Atlantic Ocean, internal cycling like interactions between dTMs and particulate TMs (pTMs) controls dTM distributions. Stronger and(or) faster top-down supply of authigenic/biogenic formations of pTMs leads to elevated concentrations of pCo, pCu, pMn, pPb and pZn in the deep waters ($\delta_\theta$ > 27.5 kg $m^{-3}$), which mask signals from their seafloor inputs. In the intermediate waters (27.5 kg $m^{-3}$ > $\delta_\theta$ > 26.5 kg $m^{-3}$), scavenging of dCo, dFe and dZn plays a role in shaping their distributions. Decreasing trend of dMn in the vertical profiles is induced by photo-reduction of Mn oxide in surface waters and authigenic Mn oxide formation in subsurface waters, corresponding to increasing trend of bulk pMn. Authigenic Mn oxide in the water column played a major scavenging role for dCo below surface layer. The ferromanganese crust could be the ultimate sink of pCo and pPb in the South Atlantic Ocean. A nutrient-like behavior was obvious for Cd within the whole water column, and for Co in the surface layer ($\delta_\theta$ < 26.5 kg $m^{-3}$, <120 m). Comparisons of uptake, recycling and external supply processes for Cd, Co and P emphasized the importance of internal cycling for these elements with >90% of plankton assimilation estimated to be supported by internal recycling. An increased dependence on Cd and Co for primary production from the Angola Basin to the South Atlantic Gyre (SAG) is aligned with the enhanced Fe-stress probably due to a higher demand of Cd and Co under Fe-limited conditions. Our work highlights the importance of interaction between dTM and pTM in understanding marine

internal cycling of TMs and regional variations of TM distribution related to nutrient co-limitation condition.

# Zusammenfassung

Die Konzentrationen von Spurenmetallen (TM, aus dem Englischen „trace metals“) können wichtige Informationen über die Produktivität der Ozeane, die Kohlenstoffbindung, die Erdgeschichte und das zukünftige Klima liefern. Die Untersuchung der biogeochemischen Zyklen von Spurenmetallen im Ozean kann aufschlussreich für ozeanische Prozesse wie biologische Assimilation und Remineralisierung, großräumige Ozeanzirkulation, Austausch zwischen den Ozeangrenzen, Sedimentaufzeichnungen und Sauerstoffverlust im Ozean sein. Einige TM sind bio-essentielle Mikronährstoffe wie Cadmium (Cd), Kobalt (Co), Kupfer (Cu), Eisen (Fe), Mangan (Mn), Nickel (Ni) und Zink (Zn) für das Phytoplankton, während andere in hohen Konzentrationen giftig sein können, wie Cu und Blei (Pb). Einige TMs reagieren empfindlich auf die Sauerstoffkonzentration im Meerwasser (Fe, Co und Mn). Andere TMs können als Indikatoren für die Ozeanzirkulation (Cd und Ni), das Angebot und die Aufnahme (Aluminium (Al)) und die anthropogene Verschmutzung (Pb) dienen. Die gleichzeitige Untersuchung mehrerer TM-Verteilungen ist daher ein leistungsfähiges Instrument, um Einblicke in die Prozesse des Ozeansystems zu erlangen. Aus diesem Grund haben wir im Rahmen der GEOTRACES-Fahrt GA08 eine detaillierte Untersuchung der TM-Verteilung im Benguela-Auftriebssystem (BUS), am Rande des Kongo-Flusses (Kongo-Schelf und Offshore-Kongo-Fahne) und im östlichen Südatlantik durchgeführt. Unser Ziel war es, TM-Quellen, -Flüsse und interne Kreisläufe zu untersuchen.

Innerhalb des BUS zeigten die gelösten TM (dTM) ein unterschiedliches Verhalten und können in zwei Gruppen eingeteilt werden: Elemente vom Nährstofftyp (dCo, dNi und dCu) und vom redoxempfindlichen Typ (dFe, dCo und dMn). Die Verteilung der TMs vom Nährstofftyp wird durch die intensive Remineralisierung auf dem namibischen Schelf und die aus der Antarktis stammenden Wassermassen im offenen östlichen Südatlantik bestimmt. Umgekehrt stellten Schelfsedimente im Vergleich zu anderen Einträgen, wie z. B. atmosphärischen Ablagerungen, eine dominante Quelle redoxempfindlicher TMs sowohl für die Küstengewässer als auch für den offenen östlichen Südatlantik dar. Die Schelfkante spielte eine Schlüsselrolle bei der

Verlagerung von dFe und dCo aus dem Schelf ins offene Meer, da ihre Flüsse unterhalb der Oberflächenschicht (200-500 m) erheblich größer waren als die Flüsse aus den oberen 200 m. Unter den künftigen Bedingungen einer stärkeren Desoxygenierung des Ozeans könnten die benthischen Flüsse von dFe, dCo und dMn weiter zunehmen und möglicherweise zu einer Verlagerung hin zu einer stärkeren regionalen Begrenzung der Primärproduktion durch die Verfügbarkeit von festem Stickstoff anstelle von Fe oder Co beitragen.

Erhöhte TM-Konzentrationen an der Oberfläche des Kongo-Schelfs deuten auf eine "fehlende" Quelle hin, die sich nicht durch Mischen des Wassersdes Kongo-Flusses mit dem küstennahen Meerwassererklären lässt. Die Analyse von TM im Regenwasser ergab eine erhebliche Zufuhr von TM durch nasse Ablagerung (Regen), was die Diskrepanz im TM-Budget auf dem Kongo-Schelf und in der Offshore-Kongo-Fahne erklärt, die in früheren Arbeiten festgestellt wurde. Die Konzentrationen von Zn, Pb, Cd und Cu im Regenwasser deuten auf eine anthropogene Quelle hin, die mit den zahlreichen Gasabfackelstellen entlang der westafrikanischen Küste in Verbindung gebracht werden kann. Unsere Ergebnisse zeigen, dass die TM-Flüsse in der Kongo-Fahne durch Regenfälle verstärkt werden, was zu einer offenbar geringeren Fe-Entfernungsrate (~50%) im Vergleich zur typischen Entfernungsrate (90-99%) bei der Vermischung von Fluss- und Meerwasser führt. Eine erhöhte Stabilität von dFe durch Komplexbildung mit organischen Stoffen und (oder) kontinuierliche Photoreduktion in Regentropfen könnten effiziente Mechanismen sein, die den distalen Transport von dFe neben beträchtlichen lateralen TM-Flüssen in der Offshore-Kongo-Fahne erleichtern.

Im offenen östlichen Südatlantik steuern interne Kreisläufe und die Interaktion zwischen dTMs und partikulären TMs (pTMs) die dTM-Verteilung. Erhöhte Konzentrationen von pCo, pCu, pMn, pPb und pZn in der Tiefenschicht sind größtenteils auf die Anreicherung des Eintrages von authigenen/biogenen Formationen von pTMs aus der Oberflächenschicht und die Aufnahme von dTMs in der Zwischenschicht (für Co, Fe und Zn) zurückzuführen, was die Signale ihrer Einträge vom Meeresboden überdeckt. Die umgekehrten Verteilungen von pMn und dMn in unserer Studie sind auf die Photoreduktion von Mn-Oxid im Oberflächenwasser und die Bildung von authigenem Mn-Oxid unterhalb der Oberfläche zurückzuführen, welches eine wichtige Rolle beim

Abfangen von dCo unter der Oberflächenschicht spielte. Die Ferromangankruste könnte die endgültige Senke für pCo und pPb im Südatlantik sein. Ein nährstoffähnliches Verhalten zeigte sich für Cd in der gesamten Wassersäule und für Co vor allem in der Oberflächenschicht. Vergleiche der Aufnahme, des Recyclings und der externen Zufuhr von Cd, Co und P unterstrichen die Bedeutung des internen Kreislaufs für diese Elemente, wobei davon ausgegangen wird, dass mehr als 90% der Planktonassimilation durch internes Recycling unterstützt wird. Eine verstärkte Abhängigkeit von Cd und Co aus dem Angola-Becken in den Südatlantikwirbel (SAG) steht im Einklang mit dem erhöhten Fe-Stress, der wahrscheinlich auf einen höheren Bedarf an Cd und Co unter Fe-limitierten Bedingungen zurückzuführen ist. Unsere Arbeit unterstreicht die Bedeutung der Interaktion zwischen dTM und pTM für das Verständnis des internen marinen Kreislaufs von TMs und der regionalen Variationen der TM-Verteilung im Zusammenhang mit Nährstoff-kolimitierenden Bedingungen.

Thanks Dr. Insa Rapp and Dr. Stephan Krisch for improving German.

# Acknowledgements

I firstly want to thank my supervisor Prof. Eric Achterberg for his guidance, advice and support and for giving me the opportunity to write this thesis on an interesting project and go on exciting cruises. Eric is always open to questions and needs. Many thanks for continuous discussions and helpful suggestions with me and for teaching me how to think and write. It has been a true pleasure to work in such an international and interdisciplinary group!

I would also like to express my gratitude to Mark Hopwood for his scientific insights and spending uncountable hours improving my English writing. Mark is intelligent and always gives fast feedbacks on my questions! Thank you to Ruifang Xie for early discussions about particle digestion and about flux calculations!

Thanks to Insa Rapp and Ali Al-Hashem for training me on experiment at east and west shore lab. Many thanks to Tim Steffens and Dominik Jasinski for technical support on the SeaFAST and ICP-MS. Tim and Dominik are irreplaceable and kind to solve problems during my sample preparation and analysis process! And thank you to André Mutzberg for analyzing nutrient data and helping me with cruise preparation!

Cruise M121 has contributed to this research. Many thanks to all the crews and scientists of M121 especially to Stephan Krisch, Tom Browning, Lúcia Vieira and Jan-Lukas Menzel-Barraquetta for their amazing work which enlightened me a lot on this project! Thanks also to Pablo Lodeiro and Christian Schlosser for trace metal sampling on the cruise!

I am grateful to Birgit Reiner for her administrative assistance during my PhD. I would like to thank the GEOTRACES programme for supporting me to participate in 2022 summer school at AWI in Bremerhaven. Thanks also to CAU Graduate Center for the opportunity to participate at international conferences by providing travel grants. I also thank GEOMAR for supporting trace element analysis and paper publish fee.

I have spent great time with everyone in AG Achterberg group and on SO289 cruise. Thanks Martha Gledhill for her patience and comfort when I felt upset. I thank my office and lab mate Kathleen Gosnell who has shared a lot of fun with me. Thanks to Kechen Zhu, Xuechao Wang, Jana Krause, Maria Martinez-Cabanas, Siao Jean Khoo, Tabea von Keitz, and Melly Lupita for exploring Kiel together with me after work. Thanks to Zvi Steiner, Aaron Beck, Mario Esposito, Münevver Nehir, Edel Mary O'Sullivan, Sayoni Bhattacharya, Peter Ukotijeikwut, Xunchi Zhu, Jaw-Chuen Yong and many more people I met during my PhD for making life a lot of fun in Kiel!

我非常感谢一直无私支持我的家人们。感谢爸爸妈妈和弟弟对我的无限的爱，包容与支持！你们给了我莫大的底气去做任何我爱的事，让我没有任何后顾之忧！我非常感谢我的爱人，许安涛。因为有你，我有了更大的追求美好生活的动力，也有了更多的享受简单生活的情趣。我们永远是彼此坚定可靠的队友！希望我的家人平安喜乐，一生幸福!

## List of Figures

## List of Tables

## Contents

# 1. Introduction

Trace metals (TMs) in the ocean are present at extremely low concentrations and their distributions reflect an interplay of biological, physical and chemical oceanographic processes. Some TMs are cofactors in enzymes that regulate assimilation and utilization of carbon (C), nitrogen (N) and phosphorus (P) by phytoplankton (Morel 2003; Twining and Baines 2013). For example, iron (Fe) complexes participate in electron transport of photosystems I and II (Raven et al. 1999), and are incorporated in enzymes that catalyze N fixation (nitrogenase and nitrate reductase) (Timmermans et al. 1994; Berman-Frank et al. 2007). Zinc (Zn), as a major component of many enzymes, is involved in many cell processes like (de)hydration of $CO_2$ (carbonic anhydrase) (Morel 2003) and organophosphates (alkaline phosphatase), cell genetic transcription and heavy metal homeostasis and detoxication (metallothionein) (Morel et al. 2020). Cadmium (Cd) and copper (Cu) can substitute Zn in carbonic anhydrase and superoxide dismutase, respectively, as they have similar atomic structure (Morel et al. 2020). Cobalt (Co) is primarily incorporated into vitamin $B_{12}$ (Rickes et al. 1948), while nickel (Ni) is associated with urease and superoxide dismutase (Ho 2013; Biscéré et al. 2018). Manganese (Mn) is mainly involved into water-splitting reaction in oxygenic photosystems II (Schmidt et al. 2016). Thus, the availability and supply of TMs support a myriad of biological processes in the ocean. Under conditions of low TM availability, TMs can limit the overall productivity of marine ecosystems (Arrigo 2005; Moore 2016a) and ultimately impact the Earth system via moderating spatial patterns of productivity in the ocean and the associated carbon sinks (Falkowski et al. 2000; Moore et al. 2013).

Some TMs can act as tracers to provide information on the supply and removal of oceanic micronutrients and ocean circulation, including aluminum (Al) for dust inputs (Measures and Vink 2000), Mn for benthic supply (Laes et al. 2007), lead (Pb) for scavenging processes (Kadko 1993) and Cd for water mass circulation (Middag et al. 2018). The key roles of TMs in the ocean and the recent development of powerful analytical techniques for assessing the concentration of multiple TMs simultaneously (Rapp et al. 2017) leads us to learn more about oceanic TM distributions and cycling. The ongoing international GEOTRACES program has made a collective effort to produce

oceanographically consistent, reproducible data of TMs in the water column of the world's oceanic basins. This thesis will focus on GEOTRACES work conducted on cruise GA08 (M121) and presents an investigation into the biogeochemical cycling of TMs in the eastern South Atlantic.

### 1.1 Trace metal concentrations

Concentrations of elements in the ocean range over 15 orders of magnitude and the residence time of different elements is similarly broad. These differences arise from the varying sources, sinks and reactivities of different elements. Units to present element concentrations in the ocean are moles with prefix or equivalents per kilogram/liter of seawater expressed as micro-molar (μmol $L^{-1}$, μM), nano-molar (nmol $L^{-1}$, nM) or pico-molar (pmol $L^{-1}$, pM). Trace metals are generally regarded as those metals with average concentrations lower than ~1 μM. In this thesis, I will focus on the distributions of the elements Cd, Co, Cu, Fe, Mn, Ni, Pb and Zn.

Concentrations of Cd in seawater have been accurately measured since the 1970s. The concentration of Cd is depleted to <1 pM in the surface waters and enriches to ~1.1 nM in old deep waters (Bruland 1980; Middag et al. 2018). In coastal and estuarine waters, Cd concentrations can be higher by a factor of >10 primarily due to weathering and anthropogenic inputs (Cullen and Maldonado 2012).

Cobalt is one of the least abundant TMs with a low ocean inventory, with concentrations ranging from <0.01 nM to ~0.2 nM in seawater. Low Co availability may affect some phytoplankton growth (Saito et al. 2002; Browning et al. 2018). Fresh and estuarine waters have the highest Co concentrations which can be 2-3 order of magnitudes higher than those in seawater (Takata et al. 2010). Cobalt concentrations can reach to ~0.3-0.4 nM in oxygen minimum zones (OMZs) associated with eastern boundary upwelling regions (EBURs) (Hawco et al. 2016; Sanial et al. 2018; Liu et al. 2022b). This is due to reduced scavenging from Mn oxides, which elsewhere, under oxic conditions, are an important sink for Co. For consistency throughout, we consider OMZs to be areas of the ocean with oxygen concentrations <100 μM in the water column.

Most observations of Cu in the open ocean are within the concentration range of 0.5-5 nM (GEOTRACES Intermediate Data Product Group 2021). The most depleted surface Cu concentrations of approximately 0.5-0.6 nM are observed in the Atlantic Ocean (Bruland 1980; Pohl et al. 2011). Near the coast, Cu concentrations in the surface may increase to 1-2 nM. Although Cu surface concentrations seems to consistently exceed to the toxic concentration threshold (0.02 nM) that might be expected to prevent some phytoplankton species from growing, more than 99% of Cu in seawaters is rendered un-bioavailable by binding to organic matter (Coale and Bruland 1990; Zitoun et al. 2021) and thus the toxicity of Cu to marine biota is greatly reduced.

Despite the relatively high abundance of Fe in Earth's crust, the concentration of Fe is generally low in the ocean and typically ranges between 0.02-2.5 nM (De Baar 2001). Fe concentrations are sufficiently low, <0.1 nM, in surface waters to limit phytoplankton growth across about 40% of the global ocean including most of the Southern Ocean, Equatorial Pacific, high latitude North Pacific and parts of the high latitude North Atlantic (De Baar 2001; Boyd et al. 2007; Ryan-Keogh et al. 2013). In contrast, relatively high concentrations have been observed in coastal waters and suboxic/anoxic basins (De Baar 2001). Elevated concentrations are associated with proximity to shelf/terrestrially derived sources, and reducing conditions which favor elevated supply of the soluble Fe(II) species.

Concentrations of Mn in seawater occur in the range of 0.1-20 nM with higher concentrations almost invariably associated with surface waters (>0.2 nM) and lower concentrations with the deep ocean (0.1-0.2 nM) (Pilson 2012). Elevated surface Mn concentrations (>10 nM) have been observed in several ocean basins including the surface Mediterranean Sea (Middag et al. 2022) and the Arctic (Jensen et al. 2020) due to a combined effect of aeolian inputs, photo-reduction and lateral transport from the shelf. The effect of photochemistry on Mn distribution is thought to be particularly strong as sunlight both favors dissolution of Mn into soluble dissolved phases and impedes biological Mn oxidation, which would otherwise remove Mn from the dissolved phase (Sunda et al. 1983; Sunda and Huntsman 1994). High surface concentrations of Mn lead to an inverse depth profile compared to other elements discussed herein.

Nickel is an essential TM for many organisms, however, unlike Cd and Zn, it is never depleted in surface waters (>1.7 nM) (John et al. 2022). This was first attributed to Ni being not bioavailable to microorganisms by binding to organic matter in the surface ocean (Pilson 2012). However, this explanation is not entirely consistent with observed experimental evidence as Ni speciation measurements in seawater suggest that 50-90% the residual Ni is bioavailable (Achterberg and Van Den Berg 1997; Glass and Dupont 2017). Instead, it has been proposed that residual Ni concentrations simply reflect the residual Ni concentration when other elements are depleted. Similar as Cd, Cu and Zn, deep water Ni concentrations are higher than those in the surface water and accumulate along the deep ocean "conveyor belt" from the younger Atlantic to the older Pacific, as Ni residence time (~6000 years) (Johnson) is longer than mean mixing time of deep ocean of about 1500 years (Broecker and Peng 1982).

Concentrations of Pb in surface water show spatial-temporal variations and the distribution of this element has been strongly affected by anthropogenic activity. A historical peak surface Pb concentration of ~160 pM was observed in the North Atlantic in the 1970s because of the release of Pb from combustion of coal and especially the use of Pb as a fuel additive to gasoline (Boyle et al. 1986). Whilst Pb emissions have now been significantly reduced, the ocean has not returned to steady-state Pb concentrations and elevated Pb concentrations compared to a pre-industrial baseline are evident across most of the ocean. Present day surface Pb concentrations have decreased to ~20-30 pM in the North Atlantic and Pacific after elimination of leaded gasoline (Wu and Boyle 1997; Olivelli et al. 2023). Lead concentrations are higher by a factor of 3-6 in the northern hemisphere than in the southern hemisphere reflecting higher population densities and more intense anthropogenic activities in the middle and high latitudes of northern hemisphere (Boyle et al. 1986; Bridgestock et al. 2016).

Utilization of Zn by phytoplankton leads to depleted dZn concentrations of typically < 1 nM in the surface ocean, with extremely low concentrations of ~ 0.005 nM measured in some regions (Lohan et al. 2002; Wyatt et al. 2014; Conway and John 2015). Concentrations of dZn increase due to accumulation along the ocean conveyor belt from ~2–3 nM in the Atlantic to ~10 nM in the Pacific Ocean (Conway and John 2014, 2015),

as water masses age and remineralization facilitates the buildup of Zn inventories in deep waters.

## 1.2 Trace metal distributions

Away from the confounding influence of point sources, the vertical profiles of elements in the ocean can be categorized into different groups according to the dominant processes influencing the vertical distribution.

### 1.2.1 Nutrient-type trace metals

Distributions of nutrient-type TMs resemble macronutrients (fixed N, P and silicic acid) with depleted concentrations in surface waters due to phytoplankton assimilation and enhanced concentrations at depth due to the breakdown of organic matter exported from surface waters. Accumulation of nutrient-type TMs in deep waters is reflected in the longer residence time of nutrient-type TMs in the ocean (a few thousand to one hundred thousand years) compared to overturning time of the ocean conveyer (1500 years), and this explains why enhanced concentrations can be found in old, deep water masses (Bruland et al. 2014). This is particularly the case for Cd, which show strong correlations with nitrate ($NO_3^-$) and phosphate ($PO_4^{3-}$) (Baars et al. 2014; Middag et al. 2018). The residence time of Cd is estimated at ~50000 years comparable to macronutrients' residence time of tens of thousand years (Johnson). In contrast to Cd that closely resembles the distribution of $NO_3^-$ and $PO_4^{3-}$, the vertical profile of Zn in the world's oceans shows a positive linear correlation with silicic acid, suggesting similar processes including biological uptake by diatoms, remineralization and reversible scavenging play key roles in controlling the vertical distribution of Zn (Conway and John 2014; John and Conway 2014). Moreover, this tight relationship between Zn and silicic acid has recently been found driving by similarly increasing Zn and silicic acid in subsurface water masses from Nordic to Southern Ocean origin (Middag et al. 2019).

### 1.2.2 Scavenged-type trace metals

Scavenged-type TMs (e.g., Fe, Mn, Pb and Co) show a strong affinity to particles and consequently have relatively short oceanic residence times (<1000 years). These TMs

show relatively enhanced concentrations in close proximity to their sources. Aluminum and Pb are typical examples. A key contribution to Al and Pb is atmospheric input, and their characteristic distributions display elevated concentrations in the surface ocean and a decrease with depth as scavenging by sinking particles depletes the water column inventory (Orians and Bruland 1985; Boyle et al. 1986; Measures and Vink 2000). Iron and Co are influenced both by biological uptake and abiotic scavenging, as well as regeneration resulting in elevated concentrations in the deep ocean.

### 1.2.3 Redox-sensitive trace metals

Redox-sensitive TMs mainly include Fe, Co and Mn. Iron has two oxidation states, the more soluble Fe(II) and less soluble Fe(III), and concentrations exhibit strong sensitivity to pH, oxygen, and photochemically induced redox cycling (Zhu et al. 2021). Iron(II) can be rapidly oxidized to Fe(III) in the presence of oxygen or other electron acceptor such as nitrate ($NO_3^-$) and hydrogen peroxide (Scholz et al. 2016; Hopwood et al. 2020), and Fe(III) quickly forms Fe(III) oxyhydroxides which precipitate from the dissolved phase (Liu and Millero 2002). However, whilst the solubility of Fe(III) in inorganic forms is extremely limited, organic ligands including bacterially produced siderophores, terrestrially derived humic acids, and other less specific biological by-products (Gledhill and Buck 2012), can complex dFe and thereby enhance its solubility. Thus Fe(III) commonly exists at concentrations exceeding the inorganic solubility of Fe(III) (~0.01 nM). The vast majority, approximately 99%, of dissolved Fe(III) in seawater is thought to be complexed by organic material thus increasing the residence time and moderating the bioavailability of Fe (Bergquist and Boyle 2006).

Three oxidation states of Mn are present under natural conditions (dissolved Mn(II), particulate Mn(III) and Mn(IV)). Atmospheric deposition together with photo-reduction of Mn oxides sustain enhanced concentration of dMn in the sunlit surface ocean (Sunda et al. 1983). Bacterially-mediated oxidation of dMn can quickly produce insoluble Mn oxides in the dark below the euphotic zone and then dTMs is removed via sinking particle (Cowen and Bruland 1985; Sunda and Huntsman 1994; Moffett and Ho 1996). The solid oxidation state of Mn is less well characterized than Fe, but may be

extremely dynamic especially in coastal and OMZs (Noble et al. 2012; Jensen et al. 2020; Liu et al. 2022b; Al-Hashem et al. 2022).

Cobalt has the similar redox potential and can be actively incorporated into Mn oxides (Moffett and Ho 1996).

## 1.3 External sources and fluxes of trace metals at ocean boundaries

### 1.3.1 Atmosphere

Atmospheric aerosols have diverse sources, sizes, and chemical composition, and are important source of TMs to the open ocean (Mahowald et al. 2011). The impact of aerosols on seawater biogeochemistry and TM budgets depends on a range of factors including TM composition and solubility of aerosol TMs in seawater in addition to atmospheric processing of particles (Mackey et al. 2015). Previous studies have shown that aerosols contribute significant amounts of Fe to the surface ocean (Jickells 1999) and can increase surface Fe concentrations on short time scales (Bonnet and Guieu 2006). For other elements, specifically Co, atmospheric deposition may be relatively less important (Noble et al. 2012; Dulaquais et al. 2014), as a biogeochemical model suggests that dust is a minor but non-negligible source of Co to the North Atlantic (Tagliabue et al. 2018). The aerosol supply of other TMs like Cd, Cu, Mn, Ni and Zn to the Mediterranean has received increasing attention due to the strong anthropogenic origin of many metal enrichments in the basin (Jordi et al. 2012; Wuttig et al. 2013; Guieu et al. 2020).

Whilst the majority of studies concerning atmospheric deposition focus on the collection of dry aerosol samples, wet deposition (rainfall) is known to provide dissolved and potentially bioavailable forms of TMs (Kieber et al. 2003, 2005; Jickells et al. 2016). Atmospheric wet deposition is sparsely sampled for TM concentrations in the ocean due to the sporadic nature of events although wet deposition appears to contribute larger fluxes of TMs to many ocean regions than dry deposition (Chance et al. 2015; Shelley et al. 2017). This is substantiated by long-term measurements of rainfall metal concentrations at coastal sites (Kieber et al. 2001b; Willey et al. 2015) but it is challenging to extrapolate these observations to offshore environments where the

anthropogenic and terrestrial influences on rainwater chemistry are likely to be less pronounced, but sampling is more challenging.

### 1.3.2 Rivers

Global rivers discharge ~$1.3 \times 10^6$ m $s^{-1}$ of freshwater that contains TMs and thus constitute a major flux of most elements from continents to the ocean. For example, the Amazon river, which is the largest river in the world and discharge ~20% of global freshwater runoff, contributes ~$3 \times 10^4$ kg $day^{-1}$ Cu and ~$9 \times 10^4$ kg $day^{-1}$ Ni to the North Atlantic Ocean and accounts for 19% and 15% of the global riverine fluxes of these elements, respectively (Hollister et al. 2022). However, sharp changes of ionic strength, temperature, and pH occur when freshwater mixes with seawater in estuaries and cause reactive metals such as Fe, Mn, Pb and Zn to be removed from solution to a large extent (typically >50%) via salt-induced coagulation and precipitation of (nano-)particles and colloids (Boyle et al. 1977; Gledhill et al. 2022). As a consequence of scavenging on Mn and Fe oxide particle surfaces, an enhanced removal of Co can also occur. In contrast to Fe and Mn, desorption from particles mobilizes excess Cd and Ni to the estuarine water in the low-salinity zone (salinity <15), resulting in increasing concentrations of these elements compared to that expected from conservative mixing (Samanta and Dalai 2018; Hollister et al. 2022). Overall, highly dynamic processes in estuaries impact TM fluxes for particle-reactive elements which may diverge significantly from those assumed by conservative mixing of fresh and seawaters.

### 1.3.3 Seafloor (shelf, slope & bottom seafloor)

Continental margins represent both sources and sinks for TMs. Sediments deposited on continental shelves supply TMs to the overlying waters as measured with benthic flux chambers in different continental margins (Heggie et al. 1987; Pakhomova et al. 2007; Homoky et al. 2012; McManus et al. 2012; Plass et al. 2020, 2021) and evidenced by observations obtained close to the shelf sediment interface (Lam and Bishop 2008; Homoky et al. 2013; Nishioka and Obata 2017; Liu et al. 2022b). In addition, the widespread presence of plumes of elevated dFe concentrations that moves seaward from continental slopes (Nishioka and Obata 2017; John et al. 2018; Lam et al.

2020) suggests significant lateral dFe supply below the surface mixed layer. The presence of extensive dFe plumes from the upper slope can be related to a stabilized dFe(III) form (Lam et al. 2020) and/or release of Fe colloids by non-reductive dissolution (Homoky et al. 2013, 2021). John et al. (2018) proposed that downward transport of Fe by reversible scavenging initially mobilized from shelf and upper-slope sediments most likely contributed to and explained the presence of the deep Fe plume. The estimated Fe flux from shelf sediments is approximately three times the flux from slope sediments, but little of the mobilized Fe on the shelf travels beyond the shelf break, resulting in large amounts of Fe remaining trapped (Liu et al. 2022b). In contrast to Fe, the highest dCo concentrations occur at depths corresponding to the shelf and upper slope (Hawco et al. 2016; Noble et al. 2017). Cobalt is associated with Mn oxides which are a powerful scavenger of dCo, and the larger flux of organic matter to shelf and upper-slope sediments generate more reducing conditions than at greater water depths, and mobilize Mn as well as facilitating higher dCo concentrations due to less scavenging onto Mn oxide particles (Hawco et al. 2016; Noble et al. 2017).

An increased Cu to silicic acid ratio in bottom waters of the North Atlantic compared to the source water of Southern Ocean indicates an accumulation of Cu inputs from the sediments (Roshan and Wu 2015b). The interaction between pPb and dPb within the nepheloid layers is also recently considered as a source of dPb above the seafloor (Chen et al. 2023) and it has been demonstrated in several diverse environments worldwide that Pb appears to be dynamically exchanged between dissolved and labile particulate phases in shelf environments (Sherrell et al. 1992; Rusiecka et al. 2018; Krisch et al. 2022). Sediments are especially a sink for reactive species that are rapidly adsorbed onto sinking particles. For example, enhanced scavenging of protactinium, thorium and Pb have been found in the margins of tropical and eastern North Atlantic and Pacific (Bacon et al. 1976).

### 1.3.4 Hydrothermal systems

Hydrothermal vents act as a major source for a range of TMs to the deep ocean. It was long assumed that metals emitted from hydrothermal vents underwent rapid

precipitation when vent fluid mixed with ambient oxic seawaters (German and Seyfried 2013), and thus hydrothermal systems were not considered as a key TM source. However, recent studies on hydrothermal systems in the Atlantic and Pacific have demonstrated that they constitute significant sources of Fe, Mn, Al, Co and Zn to the ocean at mid-depths range (2000-3000 m) and can be laterally transported thousands of kilometers (Resing et al. 2015; Hatta et al. 2015; Roshan et al. 2016; González-Santana et al. 2020). Conversely, Pb and Cu are shown to be generally removed during the hydrothermal plume process suggesting a significant sink for these TMs (Noble et al. 2015; Jacquot and Moffett 2015).

## 1.4 Internal cycling of trace metal and associated fluxes in the water column

### 1.4.1 Biological uptake and remineralization

Biological uptake by the phytoplankton is one of the main processes depleting the TMs in the surface ocean and thus strongly influences TM behavior and distributions, particularly for Fe, Mn, Ni, Co, Cu, Cd, and Zn. Micronutrient uptake by organisms is typically proportional to either C or P (Twining and Baines 2013). Moreover, labile phases leached from bulk particulate material indicated that particulate TM are associated mainly with cellular material in surface waters (Twining et al. 2015) meaning that to a certain extent, labile phase can be used to interpret the biological uptake efficiency. Remineralization is a process that solubilizes nutrients from sinking particles at depth, thus replenishing TM inventories/increasing dTM concentrations. For example, Fe regeneration and further scavenging in the sub-surface ocean was shown by the linear relationship between dFe and apparent oxygen utilization (AOU) (Hatta et al. 2015; Tagliabue et al. 2019), suggesting that 60–90% of the biogenic Fe exported from surface waters either is not regenerated or is removed by scavenging soon after being regenerated in the North Atlantic (Hatta et al. 2015). A strong correlation between dCd and $PO_4^{3-}$ and enhanced uptake of Cd under conditions of growth limitation by Fe and/or other micronutrients in the Southern Ocean suggests a nutrient-like behavior of Cd and a biological requirement (Cullen et al. 2003; Cullen and Maldonado 2012). Remineralized Cd contributes 50% of total dCd above 1,000 m in the North Atlantic and generally dominates the dCd inventory above approximately 300 m depth (Roshan et al. 2017)

suggesting the internal cycling is an important process controlling the Cd behavior in the ocean. The distribution of Co is also influenced by biological uptake and regeneration, and by abiotic scavenging, like that of Fe, although Co is also associated with Mn oxides within the euphotic zone (Hawco et al. 2016, 2018). Despite the similar distributions of Zn and silicic acid in the ocean, only 1-3% Zn is incorporated into the opal frustules and most Zn is associated with phytoplankton organic tissue like $PO_4^{3-}$ (Collier and Edmond 1984; Ellwood and Hunter 2000).

### 1.4.2 Interplay of dissolved and particulate trace metal

The interplay of dissolved and particulate TMs including two opposing processes is presented here: 1) the dissolved TM pool concentration decreases due to scavenging and/or biological uptake and 2) the dissolved TM pool concentration increases due to release from particles through reverse scavenging, remineralization, or dissolution, etc. Both processes happen throughout the ocean at least to some extent, but biological uptake mainly occurs in the surface ocean and particle release and scavenging thus largely control dTM distributions at depth. Micronutrient elements like Fe, Ni, Cd, Co, etc are strongly controlled by biological uptake and sinking particles scavenging and thus depleted in the surface ocean. In the deeper ocean, the sinking particles (including biogenic and abiotic particles) release dTMs via reverse scavenging, remineralization and dissolution producing a profile classically shown by Co, Cd, Ni and Zn (Boyd et al. 2017). One critical zone for dissolved and particulate interaction is the shelf, where large amounts of sediments are transported from continental sources and deposited. In the shelf zone the pH and oxygen level change may affect the stability of dissolved phases, leading to the release or accumulation of TMs (Severmann et al. 2010; Plass et al. 2020; Zhu et al. 2021). A particularly sensitive area is the sediment–seawater interface, where anoxic environments may occur during early diagenesis in sediment, enhanced redox sensitive TM benthic fluxes to the overlying seawater (Shaw et al. 1990; Homoky et al. 2016).

## 1.5 Anthropogenic forcing on trace metals cycling in the ocean

Anthropogenic activities including industrial production, domestic combustion processer and manufacturing of chemicals and goods have released TMs into the

environment. Anthropogenic sources of TMs can exceed their natural abundance by a factor of 10 depending on the element (NRIAGU 1979). For example, increasing concentrations of Pb were observed in Mediterranean from ~10 pM to ~500 pM in the 1980s due to increased use of lead in gasoline (Kelly et al. 2009). Atmospheric depositions and river discharges are major vectors carrying anthropogenic emissions of TMs into the ocean. For Cd, Cu and Zn, anthropogenic emissions are dominated by metal production industries, for Mn by coal combustion and for Ni and vanadium by oil combustion (Pacyna and Pacyna 2001). A large fraction of anthropogenic metals (e.g., Cu, Ni and Cd) reaches the ocean by river discharge, like the Yangtze River (Wu et al. 2009) and Meghna River (Reza and Singh 2010). The history of anthropogenic emissions can be reconstructed by the vertical distributions of dPb in the oceans regionally for a specific period due to oceanic dPb residence time of ~2 years in near-surface waters and ~100 years in deeper waters (Henderson et al. 2018).

### 1.6 Thesis aim, objectives and outline

In this thesis, I provide a new dataset of TMs in the eastern South Atlantic from GEOTRACEs cruise GA08 (M121), including several key regions of the Benguela Upwelling System (BUS), Congo River margins (Congo shelf and offshore Congo plume) and oligotrophic open ocean. The key aim of M121 is to investigate the driving factors of TM distributions, identify sources of TMs and quantify their fluxes to and in the ocean. The main objectives of this study were to obtain an improved understanding of biogeochemical cycling of TMs in the eastern South Atlantic in terms of external sources including atmospheric depositions, Namibian shelf, the Congo River and water masses (Chapter 3 and Chapter 4), and internal processes including biological uptake and remineralization and scavenging (Chapter 5).

This thesis is an attempt to describe TM distributions in the eastern South Atlantic and investigate controlling factors for distributions of each TM. The key questions to this thesis are:

- Which factor controls TM distributions in the BUS? Is the Namibian shelf a source of TMs? How are fluxes of TM from the Namibian shelf and how is it compared to the atmospheric depositions? How is the influence or implication of TM supplies to local and global oceanic primary production?
- What is the reason for discrepancy of TM budgets and distal transport of TMs (particularly Fe) in the Congo plume? Is there any "missing" source of TMs significantly contributing to the plume?
- How is the internal cycling of TMs in oligotrophic open ocean? Is the interaction between dTMs and pTMs important for shaping TM distributions in the water column? Does recycling of TMs react to different states of oligotrophic ocean such as Fe limitation?

This work is composed of 6 chapters, including this introductory section. Chapter 2 describes the methods used for our analyses in more details, as only a briefer description is included in the individual chapter.

Chapters 3, 4 and 5 have been written as manuscripts for scientific journals. Chapter 3 investigates controlling factors on TM distributions in the BUS and estimates upward and off-shelf fluxes of dFe, dCo and dMn. This has been published in *Global biogeochemical cycles* under the title "*Sediment Release in the Benguela Upwelling System Dominates Trace Metal Input to the Shelf and Eastern South Atlantic Ocean*". Chapter 4 verifies an overlooked TM source, rainfall, across the Congo shelf. Rainfall can carry anthropogenic signals from gas flaring emissions to supplement the TM fluxes from the Congo River. This work is currently under review in *Geophysical Research Letters*.

Chapter 5 presents a discussion on internal cycling of TMs and sheds light on the interactions between dTMs and pTMs within the water column. This manuscript is currently in preparation for submission.

Chapter 6 is a summary of our major findings in this work and provides some views for future research standing on my current work in eastern South Atlantic.

# 2. Study site, materials and methods

## 2.1 Characteristics of study area

Samples were collected in the eastern South Atlantic between 22 November and 27 December 2015 during Meteor cruise M121 that was part of the international GEOTRACES program (GA08). The South Atlantic Ocean is influenced by the Atlantic meridional overturning circulation, connecting the Indian and Pacific Oceans as part of the global overturning circulation system (Kuhlbrodt et al. 2007). Our study area consists of several unique biogeochemical domains characterized by the Benguela Upwelling System (BUS) to the south, Congo River margins to the north and oligotrophic open ocean along ~0°E to the west (Figure 2.1).

The BUS is one of four major eastern boundary upwelling systems and has the highest primary production (Carr 2001). The South Atlantic and South Indian Ocean atmospheric anticyclones shift and interact with the continental low, thus creating upwelling-favorable alongshore winds (Hutchings et al. 2009). Wind-driven offshore Ekman transport of surface seawater is replenished by subsurface South Atlantic Central Water (SACW), which travels towards Africa and feeds the Benguela Current (BC). The BC includes two branches: one flows offshore as part of the South Equatorial Current (SEC); the other flows equatorward along the shoreline and meets the poleward Angola Current (AnC), creating the Angola-Benguela Front (ABF) (Peterson and Stramma 1991; Lass and Mohrholz 2008). An oxygen minimum zone (OMZ) is located at depths of ~100-200 m across the Namibian shelf due to intense remineralization of sinking organic particles and advection of oxygen-poor waters (Monteiro and van der Plas 2006).

The Congo River margin is characterized by large freshwater inputs from the Congo River, which is the second largest river in the world in terms of discharge volume (Denamiel et al. 2013). The Congo freshwater plume has been traced over ~800 km away from the river mouth partly due to low Coriolis forces near the equator that reduce plume dispersion (Hopkins et al. 2013). Low salinity surface waters corresponding to the Congo plume were detected along the ~3°S transect in our study area. To the west of the Congo plume, the South Equatorial Counter Current (SECC) makes up the cyclonic Angola Gyre in the eastern South Atlantic, which features a mixing-driven offshore upwelling in the Angola Basin to the east and is bounded by

the Equatorial Undercurrent (EUC) to the north (Stramma and Mathew England 1999; Brandt et al. 2015).

The open South Atlantic Ocean is oligotrophic and has a stratified water column. Surface waters are highly saline (salinity > 35.5) and consist of a small fraction of surface-advected Congo River plume in the north and Subtropical Mode Water with temperature above ~16°C (Stramma and Mathew England 1999). The SACW located between about 100 and 500 m depths, where nutrients are enhanced in concentration and oxygen is depleted to < 50 μM (Luyten et al. 1983). Antarctic Intermediate Water (AAIW) is found at depths between 500 to 1000 m and marked by a salinity minimum between 34.6 and 34.8 and potential densities between 27.13 and 27.55 kg $m^{-3}$. However, the fraction of AAIW in the water column decreases along its path from ~70% in the south (~40°S) to ~45% in the north (~0°S) (Broecker and Takahashi 1981). Underlying the AAIW, a southward flowing NADW is characterized by salinities of 34.9 to 34.97 and potential temperatures of 1.8 to 4.3°C and found at depths below 1500 m. Antarctic Bottom Water (AABW) was observed south of ~29°S; north of this latitude, the Walvis Ridge prevents its transport further north (Stramma and Mathew England 1999) (Figure 2.1).

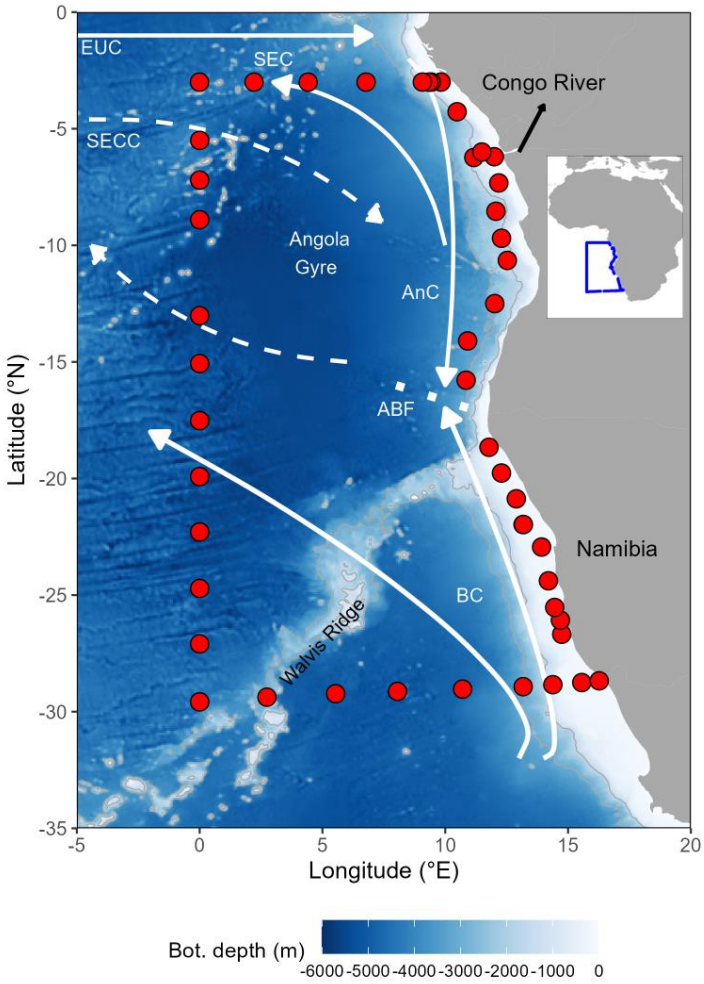


*Figure 2. 1 Map of study area with sampling sites (red circles) and major currents. Bathymetry is indicated by background color and with contour lines of 1500 m and 3000 m depths (light grey lines)* (Amante and Eakins 2009). *In-set shows a wider region of the cruse track.*

### 2.2 Sample collection

This section focuses on detailed sampling and analysis procedures that are not fully described in the following chapters. These include TM-clean sampling techniques for dissolved (filtrate through 0.8/0.2 µm Acropak$^{TM}$ 1000 cartridge filters) and suspended particles (residues on the 0.2 µm polyethersulfone (PES) membrane), preconcentration and analysis of dissolved TM (dTM), leaching and digesting of particulate TM (leachate: LpTM, digestion: RpTM). This study followed cleaning and sampling procedures that were previously described in details (Cutter et al. 2017). Preconcentration and analysis of dTM followed procedures detailed in Rapp

et al.(2017). Minor modifications on the techniques for leaching and digestion of pTM have been done in addition to procedures outlined by Berger et al. (2008) and Cullen & Sherell, (1999), respectively.

### 2.2.1 Pre-cruise/analysis preparation and cleaning

Careful handling of sample collection, filtration, storage, analysis for dissolved and particulate TMs was carried out to avoid potential contaminations. All bottles, filters, tubing, valves, connectors, filter-holders and petri-dishes used were made of TM-free materials and thoroughly acid-cleaned before usage.

Low density polyethylene (LDPE, Nalgene®), high density polyethylene (HDPE, Nalgene®) and glass bottles were used for TM, Fe(II), macronutrient and salinity and oxygen samples, respectively. All LDPE and HDPE bottles were cleaned with acids in the same manner separately. The acid-wash processes were (i) wiping and rinsing with ethanol to release oil/marker from manufacturing and labels, (ii) soaking for one week in 5% Mucasol detergent (Sigma-Aldrich®), (iii) rinsing three times with Milli-Q water (18.2 MΩ $cm^{-1}$, Milli-Q, Millipore®, hereafter as Milli-Q water), (iv) filling bottles with ~2 M HCl (reagent grade, Sigma-Aldrich®) without bubbles and soaking them in a ~2 M M HCl bath for one week, (v) rinsing three times with Milli-Q water, (vi) filling-up bottles with ~2 M $HNO_3$ (reagent grade, Sigma-Aldrich®) without bubbles and soaking them into a ~2 M $HNO_3$ bath for one week, and finally (vii) rinsing 5-6 times with Milli-Q water. Tubing, connectors, filter holders and petri-dishes were cleaned in the same sequence, but using acids with lower concentrations (1 M HCl, 1.6 M HNO3). Cleaned sample bottles and other plastic consumables were stored in sealed double bags until usage.

Fluorinated ethylene propylene bottles (FEP, Nalgene®) were used for preconcentration of seawater samples in the home laboratory. New FEP bottles were first cleaned following the same procedure as LDPE and HDPE bottles. Subsequently, FEP bottles were filled up with ~1M HCl (analytical grade, Sigma-Aldrich®) and exposed to UV-irradiation for 4 hours. We re-used these FEP bottles. Before each usage, FEP bottles were rinsed with Milli-Q water and filled with ~1 M HCl (Ultra Purity grade, Romil®) for >3 days at room temperature until the next use.

Perfluoroalkoxy alkanes (PFA) vials (7 mL and 30 mL, screw-cap, Savillex®) were used for leaching and digesting of suspended particle samples. The vials and lids were all acid cleaned following these steps: (i) wiping off labels with ethanol, rinsing three times with Milli-Q water and wiping the interior of vials and lids with dry Kimwipes (Kimberly-Clark Professional™), (ii) submerging into a 6 M HCl (reagent grade, Sigma-Aldrich®) bath and leaving the acid bath on a hotplate for 24 h at 90-120°C, (iii) rinsing three times with Milli-Q water after cooling down, then submerging into a 8 M $HNO_3$ (reagent grade, Sigma-Aldrich®) bath on a hotplate for 24 h at 90-120°C, (iv) after rinsing three times with Milli-Q water, adding ~1-2 mL digestion acid (8 M distilled $HNO_3$ and 5 M hydrofluoric acid (HF, Optima grade, Fisher Scientific®)) to cover the bottom of individual vial, capping the vials tightly and leaving them on a Teflon-hotplate (HPX-200, Savillex®) overnight at 150°C to reflux, (v) discarding the acid after cooling down and thoroughly rinsing vials and lids 5-6 times with Milli-Q water and leaving them to dry inside a laminar flow laboratory bench (class 100) before double bagging them. One should note that we use the same vials for certified reference materials (CRMs).

Pollypropylene (PP) vials (4 mL, scintillation vials, Fisher Scientific) were used for the collection of preconcentrated, leached and digested samples and ICP-MS analysis. They were cleaned in a similar manner as LDPE and HDPE bottles, but in different acid bathes. The PP vials and caps were first socked in 5% Mucasol detergent (Sigma-Aldrich®) for one week. After rinsing with tap water and Milli-Q water, PP vials and caps were submerged in a ~3 M HCl bath (analytical grade, Sigma-Aldrich®) for one week. After rinsing with Milli-Q water, PP vials and caps were next submerged in a ~2 M $HNO_3$ bath (analytical grade, Sigma-Aldrich®) for one week. After thorough rinsing with Milli-Q water, PP vials were dried under a laminar flow laboratory bench (class 100) and double bagged until use.

### 2.2.2 Sampling for seawater and particle

Full depth seawater samples between 10 and 6000 m at each station were collected using GO-FLO bottles (Ocean Test Equipment Inc., OTE) mounted on an epoxy coated Aluminum-CTD rosette (General Oceanics Inc., TM-CTD) attached to a conducting Kevlar cable. For some stations (2/51) with bottom depth < 50 m, GO-FLO bottles directly attached to the cable was

used to collect samples at individual depth. The TM-CTD was equipped with standard Seabird package including temperature, conductivity, pressure, oxygen and turbidity sensor.

Each GO-FLO bottle was closed using Seabird software when the cast was ascending to the desired depth, which allowed all bottles to be flushed with seawater on the downcast prior to sampling. Once the whole rosette was back on deck, the closed GO-FLO bottles were immediately transferred to the TM laboratory container where subsampling happened. Before subsampling, a filtered $N_2$ (0.2 μm, PTFE filter) overpressure (~ 1.2 bar) was applied to the GO-FLO bottles and an acid-washed tubing was connected to the valve. For dissolved TM seawater samples, 0.8/0.2 μm Acropak 500 cartridge filters (Pall®) were used and filtrate was dispensed into acid-clean 125 mL sampling bottles. New filters were flushed with >10 L of surface seawater, and always with ~500 mL of the sample prior to sample collection. In order to collect suspended particulate TM samples, an acid-washed filter-holder (Swinnex®) with 0.2 μm PES membranes (25mm diameter, Millipore®) inside was directly connected to the valve of the GO-FLO bottle and ~4 L seawater was filtered. Each PES membrane was rinsed with 50 mL Milli-Q water prior to usage. Opaque acid-clean HDPE bottles were filled entirely with unfiltered seawater for Fe(II), leaving no head-space to minimize the intrusion of oxygen. Another set of unfiltered samples for nutrient, salinity and oxygen analyses were directly collected in corresponding bottles.

A TM clean towed-fish system was used to collect surface seawater samples (depth ~3-4 m) along the whole cruise track. A Teflon diaphragm pump directly pumped seawater into the TM laboratory container through an acid-washed braided PVC tube. Seawater was filtered through the 0.8/0.2 μm cartridge filters (Acropak™ 1000, Pall®) into acid-clean 125 mL LDPE bottles.

All TM seawater samples were acidified to pH ~1.9 by an addition of 180 μL ultra-pure grade hydrochloric acid (HCl, Ultra Purity grade, Romil®) inside the laminar flow bench. Membranes with suspended particles were placed in acid-cleaned petri-dishes, double bagged and stored in a -20°C freezer. Macronutrients, salinity, oxygen and Fe(II) samples were analyzed onboard. Analysis of Fe(II) was immediately within 1.5 hour after subsampling. The TM

seawater samples were stored in the dark and shipped to GEOMAR, Kiel for further analysis. Suspended particle loaded PES filters were shipped frozen to GEOMAR, Kiel.

### 2.2.3 Sampling for rainwater

Rainwater samples were collected on an event basis using a collector placed at the topmost ($6^{th}$) deck where no on-board activities were taking place to avoid contamination. During the rain sampling, the vessel was always facing the wind to avoid contamination from the ship's exhaust, as the chimney was situated on the lower deck and behind the collector. The custom-made collector was made from a 25 cm diameter acid-cleaned polyethylene funnel mounted on a plastic frame with an opaque LDPE acid-clean bottles mounted underneath in a sealed cabinet. The cabinet was covered with plastic bags and was only opened manually when it rained while the ship was underway. Sampling of rainwater started at the start of each rain event and after rain events the funnel and LDPE bottle were replaced. Two aliquots of rainwater samples were syringe filtered (0.2 µm Millipore, polyvinyl difluoride) and unfiltered, respectively. Both filtered and unfiltered rainwaters were acidified to pH ~1.9 via an addition of 180 µL ultra-pure grade hydrochloric acid (HCl, Ultra Purity grade, Romil®) inside the laminar flow bench in a TM clean laboratory container. All samples were stored double bagged and shipped for analysis at GEOMAR in Kiel.

## 2.3 Dissolved samples pretreatment and trace metal analysis

Analyses of dissolved TM in seawater were performed exactly using the method developed by Rapp et al. (2017). Briefly, seawater samples were online buffered and pre-concentrated by a cation-exchange Wako resin (Wako Pure Chemical Industries, Japan) using a Sea*FAST* system (SC-4 DX Sea*FAST* pico, Elemental Scientific Inc.). Subsequent TM concentration analysis was performed on a high-resolution inductively coupled plasma mass spectrometer (HR-ICP-MS, ELEMENT XR, ThermoFisher Scientific).

Prior to preconcentration, 15 mL acidified seawater sample ($V_{sample}$) was mixed with 150 µL isotope spike solution ($V_{spike}$) containing enriched $^{111}$Cd, $^{65}$Cu, $^{57}$Fe, $^{62}$Ni, and $^{68}$Zn (ISOFLEX USA) for concentration calculation (de Jong et al. 2008) (*Equation 2.1*). Spike ratios ($R_{spike}$) for $^{110}$Cd/$^{111}$Cd, $^{63}$Cu/$^{65}$Cu, $^{56}$Fe/$^{57}$Fe, $^{60}$Ni/$^{62}$Ni and $^{66}$Zn/$^{68}$Zn were determined by multi-

collector ICP-MS (MC-ICP-MS; ThermoFisher Neptune) as 0.0037, 0.0146, 0.0146, 0.0530 and 0.0084. Original concentrations of each metal in the spikes were verified by ICP-optical emission spectroscopy (ICP-OES; 7500 Agilent) and reverse isotope dilution using MC-ICP-MS. The spike concentrations ($C_{spike}$) of $^{111}$Cd, $^{65}$Cu, $^{62}$Ni, $^{57}$Fe and $^{68}$Zn in this study were 52.2 nmol $L^{-1}$, 158.8 nmol $L^{-1}$, 148.4 nmol $L^{-1}$, 53.9 nmol $L^{-1}$ and 102.6 nmol $L^{-1}$ respectively. A six-point multi-element standard calibrating curve was additionally created for every batch of samples by a serial dilution of a concentrated multi-element standard into a low-TM surface seawater (spiked with Indium (In). The multi-element standard was produced by individual element stock standards of Al, Cd, Cu, Co, Fe, Mn, Ni, Pb, V and Zn (CentriPur, Merck®) for concentration calculation (*Equation 2.2*). All sample-spike mixtures were then UV-digested for 4 h in a home-made system equipped with four low pressure mercury vapor lamps (25 Watt, Philips®).

$$C_{sample} = \frac{V_{spike}}{V_{spike}+V_{sample}} \times C_{spike} \times \frac{^{2}A_{sipke}}{^{2}A_{nature}} \times \frac{R_{mixture}-R_{spike}}{R_{nature}-R_{mixture}} \qquad \textit{Equation 2.1}$$

*Note.* $^{2}A$ *represents the natural or artificial (spike) abundance of isotope 2, for example, for Cd is* $^{111}Cd$. $R_{mixture}$ *and* $R_{nature}$ *represent measured (mixture) and natural isotope ratios of each TM, respectively.*

$$C_{sample} = {}^{\frac{n_{sample}}{n_{In}}}\Big/_{Slope} \qquad \textit{Equation 2.2}$$

*Note.* $Slope$ *represents the slope of six-point calibration curve for each TM.*

Several reagents were prepared for preconcentration. The buffer solution, 1.5M ammonium acetate ($NH_4Ac$, pH 8.5 ± 0.05), was freshly made with glacial acetic acid (Optima grade, Fisher Scientific®) and ammonium hydroxide (20-22%, TraceMetal grade, Fisher Scientific®) for every batch of samples. 1M nitric acid used for rinsing and eluent acid were prepared by diluting in-house distilled nitric acid ($HNO_3$, Super Purity, Romil®, Savillex DST 1000) with Milli-Q water. Concentrated indium (In) solution (1000 or 10 μg $L^{-1}$, CentriPur, Merck®) was added into each eluent to a desired concentration of 250 ng In $L^{-1}$ for drift

correction during HR-ICP-MS analysis. Sample and reagent handling were always within an ISO 3 laminar flow bench equipped a with HEPA filter in a TM-clean laboratory at GEOMAR.

The preconcentration procedures on the automated system Sea*FAST* included: (i) loading a sample into a coil (10 mL) by a vacuum pump; (ii) loading the sample onto the resin whilst mixing with an optimized volume of buffer (~1.2 mL) to pH 6.4 ± 0.05 so that TM of interested were adsorbed on functional groups of chelating resin with negative charge; (iii) rinsing off the seawater matrix using Milli-Q water; (iv) cleaning the sample introduction parts with rinsing acid and eluting the sample using 1 mL elution acid (spiked with In) into 4 mL polypropylene (PP) vials for further analysis on the ICP-MS, (v) cleaning the whole pathway of introduction and resin using rinsing acid, and finally (vi) preconditioning the resin using the buffer and Milli-Q water. The Sea*FAST* system was placed in the TM-clean laboratory at GEOMAR.

Each pre-concentrated sample was analyzed for TM concentrations on a HR-ICP-MS. Calibration was carried out via isotope dilution only for Cd, Cu, Fe, Ni and Zn (*Equation 2.1*), and standard additions for all other TMs, including Co, Mn and Pb. Both calibration methods were done for Cd, Cu, Fe, Ni and Zn to verify calculations. High TM concentration samples (e.g. shelf stations) were diluted and re-analysized two to three times in different batches. Several procedural blanks in each batch were estimated including manifold blank (from eluent acid, the whole pre-concentration procedures and analysis on HR-ICP-MS) and buffer blank (Table 2.1) (Rapp et al. 2017). All reported TM concentrations in this study were corrected for total procedure blanks (manifold blank + buffer blank). Certified reference materials (CRMs) SAFe S, SAFe D2, GSP, GSC, CASS 6 and NASS 7 were routinely analyzed alongside seawater samples (Table 2.2).

*Table 2. 1 Analytical performance of dissolved trace metal measurements.*
*Trace metal procedural blanks from the SeaFAST and HR-ICP-MS systems (±1 standard deviation of repeated measurements (n)) as well as detection limits on the HR-ICP-MS (three times the standard deviation of the blanks: 3 × SD) (Rapp et al., 2017).*

| TMs | Procedural blank ± 1sd (pM) | n | Detection limit (3sd) (pM) |
|---|---|---|---|
| Fe | 60.6 ± 23.8 | 255 | 71.4 |
| Co | 1.9 ± 1.0 | 375 | 3.0 |
| Mn | 8.8 ± 3.5 | 360 | 10.6 |

| | | | |
|---|---|---|---|
| Cu | 17.0 ± 13.6 | 210 | 40.7 |
| Pb | 0.8 ± 0.8 | 375 | 2.4 |
| Zn | 144.2 ± 0.1 | 195 | 0.2 |
| Cd | 4.8 ± 2.6 | 135 | 7.7 |
| Ni | 412.4 ± 262.9 | 210 | 788.7 |

*Table 2. 2 Dissolved trace metal concentrations from seawater reference materials analyzed alongside seawater samples.*
*All values refer to means ± standard deviation. All concentrations are nM (nmol $L^{-1}$).*

| CRMs | TMs | Consensus/Reported value (nM) | Measured value (nM) |
|---|---|---|---|
| SAFe S [a] | Fe | 0.095 ± 0.008 | 0.106 ± 0.013 (n = 2) |
| | Co | 0.0049 ± 0.0012 | 0.005 ± 0.002 (n = 2) |
| | Mn | 0.81 ± 0.06 | 0.860 ± 0.099 (n = 2) |
| | Cu | 0.53 ± 0.05 | |
| | Pb | 0.049 ± 0.002 | |
| | Zn | 0.071 ± 0.010 | |
| | Cd | 0.0011 ± 0.0003 | |
| | Ni | 2.34 ± 0.09 | |
| SAFe D2 [a] | Fe | 0.956 ± 0.024 | 1.068 ± 0.275 (n = 2) |
| | Co | 0.047 ± 0.003 | 0.054 ± 0.004 (n = 2) |
| | Mn | 0.36 ± 0.05 | 0.303 ± 0.002 (n = 2) |
| | Cu | 2.34 ± 0.15 | |
| | Pb | 0.028 ± 0.0015 | |
| | Zn | 7.62 ± 0.26 | |
| | Cd | 1.011 ± 0.024 | |
| | Ni | 8.85 ± 0.26 | |
| GSC [b] | Fe | 1.535 ± 0.115 | 1.600 ± 0.156 (n = 9) |
| | Co[c] | 0.084 ± 0.004 | 0.117 ± 0.007 (n = 9) |
| | Mn | 2.180 ± 0.075 | 1.848 ± 0.340 (n = 9) |
| | Cu | 1.099 ± 0.149 | 1.293 ± 0.119 (n = 9) |
| | Pb | 0.039 ± 0.004 | 0.038 ± 0.004 (n = 9) |
| | Zn | 1.433 ± 0.103 | 1.307 ± 0.155 (n = 9) |
| | Cd | 0.364 ± 0.022 | 0.435 ± 0.037 (n = 9) |
| | Ni | 4.393 ± 0.205 | 4.270 ± 0.304 (n = 9) |
| NASS 7 [d] | Fe | 6.29 ± 0.47 | 6.67 ± 0.76 (n = 16) |
| | Co | 0.248 ± 0.024 | 0.235 ± 0.019 (n = 16) |
| | Mn | 13.63 ± 1.09 | 13.0 ± 1.74 (n = 16) |
| | Cu | 3.11 ± 0.22 | 2.78 ± 0.30 (n = 13) |
| | Pb | 0.013 ± 0.004 | 0.015 ± 0.012 (n = 10) |
| | Zn | 6.46 ± 1.23 | 6.55 ± 0.34 (n = 16) |
| | Cd | 0.143 ± 0.014 | 0.176 ± 0.039 (n = 16) |
| | Ni | 4.22 ± 0.32 | 3.96 ± 0.51 (n = 13) |
| CASS 6 [d] | Fe | 27.96 ± 2.15 | 28.10 ± 4.12 (n = 16) |

| | | |
|---|---|---|
| Co | 1.14 ± 0.09 | 1.05 ± 0.07 (n = 16) |
| Mn | 40.36 ± 2.18 | 36.26 ± 3.94 (n = 16) |
| Cu | 8.28 ± 0.50 | 7.98 ± 0.39 (n = 13) |
| Pb | 0.051 ± 0.02 | 0.043 ± 0.01 (n = 10) |
| Zn | 19.5 ± 2.77 | 18.2 ± 1.33 (n = 16) |
| Cd | 0.193 ± 0.016 | 0.219 ± 0.009 (n = 16) |
| Ni | 7.12 ± 0.68 | 6.86 ± 0.58 (n = 13) |

[a] *Bruland K.W., 2009. GEOTRACES and SAFe Intercalibrations, Consensus Values for the GEOTRACES 2008 and SAFe Reference Samples. Values were converted to molar units using a density of 1.025 kg $L^{-1}$.*
*In: https://www.geotraces.org/standards-and-reference-materials/*
[b] *In: https://www.geotraces.org/standards-and-reference-materials/*
[c] *Dissolved cobalt (Co) values reported by Wuttig et al., 2019 were obtained without UV digestion, representing only the labile fraction.*
[d] *NASS-7 and CASS-6 values refer to certified National Research Council Canada concentrations.*

Some freshwater samples including river and rain water were additionally analyzed. Both diluted and undiluted freshwater samples from the Congo River and rain water were analyzed including aluminum (Al). Samples was diluted using indium-spiked 1M HNO3 (distilled, Super Purity grade, Romil®).

### 2.4 Particulate trace metal analysis

After defrosting, suspended particle samples were first leached for the labile fraction (LpTM) (Berger et al. 2008) and then digested for the refractory fraction (RpTM) (Ohnemus et al. 2014). Both fractions were analyzed by HR-ICP-MS and calibrated by a 12-point external calibrating curve ranging from 0 nM to 400 nM as in *Equation 2.2*.

Leaching reagent containing 25% glacial acetic acid (Optima grade, Fisher Scientific®) and 0.02M hydroxylamine hydrochloride (99.999% trace metals basis, Sigma-Aldrich®) adjusted to pH ~1.8 and was freshly prepared every day before sample handling. 2.5 mL leaching reagent was first applied to the bottom of PFA vials (7 mL, screw-cap, Savillex®) before placing the PES filters with sample side down so that particles were in full contact with the reagent. The PFA vials were heated on a Teflon hotplate (HPX-200, Savillex®) fitted with heating blocks at 90°C for 10 minutes, then gradually cooled to 30°C. After a total duration of 2 hours, filters were removed and placed in their respective petri dishes waiting for digestion. Leachate was then

carefully transferred to 7 ml centrifuge tubes with pipettes and centrifuged at 14500 rpm for 10 minutes. The supernatant was transferred into acid-cleaned PFA vials (7 mL, screw-cap, Savillex®) and heated to dryness on a hotplate at 115°C. The leached fraction was subsequently dissolved in 4 mL 1M $HNO_3$ (distilled and spiked with In) at 80°C overnight.

Digestion reagent consisted of 50% v/v distilled $HNO_3$ and 10% v/v hydrofluoric (HF, Optima grade, Fisher Scientific®) and was freshly prepared for each batch of samples. 2.5 mL digestion reagent was added into the respective 30 mL PFA beakers (previously used for leaching samples). Leached filters were adhered to the wall of beakers, leaving sample side facing the interior of beakers and 0.5-1 cm distance to digestion reagent to avoid filter dissolution during digestion. The vials were tightly closed and heated on the hotplate at 150°C for 15 h to allow digestion reagent to reflux. After vials cooled down to room temperature, filters were taken out and digestion solutions were evaporated at 115°C to near-dryness. Samples were then resuspended in 500 µL freshly prepared oxidizing reagent consisting of 50% v/v distilled $HNO_3$ and 15% hydrogen peroxide ($H_2O_2$, for Trace Metal Analysis, Fisher Scientific®) and heated at 110°C to remove any presumable organic material (typically yellowish). After vigorous bubbling ceased, vials were uncapped and dried at 115°C to ensure removal of any HF left in the solution. The final dry residue was dissolved in 4 mL 1M $HNO_3$ (distilled and spiked with In) and heated at 80°C overnight.

*Table 2. 3 Trace metals values for solid reference materials analyzed alongside particulate trace metal samples.*
*All values refer to are means ± standard deviation.*

| TM | BCR 414 | | | | | PACS 2 | | | |
|---|---|---|---|---|---|---|---|---|---|
| | unit | certified[a] | reported[b] | measured | n | unit | certified[c] | measured | n |
| Al | µg g-1 | 2990±433 | 2107±309 | 1934±373 | 26 | % | 6.58±0.12 | 5.31±0.06 | 32 |
| Cd | µg g-1 | 0.383±0.014 | - | 0.404±0.064 | 32 | µg g-1 | 2.23±0.16 | 2.27±0.24 | 32 |
| Co | µg g-1 | 1.43±0.06 | - | 1.42±0.20 | 32 | µg g-1 | 12.1 | 11.6±2.5 | 32 |
| Cu | µg g-1 | 29.5±1.3 | - | 27.6±2.1 | 32 | µg g-1 | 326±10 | 302±22 | 32 |
| Fe | µg g-1 | 1850±190 | 1852±309 | 1686±184 | 32 | % | 4.106±0.064 | 3.43±0.22 | 32 |
| Mn | µg g-1 | 299±13 | 248±7 | 233±13 | 32 | µg g-1 | 432±16 | 380±26 | 32 |
| Ni | µg g-1 | - | 18.8±0.8 | 20.2±1.2 | 32 | µg g-1 | 39.5±2.2 | 41.3±4.8 | 32 |
| P | µg g-1 | - | - | 11185±755 | 32 | % | 0.0937±0.0044 | 0.0807±0.0057 | 32 |
| Zn | µg g-1 | 111.6±2.5 | - | 95.1±7.5 | 32 | µg g-1 | 376±12 | 331±23 | 32 |

[a] *Certified values of trace metals in the certificate of BCR 414 issued by European Commission-Joint Research Centre, Institute for Reference Material s and Measurements (IRMM) in http://www.irmm.jrc.be/;*

[b] *Reported values of trace metals of BCR 414* (Berger et al. 2008)*;*
[c] *Certified values of trace metals of PACS 2 can be found at GeoReM database* (Jochum et al. 2005)*, url: http://georem.mpch-mainz.gwdg.de/*

Alongside samples, two CRMs, BCR 414 (phytoplankton, for leaching and digestion) and PACS 2 (sediment, only for digestion), were weighed at ~0.02 g and digested in the same manner as the samples (Table 2.3). For each bath of samples, triple procedural blanks (leach blank, leach + digestion blank, and digestion blank) were also conducted on PES filters (0.2 µm, 25 mm, Millipore®) that previously filtered 4 L Milli-Q water (Table 2.4). All samples and CRMs were transferred into 4 mL PP vials for analysis on ICP-MS. ICP-MS counts were converted to concentrations using *Equation 2.2* and corrected for procedural blanks for each respective leach/digest batch. The concentration of target particulate TM ($C_{pTM}$) was subsequently produced by *Equation 2.3*.

$$C_{pTM} = (C_{pTM_{4mL\ solution}} - Blank) \times \frac{Mass_{4mL\ solution}}{Mass_{filtered\ seawater}} \qquad \textit{Equation 2.3}$$

*Table 2. 4 Sample blanks of each TM including blanks for leaching (Leach Blank), digestion (Digestion Blank) and total procedure.*
*Total procedure blanks are not necessarily equal to or exceeding the sum of leach and digestion blank as respective blanks were separately prepared in each preparation batch of samples.*

| TMs | Leach Blank | Digestion Blank | Total procedure blank |
|---|---|---|---|
| | | pM per filter | |
| Al | 1557±969 (n=27) | 1169±899(n=19) | 1786±919 (n=24) |
| Cd | 0.07±0.07 (n=27) | 0.04±0.04 (n=19) | 0.04±0.02 (n=24) |
| Co | 0.12±0.17 (n=27) | 0.21±0.27 (n=19) | 0.25±0.35 (n=24) |
| Cu | 27.4±13.2 (n=27) | 21.7±18.0 (n=19) | 33.8±25.0 (n=24) |
| Fe | 30.4±24.5 (n=27) | 29.0±25.0 (n=19) | 111±124 (n=24) |
| Mn | 1.03±1.71 (n=27) | 1.39±2.06 (n=19) | 1.30±1.49 (n=24) |
| Ni | 3.27±2.63 (n=27) | 3.45±2.38 (n=19) | 2.70±2.21 (n=24) |
| P | 110±82 (n=27) | 83±87 (n=19) | 251±173 (n=24) |
| Zn | 46.9±21.2 (n=27) | 43.7±33.6 (n=19) | 59.7±34.7 (n=24) |

### 2.5 Fe(II) analysis

Fe(II) was determined via flow injection analysis on a modified FeLume system using luminol chemiluminescence without preconcentration (Croot and Laan 2002; Hopwood et al. 2017) underneath a HEPA filter in the TM-clean laboratory container. The FeLume system was set up by 10-port valves (Valco®, Vici), a photomultiplier tube (PMT, H9319-11, Hamamatsu)

and a glass flow cell with a mirrored base (Waterville Analytical Products®). The luminol reagent consists of 0.13 g $L^{-1}$ Luminol (98%, Carl Roth), 0.53 g $L^{-1}$ $K_2CO_3$ (reagent grade, Roth®), 40 mL $L^{-1}$ $NH_4OH$ solution (Trace Metal grade, Fisher Scientific®) and 11 mL $L^{-1}$ concentrated HCl (Trace Metal grade, Fisher Scientific®) and Milli-Q water and was stored for >2 days in the dark prior to use. Briefly, seawater, luminol reagent and Milli-Q water were pumped using a peristaltic pump (MiniPuls 3, Gilson®). The PMT was secured inside an electrical box to minimize background light, and all reagent and sample tubing was opaque (black PTFE, Global FIA®, 0.8 mm internal diameter) except peristaltic pump tubing (PVC, Gradko®). Mixing of the sample and the reagent occurs after switching valve positions. Fe(II) was analyzed for at least four replicates for each sample. Standard additions were performed for each analytical run by spiking aged seawater with increasing amounts of an Fe(II) standard solution, which was prepared from ammonium Fe(II) sulfate hexahydrate (99.997% purity, Sigma Aldrich®) with Milli-Q water and acidified using 0.1% v/v HCl (Ultra Purity grade, Romil®). This stock solution was diluted daily with Milli-Q water to be used for standard addition.

### 2.6 Figures and statistical analysis

Figures were produced in R (version 4.1.3) or Ocean Data View (Schlitzer 2020). Data gridding in Figure 5.1 and Figure 5.3 - 5.4 was done following Barnes algorithm using R (Koch et al. 1983). All statistical analysis was performed in R (version 4.1.3).

# 3. Sediment release in the Benguela Upwelling System dominates trace metal input to the shelf and eastern South Atlantic Ocean

Te Liu[1]*, Stephan Krisch[1]†, Ruifang C. Xie[1,2], Mark J. Hopwood[1,3], Marcus Dengler[1] and Eric P. Achterberg[1]

Published in *Global Biogeochemical Cycles*

https://doi.org/10.1029/2022GB007466

[1] GEOMAR Helmholtz Centre for Ocean Research Kiel, Kiel, Germany.

[2] School of Oceanography, Shanghai Jiao Tong University, Shanghai, China.

[3] Department of Ocean Science and Engineering, Southern University of Science and Technology, Shenzhen, China.

†Now at Bundesanstalt für Gewässerkunde, Am Mainzer Tor 1, 56068 Koblenz.

**Abstract**

Upwelling of subsurface waters injects macronutrients (fixed N, P and Si) and micronutrient trace metals (TMs) into surface waters supporting elevated primary production in Eastern Boundary Upwelling Regions (EBUR). The eastern South Atlantic features a highly productive shelf sea transitioning to a low productivity N-Fe (co)limited open ocean. Whilst a gradient in most TM concentrations is expected in any off-shelf transect, the factors controlling the magnitude of cross-shelf TM fluxes are poorly constrained. Here, we present dissolved TM concentrations of Fe, Co, Mn, Cd, Ni and Cu within the Benguela Upwelling System (BUS) from the coastal section of the GEOTRACES GA08 cruise. Elevated dissolved Fe, Co, Mn, Cd, Ni, Cu and macronutrient concentrations were observed near shelf sediments. Benthic sources supplied 2.22 ± 0.99 μmol Fe $m^{-2}$ $d^{-1}$, 0.05 ± 0.03 μmol Co $m^{-2}$ $d^{-1}$, 0.28 ± 0.11 μmol Mn $m^{-2}$ $d^{-1}$ and were found to be the dominant source to shallow shelf waters compared to atmospheric depositions. Similarly, off-shelf transfer was a more important source of TMs to the eastern South Atlantic Ocean compared to atmospheric deposition. Assessment of surface (shelf, upper 200 m) and subsurface (shelf edge, 200 - 500 m) fluxes of Fe and Co indicated TM fluxes from subsurface were 2 - 5 times larger than those from surface into the eastern South Atlantic Ocean. Under future conditions of increasing ocean deoxygenation, these fluxes may increase further, potentially contributing to a shift towards more extensive regional limitation of primary production by fixed N availability.

## 3.1. Introduction

Trace metals (TM) including iron (Fe), cobalt (Co), manganese (Mn), cadmium (Cd), nickel (Ni) and copper (Cu) participate in a range of cellular processes that play a key role in phytoplankton growth and marine primary productivity (Twining and Baines 2013). Marine phytoplankton growth is often limited by the availability of macronutrients (nitrogen (N), phosphorus (P) and silicic acid (Si)) or the micronutrient Fe (Hutchins and Bruland 1998; Moore et al. 2013). Cobalt and Mn (co)limitation of marine phytoplankton growth has also been experimentally identified by in-lab culture and ship-board measurements (Saito et al. 2002; Browning et al. 2017, 2021; Wu et al. 2019).

The Benguela Upwelling System (BUS) off the Namibian shelf is the most productive one and has the highest carbon export of the four eastern boundary upwelling regions (EBUR) (Carr 2001). The upwelling of macronutrient-rich subsurface waters from the thermocline and on-shelf regeneration of nutrients in the euphotic zone of the BUS stimulates high phytoplankton growth (Dittmar and Birkicht 2001; Flynn et al. 2020).The subsequent sinking and remineralization of particulate organic matter depletes subsurface water oxygen concentrations which, in combination with poor ventilation in the subsurface, creates an oxygen minimum zone (OMZ, defined herein as oxygen < 90 µmol $kg^{-1}$) in the thermocline of the EBUR (Karstensen et al., 2008; Monteiro & van der Plas, 2006). Low oxygen concentrations overlying shelf sediments favor the release of redox-sensitive TMs (e.g., Fe, Co and Mn) (Homoky et al. 2012; Rapp et al. 2020) and alleviate Fe depletion relative to macronutrients in the upwelled waters, particularly where the shelf is broad (> 80 km) (Johnson et al., 1999; Lohan & Bruland, 2008; Moore et al., 2013; Bruland et al., 2005). The input of shelf sediment-derived micronutrients such as Fe to overlying waters is therefore critical for determining the identity of the (micro)nutrient proximally constraining primary production in OMZ regions (Browning et al. 2017, 2018). Yet quantifying how vertical and lateral fluxes of TMs scale with benthic release into the water column remains a key challenge in assessing to what extent OMZ expansion or contraction may be mediated by biogeochemical feedbacks (Landolfi et al. 2013; Wallmann et al. 2022). Observations regarding transport of TMs across shelf to the open ocean in OMZ regions are sparse limiting our understanding of the underlying processes defining spatial/temporal trends in TM (co)-limitation of primary production. The only study reported radium-derived TM fluxes across the shelf from the Peruvian OMZ also noted high uncertainty on the fluxes due to low sampling resolution and strong spatial variability in radium and TM concentrations (Sanial et al. 2018).

Here we present depth profiles of dissolved Fe, Co, Mn, Cd, Ni and Cu and macronutrient concentrations within the BUS as part of the GEOTRACES eastern South Atlantic Ocean GA08 cruise. The aim of this study was to quantify vertical and off-shelf fluxes of TMs to shelf surface waters and the eastern South Atlantic Ocean, and assess the relative importance of shelf sediment TMs sources on a regional scale.

### 3.2 Study Area

In the eastern South Atlantic Ocean, the poleward Angola Current and the equatorward Benguela Current converge at around ~15°S-17°S forming the Angola-Benguela Front. This divides the BUS into the Angola subtropical system in the north and the nutrient-rich BUS in the south (Stramma and Mathew England 1999; Shillington et al. 2006; Jarre et al. 2015). The Angola-Benguela Front and the southern tip of Africa (~35°S) thus mark the northern and southern boundaries of the BUS, respectively (Curl and Hill 1964) (Figure 3.1). The Benguela Current originates from two primary sources: the South Atlantic Current flowing from west to east as part of the South Atlantic subtropical gyre, and water flowing equatorward originating from the Agulhas Current (Garzoli and Gordon 1996; Mercier et al. 2003).

Coastal upwelling in the BUS is wind-driven. Alongshore equatorward winds driving offshore Ekman transport of surface waters, and wind stress curl driving Ekman suction near the coast, lead to cool and macronutrient-rich central water masses being upwelled to the surface (Nelson et al. 1996; Rae 2005; Bordbar et al. 2021). Upwelled water masses include macronutrient-rich and oxygen-depleted South Atlantic Central Water (SACW) and the well-oxygenated Eastern SACW (200 - 300 µM oxygen) (Rae 2005; Liu and Tanhua 2021). Wind-driven upwelling creates several distinct upwelling cells along the BUS coastline, of which the Kunene (18°S) and Lüderitz (27°S) cells are the most vigorous with high offshore advection and strong turbulent mixing (Hutchings et al. 2009; Bordbar et al. 2021). Our study region from ~17°S to 29°S has year-round upwelling while further south upwelling has a seasonal maximum during austral spring and summer, and weakens sharply in winter due to a seasonal change in wind direction and strength (Hutchings et al. 2009). This drives a hotspot of primary production (~ 976 g C $m^{-2}$ $yr^{-1}$) for the BUS (Chavez and Messié 2009).

The OMZ across the Namibian shelf results from a combination of oxygen consumption due to remineralization and southward advection of oxygen poor tropical waters (Mohrholz et al., 2008; Monteiro & van der Plas, 2006). The core of the coastal OMZ within our study area is at ~ 23°S - 26°S at depths of ~100 - 200 m. Oxygen concentrations are perennially < 90 µmol $kg^{-1}$ along the shelf and periodically suboxic (defined here as < 20 µmol $kg^{-1}$) during late austral summer to autumn due to poleward advection of SACW by the poleward under current situated on the shelf and the upper continental slope (Mohrholz et al. 2008; Junker et al. 2017).

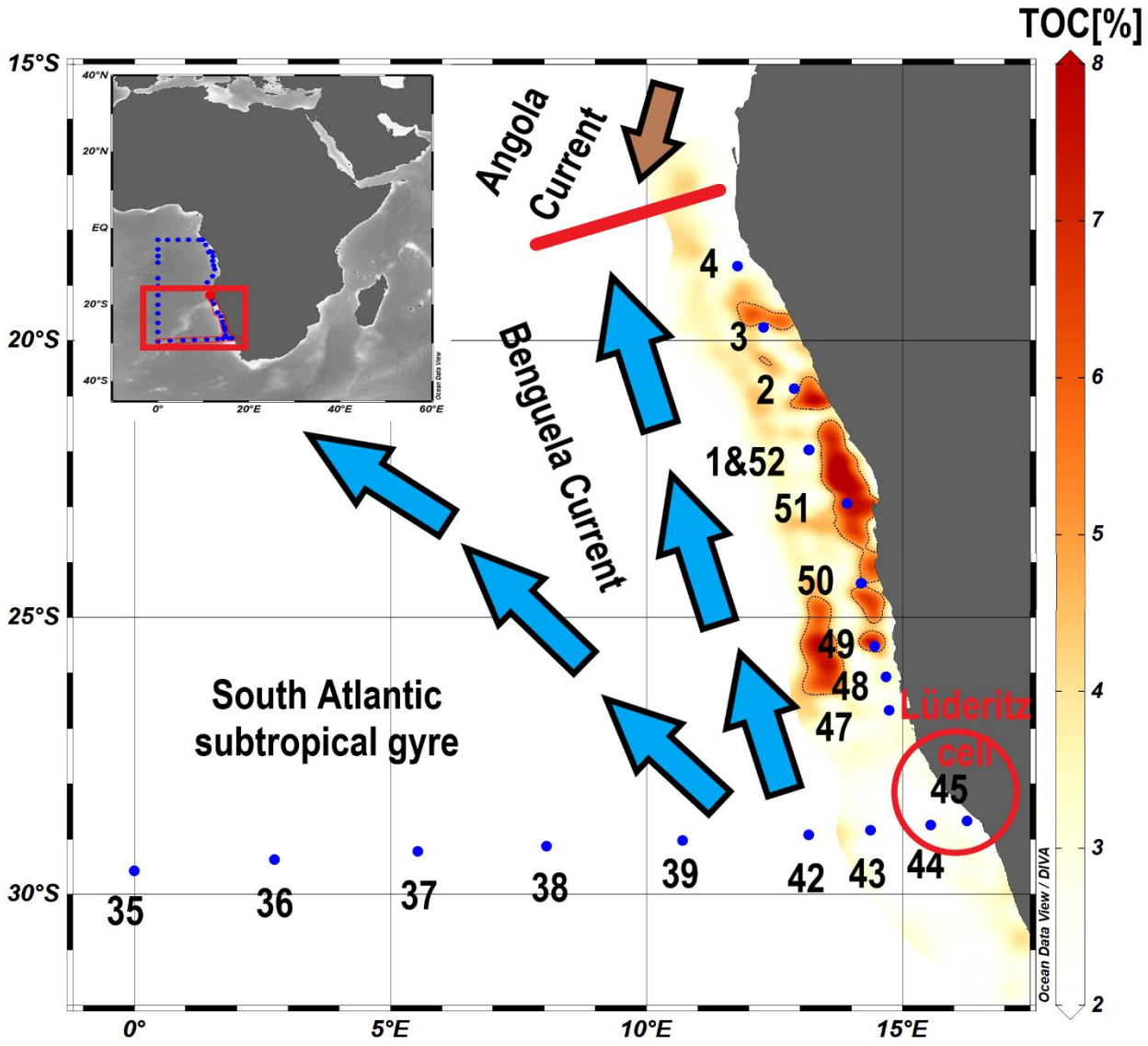


*Figure 3. 1 Map of the Benguela Upwelling System.*
*Panel on the left corner shows the whole GA08 cruise track and the red square shows our study area. Sample locations for trace metals are marked by blue dots with station numbers. Blueand brown arrows and the red circle indicate the Benguela Current, the Angola Current and Lüderitz cell, respectively* (Shillington et al. 2006; Hutchings et al. 2009). *The yellow-red shading refers to the Total Organic Carbon (TOC) content (wt%) of the surface sediments (TOC data is from Inthorn et al., (2006)* (Schlitzer 2020).

## 3.3 Materials and Methods

### 3.3.1 Seawater sampling and analysis

1) Dissolved trace metal seawater sampling

Seawater samples for dissolved TMs were collected on RV Meteor cruise M121 (GEOTRACES GA08) in the period 22 November to 27 December 2015 (late spring and early austral summer). This study focuses on samples in the BUS within the GA08 section between 17°S - 29°S (Figure 3.1). For contamination prone parameters, seawater was sampled using trace metal clean GO-FLO bottles (Ocean Test Equipment, OTE) on a powder coated aluminum CTD (Sea-Bird SBE25) rosette frame (denoted the TM-CTD), which was deployed using a Kevlar conducting cable. At Stations 1 and 2, single GO-FLO bottles were instead deployed on an aramid line because of a pronounced (4 - 5 m) swell preventing the deployment of the TM-CTD. Upon recovery of the TM-CTD, the GO-FLO bottles were moved to a custom-made clean laboratory container, where they were over-pressurized by filtered ~1.2 atm $N_2$ and seawater was subsampled through 0.8/0.2 μm cartridge filters (AcroPak® 1000) into 125 ml acid-clean, low density polyethylene (LDPE) bottles (Nalgene®). The Acropack filters were re-used between samples. New filters were flushed with at least 10 L of surface seawater, and always with at least 500 mL of the sample prior to sampling. The LDPE bottles and all plasticware for sample handling was pre-cleaned in a 3-stage process (1 day in Mucasol detergent, 1 week in 1.2 M HCl and 1 week in 1.2 M $HNO_3$) with 3 rinses of Milli-Q water between each stage. The filtered seawater samples were acidified to pH 1.9 via addition of 180 μL ultra-pure concentrated HCl (UpA grade, Romil®), double bagged in LDPE plastic bags and stored upright in the dark until analysis.

2) Dissolved trace metal analysis

UV-digested seawater samples were pre-concentrated off-line in a clean laboratory (ISO5) at GEOMAR using a WAKO chelate resin (Wako Pure Chemical Industries, Japan) on a seaFAST system (SC-4 DX SeaFAST pico, Elemental Scientific Inc.) exactly as in Rapp et al., 2017 . Calibration was carried out via isotope dilution for Fe, Ni, Cu and Cd, and standard additions for Mn and Co. Sample and reagent handling was performed within the same laboratory in an ISO 3 laminar flow bench with a HEPA filter unit. All reagents were prepared in Milli-Q water (18.2 MΩ cm)(Cutter et al. 2017). Nitric acid was distilled in house (Savillex DST 1000). High purity glacial acetic acid and ammonium hydroxide (Optima, Fisher Scientific) were used to prepare ammonium acetate buffer (pH 8.5). Each pre-concentrated sample was analyzed for TMs concentrations on a high-resolution inductively coupled plasma mass spectrometer (HR-

ICP-MS, ELEMENT XR, ThermoFisher Scientific). Data reported herein has been corrected for total procedural blanks (defined as manifold blanks plus buffer blanks) (Rapp et al. 2017). Certified reference seawater materials SAFe S, SAFe D2, GSP and GSC were routinely analyzed alongside seawater samples (Table 2.1 and Table 2.2).

3) Macronutrient and physical parameter analysis

Macronutrients sampled from the TM-CTD were analyzed for nitrate and nitrite (in the following termed $NO_x$), phosphate ($PO_4^{3-}$) and silicic acid ($Si(OH)_4$) on board by segmented flow injection analysis using a QUAATRO (Seal Analytical) auto-analyzer following (Grasshoff et al. 1999). A non-trace metal clean CTD system was deployed on a steel cable at each station. Oxygen, temperature, salinity, and depth were measured with sensors (Seabird) on the stainless steel CTD that was deployed alongside the TM rosette.

4) Fe(II) concentration analysis

Unfiltered samples for Fe(II) were collected from trace metal clean GO-FLO bottles into opaque acid-cleaned high density polyethylene bottles. Fe(II) analysis was carried out in a laminar flowhood with a HEPA filter within 90 min of subsampling of the GO-FLO bottles and in the order of the sample collection (deepest sample first). Fe(II) was determined via flow injection analysis on a modified FeLume system using luminol chemiluminescence without preconcentration (Croot and Laan 2002; Hopwood et al. 2017). Calibration via standard addition was conducted at each station on the same analytical run as samples. Peak heights from at least 3 peaks at 1 min intervals were used to calibrate the sample concentrations. The chemiluminescent response of luminol over broad ranges of Fe(II) concentration is non-linear which limits the calibration range at each station that can be made without adjusting the instrument sensitivity or diluting samples (which is analytically impractical given the sensitivity of Fe(II) decay to temperature, pH and dissolved oxygen). At stations with sharply elevated concentrations in the deepest samples a few Fe(II) concentrations (7 out of 51 total for the data herein) were beyond the highest standard addition (20 nM) and are therefore reported as >20 nM.

### 3.3.2 Flux calculations

For flux calculations, the water column was divided into two layers separated by the upper boundary of the OMZ (Figure. 2, density anomaly of ~26.5 kg $m^{-3}$). These two layers are

referred to as the surface layer and the shelf bottom layer in the following text. We are primarily interested in the upwelling flux of TMs from the shelf bottom layer to the surface layer, and the subsequent alongshore (northward) and offshore (westward) fluxes in the surface layer.

1) Vertical fluxes

Vertical TM fluxes result from vertical diffusive and wind-induced advective transfer. Here, we focus on the vertical transfer across the 26.5 kg $m^{-3}$ isopycnal, which is at depths of 20 - 50 m for shelf region. The vertical TM flux ($J_z$, μmol $m^{-2}$ $d^{-1}$) is described as (Jickells 1999):

$$J_z = K_z \frac{\partial[TM]}{\partial z} + w \cdot \Delta[TM] \quad (1a)$$

where $K_z$ is the turbulent diffusion coefficient ($m^2 \cdot s^{-1}$), $\frac{\partial[TM]}{\partial z}$ the vertical TM concentration gradient across the 26.5 kg $m^{-3}$ isopycnal (μmol $m^{-4}$), $w$ is upwelling velocity (m $s^{-1}$) at the base of 26.5 kg $m^{-3}$. $\Delta[TM]$ denotes trace metal concentration difference between the 26.5 kg $m^{-3}$ isopycnal and 10 m below this horizon in units of μmol $m^{-3}$ (Steinfeldt et al. 2015; Rapp et al. 2019).

Vertical turbulent diffusion coefficient ($K_z$) could not be determined from data collected during the cruise. An estimated $K_z$ of 1.0 - 1.7 × $10^{-4}$ $m^2 \cdot s^{-1}$ below the mixed layer at ~40°S of the South Atlantic Ocean was obtained in a previous study (Hsieh et al., 2020). Model-derived $K_z$ is broadly within the range of $10^{-6}$ - $10^{-4}$ $m^2 \cdot s^{-1}$ below the mixed layer based on temperature microstructure observations (Dunckley et al. 2012). We thus consider a $K_z$ of $10^{-4}$ $m^2 \cdot s^{-1}$ a reasonable value to use in our calculations.

For vertical advective flux quantification, the upwelling velocity ($w'$) at the base of the mixed layer (determined by a change in potential density $\Delta\sigma_\theta$ = 0.125 kg $m^{-3}$) (Monterey and DeWitt 2000) can be derived directly from the wind stress curl using Equations (1b) - (1c) (see e.g., (Bordbar et al., 2021; Gill & Adrian, 1982). Approximating a linear vertical decay of $w'$ that declines to zero at the ocean floor, we interpolated an upwelling velocity ($w$) for all stations along the Namibian shelf where the 26.5 kg $m^{-3}$ isopycnal is deeper than the mixed layer.

$$w' = -\frac{2\tau_y}{\rho f L_r} e^{2x/L_r} \quad (1b)$$

$$\tau_y = \rho_{air} C_D \lceil U \rceil U_y \quad (1c)$$

$\tau_y$ is the alongshore wind stress (N $s^{-2}$), $\rho$ the density of seawater (1025 kg $m^{-3}$), $f$ the Coriolis parameter as a function of latitude ($s^{-1}$), $x$ the distance from maximum Ekman divergence taken here as the position at 50 m isobath on the shelf. The first baroclinic Rossby radius ($L_r$, km) here used is 35 km (Chelton et al. 1998).

The monthly alongshore wind stress ($\tau$) was calculated within 60 nautical miles of the coast based on monthly wind speed magnitude ($\lceil U \rceil = \sqrt{U_x^2 + U_y^2}$, m $s^{-1}$) and alongshore wind speed ($U_y$, m $s^{-1}$) using Equation (1c) (Steinfeldt et al. 2015), where $\rho_{air}$ represents the density of air (1.225 kg $m^{-3}$) and $C_D$ is drag coefficient defined as $1.15 \times 10^{-3}$ here (Fairall et al. 2003). The monthly satellite scatterometer wind speed dataset is from Satellite Data Processing, Archiving and Distribution Center Satellitaire (CERSAT) at IFREMER, Plouzané (France) (file number 2015120100_2016010100_monthly-ifremer-L3-MWF-GLO-20160107162117-01.0). Our estimated upwelling velocities ($w'$) were generally on the order of $10^{-5}$ m $s^{-1}$ except a maximum upwelling velocity ($w'$) of $1.5 \times 10^{-4}$ m $s^{-1}$ determined at Station 47 of 26.7 °S, corresponding to the most vigorous Lüderitz cells where modelled upwelling rate was ~$1.5 \times 10^{-4}$ m $s^{-1}$ previously (Veitch et al. 2010). Due to uncertainties in the satellite wind product near the coast, we thus assume an error of 50% for the upwelling velocities (Verhoef et al. 2012; Rapp et al. 2019).

2) Shelf-to-ocean trace metal fluxes

The lateral off-shelf TM fluxes were calculated using the following one-dimension model (Glover et al. 2011; De Jong et al. 2012):

$$\frac{\partial TM}{\partial t} = -u\left(\frac{\partial TM}{\partial x}\right) + K_x\left(\frac{\partial^2 TM}{\partial x^2}\right) + J_x \quad (2a)$$

where $u$ is cross-shelf velocity (m $s^{-1}$), $K_x$ is off-shelf diffusive coefficient ($m^2$ $s^{-1}$), $\frac{\partial TM}{\partial x}$ is off-shelf gradient (nmol $L^{-1}$ $m^{-1}$) in TM concentrations (nmol $L^{-1}$) , $\frac{\partial^2 TM}{\partial x^2}$ (nmol $L^{-1}$ $m^{-2}$) is the second derivative of the TM concentration distribution with respect to the distance to the coast,

and $J_x$ represents source/sink processes. We assume steady state ($\frac{\partial TM}{\partial t} = 0$), and equation (2a) can then be rearranged as:

$$J_x = u\left(\frac{\partial TM}{\partial x}\right) - K_x\left(\frac{\partial^2 TM}{\partial x^2}\right) \qquad (2b)$$

Thus, the off-shelf flux divergence (µmol $m^{-3}$ $s^{-1}$) can be derived by equation (2b) because lateral flow in and out of the surface layer is the same under steady state. The depth of the surface layer (50 m at shelf stations, 200 m and 500 m at open ocean stations) multiplied by the off-shelf flux divergence (µmol $m^{-3}$ $s^{-1}$) yields the lateral off-shelf flux (µmol $m^{-2}$ $d^{-1}$).

Cross-shelf velocities ($u$, m $s^{-1}$) that represent the real advection offshore were determined by zonal velocities continuously measured throughout the cruise using a vessel-mounted phased-array acoustic Doppler current profiler (75kHz RDI Ocean Surveyor) and the shoreline orientation angle (21.4° from north) (Mohrholz et al. 2014; Bordbar et al. 2021). Velocities measured in the surface layer within 1° radius for stations were averaged and showed a generally off-shelf direction with $u$ ranging from 0.22 m $s^{-1}$ on the shelf to 0.03 m $s^{-1}$ in the open ocean. Taking a similar approach as in De Jong et al., (2012), the TM gradient is defined by the first derivative of the fitting power function of Fe, Co and Mn and the distance from the coast (m). The off-shelf diffusive coefficient $K_x$ was calculated from the empirical relationship $K_x$ = 0.0103 $l^{1.15}$ (Okubo 1971), where the scale length ($l$ in m) was defined as the distance that TM concentration decreases to $\frac{1}{e}$ of its initial concentration (Johnson et al. 1997). In our calculations, $K_x$ was within the range of $10^3$ $m^2$ $s^{-1}$ to $10^5$ $m^2$ $s^{-1}$.

3) Alongshore fluxes

The Benguela Current and the poleward undercurrent are well known advections governing the alongshore transportation of water masses (Peterson and Stramma 1991; Shillington et al. 2006; Veitch et al. 2010). Here, we use underway current velocity data from cruise M121 to calculate the alongshore flux as:

$$J_y = \int_0^z v\frac{\partial[TM]}{\partial y}dz \qquad (3)$$

where $v$ is the alongshore velocity (m $s^{-1}$), $\frac{\partial[TM]}{\partial y}$ is the alongshore TM concentration gradient (nmol $L^{-1}$ $m^{-1}$), and $z$ is the depth interval (m) of interest (here 50 m was used, approximately the depth of our defined surface layer).

Alongshore velocity ($v$, m $s^{-1}$) was obtained by zonal and meridional velocities from the same acoustic Doppler current profilers (VMADCP; 75kHz RDI Ocean Surveyor) and shoreline orientation angle with respect to the north (21.4°) (Bordbar et al. 2021). Velocities measured within 0.1° radian at shelf stations for the surface layer were averaged, resulting in an average equatorward alongshore current velocity of the surface layer of 0.008 m $s^{-1}$. Alongshore TM gradients were estimated from the difference in mean TM concentrations obtained by grouping stations and averaging TM concentrations within the surface layer on 1° × 1° grids.

## 3.4 Results and Discussions

### 3.4.1 Dissolved trace metal and macronutrient distributions

Concentrations of macronutrients including $NO_x$, $PO_4^{3-}$ and $Si(OH)_4$ were depleted in surface waters on the Namibian shelf and increased with depth (Figure 3.2). This trend was also observed for dissolved Fe, Fe(II), Co, Cd and Ni, due to release from shelf sediments interacting with the OMZ waters (Plass et al. 2021), biological drawdown in near-surface waters and remineralization at depth (Bruland et al. 2014). The highest concentrations of dissolved Fe, Fe(II) and Co were observed in near-bottom waters, reaching concentrations of 5.04 - 46.3 nM Fe, >20 nM Fe(II) and 0.19 - 0.44 nM Co, comparable to previous observations of Fe (7.9 nM) and Co (0.2 nM) for the same shelf area (Noble et al. 2012). Extremely high Fe concentrations in our study were similar to observations from the OMZ on the Peruvian shelf where bottom Fe concentrations over 30 nM have been observed (Bruland et al., 2005; Rapp et al., 2020). Enhanced concentrations of dissolved Mn were observed in near-bottom waters, but the maximum Mn concentration (16.2 nM) was observed in surface waters likely due to photo-reduction of Mn(IV) oxides to Mn(II) by sunlight coupled to an increased stability of Mn(II) (Sunda et al. 1983). For dissolved Cd, Ni and Cu, maximum concentrations were typically in bottom waters. Subsurface maxima at several stations (e.g., Station 1 - 3 and 48) suggest an intense subsurface remineralization of sinking organic matter with release of the nutrient-type trace elements (Biller and Bruland 2013). The southernmost, and shallowest station, (Station 45)

exhibited the highest Fe, Co, Mn concentrations (Mn, highest in surface and second highest in bottom waters) for the Namibian shelf (Figures 1 and 2).

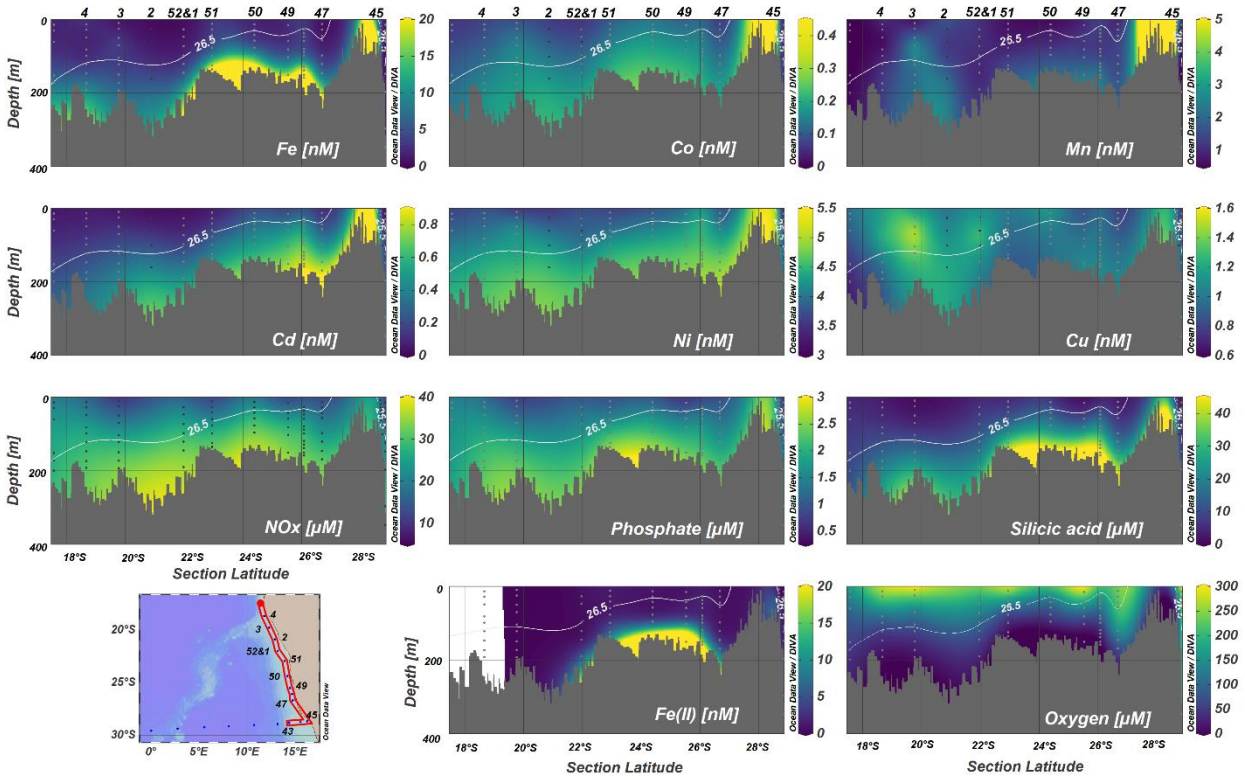


*Figure 3. 2 Shelf section plots of dissolved trace metals, Fe(II), $NO_x$ (nitrate + nitrite), oxygen, silicic acid and phosphate along the African coast for cruise M121.*
*White countour lines overlaying each panel indicate the 26.5 kg $m^{-3}$ isopycnal over the shelf. Station numbers are indicated on top of figures and the bottom left panel. Figures were produced using Ocean Data View* (Schlitzer 2020).

Compared to offshore stations, the most striking feature of TM distributions on the Namibian shelf was the enhanced concentrations in the OMZ, with, for example, dissolved Fe, Co and Mn concentrations consistently over 1.5 nM, 0.1 nM and 1 nM, respectively (Figure 3.2 and Figure 3.3). Similarly, enhanced concentrations of Fe, Co and Mn have been observed near our study area in the South Atlantic Ocean (Noble et al., 2012). Other EBUR including Mauritania, California and Peru also present enhanced Fe, Co and Mn concentrations within the OMZ (Biller and Bruland 2013; Sanial et al. 2018; Rapp et al. 2019). In contrast, $PO_4^{3-}$, silicic acid, dissolved Cd, Ni and Cu were less enhanced along the she, demonstrating a much smaller influence of low oxygen waters on these elements but a key driver on high concentrations of dissolved Fe, Co and Mn.

In the upper ocean along the shelf-to-open ocean transect at ~29°S, there was a sharp decrease in concentrations of Fe and Co moving off shelf (Figure 3.3). Conversely, distributions of dissolved Cd, Ni and Cu are lack of this features. The rapid decrease of Fe suggests an efficient removal of Fe by scavenging (Boyd and Ellwood 2010; Noble et al. 2012). Despite depleted Co in offshore surface water, relatively high Co concentrations were observed in subsurface water within the shelf plume (Figure 3.3), in agreement with observations along a zonal transect of the Peru upwelling system (Hawco et al. 2016; Sanial et al. 2018). There was also a persistent Mn maximum in offshore surface waters likely resulting from a combination of atmospheric deposition (Baker et al. 2006), photo-reduction (Sunda et al. 1983) and more efficient lateral transport of shelf sourced Mn than either Fe or Co (Sanial et al. 2018). Subsurface waters with elevated Fe, Co, Mn and $NO_x$ concentrations extended into the open ocean from the shelf edge at a depth of ~500 m (Figure 3.3). This plume was less noticeable for Mn, in agreement with observed subsurface Fe, Co and Mn plumes at ~15°S in the South Atlantic Ocean (Noble et al., 2012). This could be the results of inhibited Mn-oxide dissolution under dark conditions (Sunda et al. 1983) and/or a relative slower scavenging of organically complexed Fe and Co compared to Mn (Parker et al. 2007) along the oxic and organic-rich Namibian shelf edge (Noble et al. 2012). Deeper in the water column, a Fe plume at ~2000 m was observed (Figure 3.3), which is remarkably similar to a Fe slope plume observed in the eastern tropical South Pacific suggesting a similar mechanistic origin (John et al. 2018; Lam et al. 2020).

The overall offshore profile distributions of Fe, Co, Cd, Ni, Cu and macronutrients showed depleted surface ocean concentrations with an increase with depth. This reflects uptake in surface waters by microbial organisms and deep water remineralization of sinking / suspended biogenic particles (Bruland et al., 2014; Martin & Michael Gordon, 1988; Yee & Morel, 1996). Depth distributions of Cd and Ni at offshore stations showed strong similarities to those of phosphate, in agreement with other observations (Middag et al. 2018, 2020). Enhanced $NO_x$, phosphate, Cd and Ni concentrations were observed in the water masses of Antarctic Intermediate Water (AAIW) and Antarctic Bottom Water (AABW) relative to North Atlantic Deep Water (NADW), which is in agreement with general observations in the Atlantic Ocean (Middag et al. 2018, 2020). Silicic acid and Cu were mainly enriched in the deep and bottom

water masses of NADW and AABW. This behavior of Cu was also observed in the North Atlantic and the North Pacific Ocean (Bruland and Franks 1983; Roshan and Wu 2015b). Dissolved Cu concentration in the AABW along our transect were ~2.91 nM (Figure 3.3), similar to concentrations (~3 nM dCu) reported for the Southern Ocean (Heller and Croot 2015).

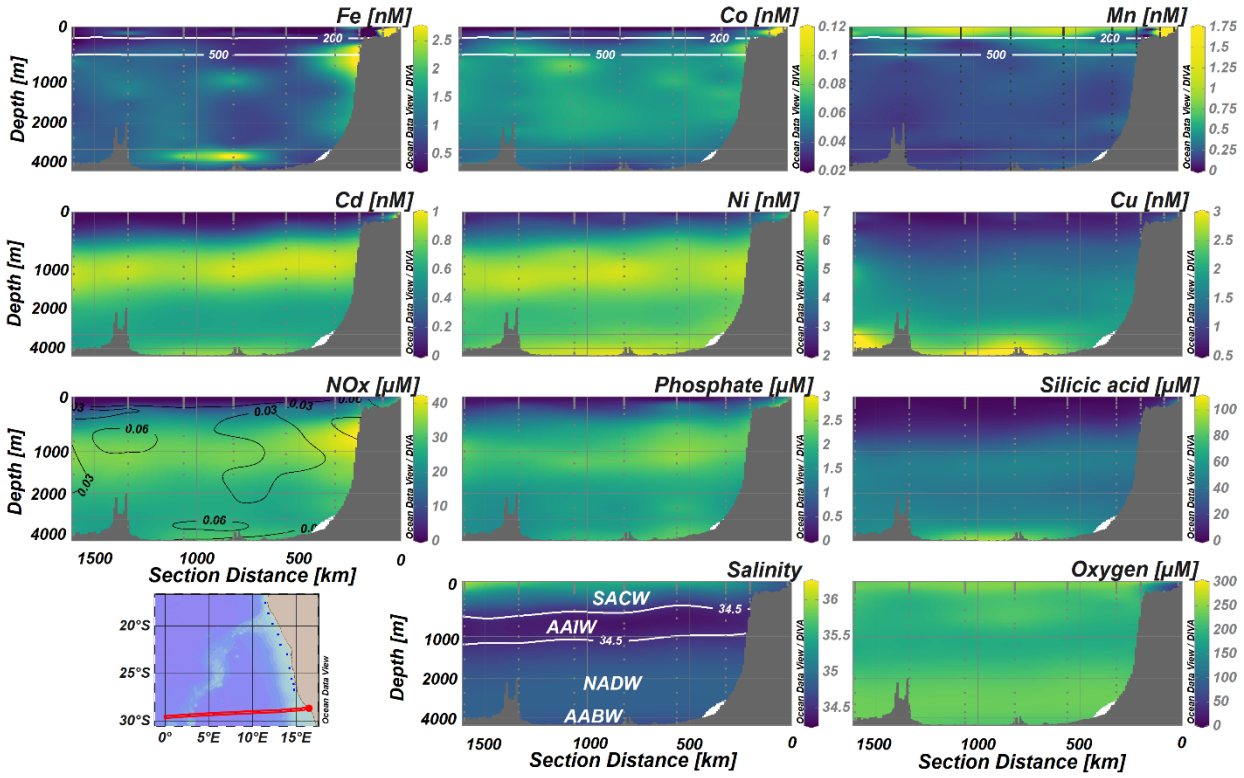


*Figure 3. 3 Zonal transect along 29°S section plots of dissolved trace metals, $NO_x$ (nitrate +nitrite), oxygen, silicic acid, phosphate and salinity in the Benguela Upwelling system from GA08.*
*Main water masses are indicated in the salinity panel* (Liu and Tanhua 2021). *SACW: South Atlantic Central Water, AAIW: Antarctic Intermediate Water, NADW: North Atlantic Deep Water, AABW: Antarctic Bottom Water. Numbers on the top are station numbers. The white horizontal lines on the Fe, Co and Mn panels denote 200 m and 500 m depth. Black countour lines in the $NO_x$ panel represent Fe : $NO_x$ = 0.03 and 0.06 nmol µmol$^{-1}$. Figures were produced by Ocean Data View* (Schlitzer 2020).

### 3.4.2 Controlling factors for trace metals in the Benguela Upwelling System

Various processes govern dissolved TM distributions in the BUS. We conducted a Principal Component Analysis (PCA) using the program R for the full BUS dataset to assess controlling factors of dissolved TM behavior and distribution in our study area (Figure 3.4, Table S3.1). Two principal components were clearly elucidated. The first principal component (PC1)

explains 51.7% of the variance and represents depth and Apparent Oxygen Utilization (AOU = $O_{2\ saturation} - O_{2\ observed}$) dependent variables including Cd, Ni, Cu and macronutrients. Nutrient-type TM distributions for Cd, Ni and Cu are similar to those of macronutrients and controlled by biological uptake in surface water and organic matter remineralization at depth. This is indicated by the positive Pearson correlations between Cd, Ni and all macronutrients, and between Cu and silicic acid ($r > 0.8$). Weaker Pearson correlations between Cu and $NO_x$ and phosphate ($r = 0.48$ and $r = 0.47$, respectively) are likely due to more pronounced benthic sources of Cu, and/or reversible-scavenging, both of which would contribute to a closer correlation between Cu and silicic acid than other macronutrients due to the deeper remineralization depth of silicic acid (Roshan and Wu 2015b)(Table S3.2). The second principal component (PC2, 29%) shows a passive association between redox-sensitive TMs (Fe, Co, Mn) and oxygen (Figure 3.4). Iron, Mn and Co are important micronutrients, but fall off the trajectory of nutrient-type elements as their distributions along our transect are also strongly influenced by water column oxygen levels alongside biological uptake and remineralization. Sediments overlain by low oxygen waters liberate dissolved reductive phase of Fe and Mn into overlying waters, and also release Co absorbed on Mn oxides. This contributes to enhanced benthic fluxes of Fe, Mn and Co (Shaw et al. 1990; Schroller-Lomnitz et al. 2019; Plass et al. 2020, 2021), explaining the discrepancies between Fe, Co and Mn and the 'classical' nutrient-type TMs observed. The sensitivity of Mn(IV) oxides to photochemical reduction in sunlit surface waters, and the enhanced stability of Mn(II) exposed to sunlight, explains the slight divergence between Fe and Co, and Mn in the PCA.

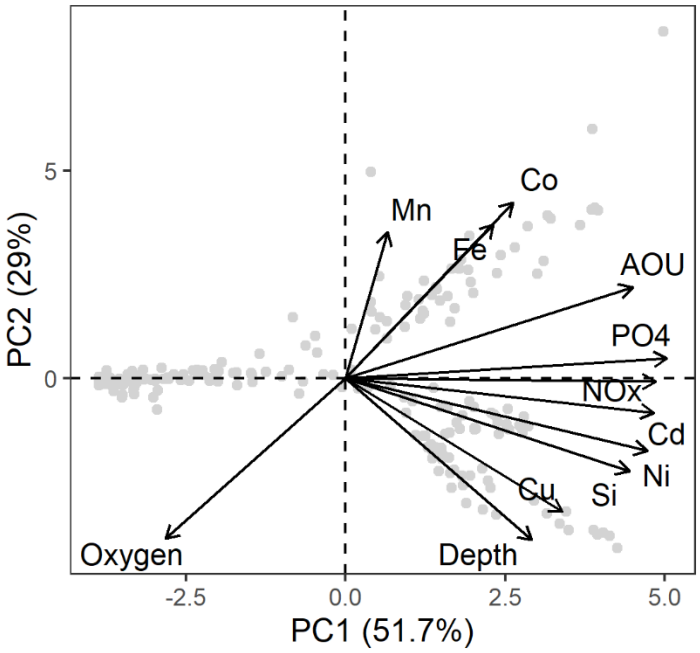


*Figure 3. 4 Principal component analysis of the M121 Benguela Upwelling system dataset. Principal component loadings for each variable are indicated by black vectors. Data points are shown by grey circles.*

1) Nutrient-type trace metals - Cd, Ni and Cu

Differences in the concentrations of Cd, Ni and Cu are clear between the AAIW, NADW and AABW along our ~29°S transect (Figure 3.5). Intermediate-depth Cd and Ni concentrations (0.84 ± 0.12 nM for Cd and 6.2 ± 0.5 nM for Ni) were higher than the average values of AAIW from its source in the Southern Ocean (~0.53 nM for Cd and ~5.59 nM for Ni) (Baars et al., 2014; Boye et al., 2012; Bruland & Franks, 1983; Middag et al., 2018, 2020; Xie et al., 2015, 2019) (Figure 3.5), probably due to a combination of mixing and accumulation of remineralized Cd and Ni along the northwards transit of AAIW from the Southern Ocean (Roshan and Wu 2015a). The accumulation of Cu in deep and bottom waters observed along our transect was similar to observations in the North Atlantic and the North Pacific (Bruland and Franks 1983; Roshan and Wu 2015b) (Figure 3.5).

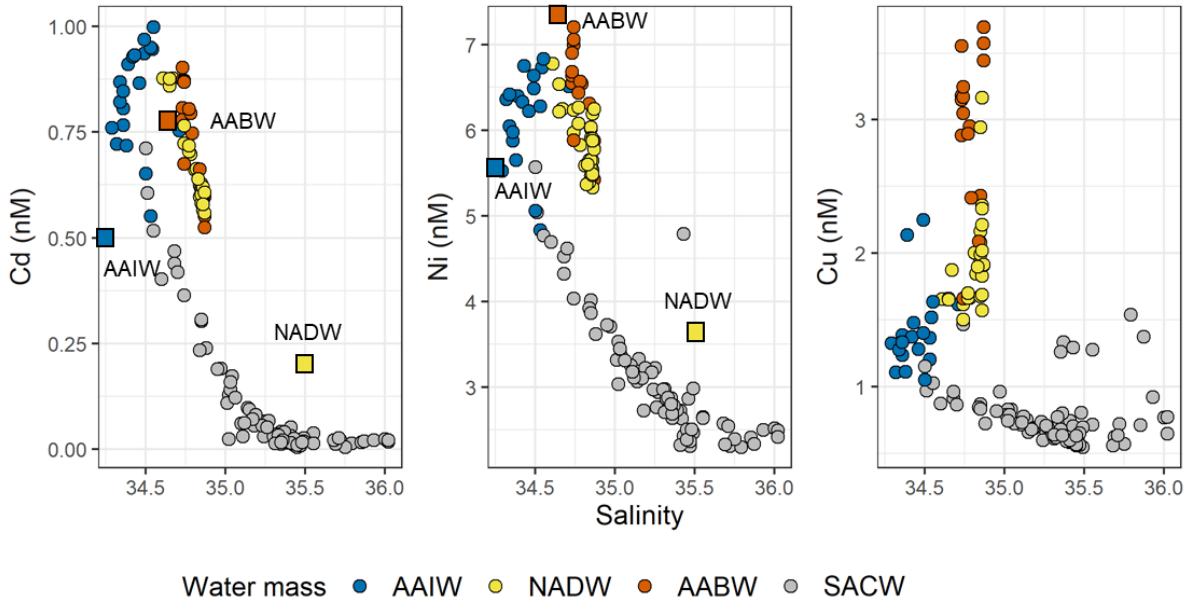


*Figure 3. 5 Plots of dissolved Cd, Ni and Cu concentrations against salinity along the ~29°S transect where water masses are subdivided by colors according to neutral density (Liu & Tanhua, 2021).*
*Blue: AAIW (Antarctic Intermediate Water); Yellow: NADW (North Atlantic Deep Water); Orange: AABW (Antarctic Bottom Water); Grey: SACW (South Atlantic Central Water). Colored rectangles are endmember water masses reported in prior works. The physical and chemical properties of the water masses in the eastern South Atlantic have been identified and described in Liu & Tanhua, (2021) and are summarized in Table S3.3 along with dissolved TM concentrations reported from previous studies (Baars et al., 2014; Boye et al., 2012; Bruland & Franks, 1983; Middag et al., 2018, 2020; Xie et al., 2015, 2019). Endmember concentrations of Cu in these water masses are unavailable to date.*

In the OMZ within and outside of the mud belt region (Figure 3.6, red and blue squares) we observed similar slopes of Ni, Cu and Cd (not outside mud belt at phosphate > 1 µM) vs. phosphate compared to ratios in phytoplankton (black dashed lines) (Figure 3.6) (Ho et al. 2003; Moore 2016a). This indicates that the supply of phosphate, Ni, Cu and Cd (not outside mud belt at phosphate > 1 µM) was determined by the remineralization of sinking phytoplankton debris derived from productive surface waters in the upwelling region. At low phosphate concentrations (phosphate < 1 µM) the slopes of Ni, Cu and Cd vs. phosphate at depths > 50 m in the open ocean (yellow solid lines) were comparable to those in the mud belt region and phytoplankton ratios (Figure 3.6). Steeper slopes of Ni, Cu and Cd vs. phosphate were observed in waters with enhanced phosphate concentrations, which can be explained by the Antarctic origin of these waters. Antarctic waters hold enhanced Cd to P (e.g. 0.32 - 0.36), Ni to P (2.1 - 2.5) (Middag et

al. 2018, 2020) and Cu to P (0.68 - 1.58) (Hassler & Ellwood, 2019; Janssen et al., 2020; this study) compared to waters with an Atlantic origin. An Antarctic influence on TM to phosphate ratios at enhanced phosphate concentrations is also noticeable in Figure. 6. The difference in the slopes of Cd vs phosphate between OMZ stations inside and outside of the mud belt region provides clear evidence against authigenic Cd removal in the upper OMZ water column as proposed in earlier studies (e.g. Conway & John, 2015; Janssen et al., 2014). Bottom dissolved Fe concentrations in the OMZ generally ranged between 5 nM and 30 nM at the mud belt stations and up to 46 nM outside the mud belt (Figure 3.2 & 3.6). The samples with highest phosphate concentrations (Figure 3.6, highlighted by black ovals) had moderate Cd, Ni and Cu concentrations and low oxygen concentrations (~13 μM), with > 25 nM Fe (Figure 3.2 and Figure 3.6). This implies a pronounced coinciding release of phosphate and Fe in the OMZ by reductive dissolution of iron oxy-hydroxides in sediments, compared to Cd, Ni and Cu (Figure 3.6 and the following discussions).

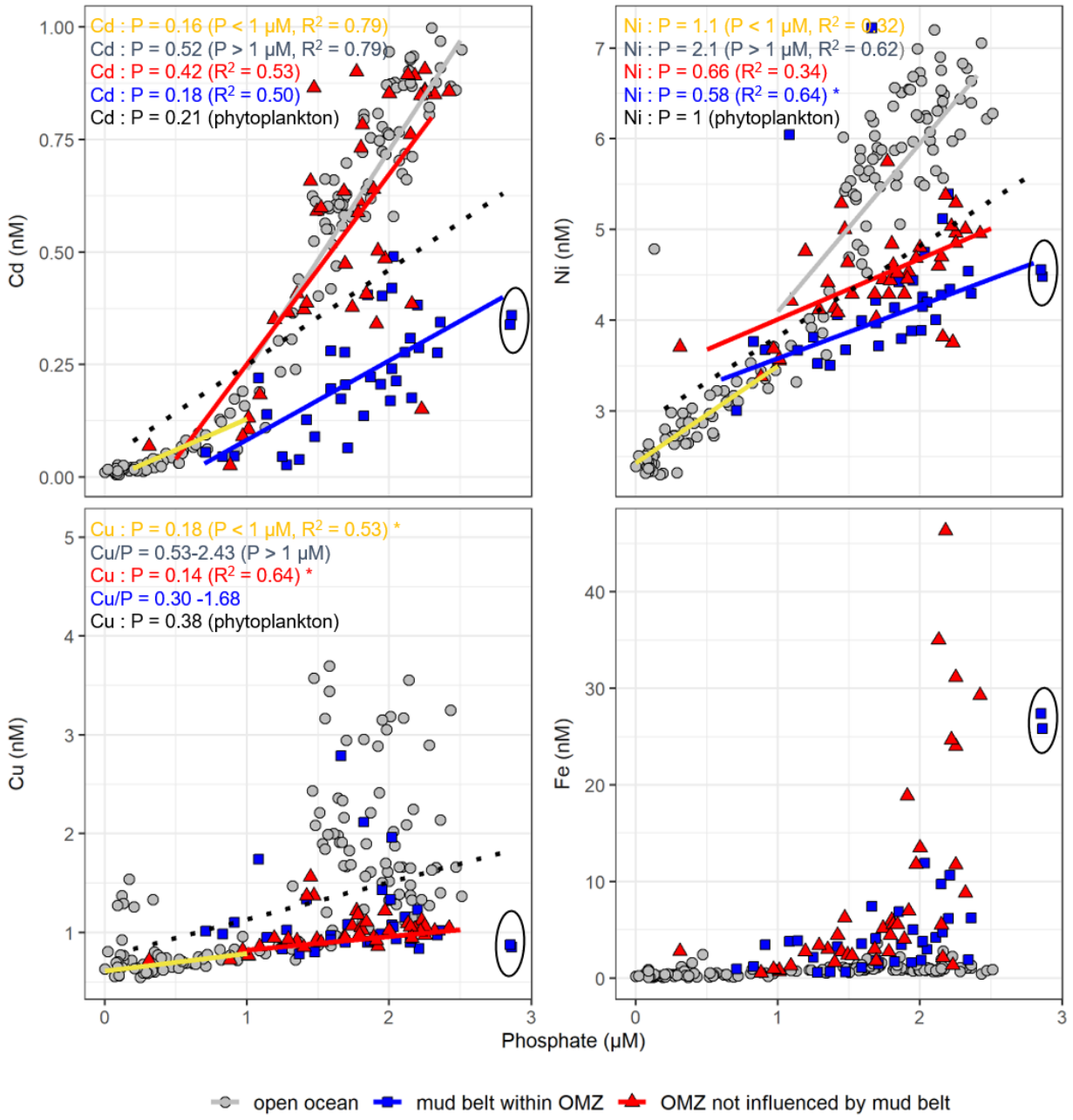


*Figure 3. 6 Plots of dissolved Cd, Ni, Cu and Fe against phosphate concentrations at different locations in the BUS.*
*Locations in open ocean include Stations 35 - 43. The location of mud belt extends from ~19°S - 24°S with sediment TOC > 3% and includes Stations 2 - 4 and Stations 51 - 52* (Bremner 1980; Borchers et al. 2005). *Stations 44 - 50 are marked as OMZ stations not influenced by the mud belt. Squares within the black oval represent highest phosphate concentrations. Cu/P denotes the spot ratio of Cu to phosphate in different regions, where slopes of Cu v.s. phosphate show weak correlations ($R^2$ < 0.3). Black dotted lines indicate TM = $[TM/P]_{phytoplankton}$ × phosphate + $[TM]_{preformed}$, where $[TM/P]_{phytoplankton}$ is from the average TM stoichiometry in phytoplankton (Ho et al., 2003; C Mark Moore, 2016)and $[TM]_{preformed}$ is mean TM concentrations in the upper*

*200 m of the open ocean. * Note datapoints with Ni > 5 nM and Cu > 1 nM were not included in the respective fit.*

2) Redox-sensitive trace metals - Fe, Co and Mn

The co-occurrence of elevated concentrations of Fe, Co, Mn and Fe(II) in suboxic bottom waters on the Namibian shelf (Figure 3.2), and their close clustering in a PCA analysis, point towards a common source for these redox-sensitive TMs. Enhanced Fe(II) concentrations of >20 nM in bottom waters indicate that reductive dissolution of sedimentary Fe(III) oxy-hydroxides is the mechanism driving enhanced near-bottom Fe concentrations (Pakhomova et al. 2007; Noffke et al. 2012; Plass et al. 2020). Soluble Fe(II) is rapidly oxidized to particulate Fe(III) in the presence of oxygen (Millero et al. 1987), and may also be oxidized under anoxic conditions via coupling to $NO_3^-$ reduction (Scholz et al. 2016). Upon oxidation of dissolved Fe(II) to Fe(III), Fe precipitates lowering dissolved Fe concentrations in the water column (Figure 3.7). Similarly, slightly increased Mn and Co concentrations in low oxygen waters of the Namibian shelf are likely due to enhanced release from sediments combined with slower oxidations kinetics (Figure 3.7) (Noble et al. 2012; Hawco et al. 2016).

Concentrations of Fe, Co, Mn and Fe(II) in the water column increased as oxygen levels decreased from 100 μM to <10 μM (Figure 3.7). Their increase under suboxic conditions (oxygen < 100 μM) was highest for Fe(II) followed by Fe and Mn, whilst changes in Co concentration were less noticeable as oxygen levels decreased in the water column (Figure 3.7). This observation is in line with a study in the same region that demonstrated Mn and Co have a relatively slow oxidation rate under these conditions (Noble et al., 2012). As sedimentary Co delivery is generally associated with Mn-oxides, the impeded oxidation of dissolved Mn under low oxygen conditions is likely a major driver of elevated dissolved Co levels (Heggie and Lewis 1984). An external shelf source of Fe, Co and Mn is evidenced by their enhanced concentrations for a given AOU in shelf bottom layer compared with open ocean waters (Figure 3.8), where relationships between Fe, Co and Mn and AOU are shaped by physics, remineralization and scavenging (e.g. Tagliabue et al., 2019). Collectively, all lines of observations provide strong evidence of shelf sedimentary supply of Fe, Co and Mn, where suboxic/anoxic environments facilitate the release of these redox-sensitive TMs from shelf sediments into the overlying waters.

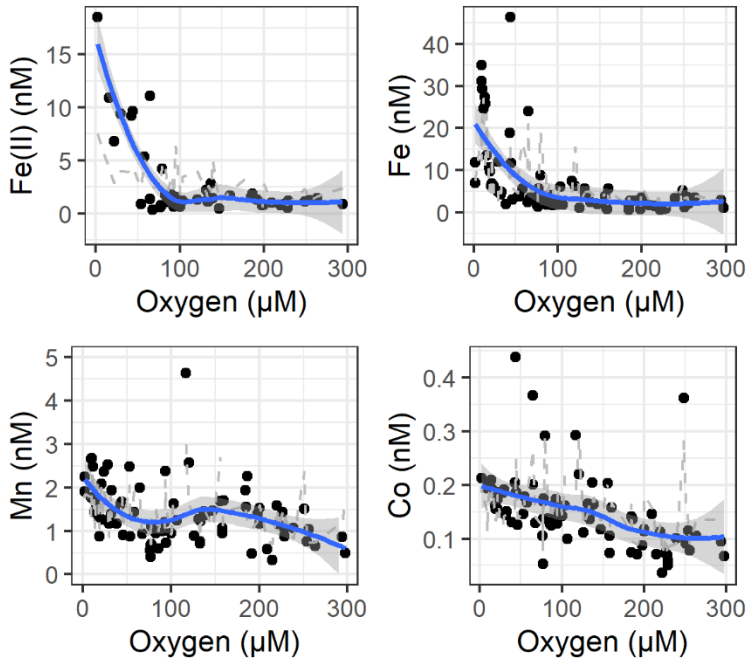


*Figure 3. 7 Plots of Fe(II), dissolved Fe, Co, Mn against oxygen concentrations for the Namibian shelf.*
*Grey dashed and blue solid lines indicate five point weighted moving average and its smoothed line, respectively, with a grey shaded 95% confidence interval. Note three datapoints with Mn > 5 nM are not shown (but are included in the fit).*

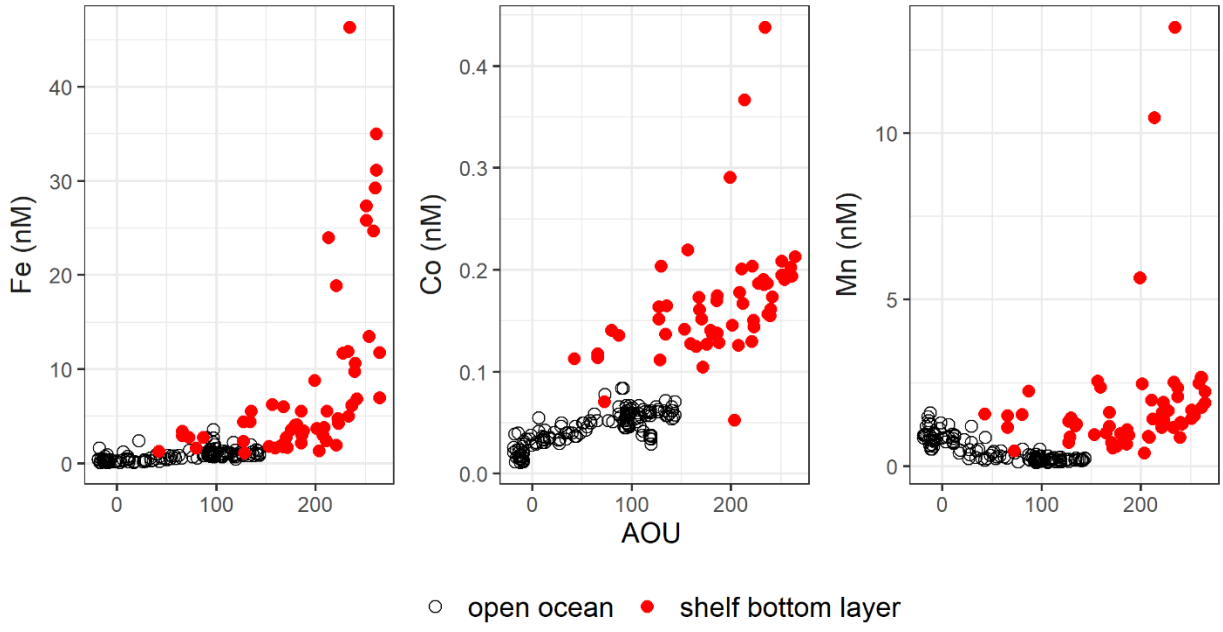


*Figure 3. 8 Plots of dissolved Fe, Co and Mn concentrations against apparent oxygen utilisation (AOU).*

*Open circles are all data points in the open ocean. Red circles are data points deeper than the 26.5 kg $m^{-3}$ isopycnal (the shelf bottom layer) on the Namibian shelf.*

### 3.4.3 Supply of sediment-derived trace metals to shelf surface waters and the open ocean

1) Vertical fluxes of sediment-derived Fe, Co and Mn to surface waters on the shelf

Coastal regions of the BUS are highly productive and no experimental evidence of micro(nutrient) limitation was detected along our shelf cruise section indicating nutrient-replete conditions for primary producers (Browning et al. 2017). However, dissolved Fe, Co and Mn are deficient relative to macronutrients in the offshore upwelled subsurface waters (e.g., Fe : N = 0.02 - 0.07 nmol $\mu mol^{-1}$, Figure 3.3). Consequently, supplies of TMs such as atmospheric deposition (Jickells et al. 2005; Ventura et al. 2021) and shelf sediments (Johnson et al. 1999) are critical to sustaining high levels of primary productivity on the shelf. We first constrain the vertical fluxes of sediment-derived TMs to shelf surface waters and compare our estimated vertical sediment-derived TM fluxes to those from atmospheric deposition (Barraqueta et al. 2019) in order to determine their relative importance to shelf surface waters.

In general, the net upward supply of Fe, Co and Mn across the 26.5 kg $m^{-3}$ boundary over the shelf is positive (Table 3.1), indicating a net TM supply to surface waters from shelf bottom layer. Average vertical Fe and Co fluxes (2.22 ± 0.99 μmol Fe $m^{-2}$ $d^{-1}$ and 0.05 ± 0.03 μmol Co $m^{-2}$ $d^{-1}$) on the Namibian shelf are similar to reported vertical Fe fluxes of 1 - 2.5 μmol $m^{-2}$ $d^{-1}$ and Co flux of 0.03 - 0.11 μmol $m^{-2}$ $d^{-1}$ on the Mauritanian shelf with similar seafloor depths (Table 3.1) (Rapp et al. 2019). Relatively high vertical Fe fluxes were reported for the very inner shelf of Mauritania (13 μmol $m^{-2}$ $d^{-1}$) and Senegal at ~12°N (16 μmol $m^{-2}$ $d^{-1}$) (Milne et al. 2017; Rapp et al. 2019), which are ~3 times higher than fluxes at our inner shelf stations (Station 45 and 47, 4.7 ± 1.4 μmol $m^{-2}$ $d^{-1}$ and 4.1 ± 1.9 μmol $m^{-2}$ $d^{-1}$, respectively, Table S3.4). A fraction of TMs reaching surface waters will be transported offshore (Lohan and Bruland 2008; De Jong et al. 2012) and alongshore (Freund 2020). Our estimates show that alongshore TM fluxes to the north are minor (Table 3.1). Alongshore fluxes of Fe, Co and Mn are < 5% of their respective upward fluxes.

Atmospheric inputs of TMs are relatively small compared to vertical inputs via upwelling and diffusion to the shelf surface waters. An aluminum-derived estimate of aerosol deposition is ~0.36 g $m^{-2}$ $yr^{-1}$ in coastal region of the BUS for cruise M121 (Barraqueta et al., 2019). To derive the associated TM fluxes, we assume the composition of dust entering the eastern South Atlantic was the same as the upper continental crust average (5 wt% for Fe, 0.1 wt% for Mn, 0.02 wt‰ for Co, Rudnick & Gao, (2014)) as TM-to-aluminum ratios in aerosols from the South Atlantic are similar to the ratio in upper continental crust (Baker et al. 2013; Jickells et al. 2016; Shelley et al. 2017). This assumption is an over simplification as the TM composition of aerosols can be highly variable depending on origin, distance to sources and deposition pathways (wet or dry deposition). However, our study area (~15-29°S, 0-17°E) is dominated by dry-deposition with a mean precipitation rate of~0.15 mm $d^{-1}$ during November and December (Figure S3.1), which is almost one order of magnitude lower than reported for the region between ~35 - 40°S (Chance et al. 2015). Aerosol trace metal solubility is similarly dependent on multiple factors and varies regionally and temporally. Here we use 7% for Fe, 20% for Mn, and 0.15% - 0.73% Co as obtained from measurements using aerosols over the eastern South Atlantic (Chance et al. 2015). Our derived aerosol TM fluxes are thereby 0.06 μmol Fe $m^{-2}$ $d^{-1}$, 0.004 μmol Mn $m^{-2}$ $d^{-1}$ and 2.1× $10^{-6}$ μmol Co $m^{-2}$ $d^{-1}$ in the shelf surface water, respectively, which are within the range of previous dry-deposition estimates of Fe, Co and Mn between ~35 - 40°S (~0.002 - 0.135 μmol Fe $m^{-2}$ $d^{-1}$, 0.0001 - 0.009 μmol Mn $m^{-2}$ $d^{-1}$ and 3 - 1400 × $10^{-6}$ μmol Co $m^{-2}$ $d^{-1}$) (Chance et al. 2015). The relatively lower estimated Co deposition fluxes in our study could be the results of the lower abundance of Co in the upper continental crust (~0.02 wt‰) we used here compared with in the anthropogenic-derived dust like coal ash (~0.2 wt‰) (Thuróczy et al. 2010; Rudnick and Gao 2014). Nevertheless, the atmospheric deposition fluxes of Fe, Co and Mn are still 1 - 4 magnitudes lower than their estimated upward fluxes from bottom waters (Table 3.1). In summary, input of sediment-derived TMs from the shelf bottom layer is the dominant source of TMs to shelf surface waters in the BUS.

*Table 3. 1 Namibian shelf TM fluxes (in μmol $m^{-2}$ $d^{-1}$).*

| TMs | Zonal | | | Upward | Alongshore | Atmospheric Deposition [b] |
|---|---|---|---|---|---|---|
| | Shelf-to-shelf edge | Shelf edge-to-open ocean | Shelf edge-to-open ocean [a] | | | |

| | | | | | | |
|---|---|---|---|---|---|---|
| Fe | 1.47 ± 0.94 | 0.29 ± 0.20 | 1.02 ± 0.42 | 2.22 ± 0.99 | 0.04 | 0.06 |
| Co | 0.03 ± 0.02 | 0.006 ± 0.004 | 0.03 ± 0.02 | 0.05 ± 0.03 | 0.002 | $2.1\times 10^{-6}$ |
| Mn | 2.06 ± 1.31 | 0.48 ± 0.31 | - | 0.28 ± 0.11 | 0.01 | 0.004 |

*Note. Zonal fluxes represent off-shelf fluxes including shelf-to-shelf edge (< 500 km from coast) and shelf edge-to-open ocean (500 - 1600 km from coast) in the surface layer; Upward fluxes represent fluxes from bottom to surface waters and alongshore fluxes represent equatorward fluxes along the African coast.* [a] *Shelf edge-to-open ocean TM fluxes within upper 500 m depth interval.* [b] *TM atmospheric deposition fluxes to the coastal region of BUS estimated by dust deposition fluxes in Barraqueta et al., (2019).*

2) Shelf release as a major source of Fe, Co and Mn to the eastern South Atlantic

Continental margins act as distinct sources for most TMs to the ocean (Lam and Bishop 2008; Milne et al. 2017). In the BUS, the overall offshore current in the surface layer can transport TMs from the shelf to the open eastern South Atlantic. To assess the significance of shelf TMs release, we split the 29°S transect into three zones: shelf (on-shelf stations 44 - 45), shelf edge (on-slope stations 42 - 43) and open ocean (Stations 35 - 39) and determine TM fluxes from shelf to shelf edge and shelf edge to open ocean in the surface layer (Table 3.1). We also calculated shelf edge-to-open ocean TM fluxes for two depth intervals, shallower than the 26.5 kg $m^{-3}$ isopycnal (~200 m) and for the upper 500 m, respectively.

Our estimated Co flux from shelf edge to open ocean (0.03 μmol $m^{-2}$ $d^{-1}$, upper 500 m) is in good agreement with the flux calculated at the shelf edge near Cape Town (0.03 μmol $m^{-2}$ $d^{-1}$, Table 3.2) using a similar method (Bown et al. 2011). Despite different depth intervals and calculation approaches, our estimated off-shelf Fe flux in the upper 500 m (1.02 μmol $m^{-2}$ $d^{-1}$) is within the range of estimates from other continental shelves (0.02 - 4 μmol $m^{-2}$ $d^{-1}$) (Charette et al. 2016; Milne et al. 2017; Sanial et al. 2018; Hsieh et al. 2021) (Table 3.2). However, Fe and Co fluxes from the Namibian shelf (1.02 μmol Fe $m^{-2}$ $d^{-1}$ and 0.03 μmol Co $m^{-2}$ $d^{-1}$) are lower than those from the Peruvian shelf into the South Pacific (Table 3.2, 4 μmol Fe $m^{-2}$ $d^{-1}$ and 0.28 μmol Co $m^{-2}$ $d^{-1}$) (Sanial et al., 2018), likely because the OMZ off the Namibian shelf is weaker than the OMZ off the Peruvian shelf. The extensive OMZ off the Peruvian shelf has been proposed to amplify Co coastal fluxes and support a pronounced Co plume within the OMZ (Hawco et al. 2016). Similarly, the persistent anoxic concentrations over the Peruvian shelf

support an extensive Fe(II) plume off the Peruvian shelf, which was estimated to account for approximately half of its total off-shelf Fe fluxes (Sanial et al. 2018; Cutter et al. 2018).

The off-shelf fluxes of TMs from shelf to shelf edge (1.47 μmol Fe $m^{-2}$ $d^{-1}$, 0.03 μmol Co $m^{-2}$ $d^{-1}$ and 2.06 μmol Mn $m^{-2}$ $d^{-1}$, Table 3.1), correspond to 60 - 70% of the Fe and Co upward fluxes. The Mn lateral off-shelf flux is larger than the corresponding upward flux (Table 3.1), indicating net Mn(II) production in surface water by photochemistry in combination with enhanced Mn(II) stability (Sunda et al. 1983). With increasing distance from the coast, the TM fluxes to the open ocean above 200 m decrease to 0.29 μmol Fe $m^{-2}$ $d^{-1}$, 0.006 μmol Co $m^{-2}$ $d^{-1}$ and 0.48 μmol Mn $m^{-2}$ $d^{-1}$, which represent an 80 - 90% reduction in the flux compared to that reaching the shelf-edge (Table 3.1). This is the result of biological uptake and scavenging of Fe (Figure 3.7) (Boyd and Ellwood 2010; Noble et al. 2012) in combination with limited upwelling at the shelf edge stations (Table S3.4). A similar magnitude of decrease was also observed for Fe fluxes along ~12°N zonal transect in the subtropical North Atlantic off Senegal (Milne et al. 2017). In comparison to upper 500 m off-shelf fluxes of Fe and Co, upper 200 m Fe and Co fluxes from shelf edge to open ocean are only 28% and 20% their fluxes in the upper 500 m (Table 3.1), respectively, indicating that a much larger fraction of Fe and Co from subsurface waters below 200 m is transferred off shelf. Upwelled Fe is quickly oxidized in the surface waters and then precipitates at the shelf edge, resulting in iron enrichment at the shelf edge below 200 m and higher off-shelf subsurface Fe fluxes compared with those in the upper 200 m.

By combining upward and off-shelf fluxes from the shelf to shelf edge, we can elucidate TM cycling within the nearshore area (Figure 3.9). Reductively mobilized Fe on the shelf is upwelled to the surface waters and transported within the surface waters to the open ocean. However, a large fraction of the Fe laterally transported within the surface water is scavenged and transferred to particulate phases, settling at shelf edge. Iron enriched in oxic sediments at the shelf edge can potentially be mobilized through non-reductive dissolution (Homoky et al. 2013) and stabilized in solution by organic matter (Gledhill and Buck 2012), and then transferred to the open ocean . Although non-reductive dissolution of Fe cannot be assessed using the data in our study, it has been observed at the shelf edge (~34°S) near our study area (Homoky et al. 2013) and likely contributed to the deep plume of Fe at 2000 m depth. Our estimated subsurface Fe flux from the shelf edge to open ocean (~0.73 μmol $m^{-2}$ $d^{-1}$, difference between upper 500 m and

upper 200 m off-shelf Fe fluxes to open ocean) is similar in magnitude to previously estimated benthic Fe fluxes from 733 m and 1182 m at shelf edge sites (0.11 - 0.23 μmol $m^{-2}$ $d^{-1}$) via non-reductive dissolution (Homoky et al. 2013). Stabilization of released Fe by organic ligands is plausibly enhanced at the organic-rich Namibian shelf edge, where > 2 wt% Total Organic Carbon (TOC) of sediment surface was observed (Figure 3.1) (Inthorn et al. 2006). This scenario could partly also explain the cycling of Co. Upwelled Co may not be readily removed via oxidation in shelf waters due to a slow oxidation rates of Co in the water column (Figure 3.7) (Noble et al. 2012). However, precipitating solid-phase iron and manganese can remove cobalt from the water column. In addition, it is possible that lateral transfer of Co within the shelf bottom layer is facilitated by complexation with organic ligands, including siderophores, at the shelf edge (Saito et al. 2005). This Co complexation is reported to have supported >75% total cobalt subsurface plume to the eastern South Atlantic (Noble et al. 2012).

*Table 3. 2 Comparison of shelf-to-open ocean Fe, Co and Mn fluxes (in μmol $m^{-2}$ $d^{-1}$) between studies.*
*$^{228}Ra$, $u$, $K_x$ and SML represent radium-228 isotope, zonal velocity, off-shelf diffusive coefficient and surface mixed layer, respectively. For comparison, Fe and Co fluxes from Hsieh et al., 2020 and Vieira et al., 2020 were normalized to the shelf area.*

| Region | Location | Method | Depth | Fe | Co | Mn | Reference |
|---|---|---|---|---|---|---|---|
| Namibian shelf | ~29°S | $u$ & $K_x$ derived | 500 m | 1.02 | 0.03 | | This study |
| Western N. Atlantic shelf | 0°-70°N | $^{228}$Ra isotope | 200 m | 0.42 | 0.16 | 0.60 | Charette et al., 2016 |
| Senegal Shelf | ~12°N | $u$ & $K_x$ derived | 500 m | 0.21 | | | Milne et al., 2017 |
| Peruvian shelf | ~12°S | $^{228}$Ra isotope | 200 m | 4.00 | 0.28 | 8.89 | Sanial et al., 2018 |
| Cape Basin shelf | ~40°S | $^{228}$Ra isotope | 150 m | 0.02-0.06 | 0.01 | | Hsieh et al., 2020 |
| near Cape Town | ~35°S | $u$ & $K_x$ derived | SML | | 0.03 | | Bown et al., 2011 |

| | | | | | | | |
|---|---|---|---|---|---|---|---|
| Congo River Margin | ~3°S | $^{228}$Ra isotope | 15 m | 20.7 | 0.14 | 9.45 | Vieira et al., 2020 |

In summary, atmospheric dry depositional TM fluxes are lower than benthic inputs to shelf surface waters and insignificant for Fe, Co and Mn to the open eastern South Atlantic (Table 3). The aerosol deposition flux over the open eastern South Atlantic (17°S - 29°S and 0°E - 10°E) obtained on the same cruise is estimated at ~0.17 g $m^{-2}$ $yr^{-1}$ based on surface water aluminum concentrations (Barraqueta et al., 2019). Using the same approach and assumptions regarding aerosol composition and TMs solubility described in Section 4.4.1, derived aerosol Fe deposition fluxes are 0.03 μmol Fe $m^{-2}$ $d^{-1}$, 1.0 × $10^{-6}$ μmol Co $m^{-2}$ $d^{-1}$ and 0.002 μmol Mn $m^{-2}$ $d^{-1}$to the open eastern South Atlantic, which are all slightly lower than our estimates to the shelf sea and within the range of estimates from Chance et al., 2015 further south of our study area. Our estimated atmospheric Fe, Co and Mn fluxes are at least one order of magnitude lower than the corresponding lateral fluxes off the Namibian shelf (Table 3). This indicates that the Namibian shelf is a dominant source of Fe, Co and Mn for the open eastern South Atlantic. In comparison, a previous study has reported much higher TM fluxes to the further north in the eastern South Atlantic from the Congo River (Vieira et al. 2020), which were 1 - 2 magnitudes higher than the inputs from the Namibian shelf in our study (Table 3.2) with a far more extensive off-shelf plume. Whilst TMs fluxes from sediments along the BUS are therefore large in a global context, and similar to those derived in other OMZ regions, Fe fluxes are dwarfed by fluxes associated with the offshore advection of the Congo plume.

*Table 3. 3 Sources of trace metals to the eastern South Atlantic from GA08 cruise.*

| TM | unit | Congo River Margin | Namibian shelf (< 500 m) | Namibian shelf (< 200 m) | Atmospheric deposition |
|---|---|---|---|---|---|
| Fe | | 20.7 ± 7.00 | 1.02 ± 0.42 | 0.29 ± 0.20 | 0.03 ± 0.03 |
| Co | μmol $m^{-2}$ $d^{-1}$ | 0.14 ± 0.06 | 0.03 ± 0.02 | 0.006 ± 0.004 | 1.0 ± 1.1 × $10^{-6}$ |
| Mn | | 9.45 ± 3.65 | | 0.48 ± 0.31 | 0.002 ± 0.002 |
| Fe | | 6.8 ± 2.3 × $10^{8}$ | 7.2 ± 2.9 × $10^{7}$ | 1.2 ± 0.8 × $10^{7}$ | 5.5 ± 5.5 × $10^{6}$ |
| Co | mol $yr^{-1}$ | 4.6 ± 1.8 × $10^{6}$ | 2.1 ± 1.4 × $10^{6}$ | 2.5 ± 1.6 × $10^{5}$ | 1.8 ± 1.8 × $10^{2}$ |
| Mn | | 3.1 ± 1.2 × $10^{8}$ | | 2.0 ± 1.2 × $10^{7}$ | 3.6 ± 3.6 × $10^{5}$ |

*Note. For comparison, Fe, Co and Mn fluxes in unit of μmol $m^{-2}$ $d^{-1}$ from Congo River margin (Vieira et al., 2020) were normalized to the shelf area. Atmospheric deposition fluxes of TMs were derived from dust deposition fluxes (0.17 g $m^{-2}$ $yr^{-1}$) in Barraqueta et al., (2019). Namibian shelf areas (1.1 × $10^{11}$ $m^2$ and 1.9 × $10^{11}$ $m^2$ above 200 m and 500 m bottom depth respectively) were estimated based on GEBCO's global gridded bathymetric data sets. Surface area of open eastern South Atlantic (17°S - 29°S, 0°E - 15°E) was 5.0 × $10^{11}$ $m^2$.*

### 3.4.4 Global implications

Shelf sediments are an important source of dissolved Fe to the coastal and open ocean (e.g. Elrod et al., 2004). However, only a small fraction of the shelf sedimentary Fe input is transferred to surface waters on the shelf and exported to the open ocean. The upward Fe fluxes from the bottom to surface waters on the shelf derived in our study (2.22 ± 0.99 μmol $m^{-2}$ $d^{-1}$) and scaled to the Namibian shelf area (1.1 × $10^{11}$ $m^2$) amount to 8.9 ± 4.0 × $10^7$ mol $yr^{-1}$, which is 0.1 - 0.5% of the global sedimentary Fe supply in shelf seas of 2.7 - 8.9 × $10^{10}$ mol $yr^{-1}$ (Elrod et al. 2004; Tagliabue et al. 2014; Dale et al. 2015). Dissolved Fe fluxes from the Namibian shelf to the ocean (Table 3.3) would account for approximately 0.2% - 2.7% of global sedimentary Fe supply in shelf seas if assuming a removal rate of 50% - 90% for Fe transported from the shelf to the open ocean (Siedlecki et al. 2012).

Trace metal inputs to shelf waters and the eastern South Atlantic Ocean within our study area are projected to change due to intensifying ocean deoxygenation induced by climate change (Figure 3.9) (Keeling et al. 2010). Ocean deoxygenation would generate an enhanced benthic Fe, Co, Mn supply on the Namibian shelf. In combination with increased upwelling in the BUS (Pardo et al. 2011; Lima et al. 2019), offshore transport of these shelf-derived TMs from surface or subsurface will alleviate Fe/Co-(co)-limitation of primary production in the eastern South Atlantic (Siedlecki et al. 2012; Browning et al. 2017). If primary productivity increased, intensified remineralization would consume more oxygen and potentially create a positive feedback loop to ocean deoxygenation. The positive feedback loop would continue until $NO_x$ losses due anammox and denitrification in subsurface waters depleted available N stocks. The offshore region would thus potentially become fixed N limited (Wallmann et al. 2022). The biological significance of increasing Fe and Co fluxes off-shelf may therefore be strongly dependent on the response of the N-cycle to intensification of deoxygenation. In any case, Fe/Co/Mn:N ratios are expected to increase following intensification of the shelf OMZ.

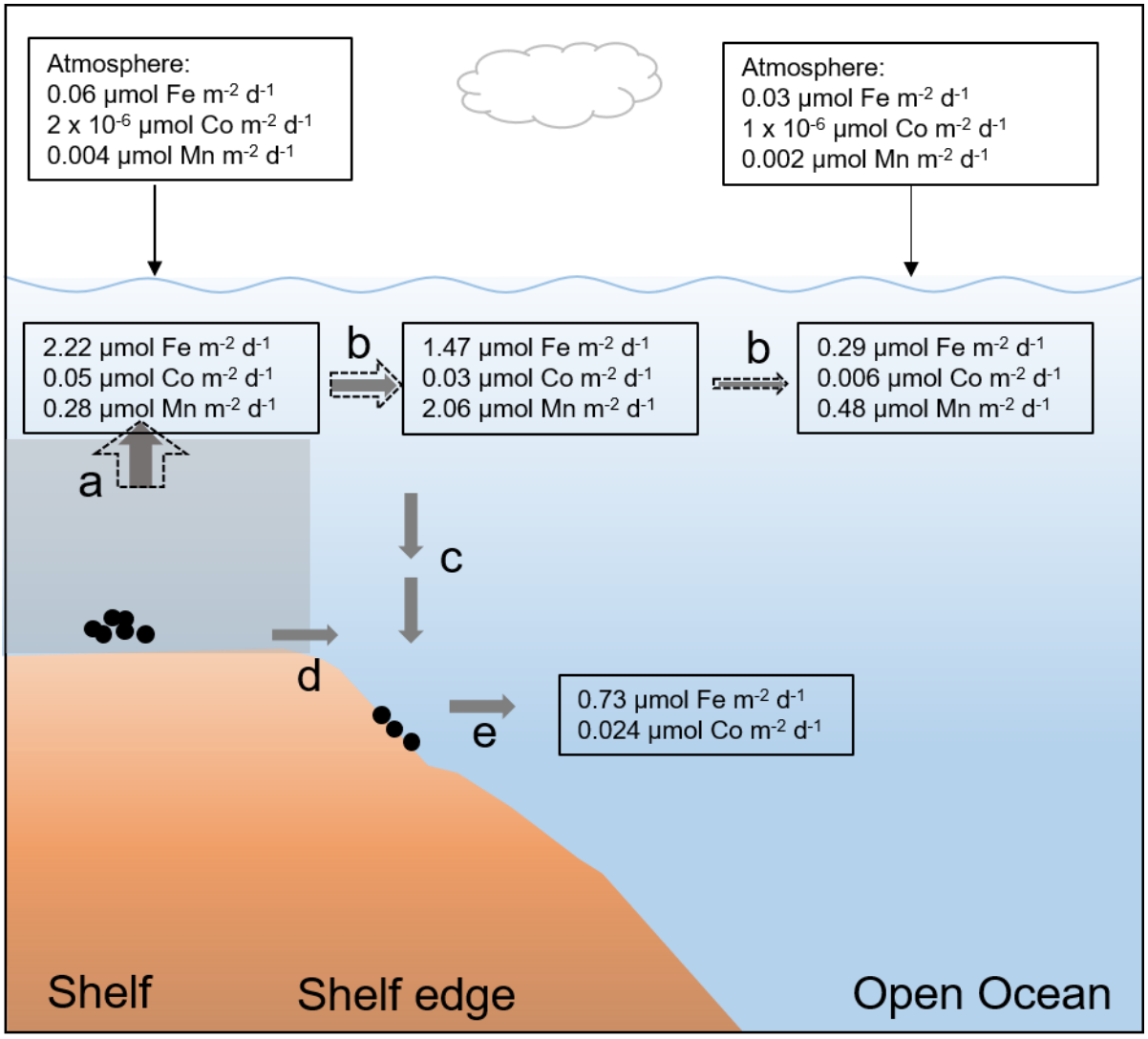


*Figure 3. 9 Schematic of different TM fluxes in the BUS. Grey shading indicates OMZ over the Namibian shelf.*
*Arrows (a - e) indicate different processes, a. upward transfer, b. lateral off-shelf transfer within the surface layer, c. precipitation/scavenging to the shelf edge, d. lateral transfer within the bottom shelf layer, e. off-shelf transfer from the shelf edge. The thickness of arrows (a, b, c and e) are scaled up to the magnitude of the associated flux. The dashed arrows indicate changes of different TM fluxes following ocean deoxygenation.*

## 3.5 Conclusions

This study shows contrasting distributions of nutrient-type (Cd, Ni and Cu) and redox-sensitive TMs (Fe, Co and Mn) in the BUS of the eastern South Atlantic. The reducing sediments on the Namibian shelf contribute redox-sensitive TMs into the overlying water column. Remineralization of sinking phytoplankton debris shapes distributions of Cd, Ni, Cu and

phosphate on the shelf. Atmospheric inputs are often considered as an important source of TMs to the surface ocean (Jickells et al., 2005; Ventura et al., 2021). However, we show shelf sediments off Namibia supply high Fe, Co and Mn fluxes to both shelf surface waters and to the eastern South Atlantic compared with atmospheric deposition. Off-shelf Fe and Co fluxes to the eastern South Atlantic largely occur from oxic sediments at the shelf edge, where organic matter complexation probably facilitates re-mobilization of Fe and Co.

## 3.6 Supplementary Materials

*Table S3. 1 The variance and coefficients of the principal components (PC).*

| Eigen-analysis of the Correlation Matrix | | | |
|---|---|---|---|
| | Eigenvalue | Variance Percent | Cumulative |
| Dim.1 | 6.210 | 51.7% | 51.7% |
| Dim.2 | 3.490 | 29% | 80.8% |
| Dim.3 | 0.982 | 8.18% | 88.9% |
| Eigenvectors | | | |
| | PC1 | PC2 | PC3 |
| Depth | 0.220 | -0.394 | 0.277 |
| Cd | 0.365 | -0.085 | -0.035 |
| Mn | 0.050 | 0.354 | 0.685 |
| Fe | 0.175 | 0.373 | 0.233 |
| Co | 0.198 | 0.426 | 0.214 |
| Ni | 0.357 | -0.177 | 0.031 |
| Cu | 0.257 | -0.325 | 0.285 |
| $NO_x$ | 0.367 | -0.009 | -0.247 |
| Si | 0.336 | -0.227 | 0.166 |
| phosphate | 0.380 | 0.048 | -0.169 |
| Oxygen | -0.213 | -0.390 | 0.295 |
| AOU | 0.339 | 0.221 | -0.259 |

*Table S3. 2 Pearson correlations of dissolved trace metal concentrations, macronutrients, Apparent Oxygen Utilization (AOU) and depth for our study area.*

| | AOU | Oxygen | Phosphate | Si | $NO_x$ | Cu | Ni | Co | Fe | Mn | Cd |
|---|---|---|---|---|---|---|---|---|---|---|---|
| Depth | 0.13 | 0.27 | 0.37 | 0.85 | 0.39 | 0.82 | 0.67 | -0.27 | -0.16 | -0.26 | 0.54 |
| Cd | 0.67 | -0.31 | 0.83 | 0.80 | 0.87 | 0.57 | 0.89 | 0.31 | 0.30 | 0.025 | 1 |
| Mn | 0.18 | -0.31 | 0.095 | -0.10 | -0.0040 | -0.14 | -0.051 | 0.72 | 0.53 | 1 | |
| Fe | 0.59 | -0.66 | 0.40 | 0.20 | 0.28 | -0.080 | 0.14 | 0.72 | 1 | | |
| Co | 0.68 | -0.77 | 0.51 | 0.080 | 0.44 | -0.057 | 0.21 | 1 | | | |
| Ni | 0.56 | -0.16 | 0.82 | 0.85 | 0.83 | 0.69 | 1 | | | | |
| Cu | 0.24 | 0.091 | 0.47 | 0.84 | 0.48 | 1 | | | | | |
| $NO_x$ | 0.81 | -0.52 | 0.96 | 0.67 | 1 | | | | | | |
| Si | 0.50 | -0.12 | 0.69 | 1 | | | | | | | |
| Phosphate | 0.85 | -0.58 | 1 | | | | | | | | |

| | | |
|---|---|---|
| Oxygen | -0.89 | 1 |

*Table S3. 3 Water masses present at our study site, and their characteristic neutral density, depth (m), salinity (psu), potential temperature (°C), dissolved Cd and Ni concentrations (nM).*

| Water Mass | Neutral Density | Depth | Salinity | Potential Temperature | Cd | Ni |
|---|---|---|---|---|---|---|
| South Atlantic Central Water (SACW) | 26.5-26.93 | | 34.9-35.4 | 9.44-13.6 | | |
| Antarctic Intermediate Water (AAIW) | 26.95-27.4 | <1500 | 34.3 | 3.8 | 0.53 | 5.59 |
| North Atlantic Deep Water (NADW) | 27.85-28.05 | <3500 | 34.97 | 2.4 | 0.22 | 3.78 |
| Antarctic Bottom Water (AABW) | 28-28.3 | >3500 | 34.66 | -0.1 | 0.78 | 7.72 |

*Note. Data is from literature* (Bruland and Franks 1983; Boye et al. 2012; Baars et al. 2014; Xie et al. 2015, 2019; Middag et al. 2018, 2020; Liu and Tanhua 2021).

*Table S3. 4 Vertical fluxes at each station across the 26.5 kg $m^{-3}$ isopycnal on the Namibian shelf including diffusive and upwelling fluxes (in unit of µmol $m^{-2}$ $d^{-1}$).*

| Station No. | Fe | Co | Mn | Location |
|---|---|---|---|---|
| 4 | 1.1 ± 0.44 | 0.048 ± 0.020 | 0.66 ± 0.27 | Shelf |
| 3 | 2.5 ± 1.1 | 0.059 ± 0.026 | 1.2 ± 0.51 | Shelf |
| 2 | 1.8 ± 0.82 | 0.061 ± 0.027 | -0.41 ± 0.18 | Shelf |
| 52 | 2.8 ± 1.2 | 0.013 ± 0.006 | -0.42 ± 0.18 | Shelf |
| 51 | 2.5 ± 1.1 | 0.083 ± 0.037 | 0.48 ± 0.22 | Shelf |
| 50 | 2.9 ± 1.2 | 0.049 ± 0.021 | 0.71 ± 0.31 | Shelf |
| 49 | 0.64 ± 0.28 | 0.078 ± 0.035 | -0.32 ± 0.14 | Shelf |
| 47 | 4.1 ± 1.9 | 0.063 ± 0.029 | 0.11 ± 0.048 | shelf |
| 45 | 4.7 ± 1.4 | 0.095 ± 0.028 | 3.7 ± 1.1 | shelf |
| 44 | 0.74 ± 0.26 | 0.022 ± 0.008 | -0.044 ± 0.015 | shelf |
| 43 | 0.24 ± 0.096 | 0.002 ± 0.001 | -0.15 ± 0.060 | shelf edge |
| 42 | 0.053 ± 0.044 | 0.002 ± 0.002 | -0.11 ± 0.091 | shelf edge |

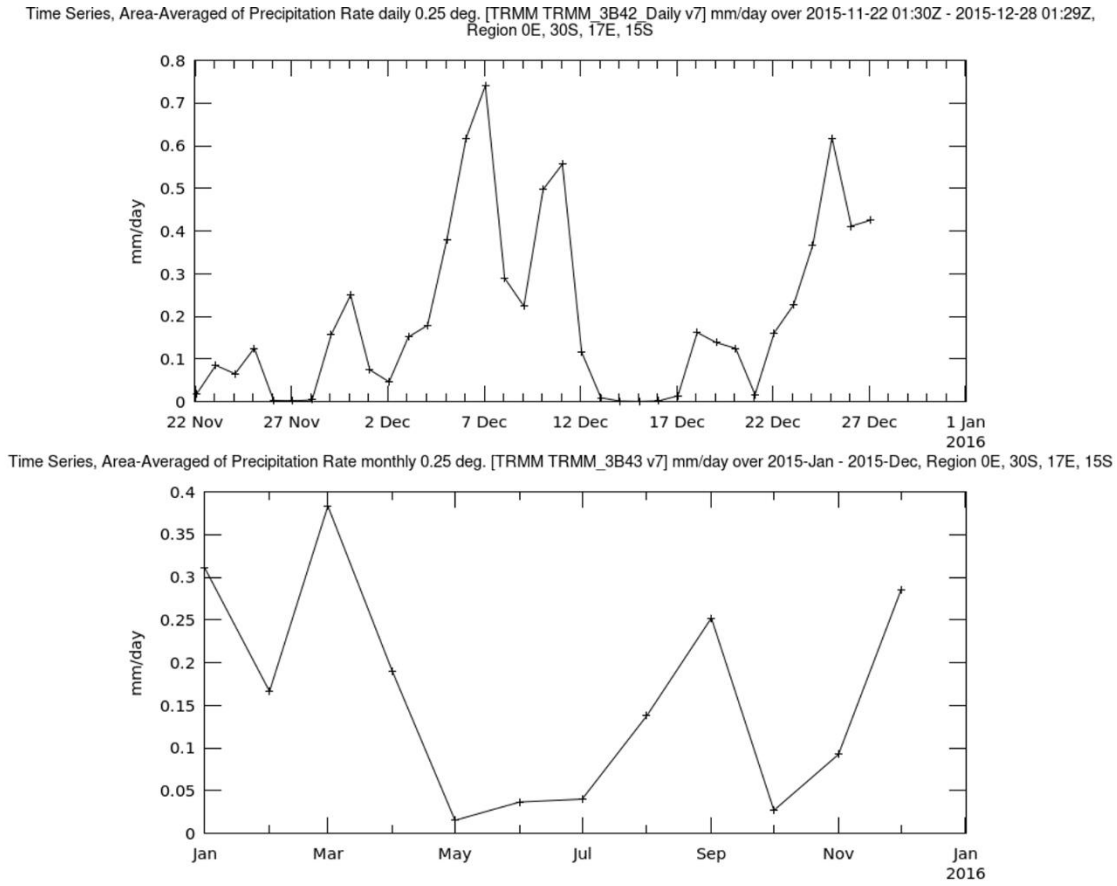


*Figure S3. 1 Plots of daily and monthly precipitation rate (upper and lower panel, respectively) during the GA08 cruise period and during the year of 2015.*
*Data and plots were retrieved from the NASA Goddard Earth Sciences Data and Information Services Center (GES DISC):*
*https://disc.gsfc.nasa.gov/datacollection/TRMM_3B42_Daily_7.html* (Huffman et al. 2016).

# 4. Trace metal fluxes from the Congo River into the South Atlantic Ocean are supplemented by atmospheric inputs from gas flaring

Te Liu[1*], Mark J. Hopwood[2], Stephan Krisch[1†], Lúcia H. Vieira[1],

Eric P. Achterberg[1]

Submitted to *Geophysical Research Letter*

[1] GEOMAR Helmholtz Centre for Ocean Research Kiel, Kiel, Germany.

[2] Department of Ocean Science and Engineering, Southern University of Science and Technology, Shenzhen, China.

[†]Now at Federal Institute of Hydrology, Koblenz, Germany

**Abstract**

The Congo River is the second largest river on Earth by discharge volume and supplies vast quantities of trace metals (TMs) to the South Atlantic, thereby supporting phytoplankton growth in a river plume reaching over 800 km offshore. The offshore distributions of TMs and two-endmember mixing model suggest an additional input which is correlated with freshwater but does not originate in the river outflow. Using dissolved TM concentrations in ocean, river and rainwater collected during the GEOTRACES GA08 cruise, we show that TM fluxes to the ocean were augmented by wet atmospheric deposition. Relative to their river inputs, additions of TMs to the ocean from rainfall, contributed inputs for cadmium of 55%, copper of 46%, lead of 35% and zinc of 86%, and were associated with local gas flaring emissions. Our findings show an important role of rainfall containing anthropogenic contaminants in supplying TMs to the South Atlantic overlapping with the region that receives substantial TM fluxes from the Congo River.

## 4.1 Introduction

Trace metals (TMs) are supplied to the surface ocean by shelf sediments (Elrod et al. 2004; Liu et al. 2022b), rivers (Buck et al. 2007) and atmospheric deposition (Jickells, 1995), affecting primary productivity and hence ocean carbon uptake and other ecosystem services (Twining and Baines 2013; Moore et al. 2013). The Congo River discharges ~41000 $m^3$ $s^{-1}$ of freshwater, and creates a freshwater plume extending over 800 km offshore, with its flow directed by a slow equatorward current and dispersal of the plume limited by low Coriolis forces in the near-equatorial southeast Atlantic Ocean (Braga et al. 2004; Laraque et al. 2009). The plume constitutes a major source of TMs to the ocean including iron (Fe), manganese (Mn) and cobalt (Co) (Vieira et al. 2020) and influences ecosystem functioning in the South Atlantic (Browning et al. 2017). Such an extensive off-shelf plume of TMs associated with a river outflow, and reaching an ocean gyre, is unusual in the global ocean. A study of the radiogenic radium isotope $^{228}Ra$, which shares the same source as TMs like Fe, Mn and Co, showed that the Congo River accounted for only ~30-35% of the $^{228}Ra$ budget in the plume, and hence an additional

source of $^{228}$Ra and TMs is required (Vieira et al. 2020). The Congo plume is up to 15 m deep and disconnected from the seafloor on the shelf immediately beyond the river outflow (Hopkins et al. 2013). Heavier $\delta^{56}$Fe in surface waters of the Congo plume relative to the typical crustal and river $\delta^{56}$Fe values consequently suggests a limited role for sedimentary derived Fe in the plume, and indicates a possible role of complexation by organic matter of isotopically heavy $\delta^{56}$Fe and thereby buffering dissolved Fe (dFe) through prevention of removal by scavenging (Hunt et al. 2022).

A freshwater source of TMs not constrained in prior budgets is wet deposition. The Congo shelf region receives high precipitation rates of >200 mm per month during the period October to December (Bultot 1971; Alsdorf et al. 2016), coincident with the timing of GEOTRACES cruise GA08 (Figure 4.1). Precipitation typically has a low pH (pH < 6) and is subject to a high photon flux, both of which increase the lability, and potentially bio-availability of a range of TMs (Johnson et al. 1981; Lim et al. 1994; Paerl et al. 1999; Kieber et al. 2001a; Kieber 2003). Given that the distribution of several TMs, including Fe, is tightly correlated with freshwater across the region (Vieira et al. 2020), wet deposition is an obvious candidate for an additional regional TM source, which across much of the ocean contributes larger fluxes of TMs than dry deposition (Chance et al. 2015; Shelley et al. 2017).

The fluxes of TMs delivered by rivers, wet and dry atmospheric deposition show pronounced variations by region and element. For example, estuarine processes can remove 90-99% riverine dFe in low salinity waters (Boyle et al. 1977), whereas TMs such as manganese (Mn) behave generally more conservative during estuarine mixing (Moore et al. 1979; Wilke and Dayal 1982). Inputs of several TMs from rivers and the atmosphere to the surface ocean, notably lead (Pb) and zinc (Zn) are strongly affected by anthropogenic activities (Boyle et al. 1994; Graedel et al. 2005). River runoff in tropical regions is strongly determined by precipitation levels (Chao et al. 2015) which are influenced by the migration of the Inter-Tropical Convergence Zone (ITCZ) under asymmetric warming/cooling in the northern and southern hemispheres (Schneider et al. 2014; Bonfils et al. 2020). Atmospheric-derived TM fluxes over the tropical eastern South Atlantic are furthermore influenced by anthropogenic air pollution originating in Africa (Vohra et al. 2022).

In order to quantify TM inputs from the Congo River and determine the relative importance of atmospheric deposition (wet and dry) to the surface ocean over the spatial scale of the river plume, we analysed dTM concentrations in surface waters, full-depth profiles and rainwater collected during GEOTRACES cruise GA08 on RV Meteor (M121)(Frank et al. 2014). Additionally, freshwater samples were collected directly in the Congo River in three seasons (May, July and October in 2017). Analysed TMs included cadmium (Cd), Co, copper (Cu), Fe, Mn, nickel (Ni), Pb and Zn. Total dissolvable TM concentrations (TdTM) in rainwater were also analysed. Cruise GA08 took place during the wet season, between 22 November and 27 December 2015. In this study, we defined two regions of interest: Congo shelf (< 500 km to the Congo River mouth; experiencing high rainfall) and offshore Congo plume at ~3°S (> 500 km to the Congo River mouth with less rainfall) (Figure 4.1).

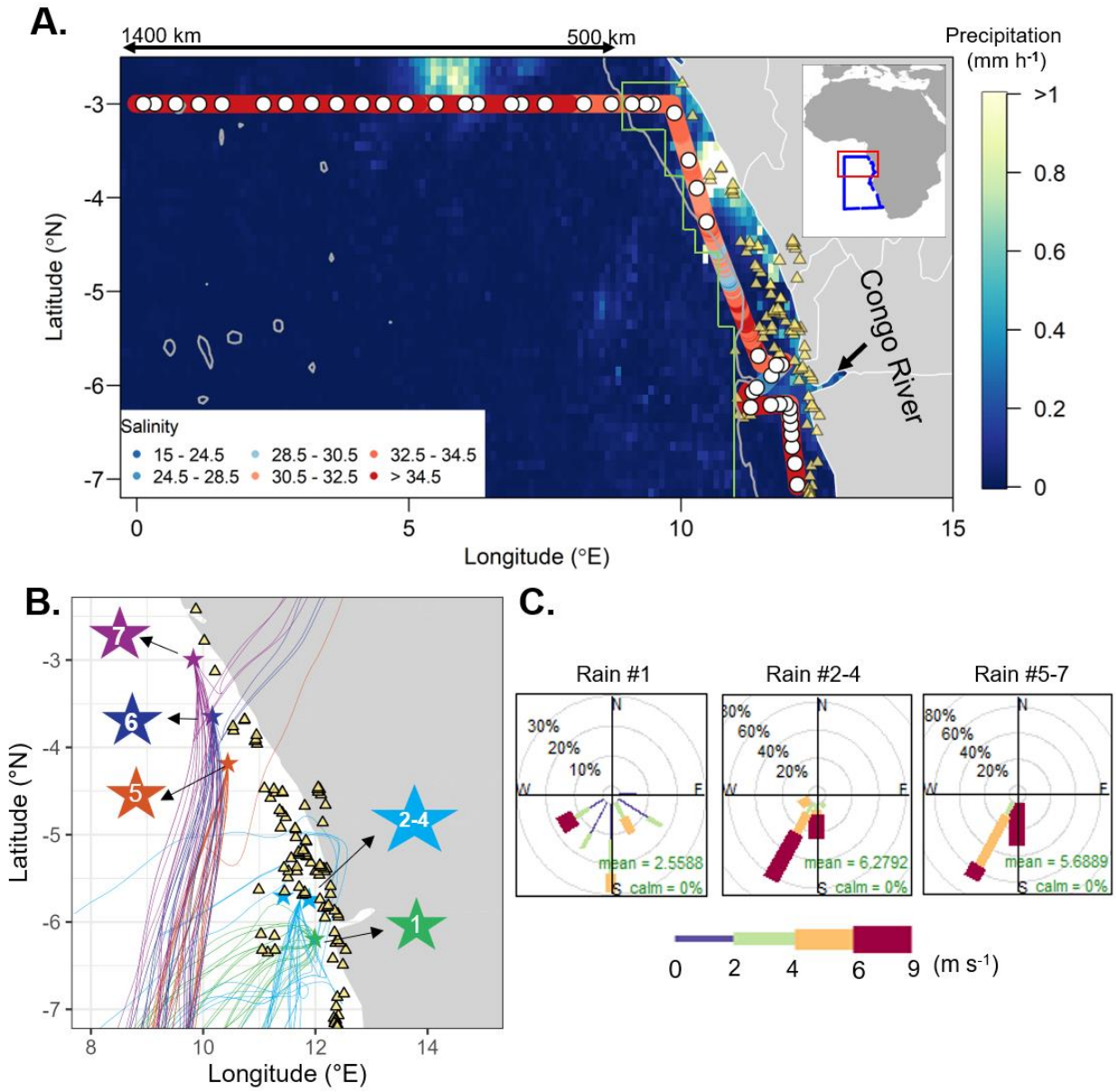


*Figure 4. 1 Overview of the Congo Margins.*
*A. Cruise track showing salinity gradients (coloured dots) and surface water sampling locations (white circles). Known gas flaring sites are indicated as yellow triangles*(Global Gas Flaring Reduction Partnership 2020). *The dark grey line shows the 1500 m depth contour (NOAA ETOPO1 database)*(Amante and Eakins 2009) *and the green line highlights the Congo shelf region used for calculating area-averaged precipitation rate (mm h$^{-1}$). Data for precipitation rates (mm h$^{-1}$) were download from satellite data product GPM IMERG Final Precipitation L3 Half Hourly 0.1° x 0.1° V06 (GPM_3IMERGHH)*(Huffman et al. 2019) *within the period of sailing within the Congo shelf region from 29 November 09:00 UTC to 02 December 05:59 UTC (colour shading). In-set map displays a wider region and the whole GA08 transect. B. 3-day air mass back-trajectories for rain events (coloured stars and lines as labelled) calculated by Hybrid Single-Particle Lagrangian Integrated Trajectory (HYSPLIT) model using a 10 m arrival*

*height from NOAA* (Stein et al. 2015). *C. Wind-rose plots showing frequency of wind direction (%) for rain events during our sampling period. Wind and salinity data were retrieved from the vessel's underway system (DSHIP Landsystem, http://dship.bsh.de/).*

## 4.2 Methods

### 4.2.1 Materials and Sampling

Seawater samples in depth profiles were collected using 12 L trace metal clean Go-Flo bottles (Ocean Test Equipment) mounted on a CTD rosette frame (trace metal clean, General Oceanics). Upon recovery, the Go-Flo bottles were transferred into a trace metal clean laboratory container for subsampling. Along the cruise track, surface seawater samples were collected at 3-4 m depth using a towfish. Water was pumped continuously while the ship was underway into the clean laboratory container using a Teflon diaphragm pump (Almatec® A15) and an acid-washed braided polyvinyl chloride tubing. Dissolved TM samples were filtered through 0.8/0.2 µm cartridge filters (AcroPak® 1000™) into acid cleaned 125 ml low-density polyethylene (LDPE) bottles (Nalgene®). Each sample was acidified to pH 1.9 by addition of 180 µL ultra-pure grade hydrochloric acid (HCl, UpA Romil®). Congo River freshwater samples were collected using a small boat during different seasons in 2017 (Table 4.1). Samples were filtered using 0.8/0.2 µm cartridge filters (AcroPak® 1000™) into acid cleaned LDPE bottles (Nalgene®). Within two hours after collection, samples were acidified to pH ~2 by addition of distilled HCl (Rahlf et al. 2021). Samples were all analysed in the home laboratory (GEOMAR).

Rainwater was sampled using a collector on the monkey island of the vessel, mounted forward of any other equipment. The custom-made collector consisted of a 25 cm diameter acid cleaned PE funnel mounted in a plastic frame with opaque LDPE acid clean bottles placed underneath in a sealed cabinet. The cabinet was covered with a plastic bag and only opened manually at the start of each rain event when the ship was underway. After a rain event, the funnel and LDPE bottle were replaced. Rainwater pH was determined onboard by a pH meter calibrated using NBS Buffers. The rainwater samples were syringe filtered (0.20 µm Millipore, polyvinyl difluoride; acid cleaned) and acidified. Both filtered (dissolved, d) and unfiltered rainwaters (total dissolvable, Td),

were acidified to pH 1.9 and stored for analysis at GEOMAR. Details of the rainwater samples are given in Table S4.1.

### 4.2.2 Analytical Methods

Concentrations of TMs in sea, river and rainwater samples were analysed via high-resolution isotope inductively coupled mass spectrometry (HR-ICP-MS, ELEMENT XR, ThermoFisher Scientific) after being pre-concentrated offline using a SeaFAST system (SC-4 DX SeaFAST pico, Elemental Scientific Inc.). Concentrations of Cd, Cu, Fe, Ni and Zn were quantified by isotope dilution, while Co, Mn and Pb concentrations were quantified using standard additions(Rapp et al. 2017). Certified reference materials SAFe S, SAFe D2, GSP, NASS 7 and CASS 6 were analysed alongside samples and were in close agreement with certified values (Table 2.2). Rainwater samples were additionally analysed without preconcentration due to the broad range of plausible TM concentrations as well as concentrations of aluminium (Al) with results from both analysis in close agreement. Two aliquots of each Congo River freshwater sample were transferred into acid-cleaned polypropylene (PP) vials (scintillation vials, Fisher Scientific®) in the home laboratory at GEOMAR. Due to high concentrations of some TMs in the river water, one aliquot of the Congo River freshwater samples was diluted using indium-spiked 1M $HNO_3$ (distilled, SpA Romil®) for analysis of Co, Cu, Mn, Fe, Ni and Zn without preconcentration. The other aliquot was analysed undiluted for relatively low Cd and Pb concentration analysis. Vertical profiles of oxygen, temperature, salinity, and depth were determined using a standard Seabird sensor package (SBE 9plus) on the CTD rosette frame.

### 4.2.3 Data Assessment

*1) Enrichment Factor and Solubility*

Enrichment Factors (EFs) were used to ascertain potential anthropogenic TM perturbations in the rainwater samples. The EF values were calculated based on TdTM concentrations as follows (Desboeufs et al. 2022):

$$EF = \frac{[TM/Al]_{sample}}{[TM/Al]_{UCC}}$$

where $[TM/Al]$ is the ratio between TdTM and TdAl concentrations in rainwater samples (subscript: sample) and upper continental crust (Rudnick and Gao 2014) (subscript: UCC). Aluminium is used as a reference crustal element due to its high crustal abundance.

Fractional solubility of TMs here was operationally defined as the soluble TM fraction of rainwater as per Baker & Croot, (2010) and Baker et al., (2013):

$$Solubility_{TM} = \frac{[TM]_d}{[TM]_{Td}} \times 100\%$$

here $Solubility_{TM}$ is the fractional solubility of a specific TM in rainwater (%), and $[TM]_d$ and $[TM]_{Td}$ are dTM and TdTM concentrations of rainwaters, respectively.

*Rain and River inputs, and the Trace Element inventory in Surface Waters*

Rain inputs of each TM ($F_{rain}$) in the unit of μmol $m^{-2}$ $d^{-1}$ were calculated as the product of volume-weighted-mean TM concentrations (dTM and TdTM) in rainwater ($C_{rain}$, nM) and precipitation rate ($P$, 6.5 mm $d^{-1}$, Figure S4.1) over the area (Congo shelf; green line in Figure 4.1):

$$C_{rain} = \frac{\sum C_i \times V_i}{\sum V_i}$$

$$F_{rain} = C_{rain} \times P$$

The precipitation data was obtained from the satellite product GPM (Huffman et al. 2019) retrieved from the Goddard Earth Sciences Data and Information Services Centre (GES DISC). The spatial extrapolation of rain inputs was based on several rain samples and may be subject to a large uncertainty, here 100% relative standard deviation (RSD) was used for $P$, and used to derive the error of $F_{rain}$ by propagation combined with the RSD of $C_{rain}$ (25% - 69%).

Concentrations of dTMs in surface waters ($C_{surface}$, nM) were integrated over the depth of the river plume ($z$, 5 - 15 m) to yield inventories ($I_{surface}$, μmol $m^{-2}$) on the Congo shelf. The surface depth interval ($z$) was indicated by the stratified waters with depleted salinities (Figure S4.2).

$$I_{surface} = C_{surface} \times z$$

River inputs of TMs to surface waters ($F_{river}$, μmol $m^{-2}$ $d^{-1}$) were calculated as follows:

$$F_{river} = \frac{C_{surface} \times z}{A}$$

Approximating that TMs discharged from the river mix across the defined Congo shelf region, the contribution of the Congo River to the shelf TM inventory was calculated using annual mean Congo River TM concentrations ($C_{river,}$ nmol $L^{-1}$, Table 4.1), river discharge at the river mouth ($Q_{river}$, 41000 $m^3$ $s^{-1}$ or 3.5 ×$10^9$ $m^3$ $d^{-1}$)(Laraque et al. 2009) and the surface area of the Congo shelf ($A$, 8.2 × $10^{10}$ $m^2$) (green line in Figure 4.1). This approach does not include any loss/gain of dTMs due to non-conservative processes, thus $F_{river}$ here would be a conservative upper-limit for dTMs that are subject to scavenging such as dFe, dPb and dZn (Krauskopf 1956; Boyle et al. 1977; Sholkovitz 1978; Elderfield et al. 1979; Mosley and Liss 2020).

*2) Freshwater Trace Metal Fluxes to the Ocean*

A surface layer of low salinity water ($S_{MIX}$= 33, Figure S4.2) was a result of mixing between freshwater from the river runoff (S = 0) and precipitation (S = 0) and seawater ($S_{SW}$ = 35.84, mean salinity of the surface water within the area of 0-40°S, -35-10°E (GEOTRACES Intermediate Data Product Group 2021)) along the offshore Congo plume. Assuming a steady state for both water volume and salinity, the water flow in and out are the same at the beginning of the offshore Congo plume (~3°S, 9°E at 500km to the Congo River mouth, Figure 4.1 and S4.3)(Vieira et al. 2020). The water flow rate ($Q$, $m^3$ $d^{-1}$) including freshwater ($Q_{FW}$) and seawater inflows ($Q_{SW}$) can be expressed as the product of water residence time ($\tau$, 7 ± 2 d) and water volume ($V$, 3.2 × $10^{11}$ $m^3$) following Vieira et al., (2020):

$$Q = Q_{FW} + Q_{SW} = \frac{V}{\tau}$$

The salinity budget of the mixed water can therefore be expressed as:

$$Q_{FW} \times 0 \; + \; Q_{SW} \times S_{SW} = \; Q \; \times S_{MIX}$$

Our estimated freshwater flow rate ($Q_{FW}$, 3.6 ± 1.0 ×$10^9$ $m^3$ $day^{-1}$) based on the two above equations is similar to a numerically simulated value (4.2 × $10^9$ $m^3$ $day^{-1}$) for a

similar area and season reported previously (Denamiel et al. 2013). Using our derived $Q_{FW}$ ($m^3$ $day^{-1}$) multiplied by freshwater TM endmember concentrations (nM) at the beginning of the offshore Congo plume (Figure 4.1 and S4.3) gives freshwater TM fluxes (mol $day^{-1}$) to the ocean.

## 4.3 Results and Discussions

### 4.3.1 Trace Metal Distributions on the Congo Shelf

Enhanced dTM concentrations were observed in surface waters on the Congo shelf and levels decreased with increasing salinity (Figure 4.2A and S4.2), suggesting mixing of Congo River water with coastal waters with lower dTM levels. We created theoretical two-endmember conservative mixing lines for each TM using the highest/lowest measured Congo River dTM concentrations (S = 0, sampled in 2017) and a high salinity coastal surface seawater sample from ~8°S (S = 35.28, Table 4.1) that was not directly affected by the Congo River plume (Vangriesheim et al. 2009). All dTMs showed apparent non-conservative mixing behaviours with respect to salinity on the Congo Shelf (Figure 4.2A). Concentrations of dCd, dCo, dCu, dMn and dNi fell above their conservative mixing lines across the whole salinity gradient between the Congo River water and coastal seawater. Apparent removal of dFe, dPb at salinity < 33 and dZn at salinity <30 is consistent with their characteristic scavenging behaviour and these TMs typically exhibit non-conservative removal in estuaries (Krauskopf 1956; Boyle et al. 1977; Sholkovitz 1978; Elderfield et al. 1979; Mosley and Liss 2020). However, weaker and insignificant correlations between dTMs and distance from the river mouth (Pearson coefficient $R < 0.45$, $P > 0.05$) could suggest the river was not the sole source for all dTMs on the Congo shelf (Table S4.2). River water was collected in a different year (2017) to the cruise (2015), and therefore a potential shift to higher river water concentrations for all dTMs could artificially create an apparent 'missing' source. However, dTM concentrations in Congo River waters in the wet season (October to December) are likely to be lower than in the dry season (April to June), as increases in discharge volume generally dilute dTM concentrations (Braungardt et al. 2003). Concentrations of dCd, dCo, dCu, dMn and dNi on the Congo shelf are higher than their

highest theoretical conservative values created using dry-season river concentrations (in May, Table 4.1 and Figure 4.2A). The observation that TMs are consistently elevated above the theoretical mixing line thus does suggest an additional dTM source in addition to river water, which is consistent with isotope studies of $^{228}Ra$ and $\delta^{30}Si$ from the same cruise which are not subject to the above caveat (Zhang et al.; Vieira et al. 2020).

*Table 4. 1 Endmember dTM concentrations (mean ± standard deviation, nM). The Congo River water and coastal seawater (-8.2°S, 12.1°E) were used to produce two-endmember conservative mixing lines. [a] Dissolved Zn concentration is unavailable for the chosen coastal seawater sample, and therefore the dZn concentration of the closest sample with similar salinity was used.*

| | Collection date/cruise | Salinity | Cd | Co | Cu | Mn | Fe | Ni | Pb | Zn |
|---|---|---|---|---|---|---|---|---|---|---|
| | | | (nM) | | | | | | | |
| Congo River | 04.05.2017 | 0 | 0.09 ± 0.00 | 2.4 ± 0.0 | 22 ± 1.0 | 138 ± 4.2 | 10827 ± 416 | 18.5 ± 6.8 | 2.0 ± 0.1 | 31.8 ± 9.2 |
| | 22.07.2017 | 0 | 0.09 ± 0.01 | 1.5 ± 0.4 | 19 ± 2.6 | 97 ± 7.6 | 6689 ± 771 | 8.8 ± 2.4 | 0.8 ± 0.0 | 14.3 ± 5.3 |
| | 08.10.2017 | 0 | 0.07 ± 0.00 | 1.2 ± 0.2 | 9.9 ± 0.9 | 76 ± 4.1 | 4638 ± 219 | 7.0 ± 0.6 | 0.5 ± 0.0 | 226 ± 23 |
| | Mean ± sd | 0 | 0.08 ± 0.01 | 1.7 ± 0.6 | 17 ± 6.3 | 104 ± 132 | 7385 ± 3153 | 11 ± 6.1 | 1.1 ± 0.8 | 91 ± 117 |
| Coastal seawater | 28.11.2015 | 35.28 | 0.01 ± 0.00 | 0.04 ± 0.00 | 0.72 ± 0.01 | 2.6 ± 0.0 | 0.52 ± 0.01 | 2.1 ± 0.0 | 0.01 ± 0.00 | 0.06 ± 0.01[a] |

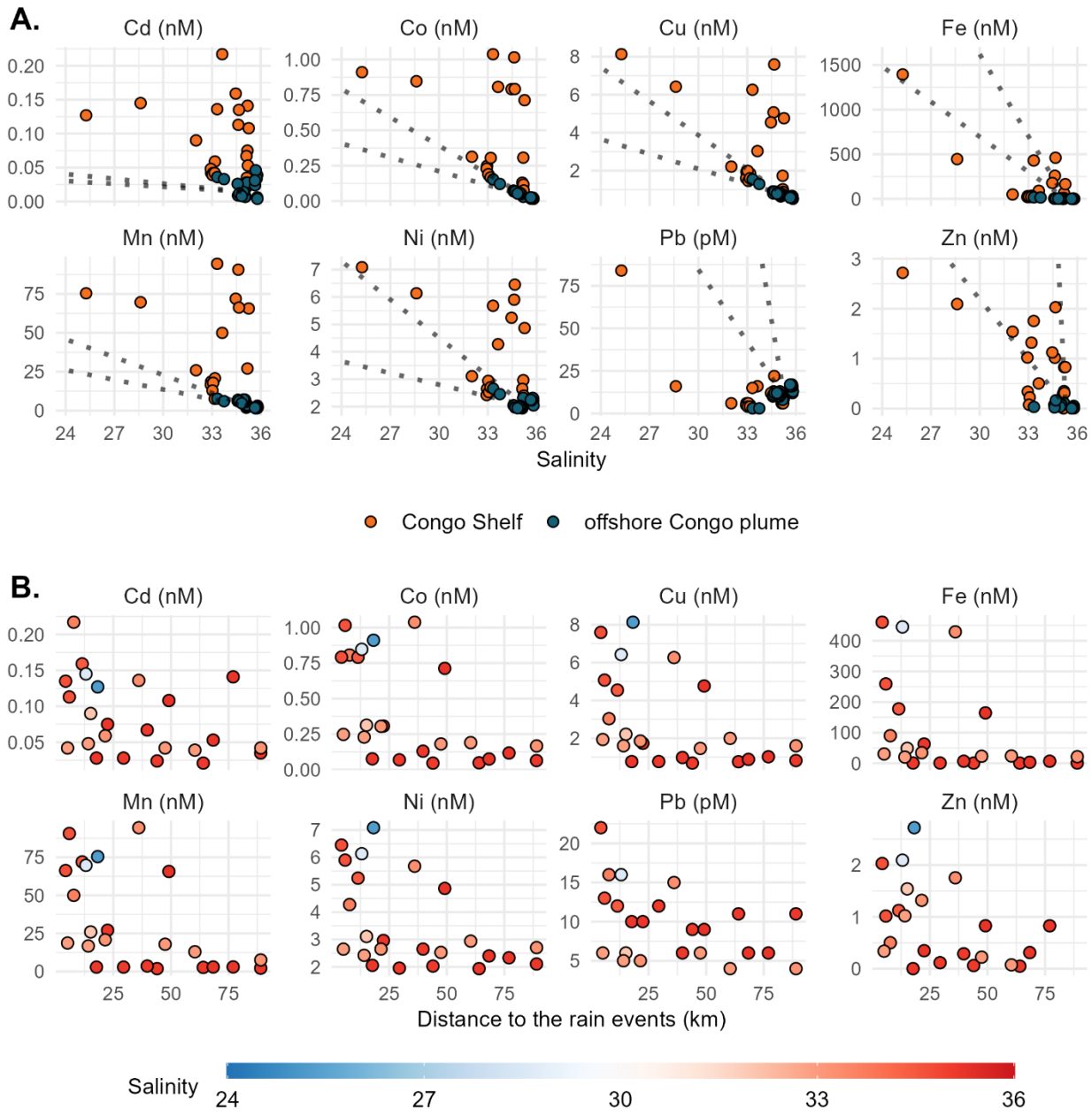


*Figure 4. 2 Concentrations of dTM in waters affected by the Congo River plume and discrete rain events.*
*A. Relationships between surface dissolved TM concentrations and salinity in the Congo shelf (orange) and offshore Congo plume (blue) zones of our study. Two dashed lines in each panel indicate theoretical conservative mixing lines associated with high and low measured Congo River endmembers (Table 4.1). B. Dissolved TM concentrations plotted against distance from discrete rain events (Figure S4.3 and rainwater sampling location in Table S4.1) along the Congo shelf during the cruise. Filled colours (colour bar) show the salinity of each sample. Note. Concentrations of dissolved TMs are in nM except Pb*

*in pM. Position of rain events is shown in Table S4.1. One datapoint with the highest Pb (84 pM) and Fe (1394 nM) concentrations and lowest salinity (S=25.3) is not shown in B.*

### 4.3.2 Trace Metals delivered by wet deposition

Several mechanisms with different strengths may simultaneously deliver TMs to the Congo shelf. A well-stratified water column (Figure S4.2) and low wind speeds (<10 m $s^{-1}$, Figure 4.1) on the Congo shelf reduced vertical mixing and upwelling, thereby limiting the transfer of TMs from subsurface to surface waters, which is in contrast to observed subsurface dTM supply further south on the Namibian shelf (Liu et al. 2022b). This is also substantiated by dissolved $\delta^{56}$Fe signatures in the Congo plume which show a minimal impact of sediment-derived Fe and other TMs with similar sources on surface water (Hunt et al. 2022). Wet deposition can be an important source of TMs to surface waters (Schlosser et al. 2014; Desboeufs et al. 2022), and may also impact the Congo shelf since our cruise crossed the southern boundary of the ITCZ and encountered numerous strong rain events with precipitation rate of up to >1 mm $day^{-1}$(Figure 4.1 and Figure S4.1)(Frank et al. 2014).

We calculated a volume-weighted-mean TM concentration in rainwater (Table S4.3) to avoid the volume effect of rain whereby heavy rain events tend to exhibit progressively lower TM loads due to washout[48]. Our volume-weighted-mean concentrations of all TMs in rainwaters were within the range of those reported in previous studies worldwide (Baker et al. 2013; Chance et al. 2015; Shelley et al. 2017; Desboeufs et al. 2022). Higher rainwater Cd, Cu, Pb and Zn concentrations were reported for the South Atlantic (Chance et al. 2015) (including this study) compared to the North Atlantic Ocean(Baker et al. 2013; Shelley et al. 2017) (Figure 4.3A), likely reflecting different regional sources of the TMs. Rainwater Fe concentrations in our study area were around one order of magnitude lower than those in most areas of the northern hemisphere (Baker et al. 2013; Shelley et al. 2017), but similar to observations in the ITCZ (Baker et al. 2013) with high rainfall, and in the western high-latitude North Atlantic (~60°N) (Shelley et al. 2017). Concentrations of most TMs in rainwaters herein, including Cd, Co, Cu, Mn, Ni, Pb and Zn, were similar to those reported for the central and western Mediterranean, where wet deposition is influenced by high dust loading and high anthropogenic emissions (Desboeufs et al. 2022). However, Fe concentrations were lower by a factor of ~20 compared to the Mediterranean study

(Desboeufs et al. 2022). The difference is likely related to the enhanced dust loadings in the Mediterranean Sea region, derived from the Sahara and Sahel areas (Sedwick et al. 2007; Nickovic et al. 2013; Baker et al. 2013).

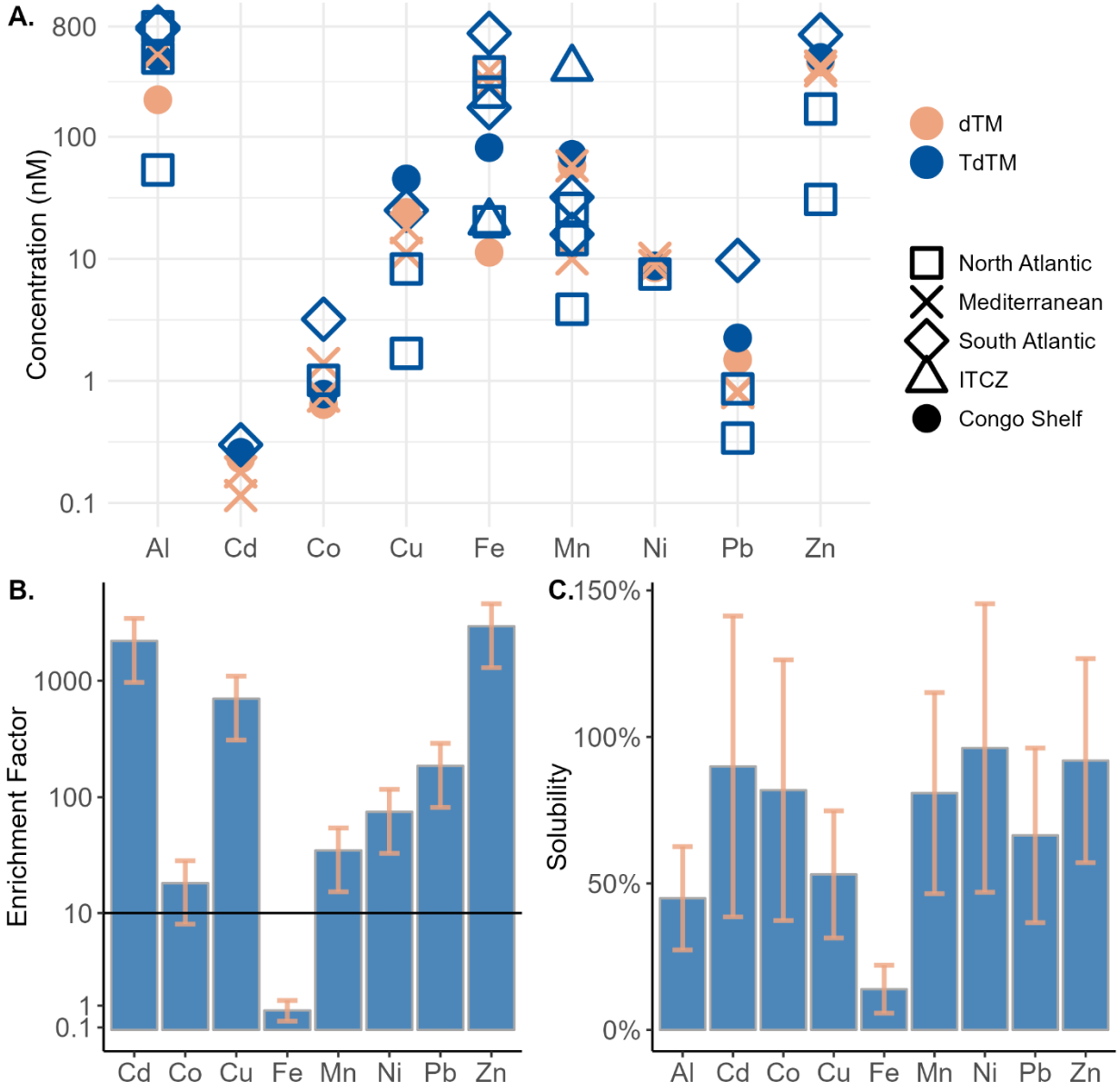


*Figure 4. 3 Trace metal concentrations in rainwater.*
*A. Dissolved (dTM, orange) and total dissolvable (TdTM, blue) volume-weighted-mean TM concentrations (log scale) in different areas including the North Atlantic*(Baker et al. 2013; Shelley et al. 2017) *(squares), Mediterranean*(Desboeufs et al. 2022) *(crosses), South Atlantic*(Baker et al. 2013; Chance et al. 2015) *(diamonds), ITCZ*(Baker et al. 2013) *(triangles) and the Congo shelf (this study, circles). B. Enrichment factor (EF, log scale) and C. fractional solubility (solubility). Error bars of EF and solubility were derived by error propagation of volume-weighted-mean concentrations for each metal.*

*Black horizontal line in B denotes EF = 10, representing a significant enrichment of TMs relative to upper continental crust. Data as per Table S4.3. Note the log scale for concentrations in panel A and Enrichment Factor in panel B.*

Enrichment Factors (EF) are used as indicators of a non-crustal source of anthropogenic TM emissions and, whilst inherently variable, EFs >10 indicate relatively strong evidence for anthropogenically perturbed atmospheric inputs with the natural ratio being exceeded by over an order of magnitude (NRIAGU 1979). All TMs except Fe were significantly enriched relative to the upper continental crust (Rudnick and Gao 2014), with Co showing the next lowest enrichment (EF = 18.2) and Zn the highest (EF = 2942). The EFs thereby indicate non-crustal sources for almost all measured TMs (Figure 4.3B). Low EF values of Fe (0.79 relative to upper continental crust, 0.20 relative to Namibian dust) (Eltayeb et al. 1993) can be interpreted by preferential washout by rain of finer anthropogenic Fe particles (Duce et al. 1976; Jickells et al. 1984; Baker and Croot 2010) compared to coarser Cd and Pb bearing particles in the atmosphere (Dulac et al. 1988; Guieu et al. 1991) at the beginning of the rain season (October, Figure S4.4), which drives the EF value down (Figure 4.3).

The fractional solubilities (hereafter referred as solubility) for Fe (14%) and Mn (81%) in our study were consistent with prior reported values of 9.4% and 74%, respectively(Baker et al. 2013), based on compiled Atlantic data. However, the solubility for Al (45%) was higher than a prior estimate of 13% (Baker et al. 2013). This could reflect increased Al solubility as a consequence of our slightly acidic (pH ~4.3-5.0, Table S4.1) rainwaters compared to typical rainwaters (pH ~5.0-5.6). Lower pH would lead to a higher Al solubility as Al minerals (e.g. aluminosilicates) release more Al at pH ~4.75 and below (Johnson et al. 1981; Losno et al. 1993; Lim et al. 1994). The pronounced enrichment of Cd, Cu and Zn (up to $10^3$ for Cd and Zn) likely reflects increased solubilities in rainwaters as a result of anthropogenic sources as also reported for other regions (Shelley et al. 2017; Desboeufs et al. 2022) (Figure 4.3). The strong anthropogenic signatures, despite high rainfall volumes in the region compared to, for example, the Mediterranean region, might be considered surprising. However, the Congo shelf is known for its extensive crude oil and gas exploitation, and elevated heavy TM emissions associated with large volumes of natural gas flaring (Global Gas Flaring Reduction Partnership 2020).

Analysis of near coastal dTM distributions with respect to salinity from cruise GA08 indicated a 'missing' dTM source associated with freshwater but not from the Congo River (Vieira et al. 2020). Rainwater could be this missing source as it would increase scavenging-type dTM (e.g. dFe) concentrations through an additional supply mechanism following substantial removal in low salinity regions, and increase concentrations of most other TMs (Schlosser et al. 2014; Desboeufs et al. 2022). In a two-endmember mixing model based on river water and coastal seawater, additional input from rainwater would result in dTM concentrations appearing higher than the conservative mixing line where rainwater concentrations were higher than those in the river and vice-versa. However, for TMs with short residence times due to scavenging, an increase of dTM concentrations might also be observed in samples close proximity to rain events even when rainwater concentrations were lower than the river water endmember (Figure 4.2).

Gas flaring has specifically been identified as a major strong TM pollution source for rainwaters in Nigeria (Ighalo et al. 2021; Uzoekwe et al. 2021), one of the top seven gas-flaring countries globally. Although few studies have investigated rainwater pollution closer to the Congo shelf (e.g. Angola and Republic of the Congo), a hundred individual gas flaring sites have been reported in the region with an official emission volume estimate of ~540 million standard cubic metres per day in 2015 (Figure 4.1)(Global Gas Flaring Reduction Partnership 2020). Hence, anthropogenic TM signals of our rainwater samples were plausibly influenced by atmospheric emissions from the gas flaring sites which were transferred by the southerly to south-westerly winds, typical to our study area (Figure 4.1), and then deposited into surface shelf waters. This would explain elevated concentrations of all TMs in surface waters despite a relatively long distance to the river mouth in the northeast corner of the Congo shelf (Figure S4.3 and S4.5). For example, elevated surface concentrations of dCd (>0.11nM), dCo (>0.25nM), dCu (>1.73 nM), dFe (>21.4 nM), dMn (>27.1 nM), dNi (>2.65 nM), dPb (>10 pM) and dZn (>0.35 nM) with salinity >33 were observed within 25 km (two datapoints within 25-50 km) from rainwater sampling locations (Figure 4.2B and Table S4.1). A rainfall TM source is also consistent with higher surface concentrations of Cd, Co, Cu, Mn and Ni compared to their theoretical Congo River-coastal seawater mixed values at $34.5 > S > 32.5$ (*Student's t-test*, $P < 0.05$) (Figure 4.2A). Together, all lines of evidence point towards rainwaters with TM perturbations from

gas flaring as an additional source to the shelf region, thereby reconciling the apparent budget discrepancies highlighted in prior work and explaining the observed dTM distributions (Figure 4.2)(Vieira et al. 2020; Hunt et al. 2022) .

### 4.3.3 River and Rainfall Contributions to Surface Trace Metal Inventories

The water column stratification in our study will have concentrated the effects of rainwater TM deposition to surface waters (Figure S4.2), and facilitates the assessment of external inputs to TM surface inventories over short time scales (hours to days). We compare TM inputs from the Congo River, rainwater and dry atmospheric deposition with TM surface inventories on the Congo shelf (Table S4.4). Atmospheric dry deposition of each TM was calculated based on an Al-derived dust deposition flux (2.67 g $m^{-2}$ $yr^{-1}$) to the Congo shelf (Barraqueta et al. 2019) assuming similar TM abundance as upper continental crust (Rudnick and Gao 2014) and using the experimental solubility of aerosols (Mackey et al. 2015). Overall, inputs from the Congo River are highest for all TMs followed by those from rainfall, which are 1-3 order of magnitudes higher than dry deposition, likely due to the washout effect of rain. Comparing the TM inventories and inputs (Figure 4.4), Fe, Pb and Zn have notably short residence times (< 3 days, Table S4.4) which is consistent with their scavenged-type behaviour. Cadmium, Co, Cu, Mn and Ni have longer residence times (18-106 days, Table S4.4), reflecting high inventories compared to riverine inputs and atmospheric deposition (Figure 4.4). Rainfall supplies Cd, Cu, Pb and Zn at similar magnitudes to the Congo River (Figure 4.4). The relative importance of rainfall calculated herein is likely an underestimation by our calculation, as a fraction of the TMs in the Congo River also likely originated from anthropogenic inputs of rain to the catchment(Best 2019). Rainfall inputs account for at least ~60% of Pb and >100% of Zn inventories over the period of surface water residence times (~2.7 days) on the Congo shelf (Eisma and Van Bennekom 1978), suggesting a considerable impact of anthropogenic inputs. Total rain input of TMs (Rain TdTM) is equivalent to 0.2%-86% of river inputs with the relative importance of rainfall as a TdTM source decreasing in the order Zn > Cd ≈ Cu > Pb > Ni ≈ Mn > Co > Fe (Figure 4.4 and Table S4.4). These calculations do not account for the complexities of freshwater-seawater mixing processes. Zinc inputs by rain would exceed those by the Congo River if taking into account

removal during transfer from the river to the Congo shelf as noted by higher inputs relative to its surface inventories (Figure 4.4). The rainfall inputs of Fe were 2-3 orders of magnitude lower than Congo River inputs, but rainwater inputs are disproportionately important as riverine dFe removal in low salinities regions efficiently removes Fe before it reaches the shelf (Boyle et al. 1977). A removal of up to 85% of dFe was reported for the Congo River at low salinities (S < 5)(Figuères et al. 1978). A much lower removal factor (~17%) of dFe has been reported for mixing of rainwater with seawater over comparable time periods and salinity change (Kieber 2003), and hence rainwater may have approximately a 6 fold larger influence than suggested by measured concentrations when compared to river water. This is consistent with observed dFe concentrations on the Congo Shelf, which suggest a removal of only ~50% of dFe, in contrast to observation at the river mouth (85% removal)(Figuères et al. 1978). The difference between 85% and 50% removal may be related to the addition of rainwater derived dFe (discussions below) which is not accounted for in a two-endmember mixing model.

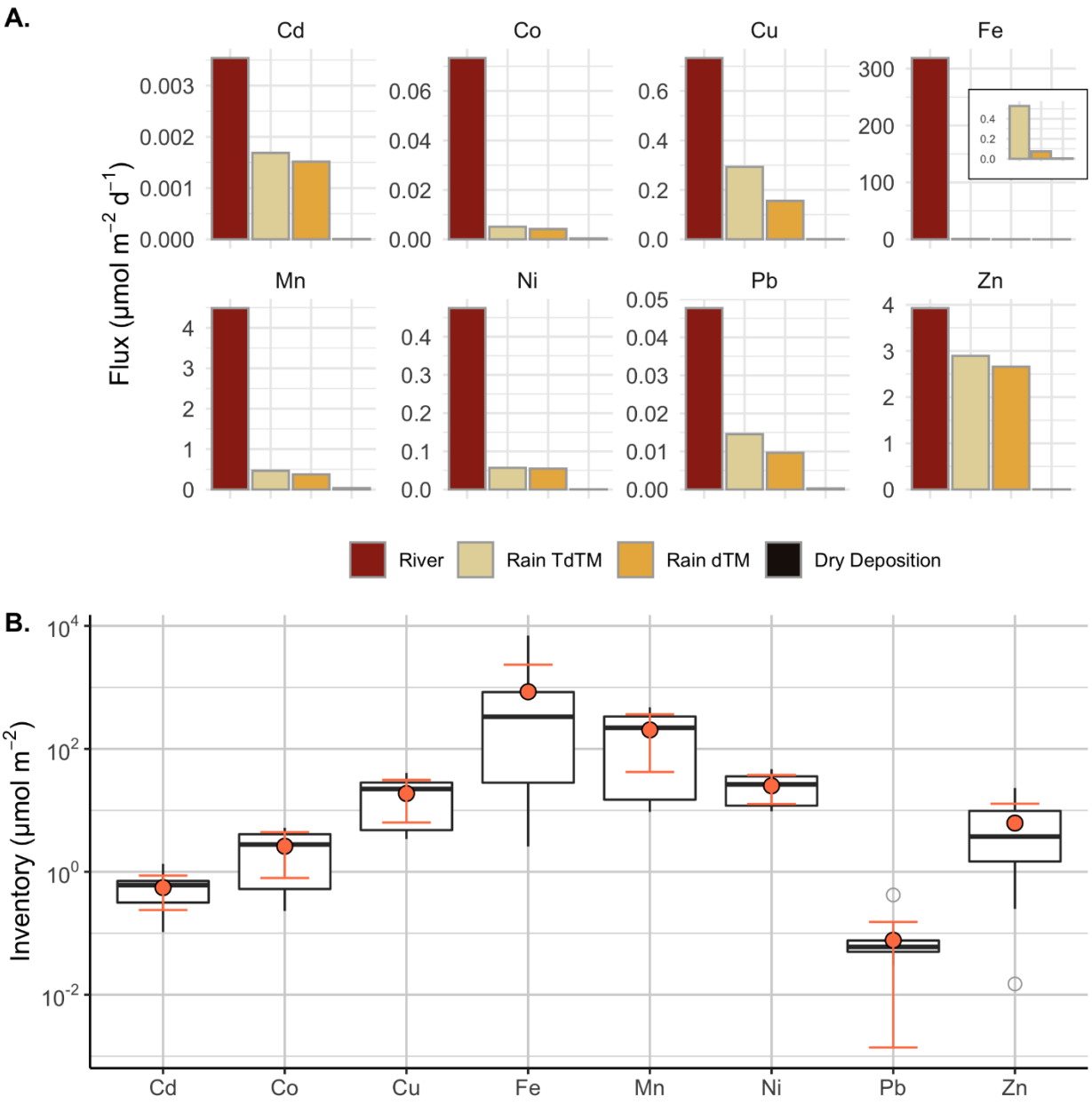


*Figure 4. 4 Fluxes and inventory of TMs at all stations along the Congo shelf. A. TM fluxes (µmol $m^{-2}$ $d^{-1}$) from the Congo River (River), rainfall (total dissolvable: Rain TdTM and dissolved: Rain dTM) and atmospheric dry deposition (Dry Deposition). In-set shows Fe fluxes from Rain TdTM, Rain dTM, and Dry Deposition. B. TM inventory (µmol $m^{-2}$) in surface water along Congo shelf. Note the log scale. Boxes represent median values, 25$^{th}$ and 75$^{th}$ percentiles. Grey points outside of box are potential outliers which are defined as above the 75$^{th}$ or below the 25$^{th}$ percentile by a factor of 1.5 times the interquartile range. Orange points represent mean values of each TM inventory with error bar (1sd). Data as per supplementary Table S4.4.*

### 4.3.4 Freshwater Trace Metal Fluxes to the South Atlantic Ocean

The Congo plume was detectable along an offshore transect of up to ~1400 km from the river mouth (Figure 4.1) to the South Atlantic subtropical gyre, by elevated surface dTM concentrations of in particular Co, Cu, Fe and Mn (Figure 4.2 and S4.5). Gradients of decreasing concentrations of dCo, dCu, dFe and dMn with increasing salinity to the open ocean indicate offshore transfer of the Congo plume (Figure 4.2). In contrast, the concentrations of Cd, Ni and Pb increased to ~0.05 nM, ~2.5 nM and ~20 pM, respectively (Figure 4.2 and S4.1), at the stations furthest west, and were similar to their surface concentrations reported for the western South Atlantic (e.g. GEOTRACES GA02 cruise: 0.01 ± 0.02 nM of Cd, 2.9 ± 0.8 nM of Ni, 17 ± 5.2 pM of Pb) (GEOTRACES Intermediate Data Product Group 2021). The increase of Cd, Ni and Pb moving offshore is due to high concentrations of these TMs in western South Atlantic surface waters and suggests that the Congo River is not likely a major source of these TMs.

We used two models (Table S4.5), a linear regression (LM, TM concentrations against salinity) and a non-linear general additive model (GAM, TM concentrations against distance to river mouth and salinity), to derive freshwater dTM endmembers at the on-set of the offshore Congo plume (salinity = 0 and distance to the river mouth = 500 km, Figure 4.1). Correspondingly, freshwater TM fluxes were computed (see "*Method*") using the two respective freshwater endmembers (LM-extrapolated and GAM-predicted). Here, all freshwater TM fluxes were slightly lower, but of the same magnitude to Ra-derived TM fluxes out of the Congo margin (Vieira et al. 2020), indicating freshwater (Congo River plume and rainfall) is the major source of Co, Cu, Fe and Mn from the Congo shelf to the South Atlantic Ocean (Table 4.2). The differences between LM-extrapolated and GAM-predicted endmembers can be attributed to various modifications on the shelf including scavenging, phytoplankton uptake and addition from atmospheric inputs., thereby differences of derived TM fluxes by two endmembers represent net additions or loss of TM fluxes in the freshwater plume. The GAM-predicted freshwater endmembers of Co, Cu and Mn at the beginning of the offshore Congo plume (2.93 ± 0.84 nM dCo, 20.1 ± 2.02 nM dCu, 182 ± 52.8 nM dMn) are significantly higher than the LM-extrapolated freshwater endmembers (1.84 ± 0.08 nM dCo, 12.7 ± 1.00 nM

dCu, 97.2 ± 16.4 nM dMn, Table 4.2), being consistent with rain additions of Co, Cu and Mn on the Congo shelf, which corresponds to 40±28%, 36±26%, 47±27% of the additions of Co, Cu and Mn, respectively. In contrast, the lower GAM-predicted freshwater Fe endmember (99.4 ± 14.3 nM) compared to LM-extrapolated freshwater value (204 ± 25.7 nM) indicates a net 51±21% loss of Fe during transfer after estuarine removal (Table 4.2). The lower Fe loss (51±21%) compared to previous observations of ~85% determined at low salinities in the Congo estuary (Figuères et al. 1978) can be related to rainwater additions, which compensated for at least a fraction of estuarine Fe removal on the Congo shelf. This notion is supported by mixing experiments between freshly collected rainwater and seawater (Kieber 2003) which indicated that rain derived dFe is stable on timescales of hours upon mixing likely due to a high fraction of Fe(II) produced by photochemical reactions in rain droplets (Kieber 2003; Kieber et al. 2003) and/or the presence of organic matter complexing Fe in rain (Kieber et al. 2001a, 2005). The specific nature of organic matter in the Congo plume has been proposed to contribute to the efficient distal transport of Fe offshore (Vieira et al. 2020; Hunt et al. 2022).

*Table 4. 2 Comparison of endmembers and fluxes between a linear regression model (LM), general additive model (GAM) and calculations based on radium (Ra) isotope.*

| | LM (S = 0) | | GAM (S = 0, distance to the river mouth = 500 km) | | Ra-derived [a] |
|---|---|---|---|---|---|
| TM | Endmember (nM) | Flux (mol $d^{-1}$) | Endmember (nM) | Flux (mol $d^{-1}$) | Flux (mol $d^{-1}$) |
| Co | 1.84 ± 0.08 | $6.6±1.9 \times 10^{3}$ | 2.93 ± 0.84 | $1.1±0.4 \times 10^{4}$ | $1.3±0.5 \times 10^{4}$ |
| Cu | 12.7 ± 1.00 | $4.6±1.3 \times 10^{4}$ | 20.1 ± 2.02 | $7.2±2.1 \times 10^{4}$ | $8.5±3.8 \times 10^{4}$ [a] |
| Fe | 204 ± 25.7 | $7.3±2.1 \times 10^{5}$ | 99.4 ± 14.3 | $3.6±1.1 \times 10^{5}$ | $1.9±0.6 \times 10^{6}$ |
| Mn | 97.2 ± 16.4 | $3.5±1.1 \times 10^{5}$ | 182 ± 52.8 | $6.6±2.6 \times 10^{5}$ | $8.5±3.3 \times 10^{5}$ |

[a] *Ra-derived Cu flux was newly calculated as previously undertaken for Co, Fe and Mn in Vieira et al., 2020.*

### 4.4 Conclusions and Implications

Rainfall supplements TM fluxes from the Congo River to the South Atlantic Ocean with the rainwaters containing high concentrations of anthropogenic TMs, and an inefficient removal of dFe after mixing with seawater due to the organic and redox chemistry of rainwater may contribute to high dFe concentrations in the Congo plume.

Most notably, rainfall fluxes of anthropogenic Cd, Cu, Pb and Zn, derived from gas flaring emissions, likely formed an additional supply to the Congo shelf. This is a hitherto unaccounted source of TMs to surface waters of the South Atlantic Ocean. Considering a rise in flaring volumes (Lorenzato et al. 2022) and hydrocarbon extraction moving offshore globally in recent years (Lu et al. 2020), the associated emission of TMs and other pollutants may be increasing and influencing larger areas of the ocean. This is particularly the case for the eastern South Atlantic with over 100 gas flaring sites reported in the cruise area, where increasing off shore gas flaring would directly impact coastal oceans and fisheries by the prevailing wind directions. Anthropogenic inputs of atmospheric TMs to the Congo shelf are concentrated in surface waters due to strong water column stratification, with this may increase the risks of TM accumulation in the food chain resulting in contamination of seafood products from fisheries in the productive area.

## 4.5 Supplementary Material

*Table S4. 1 Details of rainwater sampling.*

| Rain event | Date | Start Time (UTC) | Latitude | Longitude | Sampling duration (min) | pH | Volume (mL) |
|---|---|---|---|---|---|---|---|
| Rain#1 | 29/11/2015 | 09:45 | -6.306 | 12.005 | 108 | 5.03 | 100 |
| Rain#2 | 30/11/2015 | 09:15 | -5.776 | 11.858 | 55 | 4.76 | 1500 |
| Rain#3 | 30/11/2015 | 10:10 | -5.749 | 11.882 | 85 | 4.72 | 200 |
| Rain#4 | 30/11/2015 | 14:05 | -5.763 | 11.474 | 20 | 4.55 | 40 |
| Rain#5 | 01/12/2015 | 00:01 | -4.272 | 10.482 | 299 | 4.33 | 20 |
| Rain#6 | 01/12/2015 | 06:30 | -3.898 | 10.289 | 75 | 4.41 | 140 |
| Rain#7 | 01/12/2015 | 09:55 | -3.227 | 9.945 | 120 | 4.72 | 300 |

*Table S4. 2 Pearson's Rank Correlation Coefficients for TMs, salinity and distance to the river mouth (Distance) along the Congo shelf.*

| | Distance | Salinity | Cd | Co | Cu | Mn | Fe | Ni | Pb | Zn |
|---|---|---|---|---|---|---|---|---|---|---|
| Distance | - | | | | | | | | | |
| Salinity | -0.128 | - | | | | | | | | |
| Cd | **-0.443** | -0.264 | - | | | | | | | |
| Co | -0.316 | -0.416 | **0.797** | - | | | | | | |
| Cu | -0.369 | **-0.570** | **0.665** | **0.915** | - | | | | | |
| Mn | -0.293 | -0.388 | **0.727** | **0.988** | **0.916** | - | | | | |
| Fe | -0.387 | **-0.790** | **0.442** | **0.667** | **0.833** | **0.658** | - | | | |
| Ni | -0.380 | -0.532 | **0.730** | **0.952** | **0.984** | **0.946** | **0.801** | - | | |
| Pb | -0.326 | **-0.743** | 0.327 | **0.481** | **0.644** | **0.457** | **0.945** | **0.616** | - | |

| | | | | | | | | | | |
|---|---|---|---|---|---|---|---|---|---|---|
| Zn | -0.270 | **-0.681** | **0.633** | **0.758** | **0.882** | **0.758** | **0.824** | **0.849** | **0.660** | - |

*Note. Values in bold represent correlations that are statistically significant (P-values of <0.05).*

*Table S4. 3 Volume-weighted-mean TM concentrations (dissolved and total dissolvable), average enrichment factors (EF), fractional solubility (%).*

| | This study (the Congo shelf) | | | | |
|---|---|---|---|---|---|
| TM | Dissolved (nM) | Total dissolvable (nM) | n(>LOD) | Average EF | Solubility (%) |
| Al | 201 ± 65.6 | 447 ± 97.4 | 7 | - | 44.9% |
| Cd | 0.23 ± 0.10 | 0.26 ± 0.10 | 7 | 2199 | 89.9% |
| Co | 0.64 ± 0.26 | 0.78 ± 0.28 | 7 | 18.2 | 81.8% |
| Cu | 24.0 ± 7.80 | 45.2 ± 11.2 | 7(5) | 702 | 53.1% |
| Mn | 58.0 ± 16.2 | 71.8 ± 23.0 | 7 | 34.8 | 80.8% |
| Fe | 11.3 ± 4.93 | 81.5 ± 32.3 | 7 | 0.79 | 13.9% |
| Ni | 8.43 ± 3.16 | 8.76 ± 3.06 | 7 | 74.7 | 96.2% |
| Pb | 1.49 ± 0.53 | 2.25 ± 0.62 | 7 | 186 | 66.4% |
| Zn | 410 ± 113 | 447 ± 117 | 7 | 2942 | 91.9% |

*Table S4. 4 Surface water inventory ($I_{surface}$) in unit of µmol m$^{-2}$, inputs from Congo River ($F_{river}$) and rainfall ($F_{rain}$, D and Td for dissolved and total dissolvable) in unit of µmol m$^{-2}$ d$^{-1}$ and TM residence time across the Congo shelf.*

| TM | $I_{surface}$ (µmol m$^{-2}$) | | | Fluxes (µmol m$^{-2}$ d$^{-1}$) | | | | Residence time (d) |
|---|---|---|---|---|---|---|---|---|
| | Range | Average ± | n | $F_{river}$ | $F_{rain}$(dTM) | $F_{rain}$(TdTM) | $F_{dry}$ | |
| Cd | 0.11-1.35 | 0.55 ± 0.31 | 24 | 0.004 ± 0.000 | 0.002 ± 0.002 | 0.002 ± 0.002 | 4.5E-06 | 106 |
| Co | 0.23-5.19 | 2.60 ± 1.81 | 24 | 0.073 ± 0.026 | 0.004 ± 0.004 | 0.01 ± 0.01 | 3.6E-04 | 33 |
| Cu | 3.42-40.7 | 18.8 ± 12.5 | 24 | 0.73 ± 0.27 | 0.16 ± 0.16 | 0.29 ± 0.30 | 4.6E-04 | 18 |
| Mn | 9.41-472 | 203 ± 161 | 24 | 4.49 ± 5.70 | 0.38 ± 0.39 | 0.47 ± 0.49 | 3.7E-02 | 41 |
| Fe | 2.58-6970 | 850 ± 1488 | 24 | 319 ± 136 | 0.07 ± 0.08 | 0.53 ± 0.57 | 4.3E-03 | 2.7 |
| Ni | 9.68-46.6 | 25.1 ± 12.4 | 24 | 0.47 ± 0.26 | 0.05 ± 0.06 | 0.06 ± 0.06 | 7.0E-04 | 47 |
| Pb | 0.03-0.42 | 0.08 ± 0.08 | 24 | 0.05 ± 0.03 | 0.01± 0.01 | 0.01 ± 0.02 | 2.8E-04 | 1.2 |
| Zn | 0.02-23.1 | 6.20 ± 6.61 | 22 | 3.93 ± 5.05 | 2.66 ± 2.76 | 2.89 ± 2.99 | 4.3E-03 | 0.9 |

Note. *Error on $\boldsymbol{F_{rain}}$ calculated by propagation of volume-weighted-concentrations error (25%-69%) and 100% RSD of the precipitation rate. Residence time of each TM was calculated as $\boldsymbol{I_{surface}/(F_{river} + F_{rain}(TdTM) + F_{dry})}$.*

*Table S4. 5 Comparison between linear regression model (LM) and general additive model (GAM) indicated by explanatory power (deviance explained) and root mean standard error for each TM (RMSE).*

| TMs | Linear Regression Model (TM ~ Salinity) | General Additive Model (TM ~ Salinity and Distance to the river |
|---|---|---|

| | Deviance explained | RMSE | Deviance explained | RMSE |
|---|---|---|---|---|
| Co | 96.6% | 0.006 | 99.5% | 0.003 |
| Cu | 88.7% | 0.082 | 96.0% | 0.049 |
| Fe | 77.3% | 2.09 | 99.9% | 0.20 |
| Mn | 64.0% | 1.33 | 97.7% | 0.34 |

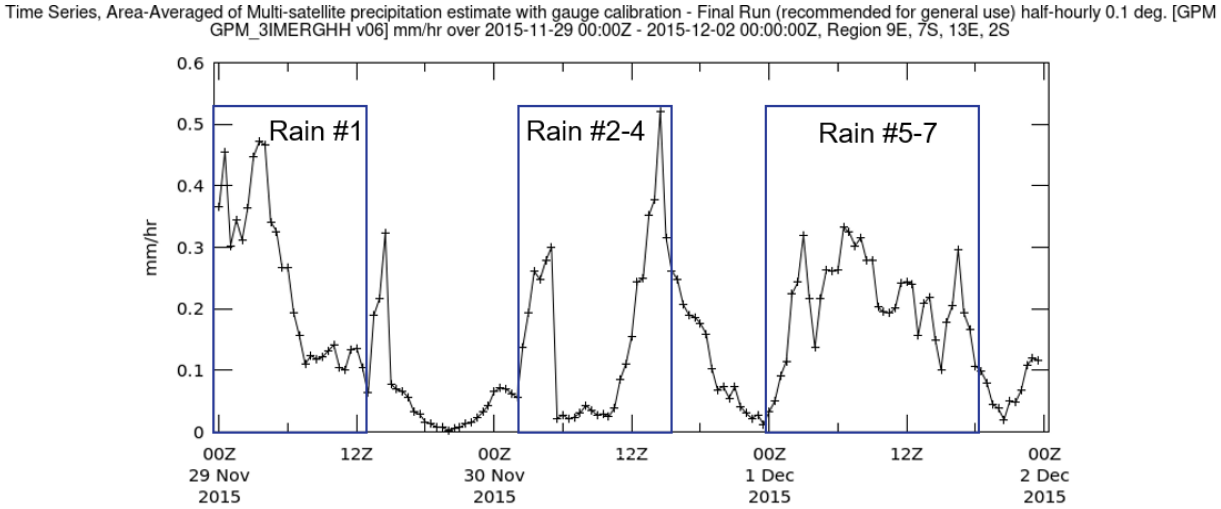


*Figure S4. 1 Plots of precipitation rate (mm hr$^{-1}$) and discrete rain events within the period of sailing within the Congo shelf region from 29 November 09:00 UTC to 02 December 05:59 UTC.*
*Data and plots were retrieved from satellite product of GPM IMERG Final Precipitation L3 Half Hourly 0.1° x 0.1° V06 in NASA Goddard Earth Sciences Data and Information Services Centre (GES DISC)*(Huffman et al. 2019).

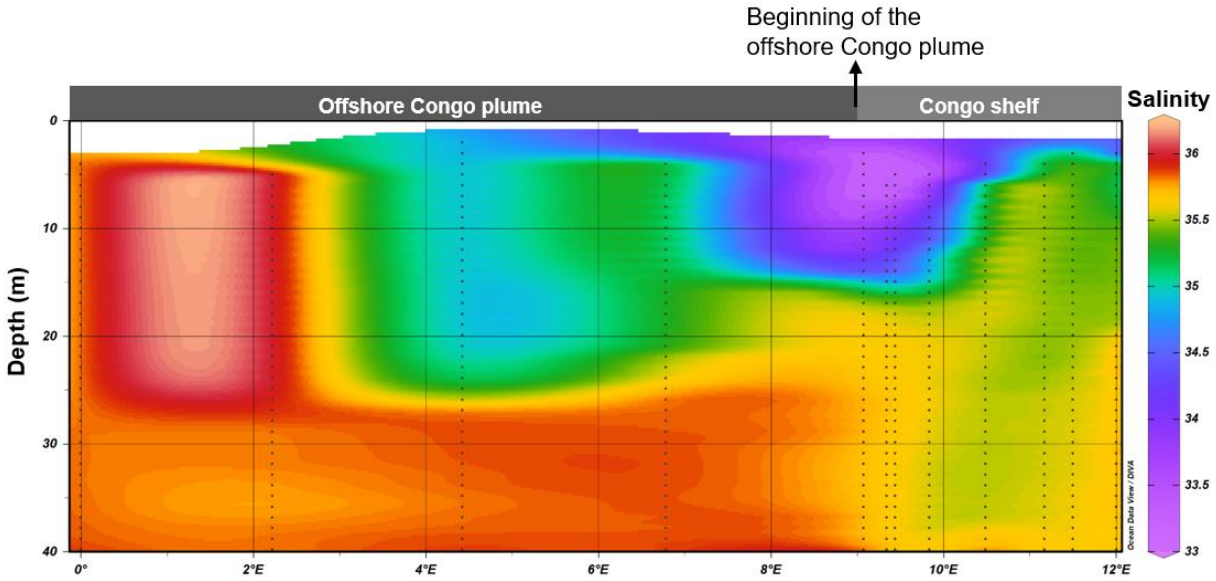


*Figure S4. 2 Section plot of stratified salinity within our study area.*

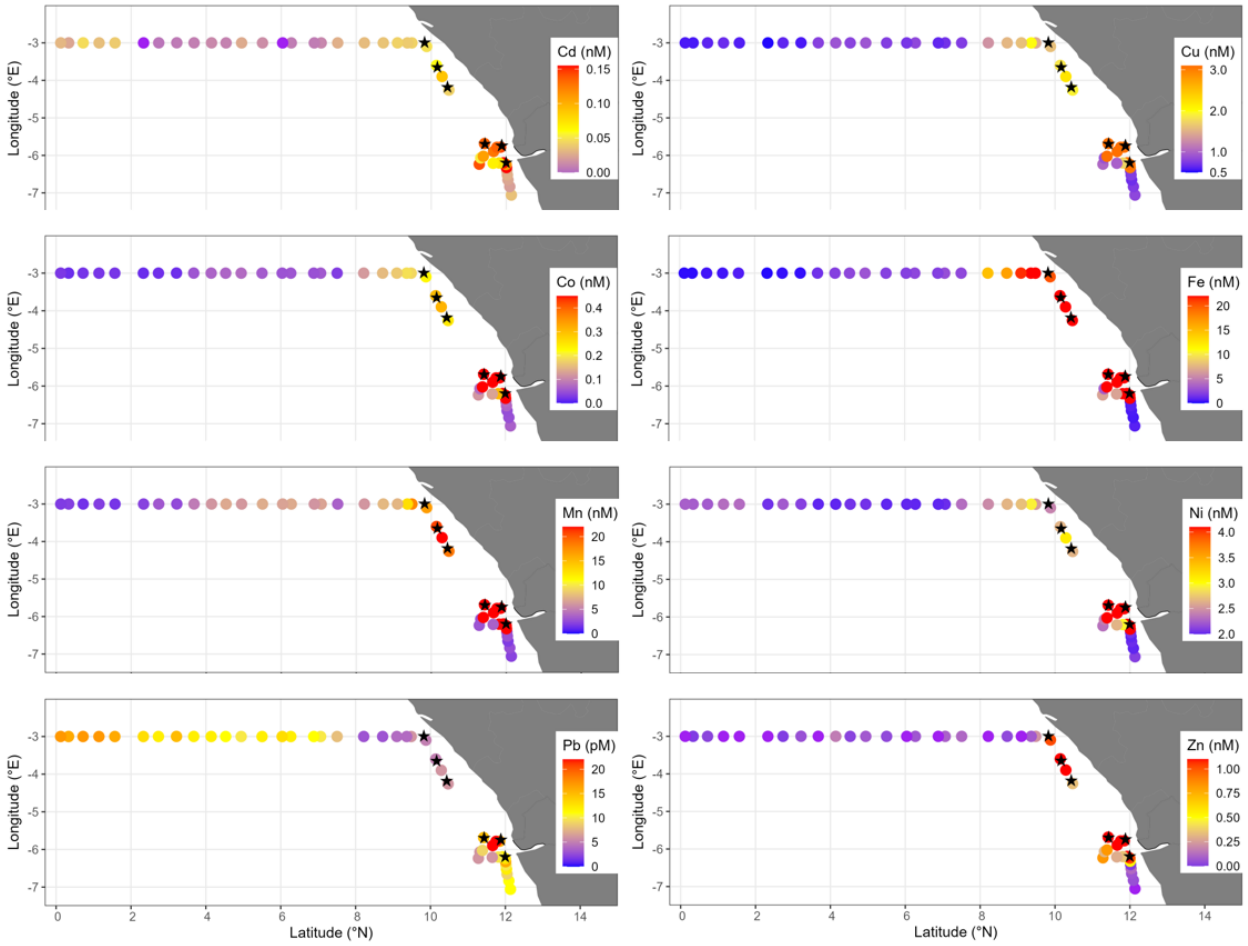


*Figure S4. 3 Selective surface water concentrations (colour circles) of dissolved Cd, Co, Cu, Fe, Mn, Ni, Pb and Zn and rain events (black stars) in our study area.*
*Note. Black stars representing rain events #2 and #3 are overlapped.*

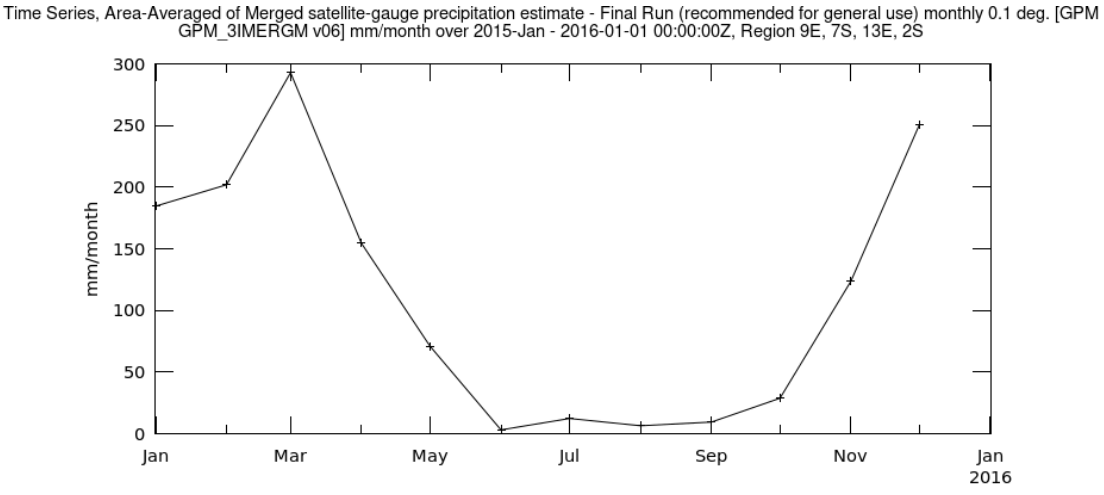


*Figure S4. 4 Plots of monthly precipitation rate during the year of 2015.*

*Data and plots were retrieved from satellite product of GPM IMERG Final Precipitation L3 Half Hourly 0.1° x 0.1° V06 in NASA Goddard Earth Sciences Data and Information Services Centre (GES DISC)*(Huffman et al. 2019).

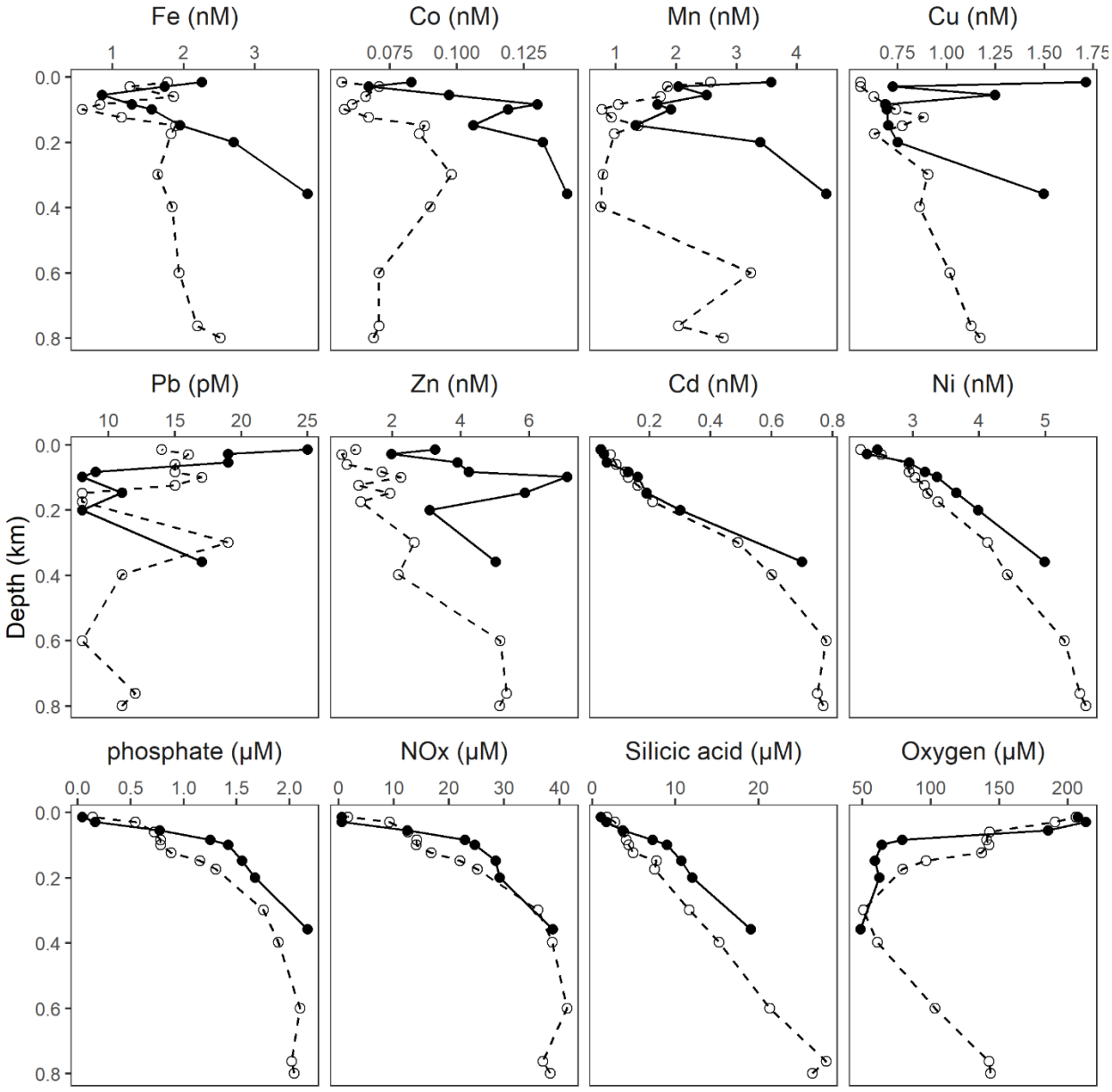


*Figure S4. 5 Representative depth profiles for trace metals, macronutrients (phosphate, nitrate + nitrite: $NO_X$, silicic acid) and oxygen concentrations.*
*Solid circle: Station 15 on the Congo shelf; Open circle: Station 20 at the beginning of the offshore Congo plume. Units are indicated.*

**Text S4.1**

Macronutrient samples were collected alongside dissolved trace element samples using the same sampling/filtration equipment rinsing vials once with sample water. Samples were then stored at 4°C in darkness and analysed within 8 h on board via an autoanalyzer. Nanomolar level macronutrient samples (mainly nitrate + nitrite ($NO_x$) < 100 nM) were stored frozen at -20°C to be reanalysed onboard.

Analysis of macronutrients including nitrate + nitrite ($NO_x$), $PO_4^{3-}$ and silicic acid concentrations was undertaken onboard by segmented flow injection analysis using a QUAATRO (Seal Analytical) auto-analyser (Grasshoff et al. 1999). Re-analysis of nanomolar macronutrient samples was following the method of Patey et al. (2008) after defrosting retained water samples.

**Competing interests**

The corresponding author has declared that neither she nor other co-authors have any competing interests.

**Acknowledgements**

We thank the captain and crew of the RV Meteor M121 cruise/GEOTRACES GA08 section and the chief scientist Martin Frank for cruise support. We thank Pablo Lodeiro, Christian Schlosser and Jan-Lucas Menzel Barraqueta for their assistance in sample collection on the GA08 expedition. We thank Mr Bomba Sangolay from the National Institute of Fisheries Research (Instituto Nacional de Investigação Pesqueira, Luanda, Angola) for collection of samples in the Congo River. The PhD Fellowship to T.L. was funded by China Scholarship Council. Additional financial aid to T.L. from the German Academic Exchange Service is acknowledged (DAAD). The cruise was funded by the Deutsche Forschungsgemeinschaft (DFG). GEOMAR supported trace metal analysis.

**Contributions**

T.L. conceived and investigated the study and wrote the first draft of the manuscript. M.J.H., S.K. and T.L. analysed trace metal samples. M.J.H., E.P.A, and T.L. improved subsequent drafts. M.J.H. helped with interpretation of results. L.H.V. provided radium-derived Cu fluxes. E.P.A. co-led the research cruise and oversaw sample analyses. All authors edited on the final manuscript.

# 5. Internal cycling of trace metals in the eastern South Atlantic: insights from dissolved and particulate trace metals

**Te Liu**

To be submitted

**Abstract**

Trace metals (TMs) exert an important role in shaping biogeochemical conditions in the ocean and several TMs act as micronutrients supporting primary production. The internal transformation of TMs between dissolved TM (dTM) and particulate TM (pTM) phases in the water column determines TM residence time and bioavailability. The internal cycling of TMs in the remote open ocean with a limited external TM supply forms a strong control on micronutrient availability to primary producers, but until recently has been poorly investigated due to the absence of extensive full depth-profiles of TMs including both dTM and pTM phases. Here, we present full-depth profiles of paired dTM and pTM distributions along a meridional section (0°E) of the GEOTRACES GA08 cruise in the South Atlantic Ocean. We find that elevated concentrations of particulate cobalt (Co), copper (Cu), manganese (Mn), lead (Pb) and zinc (Zn) in the deep waters were caused by sinking of authigenic/biogenic phases from the surface ocean with only modest TM signatures evident that originated by ocean seafloor processes. Accumulation of dCo, dissolved iron (dFe), and dZn in intermediate waters is over one to tens of times lower than expected from regeneration of biogenic particles from surface waters, suggesting scavenging of dCo, dFe and dZn in intermediate waters. Variations of dMn and total particulate Mn (Tp-Mn) with depth reveal that authigenic Mn oxide formation is the major process through which dMn was removed. Scavenging onto Mn oxides accounts for a major sink for dCo due to scavenging, leading to enriched Tp-Mn and Tp-Co concentrations in deep waters. Enhanced concentrations of biogenic elements Tp-Cd, Tp-Co, Tp-P, and chlorophyll a (Chl.a) in surface waters were in contrast to depleted concentrations of dCd, dCo and phosphate ($PO_4^{3-}$), and indicated biological control of Cd, Co and P distributions. A comparison of estimated uptake, recycling and external supply for Cd, Co and P indicated recycling was responsible for >90% of the assimilation of these elements in the oligotrophic surface waters of the South Atlantic Ocean. Regional primary production shows a more dependence (lower $fe$ ratio) on recycling of Cd and Co in the South Atlantic Gyre (SAG) compared to the Angola Basin, in line with observations of prior bioassay work which indicated phytoplankton growth under Fe-(co)limitation and serial limitation with Co and vitamin $B_{12}$ in the SAG due to a limited supply of these micronutrients. Our study contributes the growing body of

datasets that report both dTM and pTM concentrations, and emphasizes the importance of internal cycling of TMs for biogeochemical conditions, and adds to the increasing evidence of well-defined general trends in elemental distributions particularly for Cd, Co, Mn and Pb.

## 5.1 Introduction

The cycling of trace metals (TMs) in the ocean reflects a balance between external supply, internal cycling and removal. A variety of TMs are crucial as bio-essential micronutrients for phytoplankton growth and can impact oceanic primary productivity (Twining and Baines 2013; Moore et al. 2013). A range of TMs, including iron (Fe), cobalt (Co), manganese (Mn) and zinc (Zn) have been shown to be (co)-limiting primary productivity in response to a deficiency in their supply or availability relative to the macronutrients nitrogen (N, fixed N: nitrate and nitrite, $NO_x$) and phosphate ($PO_4^{3-}$) (Morel et al. 1994; Hutchins and Bruland 1998; Browning et al. 2018, 2021). Trace metal sources to the ocean include atmospheric deposition, and inputs by rivers, shelf sediments and hydrothermal vents. Many studies focus on the identification of external TM supply, and boundary exchange between land and ocean in an attempt to constrain these fluxes and assess their relative importance in relieving TM (co-)limitation for phytoplankton growth (Jickells et al. 2005; Resing et al. 2015; Liu et al. 2022b). However, internal cycling of TMs is particularly important to sustain productivity as remineralization recycles micronutrients in surface waters and replenishes their inventories at depth (Boyd et al. 2017; Tagliabue et al. 2019). Broadly, this can be characterised as the exchange of TMs between dissolved TMs (dTMs) and particulate TMs (pTMs) phases. Trace metals are exchanged between these phases until ultimately sinking particles deliver pTMs to the seafloor where subsequent diagenetic processes may occur and also long-term storage. Given the reliance of ecosystems on internal cycling of TMs to supply micronutrients across the coastal and open ocean, there is a need to identify the processes that regulate the internal cycles and quantify fluxes of TMs associated with these processes.

Marine particles are important TM reservoirs and act as vectors that transport TMs both laterally and vertically in the water column (Lam and Bishop 2008; Jeandel et al. 2015). The significance of sources/sinks *vs.* internal cycling in driving the marine

biogeochemistry of TMs differs between elements. For example, aluminium (Al) in the ocean is largely derived from inputs of dust and sediments (Moran and Moore 1991; Chester 2009; Barraqueta et al. 2018) and its distribution in the ocean reflects recent atmospheric dust deposition. Cadmium (Cd) Co, copper (Cu), Fe, Mn, phosphorus (P) and Zinc (Zn) are cycled with bio-assimilation into biogenic particles and subsequently released into the water column through remineralization of the biogenic material (Boyd and Ellwood 2010; Bruland et al. 2014; Tagliabue et al. 2018). Cobalt, Cu, Fe, lead (Pb) and Zn can also be removed from the water column through scavenging and precipitation of authigenic minerals including Mn-Fe oxyhydroxides (Cowen and Bruland 1985; Moffett and Ho 1996; Little et al. 2014).

Marine particles can exist in several phases and distribute heterogeneously in the water column. Lithogenic particles are derived from weathering and erosion of the continents and resuspension of seafloor sediments (Jeandel and Oelkers 2015). Biogenic particles are produced in surface water through biological assimilation of carbon, dTMs and macronutrients (Twining et al. 2015). Finally, authigenic particles such as Fe and Mn oxide are produced within the water column (Bruland et al. 2014). Marine particles can also develop internal chemical gradients like dissolved oxygen and TM concentrations by remineralization and scavenging in the water column (Balzano et al. 2009; Raven et al. 2021). In addition, marine particle formation can be subjected to redox state of water column. For example, Fe and Mn in seawater are often present in dissolved or (authigenic) particulate phase depending on various redox states (Heller et al. 2017; van Genuchten et al. 2022). Therefore, studying interaction and exchange between and within dTM and pTM improves our understanding of a complex network of dynamic interactions.

Here, we report on a full-depth meridional section of dTM and pTM concentrations along 0°E in the eastern South Atlantic from GEOTRACES cruise GA08. The region receives relatively little dust input and crosses an oligotrophic gyre (Figure 5.1)(Barraqueta et al. 2019), although in the northern most stations an influence of the Congo plume is evident in near-surface waters (Vieira et al. 2020). The aim of this study is to assess the mechanisms controlling the dTM and pTM distributions in the region and quantify internal fluxes of bio-essential TMs.

## 5.2 Materials and Methods

### 5.2.1 Study Area

Two contrasting oligotrophic conditions were observed along the study section. The transition was generally characterized by a shift from N limitation to N-Fe co-limitation and Co serial limitation of primary productivity whilst moving from the Angola Basin in the north to the South Atlantic Gyre (SAG) in the south. The Angola Basin typically features relatively higher net primary productivity (NPP, 37.1 ± 8.6 mmol C $m^{-2}$ $d^{-1}$) due to offshore upwelling and the influence of the Congo plume compared to the SAG with a NPP of 23.5 ± 4.9 mmol C $m^{-2}$ $d^{-1}$ (NOAA NMFS SWFSC ERD (National Oceanic and Administration, National Marine Fisheries Service, Southwest Fisheries Science Center).

The surface ocean circulation in the eastern South Atlantic Ocean was reported by Rahlf et al., (2021) (Figure 5.1). Briefly, the Angola Gyre is separated at ~15-20°S from the Benguela Offshore Current (BOC), which is detectable to depths of ~200 m (Peterson and Stramma 1991; Lass and Mohrholz 2008). In the Angola Basin, the vigorous zonal Equatorial Undercurrent (EUC) transports South Atlantic Central Water (SACW), originating near the equatorial belt from the western to eastern South Atlantic, feeding the South Equatorial Current (SEC) near the African coast. Additional transport of SACW toward the east and south takes place by the South Equatorial Counter Current (SECC) in subsurface waters. The cyclonic Angola Gyre is a prominent feature in the offshore upwelling zone of the Angola Basin (Stramma and Mathew England 1999; Brandt et al. 2015). In the SAG, the BOC flows northwards in an offshore direction and transports colder and fresher Eastern SACW (ESACW) (Rae 2005; Liu and Tanhua 2021).

Our study site is influenced by a series of water masses. The surface waters in the Angola Basin are influenced by the Congo plume. The subsurface water (~100 -500 m) is dominated by SACW with potential temperatures of 8.5-15.8°C (Figure 5.1). The intermediate water mass in our study area is mainly Antarctic Intermediate Water (AAIW) with potential temperature between 4.6 - 8.5°C, overlying North Atlantic Deep Water (NADW). The NADW is characterized by elevated salinity and low potential temperature of 1.8 - 4.3°C. Although Antarctic Bottom Water (AABW) propagates to the

South Atlantic, its northward transport is blocked by Walvis Ridge (Stramma and Mathew England 1999). Therefore, AABW was undetectable in our study area.

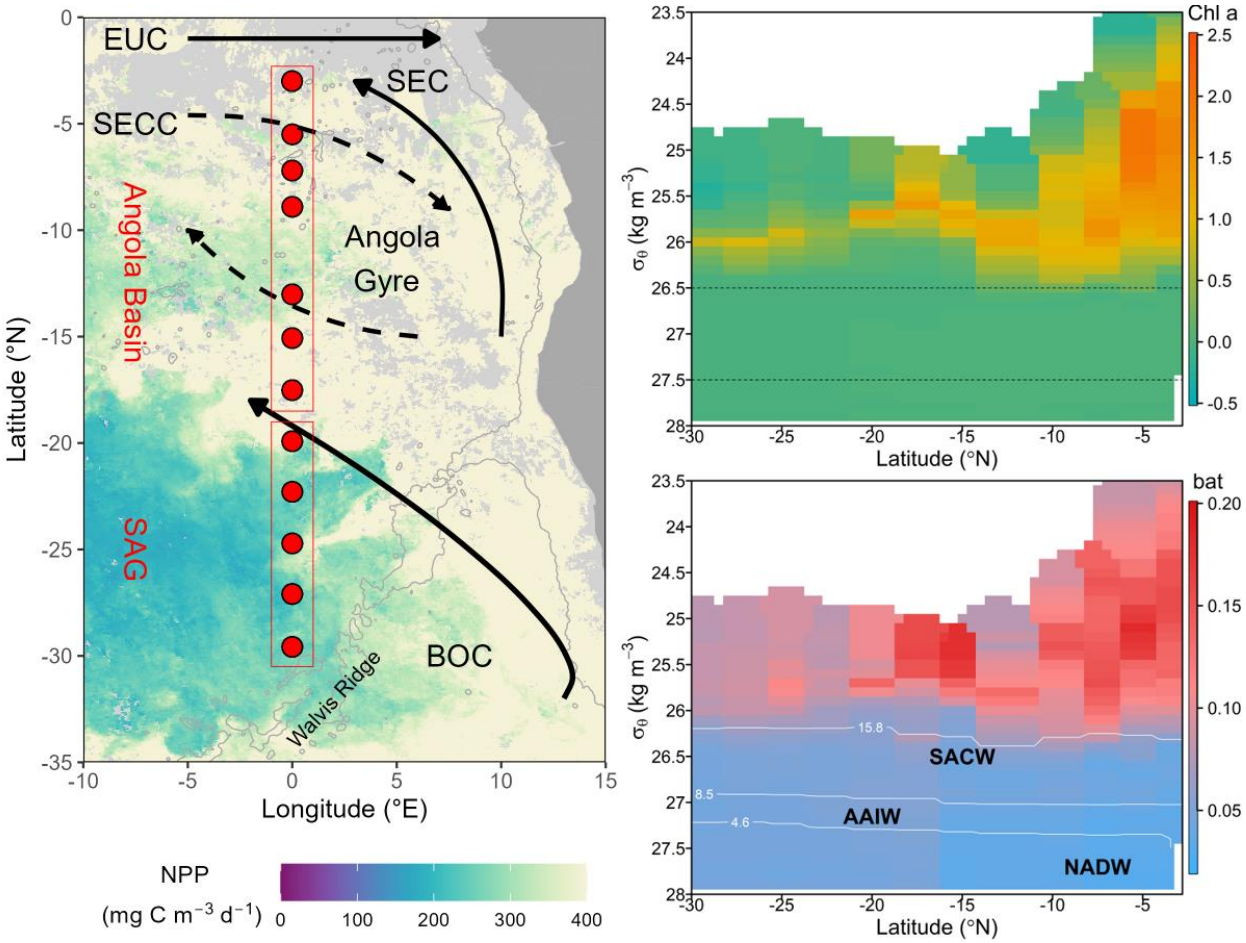


*Figure 5. 1 Map and profile sites (red circles) in the oligotrophic South Atlantic. Left panel shows estimated net primary production (NPP) (color background) from the Moderate Resolution Imaging Spectroradiometer NOAA satellite database (https://www.noaa.gov/) (NOAA NMFS SWFSC ERD (National Oceanic and Administration, National Marine Fisheries Service, Southwest Fisheries Science Center) annotated with the main offshore surface ocean currents: Equatorial Undercurrent (EUC), South Equatorial Current (SEC), South Equatorial Counter Current (SECC), Angola Gyre and the offshore branch of Benguela Offshore Current (BOC). A bottom depth contour of 3000 km is shown as a greyline to delineate Walvis Ridge. We refer to two study regions: the Angola Basin and South Atlantic Gyre (SAG). Right panels show (top) distributions of chlorophyll. a (Chl a, raw data in relative unit from fluorescence sensor of WETlabs) with potential density contour lines of 26.5 and 27.5 kg $m^{-3}$ (black dashed lines) and (bottom) beam attenuation (bat, arbitrary units) overlaid by contour lines of potential temperature to indicate water masses.*

### 5.2.2 Sample Collection

Seawater samples were collected along the offshore 0°E transect from ~3°S-30°S during the GEOTRACES GA08 cruise in the eastern South Atlantic (Figure 5.1). A total of 12 stations with a vertical resolution of 22-24 depths between 12 m and 5400 m were sampled for TMs using 12 L trace metal clean Go-Flo bottles (Ocean Test Equipment) mounted on a CTD rosette frame (trace metal clean, General Oceanics). Upon recovery, the Go-Flo bottles were transferred into a trace metal clean laboratory container, where they were over pressurized with ~0.2 bar nitrogen for sampling for dissolved (d, filtered through 0.8/0.2 μm AcroPak® cartridge filter) and particulate TMs (p, materials onto acid washed 0.2 μm pore-size PES membrane filter). Seawater samples for dTM concentrations were acidified to pH ~1.9 by an addition of 180 μL ultra-pure grade hydrochloric acid (HCl, UpA Romil®) to 125 mL seawater (in acid cleaned low density polyethylene (LDPE) bottles, Nalgene®) and stored double-bagged in the dark for > 6 months until analysis. Membrane filters for pTM analysis were lightly rinsed with 50 mL Milli-Q water, placed in an acid clean Petri-dishes and stored double-bagged in a -20°C freezer until analysis.

Macronutrient samples were collected from the Go-Flo bottles into vials that were rinsed with sample seawater. Samples were then stored at 4°C in darkness until analysis within 8 h onboard.

### 5.2.3 Analytical Methods

Samples of dTMs were pre-concentrated offline using a SeaFAST system (SC-4 DX SeaFAST pico, Elemental Scientific Inc.) exactly as per Rapp et al., (2017) and concentrations of dTMs were analysed on a high-resolution isotope inductively coupled mass spectrometry (HR-ICP-MS, ELEMENT XR, ThermoFisher Scientific®). Concentrations of Cd, Cu, Fe, Ni and Zn were quantified by isotope dilution, while Co, Mn and Pb concentrations were quantified using standard additions (Rapp et al. 2017). Certified reference materials SAFe S, SAFe D2, GSP, NASS 7 and CASS 6 were analysed alongside samples and were in close agreement with their certified values (Table 2.2). All acids used were distilled or of optima or ultra pure grade. All plasticwares were vigorously cleaned with HCl and $HNO_3$ acids according to

GEOTRACES protocols (Cutter et al. 2017). Sample handling was carried out within Class 100 lamina flow hoods in Class 1000 clean laboratory at GEOMAR.

Methods for leaching and digesting of particulate samples followed those described in Al-Hashem et al. (2022). Briefly, particulate samples were first leached by a mixture of 2.5 mL 25% acetic acid (Optima grade, Fisher Scientific®) and 0.02 M hydroxylamine hydrochloride (Sigma® TM grade) at 95°C for 10 min, followed by continued leaching during a cool down period of ~2 hr. The leachate (L-pTM) was then transferred to PP centrifuge tubes, centrifuged, dried and re-diluted. The refractory residue (R-pTM) was completely digested by refluxing with 2.5 mL of a strong acid mixture consisting of 50% $HNO_3$ and 10% HF at 150°C for 15 h, dried down, and re-dissolved by an addition of ~0.5 mL 50% $HNO_3$/15% $H_2O_2$ (v/v%). Samples were dried down again, then re-dissolved in 4 ml 1 M indium-spiked $HNO_3$ and analyzed on an HR-ICP-MS. Concentrations were quantified via an external multi-element calibration curve prepared in a similar 1 M indium-spiked $HNO_3$. The reported total particulate concentrations (T-pTM) are the sum of L-pTM and R-pTM concentrations of corresponding samples after deducting procedural blanks (leaching + digest) for each element (Table 2.4) in each processed batch of samples. Two certified reference materials (BCR-414 freshwater plankton and PACS-2 marine sediments) were processed alongside samples to monitor total recoveries (leach + digest) and digestion performance (only digest), respectively (Table 2.3).

Analysis of macronutrients including nitrate + nitrite ($NO_x$), $PO_4^{3-}$ and silicic acid concentrations was undertaken onboard by segmented flow injection analysis using a QUAATRO (Seal Analytical) auto-analyser (Grasshoff et al. 1999). Analysis of nanomolar macronutrient samples (mainly nitrate + nitrite ($NO_x$) < 100 nM) followed the method of Patey et al. (2008).

Vertical profiles of oxygen, temperature, salinity, pressure, turbidity and beam attenuation were obtained using a standard Seabird sensor package (SBE 9plus) on the CTD rosette frame.

## 5.3 Results and Discussions

### 5.3.1 Vertical Distributions of Dissolved and Particulate Trace Metals

In order to illustrate the similarities, contrasts and connections in TM behaviors in the water column in the eastern South Atlantic, we first present depth profiles of dTM and T-pTM for two selected stations in the Angola Basin and SAG (Figure 5.2). We then consider the results of bivariate Pearson correlations for the full dataset (Figure S5.1-S5.2).

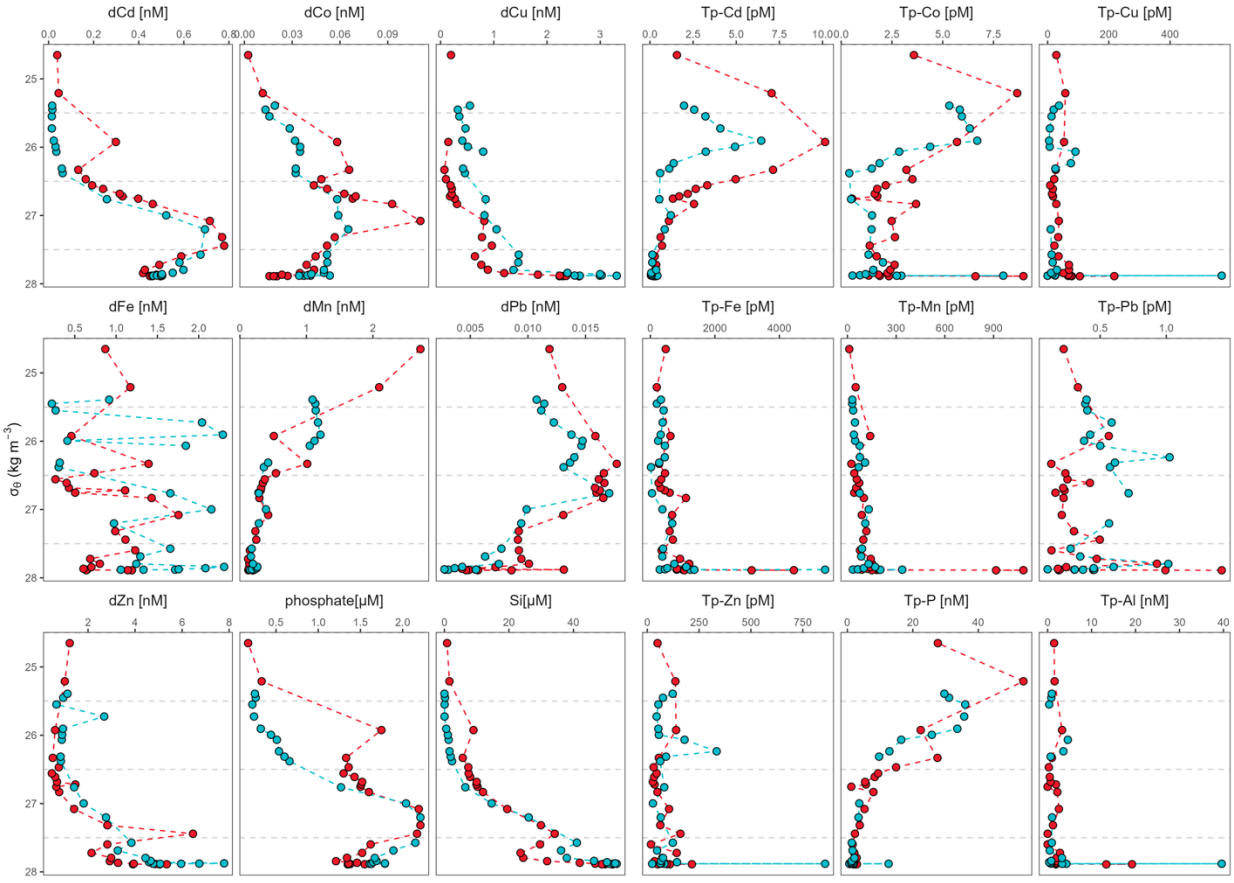


*Figure 5. 2 Distributions of dTMs, Tp-TMs and macronutrients in the water column plotted against potential density ($\delta_\theta$, kg $m^{-3}$) for station 27 (-8.9°N, 0°E) in the Angola Basin (red) and station 33 (-24.7°N, 0°E) in the South Atlantic Gyre (SAG, blue).*

The vertical distributions of dCd, dCo, dFe, dCu and dZn all show depleted surface ocean concentrations and an increase with depth, although this feature is less noticeable for dFe (~0.64 nM in surface waters ($\delta_\theta \leq 26.5$ kg $m^{-3}$) to ~1.00 nM in intermediate waters ($\delta_\theta$ ~26.5 - 27.5 kg $m^{-3}$) for dFe), resembling distributions of macronutrients ($NO_x$, $PO_4^{3-}$ and silicic acid (Si), profiles for $NO_x$ in Figure S5.1). This

nutrient-like trend is induced by biological uptake in surface waters and remineralization at depth of biogenic debris exported from the surface ocean. Lateral transfer of nutrient-rich intermediate and deep water masses also plays a role in defining the profiles due to the accumulation of nutrients along the flow paths of ocean currents (Bruland et al. 2014; Middag et al. 2018). In the surface waters ($\delta_\theta \leq 26.5$ kg $m^{-3}$), relatively high Tp-Cd, Tp-Cu, Tp-Co, Tp-P, Tp-Zn, Chl. a and beam attenuation (an index of particle abundance in water column) indicated the presence of biogenic particles, and these elements are associated with phytoplankton (Figure 5.1). The distribution of dCd in full depth profiles and dCo for surface waters ($\delta_\theta \leq 26.5$ kg $m^{-3}$) showed strong correlations with $NO_x$ (Figure S5.1) and $PO_4^{3-}$ ($R > 0.5$) due to biological processes. Distributions of Tp-Cd, Tp-Co and Tp-P with a near-surface maximum concentrations and decreasing concentrations with depths mirror distributions of these elements in dissolved phase. The surface depletion of dCd and dCo in the Angola Basin was not as pronounced as in the SAG probably due to different TM stocks, recycling rate of dTMs in reaction to their surface supplies, and(or) primary productivity (Figure 5.1). Highest dCo concentrations of 0.11 nM were observed in intermediate waters ($\delta_\theta$ ~26.5 - 27.5 kg $m^{-3}$) of the Angola Basin with depleted dissolved oxygen concentration of 39.7 µM. This is in agreement with previous observations showing enhanced dCo concentrations in the Angola OMZ (Noble et al. 2012). However, no enhanced dFe was observed within the Angola OMZ in our study due to a faster removal of dFe compared to dCo when oxygen level increases (Noble et al. 2012; Liu et al. 2022b). The distributions of dCu and dZn largely resembled the distribution of silicic acid ($R > 0.8$) likely due to their similar accumulation in deep waters that are mixing from Southern ocean sources (Roshan and Wu 2015b; Middag et al. 2019). This is also in accordance with relatively higher Tp-Cu and Tp-Zn concentrations in the surface waters (~56.6 pM Tp-Cu and ~103.2 pM Tp-Zn) compared to the intermediate waters (~32.4 pM Tp-Cu and 63.5 pM Tp-Zn). Increasing concentrations of Tp-Cu and Tp-Zn with depth within the intermediate waters contrasted with trends of Tp-Cd and Tp-P, which showed a decrease mainly by remineralization, indicating that other processes than remineralization determined Tp-Cu and Tp-Zn distributions at depth.

Dissolved Mn showed enhanced surface water concentrations and a decrease with depth. This trend is opposite to distributions of Tp-Mn with increasing trend from surface to depth regardless of highest concentrations at the bottom. Such distributions of dMn and Tp-Mn are likely associated with the dissolution of pMn by photoreduction in sunlit surface waters and the removal of dMn through Mn oxide formation in the dark subsurface waters (Sunda et al. 1983; Moffett and Ho 1996)(Figure 5.2 and Figure S5.4). Surface concentrations of dMn in the SAG (~0.92 nM) were lower than in the Angola Basin (~1.34 nM) where there are large freshwater inputs associated with distal transfer of dMn from Congo plume (Vieira et al. 2020). In contrast, concentrations of dPb were depleted in surface waters and increased gradually with depth reaching maximum concentrations in the SACW ($\delta_\theta$ ~26.3-26.8 kg $m^{-3}$, ~50-300 m depth, ~0.02 nM dPb). This is potentially due to historical anthropogenic Pb inputs to water masses that have a surface origin (e.g. Subantarctic Mode Water) and ventilate on timescales of decades to years in the South Atlantic (Stramma and Mathew England 1999; Echegoyen et al. 2014). Dissolved Pb concentrations in surface waters of North and South Atlantic are generally declining and thus are not in steady-state due to a pronounced decline in anthropogenic emissions since the 1980s (Bridgestock et al. 2016; Olivelli et al. 2023). A gradual decrease of dPb concentrations is evident at greater depth to the bottom likely due to scavenging of dPb onto particles and waters have not been exposed to anthropogenic Pb inputs (AAIW and NADW). Coinciding scavenging of dMn and dPb is indicated by positive correlations of Tp-Pb with Tp-Mn and dPb with dMn in subsurface waters ($R > 0.4$) (Figure S5.2).

The distribution of dFe showed a mixed behavior between that of a scavenged and a nutrient type TM. Elevated dFe concentrations in surface and bottom waters were likely related to lateral shelf inputs and sedimentary effluxes from the seafloor, whereas the dFe distribution in intermediate waters was due to a balance between remineralization and scavenging (Bruland et al. 2014). Similarly, minimum concentrations of dCu and dZn just below the maximum beam attenuation (high particle loading) were seen in a similar $\delta_\theta$ isopycnal interval ($\delta_\theta$ ~26.5-27 kg $m^{-3}$) where dFe concentrations were at their minimum, likely as a result of scavenging onto exported particles (Bruland et al. 1994; John and Conway 2014; Roshan and Wu 2015b).

All Tp-TMs showed lower concentrations in the ~26.5 kg $m^{-3}$ isopycnal corresponding to a significantly lower beam attenuation (<0.05, Figure 5.1 and 5.2) and dissolved oxygen concentrations (< 100 µM, Figure 5.3) due to particle export and remineralization. Notably enhanced concentrations of Tp-Cu, Tp-Fe, Tp-Mn, Tp-Zn and Tp-Al were observed in bottom waters, likely associated with sediment re-suspension.

### 5.3.2 Sectional Distributions of Dissolved and Particulate TMs

Sections for dissolved and particulate TMs along the 0°E transect are presented in Figure 5.3 and Figure 5.4. Concentrations of TMs are mostly lower in particle phase than in dissolved phase due to gravitationally faster sinking of particles from upper to deep ocean on a time scale of a few days to years. Overall, dissolved to total (dissolved + particulate) elemental concentration ratios for the whole transect: Cd (~68%-99%), Co (~32%-99%), Cu (~20%-99%), Fe (~8.4%-98%), Mn (~11%-99%), Pb (~74%-99%) and Zn (~43%-99%). Our observed dissolved to total Zn and Pb ratios show a similar range as previous observations in North Atlantic (Rusiecka et al. 2018; Achterberg et al. 2020), but a broader range for Cd, Co, Cu and Mn (Achterberg et al. 2020). This is because of enhanced particulate fraction (particulate: total ratio) in surface waters for Cd (~1%-32%), Co (~1%-68%) and Cu (~1%-80%) and in deep waters for Mn (~3%-90%) in this study. Particulate fractions of Cd, Cu, Cu and Zn show a steady decrease with depth due to biogenic particle production in surface waters, whereas a general increase for Fe, Mn and Pb due to accumulation of sinking particles or sediment input at depth.

The noticeable features of Tp-TM distributions along the transect are highest concentrations in surface waters for Tp-Cd, Tp-Co and Tp-P and at bottom for Tp-Al, Tp-Co, Tp-Cu, Tp-Mn, Tp-Fe, Tp-Pb and Tp-Zn (Figure 5.3) as indicated by their vertical profiles (section 5.3.1). This suggests Tp-TM distributions are generally affected by one-dimensional dynamics (vertically) in water column. Despite of this, Figure 5.3 allows for a comparison between two regions of Angola Basin and SAG. Surface concentrations of Tp-Cd and Tp-Co are both significantly higher in the Angola Basin (up to 15.6 pM Tp-Cd and 17.5 pM Tp-Co) than in the SAG (up to 7.5 pM Tp-Cd and 8.9 pM Tp-Co) (*t-test*, $P < 0.05$), corresponding to higher NPP in the Angola Basin (Figure 5.1).

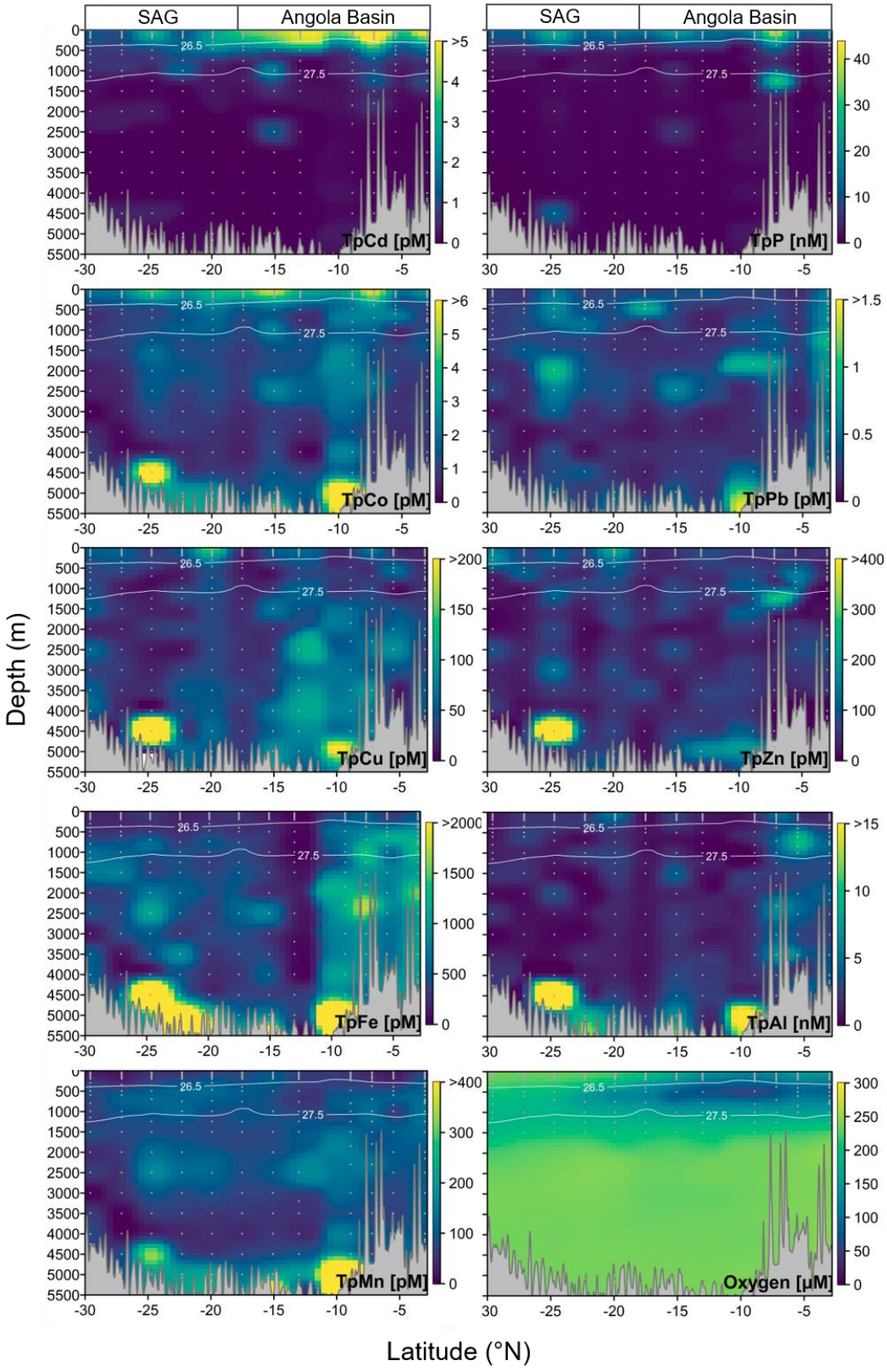


*Figure 5. 3 Section plots of T-pTMs, T-pAl and T-pP.*
*White contour lines indicate density isopycnals of 26.5 and 27 kg m$^{-3}$.*

Maximum concentrations of dCd, dCo, $NO_x$ and $PO_4^{3-}$ were observed in intermediate waters (Figure 5.4). Concentrations of dCd and dZn within depth range of AAIW show less differences between Angola Basin and SAG (*t-test*, $P > 0.05$). Their average concentrations in AAIW are 0.68 ± 0.12 nM dCd and 2.04 ± 0.68 nM dZn agree with estimated AAIW endmember concentrations of dCd and dZn in previous studies, respectively (0.53 nM dCd and 1.29 nM dZn) (Middag et al. 2018, 2019). In contrast, there are increasing concentrations of $PO_4^{3-}$ and $NO_x$ from the SAG (2.02 ± 0.27 µM $PO_4^{3-}$ and 33.2 ± 3.44 µM $NO_x$) to Angola Basin (2.29 ± 0.30 µM $PO_4^{3-}$ and 36.2 ± 7.64 µM $NO_x$) (*t-test*, $P < 0.05$) (Figure 5.4), indicating accumulation of remineralized nutrients during northward transport of AAIW. Concentrations of dPb within the AAIW ($\delta_\theta$ ~27.1-27.3 kg $m^{-3}$) were 0.01 - 0.015 nM (Figure 5.1 and Figure 5.2), in agreement with previous observations in the eastern and tropical Atlantic ocean and South Atlantic (Bridgestock et al. 2018; Schlosser et al. 2019). Below AAIW, significantly higher concentrations of dCu, dZn and silicic acid in the SAG (2.35 ± 0.79 nM dCu, 4.73 ± 1.42 nM dZn, and 48.2 ± 6.22 µM silicic acid) than in the Angola Basin (1.88 ± 0.85 nM dCu, 3.95 ± 1.31 nM dZn, and 38.2 ± 12.1 µM silicic acid) are probably driven by increasing fraction of Southern Ocean sourced deep waters from south to north (Roshan and Wu 2015b; Middag et al. 2019).

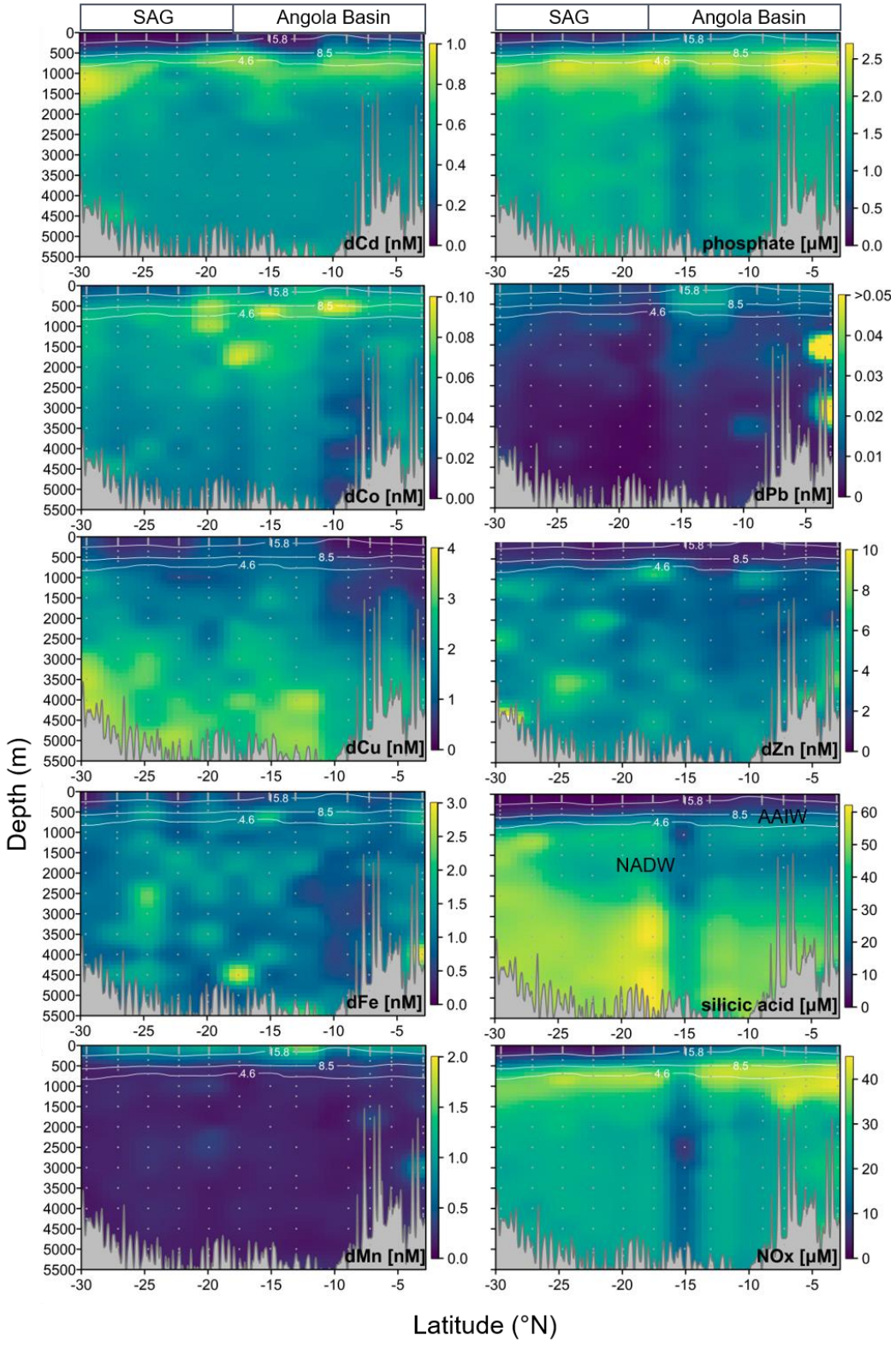


*Figure 5. 4 Section plots of dTMs and macronutrients (phosphate, silicic acid and NOx). White contour lines are potential temperature of 15.8°C, 8.5°C, 4.6°C to indicate water masses as labeled in Figure 5.1 and silicic acid panel of this figure.*

### 5.3.3 Characterization of particle-reactive *vs.* biogenic TMs

Clear differences were apparent between the distributions of the various dTMs and pTMs (Figure 5.5). Phosphorus is primarily associated with organic (biogenic) particles. The lability of biogenic pP may be variable between different phytoplankton taxa, we thus use Tp-P as an indicator of biogenic particles (Al-Hashem et al. 2022). Aluminum has a high abundance in earth's crust, few anthropogenic sources, is not required by biology during photosynthesis, and is characterized by a relatively short oceanic residence time facilitated by high external sources (e.g. dust and sediments) and rapid particle scavenging in the ocean (Orians and Bruland 1985; Moran and Moore 1991; Chester 2009; Rudnick and Gao 2014). Hence we used Tp-Al as a tracer to indicate particle-reactive pTMs (Lam et al. 2018; Xiang and Lam 2020).

Three distinct distributions of dTMs and pTMs were shown by hierarchical clustering. The first cluster reflects a nutrient-like distribution including dCd, dCo, dCu, dFe, dZn and macronutrients with relatively stronger correlations between dZn, dCu, dFe and silicic acid and dCd, dCo, $PO_4^{3-}$ and $NO_x$. All these elements are involved in biological processes and controlled by particle production in surface waters and remineralization at depth (Bruland et al. 2014). Biogenic pTMs (second cluster, Figure 5.5) include Tp-Cd, Tp-Co and Tp-P with decreasing concentrations from the surface to depth, similar as distributions of Chl. a in the top of the water column (Figure 5.2 and Figure 5.1). Dissolved Pb and Mn fall in the same cluster as biogenic pTMs, though scavenging of dPb and dMn rather than biological assimilation-remineralization is responsible for their decrease in concentrations with depth (Goldberg 1954; Boyle et al. 1994). Variables in the second cluster overall negatively correlated with those in the first cluster. The last cluster represents the particle-reactive TMs including Tp-Cu, Tp-Zn, Tp-Fe, Tp-Pb and Tp-Mn, and were associated strongly and positively with Tp-Al.

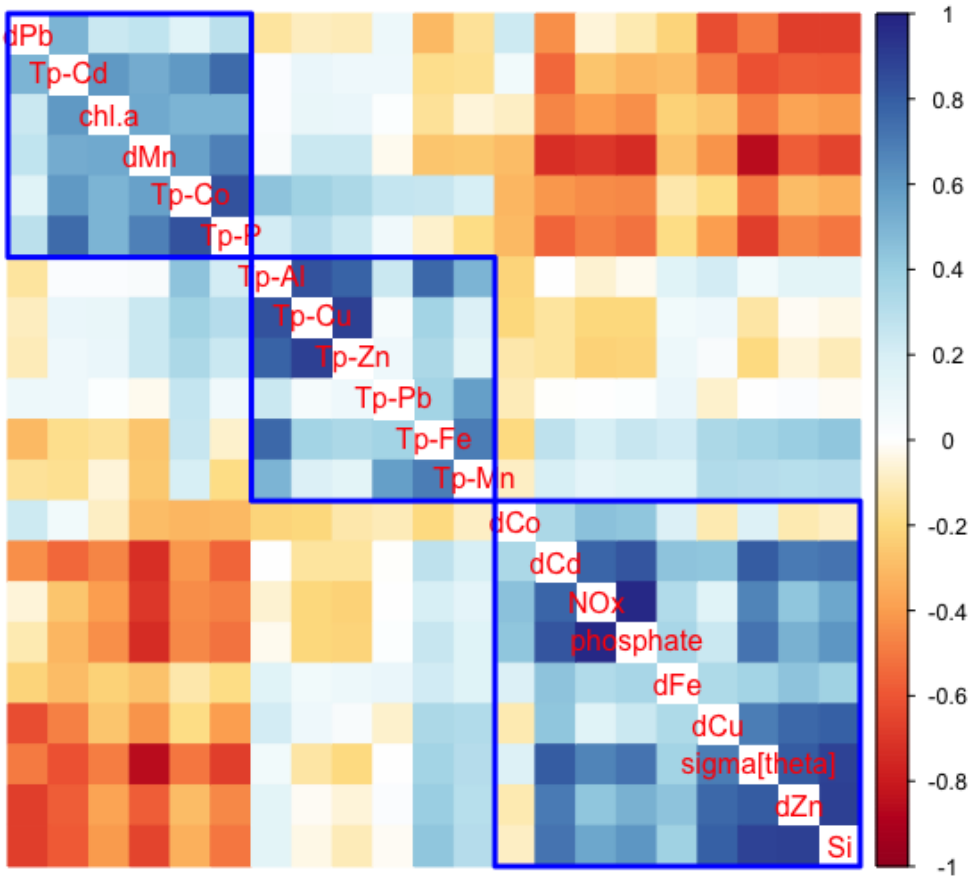


*Figure 5. 5 Pearson correlations and hierarchical clustering between variables. Coefficient R and hierarchical clustering results are indicated by a color bar on the right and blue rectangles, respectively where 0 to +1 indicates positive correlation (blue), -1 to 0 indicates negative correlation (red) and 0 indicates no correlation (white).*

### 5.3.4 Particle-reactive TMs

Assuming that all measured Tp-Al was lithogenic, we can compare the element to Tp-Al ratios against the average upper continental crustal (UCC) ratios (Rudnick and Gao 2014) in order to elucidate phases hosting pTMs in different layers. Despite differences in TM compositions between UCC and the bulk oceanic crusts, Tp-TM:Tp-Al ratios including Co, Cu, Fe, Mn and Zn for both crusts are of a similar order of magnitude (White and Klein 2013; Rudnick and Gao 2014). A Tp-TM:Tp-Al ratio close to the UCC ratio is thus expected to reflect a large contribution of dust in surface waters or particle re-suspension from the seafloor. Additional comparisons of element to Tp-P ratios to average phytoplankton stoichiometry (Ho et al. 2003) can differentiate biogenic *vs.* non-biogenic phases of particles.

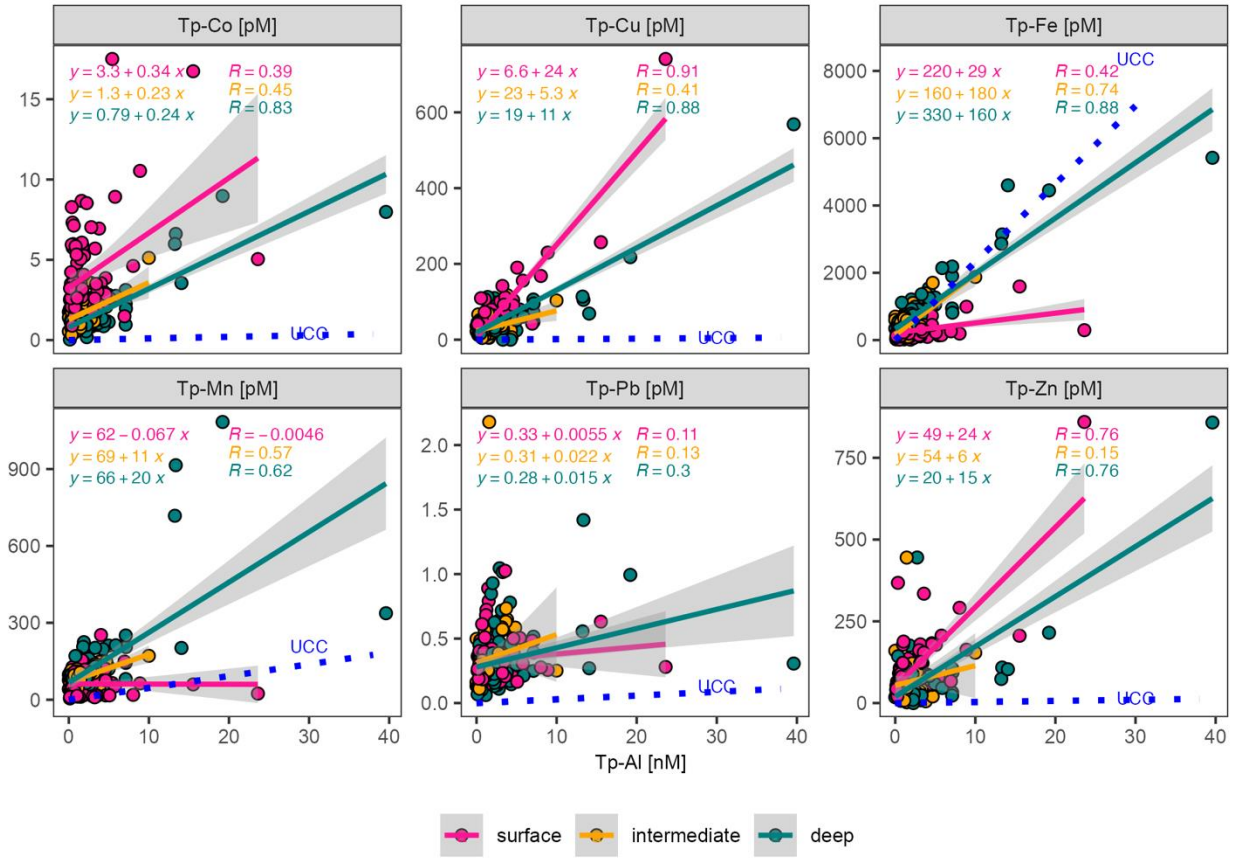


*Figure 5. 6 Cross plots of Tp-TMs against Tp-Al with best linear regression lines for different water depth layers (colored circles and lines).*
*Grey shading around colored lines indicate the 95% confidence interval. Reference ratios of Tp-TM to Tp-Al for the upper continental crust (UCC)* (Rudnick and Gao 2014) *are shown by a blue dotted line in each panel.*

*Table 5. 1 Compiled slopes of linear regression between elements in different layers and reference sources.*

| | Layer/reference | Cd | Co | Cu | Fe | Mn | Pb | Zn |
|---|---|---|---|---|---|---|---|---|
| Tp-TM:Tp-Al (mmol:mol$^{-1}$) | Surface | NA | 0.343 | **24.4** | **29.1** | NA | 0.006 | **24.4** |
| | Intermediate | NA | **0.230** | **5.34** | **180** | **10.8** | 0.022 | 6.0 |
| | Deep | NA | **0.241** | **11.2** | **165** | **19.6** | 0.015 | **15.3** |
| | UCC | 0.0003 | 0.097 | 0.14 | 230 | 4.61 | 0.027 | 0.34 |
| Tp-TM:Tp-P (mmol:mol$^{-1}$) | Surface | **0.112** | **0.153** | 1.65 | **6.89** | NA | NA | NA |
| | Intermediate | **0.278** | **0.095** | NA | NA | NA | NA | NA |

| | | | | | | | | |
|---|---|---|---|---|---|---|---|---|
| | Deep | **0.039** | NA | NA | NA | NA | NA | **11.27** |
| | phytoplankton | 0.21 | 0.19 | 0.38 | 7.5 | 3.8 | - | 0.8 |
| Tp-TM:Tp-Mn (mol:mol$^{-1}$) after normalized to Tp-Al | Surface | NA | **0.038** | NA | **3.1** | - | **0.003** | NA |
| | Intermediate | NA | **0.014** | **0.360** | **1.3** | - | **0.002** | **0.51** |
| | Deep | NA | **0.013** | 0.160 | **4.2** | - | **0.003** | 0.52 |
| | Fe-Mn crusts | - | 0.029 | 0.005 | 0.903 | - | 0.002 | 0.003 |

*Note. NA-not available as R < 0.3; values shown in bold have R > 0.3 & P < 0.001; Reference material are average upper continent crustal ratios (UCC)* (Rudnick and Gao 2014), *average phytoplankton stoichiometry* (Ho et al. 2003), *and average elemental ratios in Atlantic ferromanganese crusts (Fe-Mn crusts)* (Manheim and Lane-Bostwick 1989).

1) Authigenic and/or biogenic pTMs dominate in surface waters:

Concentrations of Tp-TMs against Tp-Al show three distinctive patterns in the surface layer (Figure 5.6). The lower surface slope for Fe of either UCC (Rudnick and Gao 2014) or Namibian and South Atlantic aerosol (650-2389 mmol mol$^{-1}$) (Annegarn et al. 1983; Eltayeb et al. 1993; Chance et al. 2015) indicates a depletion of Fe, although there remains a moderate correlation of Tp-Fe and Tp-Al in the surface layer (R = 0.42). Considering limited lateral transfer of Tp-Fe from the Congo plume in the north part of the cruise transect (Al‐Hashem et al. 2022), and Namibian sediments in the south (Liu et al. 2022b), dust is the major input of Fe to the surface waters in our study area. However, Tp-Fe:Tp-Al in surface waters (29.1 mmol mol$^{-1}$) is significantly lower than that in either UCC (Rudnick and Gao 2014) or Namibian aerosol (650-2389 mmol mol$^{-1}$) (Eltayeb et al. 1993; Chance et al. 2015) (Table 5.1 and Figure 5.1). Weathering and atmospheric processes such as exposure to solar radiation during aerosol transport can efficiently transform mineral/lithogenic pFe to soluble $Fe^{2+}$ within a few hours before deposition in seawater (Shi et al. 2012). This means a relatively low mineral/lithogenic pFe fraction is observed in seawater. Our observed Tp-Fe in surface waters thus could likely have a biogenic and/or authigenic origin. The Tp-Fe:Tp-P slope in surface waters was 6.89 mmol mol$^{-1}$, which is close to average stoichiometry in phytoplankton (7.5 mmol mol$^{-1}$)

(Ho et al. 2003) reflecting predominant biogenic pFe or a biological-driven removal of some fraction of lithogenic pFe (Johnson et al. 1997; Barrett et al. 2012).

There were hence moderate correlations of Tp-Fe with Tp-Al and Tp-P ($R > 0.3$), but no correlations between Tp-Mn and Tp-Al or Tp-P in surface waters ($R < 0.2$, Figure S5.2) suggesting minor or negligible lithogenic and biogenic phase of Tp-Mn in surface waters. Inverse variations of Tp-Mn and dMn with depth indicate authigenic formation of Tp-Mn (Figure S5.4) due to Mn(II) oxidation to particulate $MnO_2$ (Mn oxide) in dark deeper waters. This process removes dMn from the water column as particles which ultimately sink (Sunda et al. 1983). Relative enrichment of Tp-Pb in the surface layer compared to UCC is due to anthropogenic inputs associated with authigenic phase of Tp-Pb (Echegoyen et al. 2014).

Slopes of Tp-Cu:Tp-Al and Tp-Zn:Tp-Al were three order of magnitudes higher in surface waters than in the UCC, implying that biogenic and/or authigenic phases mask lithogenic Tp-Cu and Tp-Zn. The most prominent authigenic particles are Mn oxides, which can also serve a scavenger for other TMs including Co, Cu and Zn (Goldberg 1954). This is expected due to the unique behavior of dMn, the strong scavenging capacity of Mn oxides and their formation at the base of the photic zone. Our data show that neither Tp-Cu nor Tp-Zn correlates with Tp-Mn in surface waters (Figure S5.2), indicating phases other than Mn oxides are associated with Tp-Cu and Tp-Zn. The weak correlation between Tp-Cu and Tp-P in surface waters ($R = 0.3$) with a regression slope of 1.65 mmol $mol^{-1}$, that is higher than average phytoplankton stoichiometry (0.38 mmol $mol^{-1}$) (Ho et al. 2003) (Table 1) but similar to cellular Cu:P in diatoms in the Southern Ocean (1.72 mmol $mol^{-1}$) (Twining and Baines 2013). The average ratio of Tp-Zn/Tp-P of ~6.48 mmol $mol^{-1}$ in surface waters is also consistent with the cellular Zn:P ratios reported for diatoms in the South Ocean ($6 \pm 2.6$ mmol $mol^{-1}$) (Twining and Baines 2013) although the correlation between Tp-Zn and Tp-P is weak in surface waters ($R < 0.3$). Biogenic Tp-Zn and Tp-Cu in surface waters are therefore plausibly their dominating phase. Surface Tp-Co is dominated by the biogenic fraction as shown by a strong correlation with Tp-P ($R = 0.89$) (Figure S5.2). This is consistent with a low lithogenic fraction estimated using the Co:Al ratio in UCC (Table 1) of only ~7%.

2) Intermediate and deep waters characterized by scavenging and top-down supply of pTMs

In intermediate waters, Co, Fe and Zn were influenced by regeneration and scavenging (Boyd et al. 2010; Boyd and Ellwood 2010; Hawco et al. 2018; Roshan et al. 2018). Enhanced dCo, dFe and dZn concentrations in intermediate depth are due to regeneration of sinking organic (biogenic) particles. Conversely, dCo, dFe and dZn may subsequently be scavenged onto the particulate phases of sinking particles. We can roughly estimate the extent of scavenging of these elements. Assuming that regeneration primarily leads to accumulation of dTMs and $PO_4^{3-}$ ($\Delta[dTM]/\Delta[PO_4^{3-}]$) in intermediate waters, the pseudo regeneration ratio (accumulation) of $\Delta[dTM]/\Delta[PO_4^{3-}]$ for dCo, dFe and dZn could be approximated by slopes of their best linear fitting against $PO_4^{3-}$ at 0.004, 3.1 and 1.6 mmol $mol^{-1}$, respectively ($R > 0.3$). These "regeneration" ratios are low in comparison to their particulate stock ratios (0.15 and 6.85 mmol $mol^{-1}$) for Tp-Co:Tp-P and Tp-Fe:Tp-P and average ratio of Tp-Zn/Tp-P (6.48 mmol $mol^{-1}$) in the surface layer. Hence, accumulation of dCo, dFe and dZn in intermediate waters only represents ~2.7%, ~45% and ~24.7% regeneration of biogenic Tp-Co, Tp-Fe and Tp-Zn exported from surface waters, respectively. It is possible that scavenging of dCo, dFe and dZn to the particle phase accounts for their low accumulation by regeneration in the intermediate layer.

Concentrations of Tp-Al, Tp-Cu, Tp-Fe, Tp-Mn, Tp-Pb and Tp-Zn were all highest near the seafloor, reflecting the influence of resuspended sediments for these elements. The similarity of Tp-Fe:Tp-Al slopes in the intermediate and deep waters to the average ratio in UCC suggests that much of the Tp-Fe at depth was lithogenic with estimated fraction of ~105% and ~151.2%, respectively (Figure 5.6). In contrast, respective slopes of Tp-Co, Tp-Cu, Tp-Mn, Tp-Pb and Tp-Zn to Tp-Al in deep waters are one to two orders of magnitude higher than their ratios in UCC with estimated lithogenic fractions < 30% for these TMs. This implies significant enrichment of pTMs exceeding TM supplies from bottom sediments. The enrichment of these pTMs could be explained by the top-down (surface to deep water) supply of scavenged pTMs and authigenic formation of pTMs in the upper water column, which is ultimately buried in bottom sediments in the ocean. Distributions of Tp-Mn throughout the whole water column were

dominantly controlled by the authigenic phase with lithogenic contribution < 2%. Strong correlations between Tp-Co and Tp-Mn concentrations (R > 0.8, Figure S5.5) in intermediate and deep waters after normalization to Tp-Al indicates Co being scavenged onto Mn oxide thus explaining enriched Tp-Co in subsurface waters. The Tp-Co to Tp-Mn ratio in the intermediate and deep water (0.013-0.014) is of the same order of magnitude as those of Atlantic ferromanganese crusts (0.03) (Table 5.1), suggesting that Tp-Co within these layers is mostly bond to Tp-Mn and subsequently supplied to the seafloor. A similar behavior was also observed for Tp-Pb in the whole water column (Table 5.1). Our data shows similar Tp-Pb:Tp-Mn ratios in the water column to Atlantic Fe-Mn crusts (Table 5.1), providing evidence that Pb in Fe-Mn crusts to reflect ambient seawater compositions (Christensen et al. 1997).

Similarly, top-down supply of pCu and pZn counteracts their bottom-up (benthic to deep water) supply, resulting in slope values of Tp-Cu and Tp-Zn against Tp-Al in deep waters bracketed by their slopes in surface and UCC. As the slopes (Tp-Cu v.s. Tp-Al and Tp-Zn v.s. Tp-Al) in deep water are closer to those in surface water compared to UCC (Figure 5.6), the top-down supplies of Tp-Cu and Tp-Zn is plausibly stronger or(and) faster than their bottom-up supply. However, scavenging of Tp-Cu and Tp-Zn by Mn oxides cannot fully explain the distributions of Tp-Cu and Tp-Zn in the intermediate and deep water (R= 0.45 for Tp-Cu with Tp-Mn and 0.56 for Tp-Zn with Tp-Mn when normalized to Tp-Al) (Figure S5.5). In addition, slopes (0.16-0.36 of Tp-Cu:Tp-Mn and mean 0.51-0.52 of Tp-Zn:Tp:Mn) are both one order of magnitude higher than those of Atlantic ferromanganese crusts (0.005 of Cu:Mn and 0.003 of Zn:Mn). This suggests that cycling of Tp-Cu and Tp-Zn is not only occur through adsorption/desorption processes with Mn oxide but also with other particle phases (Boye et al. 2012; Le Moigne et al. 2013).

### 5.3.5 Shelf-open ocean transect: boundary exchange for Fe, Pb and Mn

Lateral transport of sedimentary and river plumes can lead to enhanced TM concentrations at shelf (<100 m) and slope depths (100-2000 m) (Lam et al. 2020; Colombo et al. 2022; Hunt et al. 2022; Al-Hashem et al. 2022). This is particularly a case for particle-reactive TMs with relatively high partition coefficient ($K_D =$

$Concentration_{Tp-TM}/Concentration_{dTM}$) (Balls 1989). This is also evident from observations along ~3°S transect (Figure 5.7) that shows an offshore decrease in $K_D$ as the particulate load decreases. For example, from inner shelf to open ocean, average $K_D$ values decrease from 28.5 to 0.76, from 1.3 to 0.05 and from 1.1 to 0.03 for Fe, Mn and Pb, respectively. In addition, enhanced $K_D$ values were also observed at bottom except shelf surface that was influenced by Congo plume. These indicate a stronger "boundary exchange" (as well as particle-dissolved exchange processes) when closer to land-ocean contact (Stichel et al. 2020; Al-Hashem et al. 2022; Chen et al. 2023).

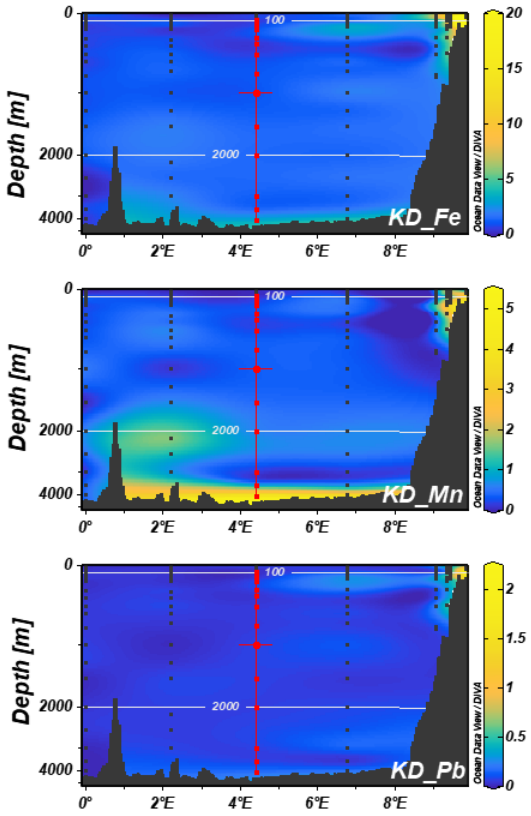


*Figure 5. 7 Distributions of $K_D$ for Fe, Mn and Pb along ~3°S transect. White contour lines indicate depths of 100 m and 2000 m, respectively.*
*Paired dissolved and particulate TM concentrations were retrieved from published datasets (Al-Hashem et al. 2022; Liu et al. 2022a).*

### 5.3.6 Biogenic TMs – Cd and Co

1) Relationship between TMs and P

Strong linear correlations between dCd, dCo and $PO_4^{3-}$ ($R > 0.5$), and between Tp-Cd, Tp-Co and Tp-P ($R > 0.6$) indicate that the processes controlling P in surface waters

– upwelling, mixing, biological uptake, recycling and export are also the main drivers of Cd and Co cycling (Figure 5.7), in agreement with previous studies in the South Atlantic and global oceans (Bown et al. 2011; Boye et al. 2012; Middag et al. 2018). These correlations suggest that the biological uptake of dCd and dCo is proportional to that of P in surface waters. Along our study section, >99% Tp-Cd and >90% Tp-Co were biogenic. Slopes of Tp-Cd:Tp-P and Tp-Co:Tp-P in surface waters are within the range of cellular TM:P ratios (0.02-0.56 mmol $mol^{-1}$ of Cd:P and 0.01-0.19 mmol $mol^{-1}$ of Co:P) despite considerable variability for TM:P in different phytoplankton species (Twining and Baines 2013). The positive intercepts of Tp-TM concentrations in surface waters indicate a faster regeneration of Tp-P compared to Tp-TM (Boyd et al. 2017). Higher Tp-TM intercepts suggest an incomplete removal of Tp-TM (e.g by regeneration or export) in the Angola Basin compared to the SAG.

The surface slopes of dTM:$PO_4^{3-}$ did not match the "balanced" cellular ratios of Tp-TM:Tp-P as they indicate a net interplay between biological uptake and regenerations in the surface layer (Figure 5.7). Concentrations of dCd and $PO_4^{3-}$ in the SAG are broadly consistent with mixing between Equatorial Surface Water (model-optimized 0 nM dCd and 0 μM $PO_4^{3-}$) and Sub-Antarctic Mode Water (model-optimized 0.073 nM dCd and 0.74 μM $PO_4^{3-}$) (Middag et al. 2018). Thus, the slope of dCd: $PO_4^{3-}$ and negative intercept for dCd in the SAG is possibly driven by mixing from Sub-Antarctic waters (Boyle 1988; Frew and Hunter 1992; Baars et al. 2014). Slopes of dCo: $PO_4^{3-}$ in Angola Basin and SAG are similar to previous observations at similar latitudes of the western Atlantic (0.027 and 0.065 mmol $mol^{-1}$) (Dulaquais et al. 2014).

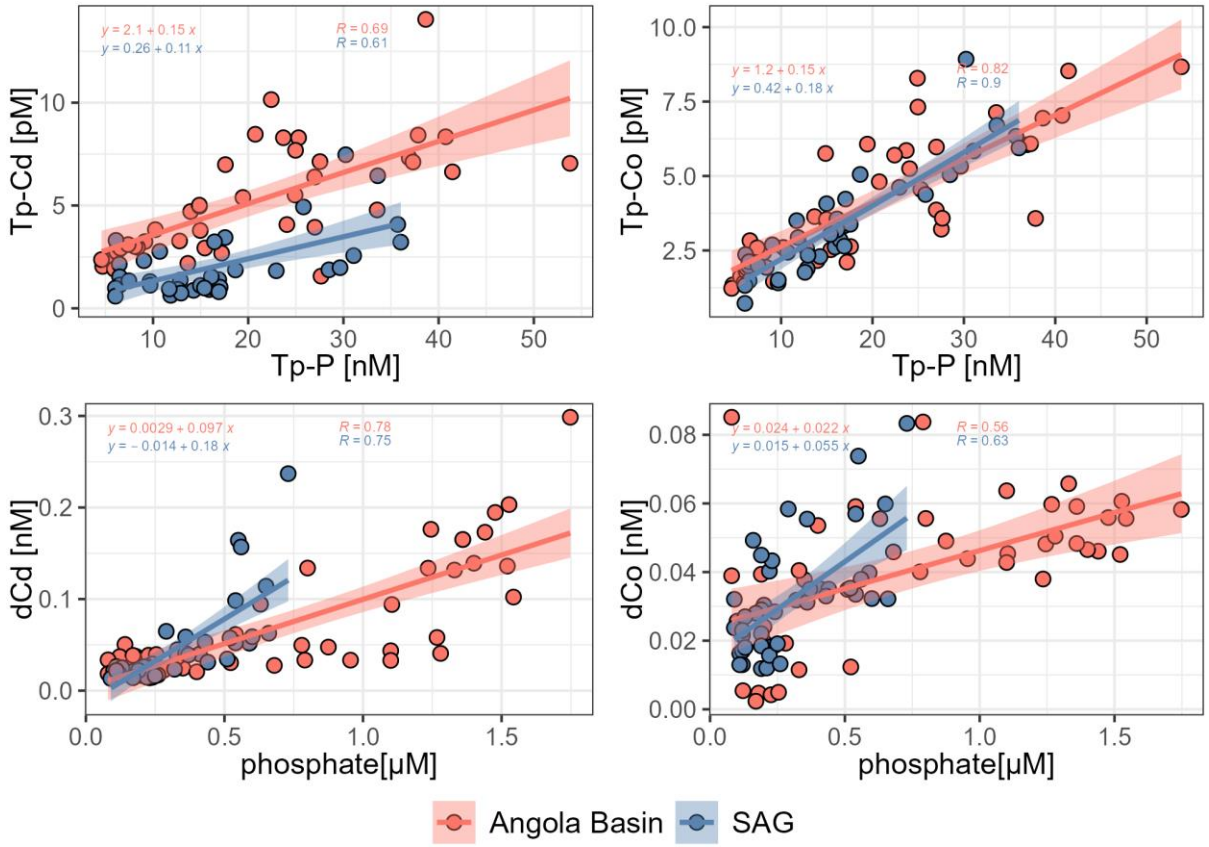


*Figure 5. 8 Linear regression of between TMs and P for samples from surface waters.*

2) Internal cycle of Cd and Co in surface waters of the Angola Basin and SAG

A proportion of nutrients that is produced in the surface ocean is recycled *in situ* rather than being exported. During the timeframe of the cruise, stronger NPP, higher Chl. a and significantly higher concentrations of Tp-Cd, Tp-Co and Tp-P (*t-test*, $P < 0.001$) were observed in the Angola Basin compared to the SAG. A stronger drawdown of dTMs was therefore expected in the Angola Basin compared to SAG (Figure 5.1), but this is not consistent with the higher observed concentrations of dTMs. For example, concentrations of dCd, dCo and $PO_4^{3-}$ in surface waters were relatively higher in the Angola Basin (~0.078 nM dCd, ~0.042 nM dCo and ~0.76 μM $PO_4^{3-}$) compared to the SAG (~0.043 nM dCd, ~0.032 nM dCo and 0.30 μM $PO_4^{3-}$) (*t-test*, $P < 0.01$). Concentrations of nutrients in the surface ocean are determined by a combining effect of external supply, biological uptake and recycling efficiency. We thus evaluate fluxes of TMs and P

including external supply, uptake and recycling in surface layer to assess relative importance of these processes (Table 5.2).

Estimated P uptake fluxes were derived from satellite-based NPP estimates of 37.1± 8.6 and 23.5 ± 4.9 mmol C $m^{-2}$ $d^{-1}$ for Angola Basin and SAG, respectively (NOAA NMFS SWFSC ERD (National Oceanic and Administration, National Marine Fisheries Service, Southwest Fisheries Science Center), and an assumed phytoplankton P/C ratio of 0.008 mol $mol^{-1}$ (Ho et al. 2003; Moore 2016b). We then multiply the P uptake fluxes by the slope of Tp-TM:Tp-P in the surface layer and derive Cd and Co uptake fluxes. These calculations lead to uptake fluxes of 45.4 ± 10.5 dCd nmol $m^{-2}$ $d^{-1}$ and 44.0 ± 10.1 dCo nmol $m^{-2}$ $d^{-1}$ in the Angola Basin and of 20.3 ± 4.2 dCd nmol $m^{-2}$ $d^{-1}$ and 33.9 ± 7.0 dCo nmol $m^{-2}$ $d^{-1}$ in SAG. Our estimated Cd uptake fluxes are lower than estimates in tropical Pacific (410 nmol $m^{-2}$ $d^{-1}$) driven by lower NPP in our study area (Black et al. 2019). Our estimated Co uptake fluxes were within the range of previous estimates in surface waters of the South and Western Atlantic and South Pacific (7 - 270 nmol Co $m^{-2}$ $d^{-1}$) (Bown et al. 2011; Dulaquais et al. 2014; Black et al. 2019), but slightly higher than estimates in the open ocean of tropical Pacific (19 - 29 nmol $m^{-2}$ $d^{-1}$) although NPP is higher there (Black et al. 2019). This suggests a higher demand of Co in the South Atlantic compared to the tropical Pacific plausibly related to different phytoplankton assemblage. This can be evidenced by higher Co:P cellular ratios in picophytoplankton (*Synechococcus* and *Prochlorococcus*), nanophytoplankton of haptophytes and dinoflagellates (Saito et al. 2002, 2005; Ho et al. 2003) whose abundances are enhanced in the South Atlantic (Browning et al. 2014).

The minimum concentrations of Tp-Cd, Tp-Co and Tp-P were noticeable around $\delta_\theta$ = 26.5 kg $m^{-3}$ isopycnal due to export from the surface layer. Due to the predominance of biogenic phases of these elements in the surface layer, a fraction ($e$) of the NPP exported from the surface layer was estimated using measured Chlorophyll a concentrations ($Chl.a$) and surface temperature ($T$) based on the empirical algorithm $max\{0.042, min(-0.0078 * T + 0.0806 * ln(Chl.a) + 0.433)\}$ (Dunne et al. 2005). The estimated particulate organic (biogenic) matter export ratios are 0.15 and 0.09 in the Angola Basin and SAG, respectively. As P undergoes faster regeneration than TMs, it is reasonable to assume total recycling of residual P in the surface layer. Recycled P thus

represents 81.2% and 90% of uptake P in Angola Basin and SAG, respectively (Table 2). Using slopes of dTM:$PO_4^{3-}$ in the surface layer allows us to examine the recycling fluxes of TMs on this basis of fluxes of $PO_4^{3-}$ ($F_{PO_4^{3-}}$) following $F_{rec\_TM} = \left[[dTM: PO_4^{3-}] * \Sigma F_{PO_4^{3-}}\right] - \left[F_{vertical\_TM} + F_{lateral\_TM} + F_{atmosphere\_TM} + F_{uptake\_TM}\right]$ (Dulaquais et al. 2014) because the dTM:$PO_4^{3-}$ slopes should reflect a net interplay between sink and source terms.

The recycled fluxes of dCd and dCo represent >80% and >90% of their respective uptake fluxes in both regions, corresponding to $fe$ ratios < 0.1 following the definition in Boyd et al. (2005) ($fe\ ratio\ = external\ supply/[external\ supply\ +\ recycling]$). This indicates approximately 90% of productivity is fueled by internal cycling in the oligotrophic South Atlantic. The uptake and recycling fluxes together constrain a rapid pTM turnover of ~1.2 days for Cd and ~1.1 days for Co in the surface layer, consistent with a similar turnover time of Co in cyanobacteria (~1.3 days) (Dulaquais et al. 2014) which dominate picophytoplankton assemblages in oligotrophic oceans (Saito et al. 2002). Accordingly, higher recycling efficiency of Co (>90%) than has been reported for the North Atlantic (9.4-77%) could be the response of serial limitation of phytoplankton growth by Co/vitamin $B_{12}$ and phytoplankton assemblages with a high Co-requirement in our study area (Browning et al. 2017). Culture experiments have shown a twofold higher demand for Cd and Co under Fe-limited conditions relative to Fe-replete conditions (Cunningham and John 2017). Slightly decreased $fe$ ratios of dCd and dCo moving from the Angola Basin to the SAG showed a transition towards a stronger dependence on recycled TMs due to lower external inputs and Fe-stress in the SAG (Table 2) (Browning et al. 2017).

*Table 5. 2 Fluxes of Cd, Co, P in the Angola Basin and SAG.*

| Regions | | dCd (nmol $m^{-2}$ $d^{-1}$) | dCo (nmol $m^{-2}$ $d^{-1}$) | $PO_4^{3-}$ (μmol $m^{-2}$ $d^{-1}$) |
|---|---|---|---|---|
| Angola Basin | uptake | -45.4 ± 10.5 | -44.0 ± 10.1 | -299.0 ± 69.0 |
| | vertical [a] | +2.4 | +0.3 | +11.7 |
| | lateral [b] | negligible | +0.3 ± 0.1 | negligible |
| | atmospheric [c] | +0.005 | +2.0 | +0.03 [d] |
| | recycling | +38.7 ± 14.3 | +40.4 ± 10.3 | +242.7 ± 72.5 |

| | | | | |
|---|---|---|---|---|
| | $fe$ ratio [e] | 0.06 | 0.06 | |
| SAG | uptake | -20.3 ± 4.2 | -33.9 ± 7.0 | -189.6 ± 39.1 |
| | vertical [a] | +0.9 | +0.1 | +2.9 |
| | lateral [b] | negligible | +0.5 ± 0.2 | negligible |
| | atmospheric [c] | +0.001 | +0.6 | +0.01[d] |
| | recycling | +16.4 ± 11.0 | +31.8 ± 7.6 | +170.6 ± 39.3 |
| | $fe$ ratio [e] | 0.05 | 0.04 | |

*[a] the vertical fluxes of TMs across the base of surface layer (26.5 kg $m^{-3}$ isopycnal) can be estimated by $K_z \frac{\partial[dTM]}{\partial z} + w \cdot \Delta[dTM]$ (Jickells et al., 1999), where $K_z$ is the vertical diffusion coefficient of $10^{-5}$ $m^2$ $s^{-1}$ in the open South Atlantic Ocean (Dunckley et al., 2012), $\frac{\partial[dTM]}{\partial z}$ is dTM and $PO_4^{3-}$ concentration gradient relative to depth in each area, w is upwelling velocity at the base of surface layer taken as $10^{-6}$ m $s^{-1}$ in Angola Basin and 0 m $s^{-1}$ in SAG (Doi et al. 2007), and $\Delta[dTM]$ represents difference of dTM concentrations between 26.5 kg $m^{-3}$ isopycnal and 10 m below this horizon (Liu et al., 2022).*
*[b] Assuming 0.56% freshwater input in the Angola Basin (Chapter 4) and 1% off-shelf input in the SAG (Liu et al., 2022) normalized to the surface area of each region. Negligible lateral input of Cd and $PO_4^{3-}$.*
*[c] Bulk atmospheric inputs of TMs estimated based on Al-derived dust deposition fluxes of 0.016 and 0.005 mg $m^{-2}$ $d^{-1}$ in Angola Basin and SAG, respectively and abundance of Cd and Co in UCC (0.09 and 17.3 µg $g^{-1}$, respectively).*
*[d] From Baker et al., 2003.*
*[e] $fe\ ratio = external\ supply/[external\ supply + recycling]$ (Boyd et al., 2005).*

### 5.4 Conclusions

The present study investigated the biogeochemical cycling of TMs in the South Atlantic. Contrasting distributions of dTMs and pTMs delineate a particle-reactive group of Al, Cu, Fe, Mn, Pb and Zn, as well as Co particularly in deep waters, and a biogenic group of Cd, Co and P. Authigenic phases dominated Tp-Mn in the water column presumably in the form of Mn oxides, whereas both authigenic and biogenic phases host Tp-Cu, Tp-Fe, Tp-Pb and Tp-Zn in surface waters. Scavenging of dFe, dCo and dZn in intermediate waters leads to a lower accumulation rate than expected from regeneration of their particle stocks exported from surface waters. In deep water, the bottom-up supply of Tp-Mn, Tp-Co, Tp-Cu, Tp-Zn was overprinted by their top-down supply. Ferromanganese crusts in the Atlantic record Tp-Co and Tp-Pb compositions in ambient water. The distributions and cycling of Cd, Co and P in surface waters are tightly linked

to biological processes of uptake and recycling. We found internal cycling of TMs fueled >90% productivity in the oligotrophic South Atlantic. Higher Co recycling efficiency (>90%) relative to observations in the North Atlantic likely reflects serial $Co/B_{12}$ limiting conditions for phytoplankton growth in our study area, possibly related to high Co-requirements of phytoplankton assemblages in the South Atlantic. A steeper slope between dTM and $PO_4^{3-}$ and a lower $fe$ ratio can be attributed to stronger Fe-limiting conditions in the SAG than the Angola Basin, corresponding to a higher dependence on recycled Cd and Co.

## 5.5 Supplementary Materials


*Figure S5. 1 Pearson's correlation (upper right), density plot (middle) and scatters (bottom left) of dataset with dTMs and macronutrients.*

*Pearson correlation coefficients are shown for the whole water column (grey) and in different layers (color). Deep, intermediate and surface waters are marked in red, green and blue, respectively. Note. * P <= 0.05; ** P <= 0.01; *** P <= 0.001*

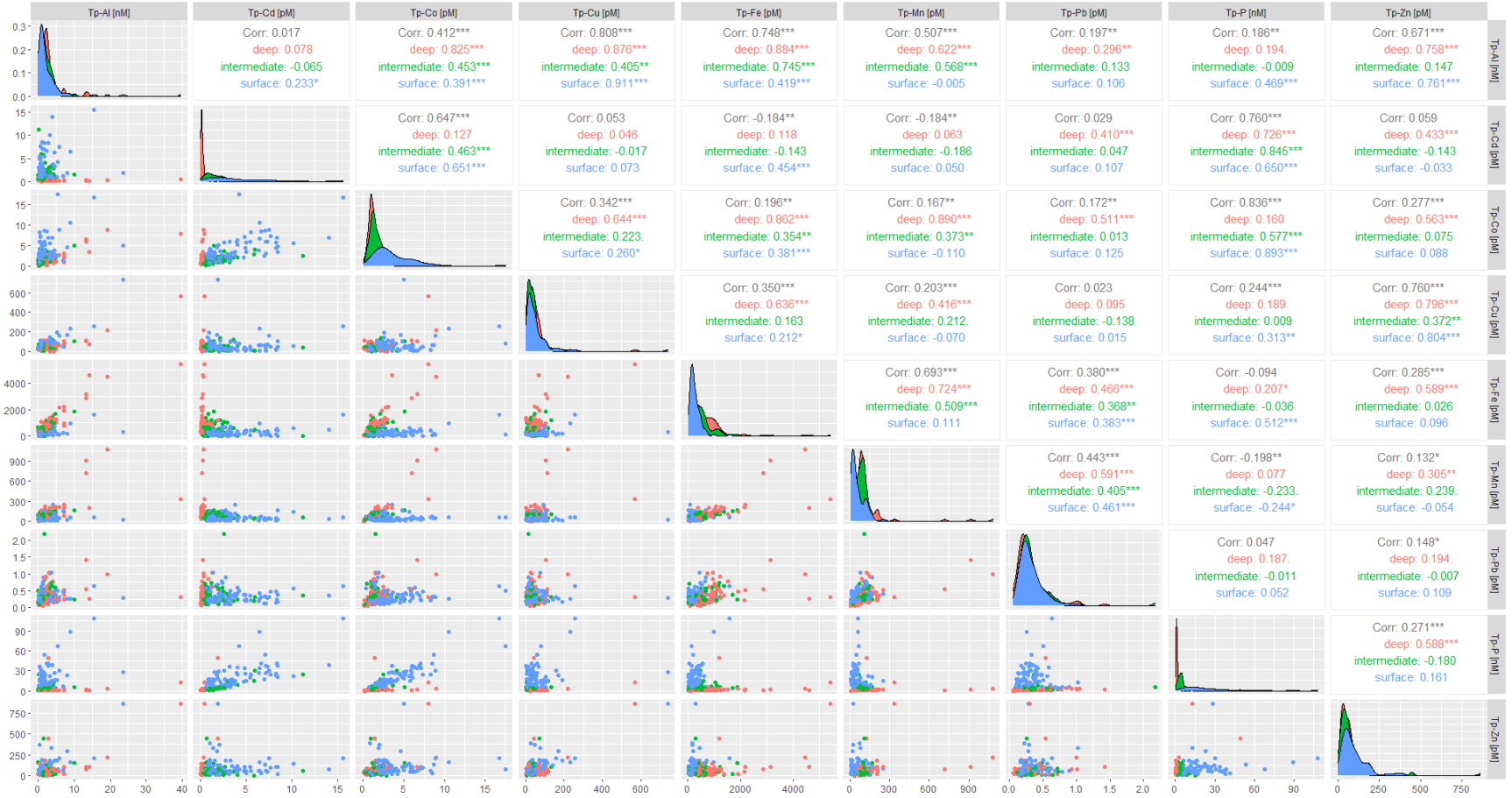


*Figure S5. 2 Pearson's correlation (upper right), density plot (middle) and scatters (bottom left) of dataset with Tp-TMs. Pearson correlation coefficients were shown for the whole water column (grey) and in different layers (color). Deep, intermediate and surface waters are marked in red, green and blue, respectively. Note. * P <= 0.05; ** P <= 0.01; *** P <= 0.001*

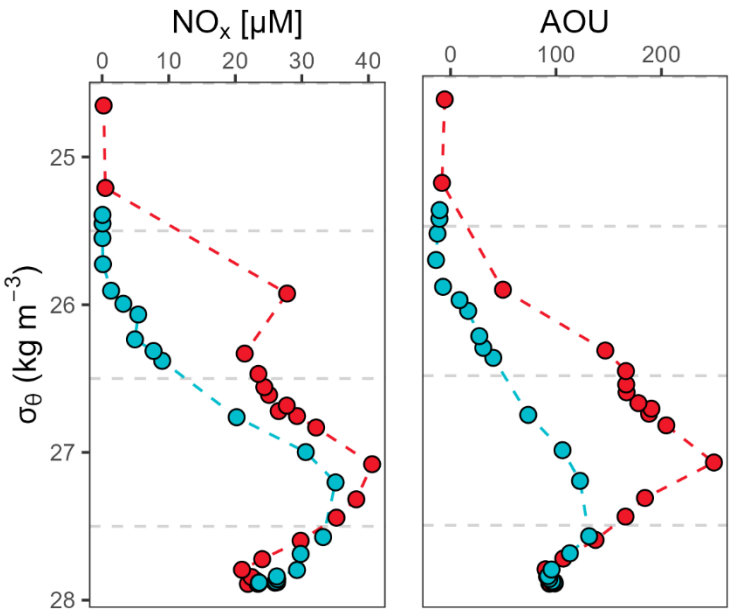


*Figure S5. 3 Representative depth profiles of nitrate + nitrite (NOx) and apparent oxygen utilization (AOU) in Angola Basin (red) and SAG (blue).*

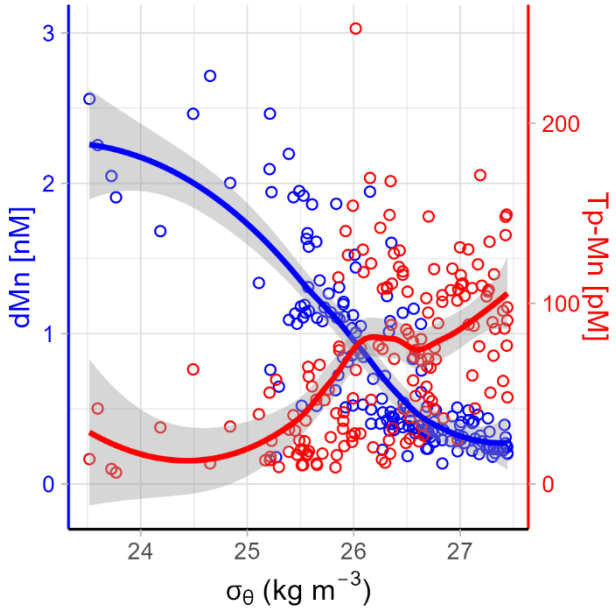


*Figure S5. 4 Inverse variation of dMn and Tp-Mn in the surface and intermediate layers.* Smoothed lines represent five-point weighted moving average and the gray shaded area indicates the 95% confidence interval.

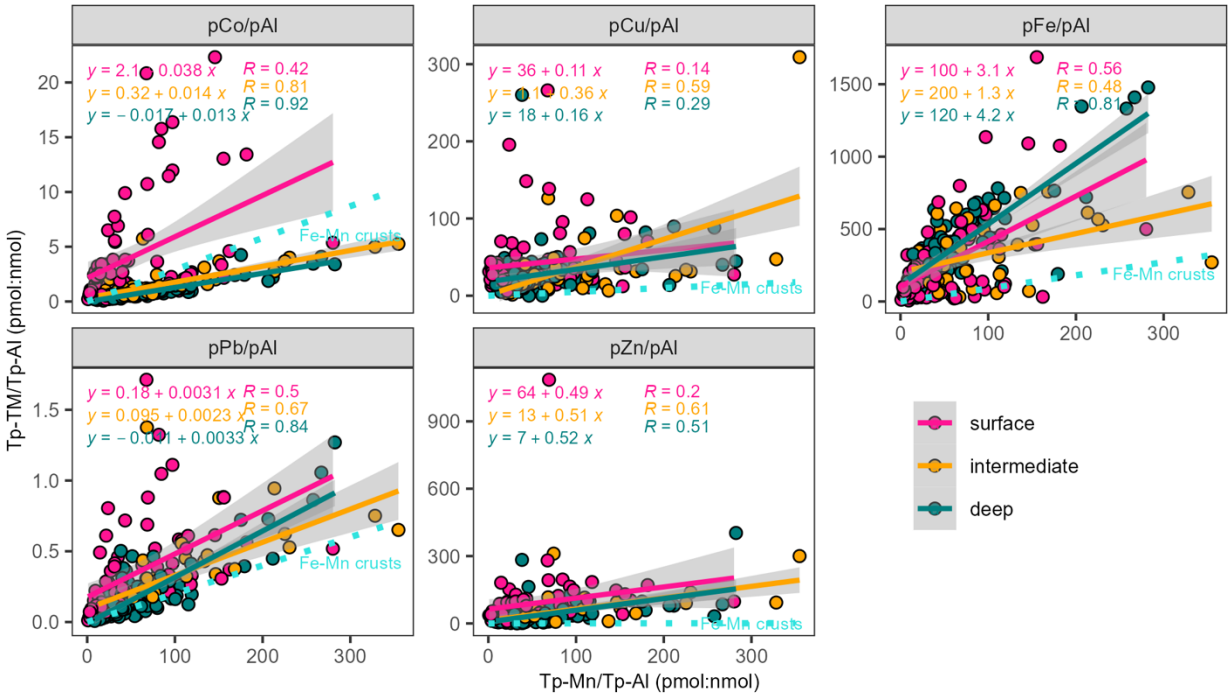


*Figure S5. 5 Cross plots between Tp-Al-normalized TM and Mn in the different water depth layers.*
*Ratios in Atlantic ferromanganese crust (labelled as Fe-Mn crusts) derived from USGS database* (Manheim and Lane-Bostwick 1989) *are plotted as cyan dotted line. Note that one datapoint with extremely high Tp-TM/Tp-Al ratios in the intermediate layer is excluded in the right panel (Peason Coefficient R would increase and slopes remain similar if included).*

**Acknowledgments**

We thank the captain and crew of the RV Meteor M121 cruise/GEOTRACES GA08 section and the chief scientist Martin Frank for cruise support. We thank Pablo Lodeiro and Christian Schlosser for their assistance in sample collection on the GA08 expedition. Thomas Browning is thanked for providing measured chlorophyll. *a* concentrations. We also thank Insa Rapp for training in sample analysis. The PhD Fellowship to T.L. was funded by China Scholarship Council. Additional financial aid to T.L. from the German Academic Exchange Service is acknowledged (DAAD). The cruise was funded by the Deutsche Forschungsgemeinschaft (DFG). GEOMAR supported trace metal analysis.

# 6. Summary and future perspectives

## 6.1 Summary

The major aim of this study was to improve our understanding of the biogeochemical cycling of trace metals (TMs), identify TM sources and quantify their fluxes in the ocean. Our dataset of TM concentrations from the GEOTRACES cruise GA08 (M121) is unique and provides insights into biogeochemical cycling of TMs at land-ocean boundaries with different features (upwelling-dominated BUS and rain and river runoff-dominated Congo River margin) and the decay of these features moving offshore into the oligotrophic open ocean. We observed distributions of a suite of TMs (Cd, Co, Cu, Fe, Mn, Ni, Pb and Zn) with different behaviors in different regions of the eastern South Atlantic. The dissolved and particulate TM data is provided as part of my Ph.D study and has been deposited in the Pangaea depository and will be published in the GEOTRACES dataset soon.

In Chapter 3, we present TM distribution in the BUS with a transect across the Namibian shelf extending to the open ocean. The distributions of TMs in the BUS showed two distinct behaviors – nutrient-type TM distributions for dCd, dNi and dCu and redox-sensitive TM distributions for dFe, dCo and dMn. Intense remineralization shaped the relationships between $PO_4^{3-}$ and nutrient-type TMs across the Namibian shelf, leading to a similar ratio of TM:P as in phytoplankton (Ho et al. 2003; Moore 2016b); whereas water masses that originated in the Southern Ocean showed higher TM to P ratios and drove steeper slopes of TM:P at depth in the open ocean, in agreement with previous observations (Middag et al. 2018, 2020; Hassler and Ellwood 2019; Janssen et al. 2020). Reducing shelf sediments supplied redox-sensitive TMs to the overlying water column revealed by enhanced concentrations across the Namibian shelf associated with low oxygen levels. We applied the classic one-dimension advective and diffusive model to estimate upward, shelf-to-shelf edge and shelf edge-to-open ocean fluxes of redox-sensitive TMs. Results indicated TM supply from the shelf sediments was the major source of these TMs to the shelf surface waters and open ocean compared to its regional atmospheric depositions (Barraqueta et al. 2019). A reduction of 80%-90% contrasting the shelf-to shelf edge Fe fluxes to the shelf edge-to-open ocean Fe fluxes suggested a limited offshore transfer of TM from the Namibian shelf due to scavenging and settling at the shelf edge, consistent with our observation of a faster oxidation rate of Fe. This process may subsequently lead to a larger off-

shelf dFe from the oxic shelf edge (200-500 m) than the fluxes in the surface (<200 m) probably due to non-reductive dissolution of dFe (Homoky et al. 2013) and stabilization by organic matter (Gledhill and Buck 2012). The larger subsurface dCo fluxes were plausibly due to enrichment of Co scavenged by Fe and Mn precipitates and organic matter complexation of dCo on the shelf edge (Saito et al. 2005; Noble et al. 2012).

The main finding of Chapter 4 was that TMs from rainfall supplemented TM fluxes from the Congo River which critically updates perspectives deduced using Fe isotopic compositions (Hunt et al. 2022) and radium (Vieira et al. 2020) data that were unable to identify this source. Surface distributions of TMs indicated an additional source of TMs along the Congo shelf as observed by higher concentrations above the theoretical conservative mixing line of Congo River water and coastal seawater. However, this source was unlikely to constitute TM inputs from subsurface or shelf sediments by vertical mixing and upwelling due to the well-stratified water column and weak wind speed along the shelf. Considering high precipitation rates in our sampling season, wet deposition (rainfall) was a key consideration in the study area, and is considered to contribute larger TM fluxes than dry deposition across much of the ocean (Chance et al. 2015; Shelley et al. 2017). Our results suggested rainfall was indeed the "missing" source of TMs and TM fluxes from rainfall were on the similar magnitude of those from the Congo River, particularly for Zn, Cu, Cd and Pb. These elements showed an anthropogenic source in rainwater reflected by a high EF and solubility, plausibly resulting from the gas flaring sites across the shelf (Lorenzato et al. 2022). In addition, Fe concentrations in the Congo plume indicated a lower removal rate of Fe (~50%) compared to its typical removal rate in estuaries (90-99%) (Boyle et al. 1977; Figuères et al. 1978). Rainwater supplying TMs to the surface water could via several distinct mechanisms lead to this apparent low removal rate, which would also partially account for the distal transfer and substantial Fe fluxes of the Congo plume. A high fraction of organic matter complexing dFe, and(or) Fe(II) formation by continuous photo-reduction in rain droplets can increase the stability of Fe in surface water and thus decrease the Fe removal rate after mixing between river and seawater (Kieber et al. 2001a; Kieber 2003).

The dTM and pTM distributions in the open eastern South Atlantic Ocean, described in Chapter 5, revealed that internal cycling and interaction between dTMs and pTMs are key features of the offshore region beyond the influence of the shelf. The dominated phase of pTMs in the water column was clearly biogenic or authigenic due to stronger correlations between pCd,

pCo and pP and the deviations of the ratios of pTM and pAl between the water column and the UCC. Scavenging of Co, Fe and Zn in the intermediate layer caused a mismatch between the particulate stock of pTM:pP in the surface layer and pseudo regeneration ratio of dTM:$PO_4^{3-}$ in the intermediate layer. Authigenic Mn oxides played a dominant role as a scavenger for Co and Pb evidenced by similar pTM:pMn ratios below the surface layer as found in Atlantic ferromanganese crusts (Manheim and Lane-Bostwick 1989). The enhanced pTM concentrations in bottom waters were caused by a combination of sinking particle supply and resuspension, where the sinking particle supply was more prominent. In the surface layer, the internal recycling of Cd and Co fueled >90% of their production, indicating a limiting role of external supply and emphasizing the importance of internal cycling of these TMs. When compared with the North Atlantic (Dulaquais et al. 2014), the eastern South Atlantic Ocean showed larger recycling of Co probably due to higher Co demand by the phytoplankton assemblage there (Saito et al. 2002; Browning et al. 2014). Comparing the two regions of our study transect, primary production in the SAG showed more dependence on recycling of Cd and Co relative to the Angola Basin due to enhanced utilization of Cd and Co under Fe-(co)limiting conditions (Cullen et al. 2003; Cunningham and John 2017; Browning et al. 2017).

## 6.2 Future perspectives

### 6.2.1 Additional sources of TMs

Our study encountered various sources of TMs including shelf sediments, shelf edge, water masses, river, dry and wet atmospheric deposition and the ocean seafloor. However, there are also other inputs of TMs to the ocean which are not investigated in this work. The slope sediments (>1000 m) from the Peruvian margins is also known to supply significant fluxes of Fe to the open ocean (John et al. 2018; Lam et al. 2020). This could be also an important source of dFe in the BUS as a plume of dFe at 1500-3000 m out of the slope was captured at only one station in our cross-shelf section, thus has not been discussed herein (Figure 2.3). A combination of investigations on Fe speciation to probe the persistence of this slope plume would be helpful to improve our understanding of the mechanism of ocean-land boundary exchange of Fe and its influence on deep ocean Fe budget.

The eastern South Atlantic contains 25% of earth's seamounts (rising to above 2000 m depth), which are especially abundant in the Walvis Ridge forming an important habitat for macrofauna and demersal fish (Zeller et al. 2016). Yet, little is known about seamounts supplying TMs to the deep waters. Indeed, we observed elevated concentrations of L-pFe and L-pMn at the one station crossing the Walvis Ridge. Future work dealing with a more enriched dataset along the Walvis Ridge could help to identify the importance of seamounts on TM budgets in the South Atlantic Ocean.

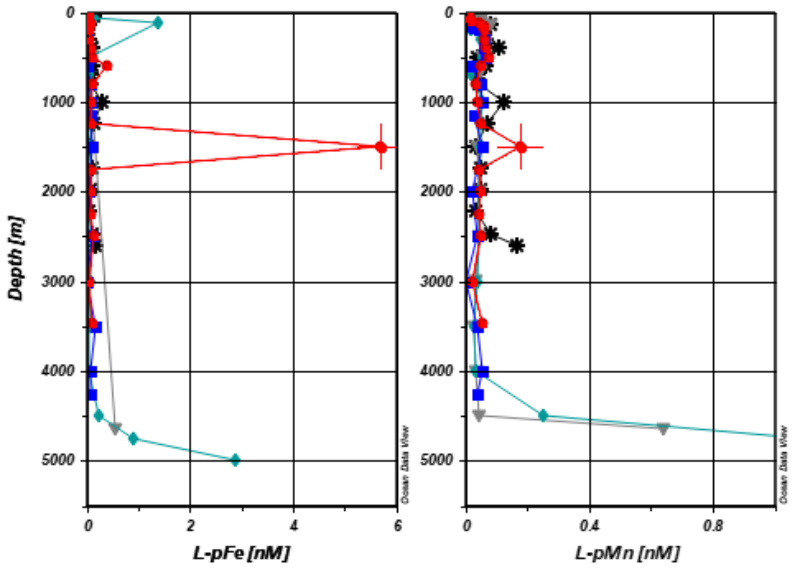


*Figure 6. 1 Depth profiles of L-pFe and L-pMn at open ocean stations along the ~29°S transect. The red dots indicate Station 36 positioned just over the Walvis Ridge. Plots were produced in Ocean Data View* (Schlitzer 2020).

Reducing shelf sediments release dFe, dMn and dCo to the water column and this has been explicitly tested in benthic incubation experiments in various ocean boundary regions globally. However, these fluxes can be underestimated due to scavenging or sinks of dTMs within the water column. Our results in Chapter 3 would have benefited from more data of benthic TM fluxes across the Namibian shelf but unfortunately benthic incubations and water column observations are not usually tightly coupled due to logistics constraints.

Chapter 4 attributed anthropogenic features of TMs in rainwater to gas flaring sites. This is a hitherto unaccounted source of TMs in this region. However, it is still impossible to estimate

how much TMs are contributed by gas flaring as no reliable TM data is available for gas flaring emissions at sea. Future studies on TM emissions (and other greenhouse gases or pollutants) from gas flaring and its influence on surface ocean and seafood products deserve more attention.

### 6.2.2 Comparison between regions

Ocean deoxygenation can cause biogeochemical feedbacks including enhanced TM supply from the reducing shelf sediments, which can transport offshore to open ocean and limit local primary productivity. Feedback effects are possible whereby increased micronutrient supply (Scholz et al. 2014) contributes to increased primary production, thus increasing the organic carbon fluxes that drive oxygen loss in the water column and further enhancing deoxygenation (Wallmann et al. 2022). But such links are difficult to quantify due to uncertainties in the effects of deoxygenation on carbon export, and also the extent to which changes in iron supply affect nitrogen fixation (Engel et al. 2017; Kittu et al. 2023) . Such a feedback could particularly be the case for highly productive EBURs characterized by reducing shelf sediments and large shelf-derived TM fluxes (Dale et al. 2015). In spite of similar features of EBURs, there are however also differences between them. For example, the oxygen level and the extent of OMZ in the BUS in our study area is not as depleted and extensive as the Peruvian Upwelling System (Figure 6.2). This differences could be the reason for the lower TM fluxes in the BUS (Sanial et al. 2018; Liu et al. 2022b). Comparison between EBURs in multiple dimensions in terms of seasonal variations, physical properties, nutrient budgets and TM bioavailabilities in further modeling exercises might improve our understanding on biogeochemical responses to ocean deoxygenation.

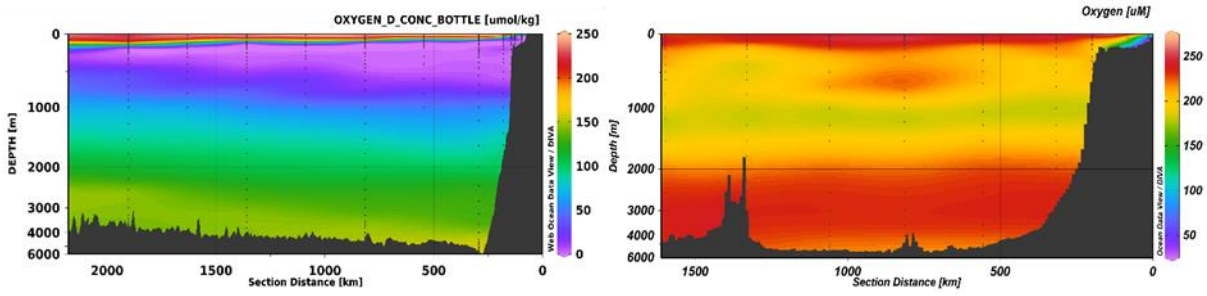


*Figure 6. 2 Comparison between Peruvian and Namibian OMZ.*
*Panels are section plots of oxygen levels along transects from the Peruvian shelf to the open ocean (GEOTRACES cruise GP16) (left) (GEOTRACES Intermediate Data Product Group*

*2021) and from the Namibian shelf to open ocean (GEOTRACES cruise GA08) (right) (this study), respectively.*

### 6.2.3 Seasonal/yearly variations

Variation of upwelling dynamics and water oxygen level in the southern BUS (>32°S) is associated with El Niño-Southern Oscillation (ENSO) (Shannon and Brundrie 1986). Precipitation and Congo River discharge are also subject to a seasonal cycle (Chao et al. 2015). This seasonal/yearly variation can thus impact TM distributions and fluxes to the open ocean (Shannon and Brundrie 1986; Rapp et al. 2020). Revisiting to the BUS and Congo shelf in another season in the future would facilitate a better understanding of TM dynamics, responses to changing redox state and better constrain annual TM inputs in the Congo plume.

### 6.2.4 Internal cycling of TMs

In Chapter 5, we interpreted internal cycling of TMs (dTMs and pTMs) principally in a vertical dimension (depth profiles) and estimated recycling fluxes of biogenic TMs in surface waters. However, deep water age is also a critical factor in determining the trace metal signatures of the deep ocean and misinterpretation of water mass signals as local processes can lead to erroneous interpretation of data, for example the widely critiqued hypothesis of a CdS sink in OMZ waters (Janssen et al. 2014) has been shown to arisen from such a misinterpretation (de Souza et al. 2022). Concentrations of dTMs (including particle-reactive TMs) can be accumulated in deep waters, overprinting their remineralization signals. Therefore, changes in water masses and the age of water masses should be considered in parallel with vertical remineralization processes.

In coastal area, stronger exchange between particle and seawater is expected. This could affect the net TM input fluxes as riverine discharge far more suspended sediments than dissolved chemicals. In the future, particle-seawater interaction in the coastal area would be helpful for us to re-estimate TM budget in the ocean particularly for those TMs with high partition coefficients.

# References

Achterberg, E. P., and C. M. G. Van Den Berg. 1997. Chemical speciation of chromium and nickel in the western Mediterranean. Deep Sea Res. Part II Top. Stud. Oceanogr. **44**: 693–720. doi:10.1016/S0967-0645(96)00086-0

Achterberg, E. P., S. Steigenberger, J. K. Klar, and others. 2020. Trace element biogeochemistry in the high latitude North Atlantic Ocean: seasonal variations and volcanic inputs. Global Biogeochem. Cycles 0–3. doi:10.1016/B978-0-08-095975-7.00602-1

Al-Hashem, A. A., A. Beck, and E. P. Achterberg. 2022. Labile, Refractory, and Total Particulate Trace Metal Concentrations from the GEOTRACES GA08 Shelf section and 3-degree Latitudinal transect.doi:10.1594/PANGAEA.945498

Al-Hashem, A. A., A. J. Beck, S. Krisch, J.-L. Menzel Barraqueta, T. Steffens, and E. P. Achterberg. 2022. Particulate Trace Metal Sources, Cycling, and Distributions on the Southwest African Shelf. Global Biogeochem. Cycles **36**. doi:10.1029/2022GB007453

Alsdorf, D., E. Beighley, A. Laraque, and others. 2016. Opportunities for hydrologic research in the Congo Basin. Rev. Geophys. **54**: 378–409. doi:10.1002/2016RG000517

Amante, C., and B. W. Eakins. 2009. ETOPO1 arc-minute global relief model: procedures, data sources and analysis.

Annegarn, H. ., R. . Van Grieken, D. . Bibby, and F. Von Blottnitz. 1983. Background aerosol composition in the namib desert, South West Africa (Namibia). Atmos. Environ. **17**: 2045–2053. doi:10.1016/0004-6981(83)90361-X

Arrigo, K. R. 2005. Marine microorganisms and global nutrient cycles. Nature **437**: 349–355.

De Baar, H. J. W. 2001. Distributions, sources and sinks of iron in seawater. Biogeochem. iron seawater.

Baars, O., W. Abouchami, S. J. G. Galer, M. Boye, and P. L. Croot. 2014. Dissolved cadmium in the Southern Ocean: Distribution, speciation, and relation to phosphate. Limnol. Oceanogr. **59**: 385–399. doi:10.4319/lo.2014.59.2.0385

Bacon, M. P., D. W. Spencer, and P. G. Brewer. 1976. 210Pb/226Ra and 210Po/210Pb disequilibria in seawater and suspended particulate matter. Earth Planet. Sci. Lett. **32**: 277–296.

Baker, A. R., C. Adams, T. G. Bell, T. D. Jickells, and L. Ganzeveld. 2013. Estimation of atmospheric nutrient inputs to the Atlantic Ocean from 50°N to 50°S based on large-scale field sampling: Iron and other dust-associated elements. Global Biogeochem. Cycles **27**: 755–767. doi:10.1002/gbc.20062

Baker, A. R., and P. L. Croot. 2010. Atmospheric and marine controls on aerosol iron solubility in seawater. Mar. Chem. **120**: 4–13. doi:10.1016/j.marchem.2008.09.003

Baker, A. R., T. D. Jickells, M. Witt, and K. L. Linge. 2006. Trends in the solubility of iron, aluminium, manganese and phosphorus in aerosol collected over the Atlantic Ocean. Mar. Chem. **98**: 43–58. doi:10.1016/j.marchem.2005.06.004

Balls, P. W. 1989. The partition of trace metals between dissolved and particulate phases in european coastal waters: A compilation of field data and comparison with laboratory studies. Netherlands J. Sea Res. **23**: 7–14. doi:10.1016/0077-7579(89)90037-9

Balzano, S., P. J. Statham, R. D. Pancost, and J. R. Lloyd. 2009. Role of microbial populations in the release of reduced iron to the water column from marine aggregates. Aquat. Microb. Ecol. **54**: 291–303.

Barraqueta, J. L. M., J. Klar, M. Gledhill, and others. 2019. Atmospheric deposition fluxes over the Atlantic Ocean: A GEOTRACES case study. Biogeosciences **16**: 1525–1542. doi:10.5194/bg-16-1525-2019

Barraqueta, J. L. M., C. Schlosser, H. Planquette, and others. 2018. Aluminium in the North Atlantic Ocean and the Labrador Sea (GEOTRACES GA01 section): roles of continental inputs and biogenic particle removal. Biogeosciences **15**: 5271–5286.

Barrett, P. M., J. A. Resing, N. J. Buck, C. S. Buck, W. M. Landing, and C. I. Measures. 2012. The trace element composition of suspended particulate matter in the upper 1000 m of the eastern North Atlantic Ocean: A16N. Mar. Chem. **142**–**144**: 41–53. doi:10.1016/J.MARCHEM.2012.07.006

Berger, C. J. M., S. M. Lippiatt, M. G. Lawrence, and K. W. Bruland. 2008. Application of a chemical leach technique for estimating labile particulate aluminum, iron, and manganese in the Columbia River plume and coastal waters off Oregon and Washington. J. Geophys. Res. **113**: 1–16. doi:10.1029/2007jc004703

Bergquist, B. A., and E. A. Boyle. 2006. Dissolved iron in the tropical and subtropical Atlantic Ocean. Global Biogeochem. Cycles **20**: 1–14. doi:10.1029/2005GB002505

Berman-Frank, I., A. Quigg, Z. V Finkel, A. J. Irwin, and L. Haramaty. 2007. Nitrogen-fixation strategies and Fe requirements in cyanobacteria. Limnol. Oceanogr. **52**: 2260–2269.

Best, J. 2019. Anthropogenic stresses on the world's big rivers. Nat. Geosci. **12**: 7–21. doi:10.1038/s41561-018-0262-x

Biller, D. V., and K. W. Bruland. 2013. Sources and distributions of Mn, Fe, Co, Ni, Cu, Zn, and Cd relative to macronutrients along the central California coast during the spring and summer upwelling season. Mar. Chem. **155**: 50–70. doi:10.1016/j.marchem.2013.06.003

Biscéré, T., C. Ferrier-Pagès, R. Grover, A. Gilbert, C. Rottier, A. Wright, C. Payri, and F. Houlbrèque. 2018. Enhancement of coral calcification via the interplay of nickel and urease. Aquat. Toxicol. **200**: 247–256.

Black, E. E., P. J. Lam, J. -M. Lee, and K. O. Buesseler. 2019. Insights From the 238 U- 234 Th Method Into the Coupling of Biological Export and the Cycling of Cadmium, Cobalt, and Manganese in the Southeast Pacific Ocean. Global Biogeochem. Cycles **33**: 15–36. doi:10.1029/2018GB005985

Bonfils, C. J. W., B. D. Santer, J. C. Fyfe, K. Marvel, T. J. Phillips, and S. R. H. Zimmerman. 2020. Human influence on joint changes in temperature, rainfall and continental aridity. Nat. Clim. Chang. **10**: 726–731. doi:10.1038/s41558-020-0821-1

Bonnet, S., and C. Guieu. 2006. Atmospheric forcing on the annual iron cycle in the western Mediterranean Sea: A 1-year survey. J. Geophys. Res. Ocean. **111**.

Borchers, S. L., B. Schnetger, P. Böning, and H.-J. J. Brumsack. 2005. Geochemical signatures of the Namibian diatom belt: Perennial upwelling and intermittent anoxia. Geochemistry, Geophys. Geosystems **6**: 6006. doi:10.1029/2004GC000886

Bordbar, M. H., V. Mohrholz, and M. Schmidt. 2021. The relation of wind-driven coastal and offshore upwelling in the Benguela Upwelling System. J. Phys. Oceanogr. **51**: 3117–3133. doi:10.1175/JPO-D-20-0297.1

Bown, J., M. Boye, A. Baker, and others. 2011. The biogeochemical cycle of dissolved cobalt in the Atlantic and the Southern Ocean south off the coast of South Africa. Mar. Chem. **126**: 193–206. doi:10.1016/j.marchem.2011.03.008

Boyd, P. W., and M. J. Ellwood. 2010. The biogeochemical cycle of iron in the ocean. Nat. Geosci. **3**: 675–682. doi:10.1038/ngeo964

Boyd, P. W., M. J. Ellwood, A. Tagliabue, and B. S. Twining. 2017. Biotic and abiotic retention, recycling and remineralization of metals in the ocean. Nat. Geosci. **10**: 167–173. doi:10.1038/ngeo2876

Boyd, P. W., E. Ibisanmi, S. G. Sander, K. A. Hunter, and G. A. Jackson. 2010. Remineralization of upper ocean particles: Implications for iron biogeochemistry. Limnol. Oceanogr. **55**: 1271–1288. doi:10.4319/lo.2010.55.3.1271

Boyd, P. W., T. Jickells, C. S. Law, and others. 2007. Mesoscale iron enrichment experiments 1993-2005: Synthesis and future directions. Science (80-. ). **315**: 612–617. doi:10.1126/science.1131669

Boyd, P. W., C. S. Law, D. A. Hutchins, and others. 2005. FeCycle: Attempting an iron biogeochemical budget from a mesoscale SF 6 tracer experiment in unperturbed low iron waters. Global Biogeochem. Cycles **19**: n/a-n/a. doi:10.1029/2005GB002494

Boye, M., B. D. Wake, P. Lopez Garcia, J. Bown, A. R. Baker, and E. P. Achterberg. 2012. Distributions of dissolved trace metals (Cd, Cu, Mn, Pb, Ag) in the southeastern Atlantic and the Southern Ocean. Biogeosciences **9**: 3231–3246. doi:10.5194/bg-9-3231-2012

Boyle, E. A. 1988. Cadmium: Chemical tracer of deepwater paleoceanography. Paleoceanography **3**: 471–489.

Boyle, E. A., S. D. Chapnick, G. T. Shen, and M. P. Bacon. 1986. Temporal variability of lead in the western North Atlantic. J. Geophys. Res. **91**: 8573. doi:10.1029/JC091iC07p08573

Boyle, E. A., J. M. Edmond, and E. R. Sholkovitz. 1977. The mechanism of iron removal in estuaries. Geochim. Cosmochim. Acta **41**: 1313–1324. doi:10.1016/0016-7037(77)90075-8

Boyle, E. A., R. M. Sherrell, and M. P. Bacon. 1994. Lead variability in the western North Atlantic Ocean and central Greenland ice: Implications for the search for decadal trends in anthropogenic emissions. Geochim. Cosmochim. Acta **58**: 3227–3238. doi:10.1016/0016-7037(94)90050-7

Braga, E. ., C. Andrié, B. Bourlès, A. Vangriesheim, F. Baurand, and R. Chuchla. 2004. Congo River signature and deep circulation in the eastern Guinea Basin. Deep Sea Res. Part I Oceanogr. Res. Pap. **51**: 1057–1073. doi:10.1016/j.dsr.2004.03.005

Brandt, P., H. W. Bange, D. Banyte, and others. 2015. On the role of circulation and mixing in the ventilation of oxygen minimum zones with a focus on the eastern tropical North Atlantic. Biogeosciences **12**: 489–512. doi:10.5194/bg-12-489-2015

Braungardt, C. B., E. P. Achterberg, F. Elbaz-Poulichet, and N. H. Morley. 2003. Metal geochemistry in a mine-polluted estuarine system in Spain. Appl. Geochemistry **18**: 1757–

1771. doi:10.1016/S0883-2927(03)00079-9

Bremner, J. M. 1980. Physical parameters of the diatomaceous mud belt off South West Africa. Mar. Geol. **34**: 67–76. doi:10.1016/0025-3227(80)90064-X

Bridgestock, L., T. Van De Flierdt, M. Rehkämper, and others. 2016. Return of naturally sourced Pb to Atlantic surface waters. Nat. Commun. **7**: 12921.

Bridgestock, L., M. Rehkämper, T. van de Flierdt, M. Paul, A. Milne, M. C. Lohan, and E. P. Achterberg. 2018. The distribution of lead concentrations and isotope compositions in the eastern Tropical Atlantic Ocean. Geochim. Cosmochim. Acta **225**: 36–51. doi:10.1016/J.GCA.2018.01.018

Broecker, W. S., and T.-H. Peng. 1982. Tracers in the Sea, Lamont-Doherty Geological Observatory, Columbia University Palisades, New York.

Broecker, W. S., and T. Takahashi. 1981. Hydrography of the central Atlantic—IV. Intermediate waters of antarctic origin. Deep Sea Res. Part A. Oceanogr. Res. Pap. **28**: 177–193. doi:10.1016/0198-0149(81)90061-3

Browning, T. J., E. P. Achterberg, A. Engel, and E. Mawji. 2021. Manganese co-limitation of phytoplankton growth and major nutrient drawdown in the Southern Ocean. Nat. Commun. **12**: 884. doi:10.1038/s41467-021-21122-6

Browning, T. J., E. P. Achterberg, I. Rapp, A. Engel, E. M. Bertrand, A. Tagliabue, and C. M. Moore. 2017. Nutrient co-limitation at the boundary of an oceanic gyre. Nature **551**: 242–246. doi:10.1038/nature24063

Browning, T. J., H. A. Bouman, C. M. Moore, C. Schlosser, G. A. Tarran, E. M. S. Woodward, and G. M. Henderson. 2014. Nutrient regimes control phytoplankton ecophysiology in the South Atlantic. Biogeosciences **11**: 463–479.

Browning, T. J., I. Rapp, C. Schlosser, M. Gledhill, E. P. Achterberg, A. Bracher, and F. A. C. Le Moigne. 2018. Influence of Iron, Cobalt, and Vitamin B 12 Supply on Phytoplankton Growth in the Tropical East Pacific During the 2015 El Niño. Geophys. Res. Lett. doi:10.1029/2018GL077972

Bruland, K. W. 1980. Oceanographic distributions of cadmium, zinc, nickel, and copper in the North Pacific. Earth Planet. Sci. Lett. **47**: 176–198. doi:10.1016/0012-821X(80)90035-7

Bruland, K. W., and R. P. Franks. 1983. Mn, Ni, Cu, Zn and Cd in the Western North Atlantic, p. 395–414. *In* Trace Metals in Sea Water. Springer US.

Bruland, K. W., R. Middag, and M. C. Lohan. 2014. Controls of Trace Metals in Seawater, p. 19–51. *In* Treatise on Geochemistry. Elsevier.

Bruland, K. W., K. J. Orians, and J. P. Cowen. 1994. Reactive trace metals in the stratified central North Pacific. Geochim. Cosmochim. Acta **58**: 3171–3182. doi:10.1016/0016-7037(94)90044-2

Bruland, K. W., E. L. Rue, G. J. Smith, and G. R. DiTullio. 2005. Iron, macronutrients and diatom blooms in the Peru upwelling regime: brown and blue waters of Peru. Mar. Chem. **93**: 81–103. doi:10.1016/j.marchem.2004.06.011

Buck, K. N., M. C. Lohan, C. J. M. Berger, and K. W. Bruland. 2007. Dissolved iron speciation in two distinct river plumes and an estuary: Implications for riverine iron supply. Limnol.

Oceanogr. **52**: 843–855. doi:10.4319/lo.2007.52.2.0843

Bultot, F. 1971. Atlas climatique du bassin congolais, Institut National pour l'étude agronomique du Congo.

Carr, M.-E. 2001. Estimation of potential productivity in Eastern Boundary Currents using remote sensing. Deep Sea Res. Part II Top. Stud. Oceanogr. **49**: 59–80. doi:10.1016/S0967-0645(01)00094-7

Chance, R., T. D. Jickells, and A. R. Baker. 2015. Atmospheric trace metal concentrations, solubility and deposition fluxes in remote marine air over the south-east Atlantic. Mar. Chem. **177**: 45–56. doi:10.1016/j.marchem.2015.06.028

Chao, Y., J. D. Farrara, G. Schumann, K. M. Andreadis, and D. Moller. 2015. Sea surface salinity variability in response to the Congo river discharge. Cont. Shelf Res. **99**: 35–45. doi:10.1016/j.csr.2015.03.005

Charette, M. A., P. J. Lam, M. C. Lohan, and others. 2016. Coastal ocean and shelf-sea biogeochemical cycling of trace elements and isotopes: lessons learned from GEOTRACES. Philos. Trans. R. Soc. A Math. Phys. Eng. Sci. **374**: 20160076. doi:10.1098/rsta.2016.0076

Chavez, F. P., and M. Messié. 2009. A comparison of Eastern Boundary Upwelling Ecosystems. Prog. Oceanogr. **83**: 80–96. doi:10.1016/j.pocean.2009.07.032

Chelton, D. B., R. A. DeSzoeke, M. G. Schlax, K. El Naggar, N. Siwertz, and C. D. B. D. R. A. S. M. G. E. N. K. S. Nicolas. 1998. Geographical variability of the first baroclinic Rossby radius of deformation. J. Phys. Oceanogr. **28**: 433–460. doi:https://doi.org/10.1175/1520-0485(1998)028%3C0433:GVOTFB%3E2.0.CO;2

Chen, M., G. Carrasco, N. Zhao, and others. 2023. Boundary exchange completes the marine Pb cycle jigsaw. Proc. Natl. Acad. Sci. **120**: 2017. doi:10.1073/pnas.2213163120

Chester, R. 2009. Marine geochemistry, John Wiley & Sons.

Christensen, J. N., A. N. Halliday, L. V Godfrey, J. R. Hein, and D. K. Rea. 1997. Climate and ocean dynamics and the lead isotopic records in Pacific ferromanganese crusts. Science (80-. ). **277**: 913–918.

Coale, K. H., and K. W. Bruland. 1990. Spatial and temporal variability in copper complexation in the North Pacific. Deep Sea Res. Part A, Oceanogr. Res. Pap. **37**: 317–336. doi:10.1016/0198-0149(90)90130-N

Collier, R., and J. Edmond. 1984. The trace element geochemistry of marine biogenic particulate matter. Prog. Oceanogr. **13**: 113–199. doi:https://doi.org/10.1016/0079-6611(84)90008-9

Colombo, M., J. Li, B. Rogalla, S. E. Allen, and M. T. Maldonado. 2022. Particulate trace element distributions along the Canadian Arctic GEOTRACES section: shelf-water interactions, advective transport and contrasting biological production. Geochim. Cosmochim. Acta **323**: 183–201. doi:10.1016/j.gca.2022.02.013

Conway, T. M., and S. G. John. 2014. Global Biogeochemical Cycles isotopes in the North Atlantic Ocean. Glob. Biogeochem. Cycles Res. 1111–1128. doi:10.1002/2014GB004862.Received

Conway, T. M., and S. G. John. 2015. The cycling of iron, zinc and cadmium in the North East

Pacific Ocean – Insights from stable isotopes. Geochim. Cosmochim. Acta **164**: 262–283. doi:10.1016/j.gca.2015.05.023

Cowen, J. P., and K. W. Bruland. 1985. Metal deposits associated with bacteria: implications for Fe and Mn marine biogeochemistry. Deep Sea Res. Part A, Oceanogr. Res. Pap. **32**: 253–272. doi:10.1016/0198-0149(85)90078-0

Croot, P. L., and P. Laan. 2002. Continuous shipboard determination of Fe(II) in polar waters using flow injection analysis with chemiluminescence detection. Anal. Chim. Acta **466**: 261–273. doi:10.1016/S0003-2670(02)00596-2

Cullen, J. T., Z. Chase, K. H. Coale, S. E. Fitzwater, and R. M. Sherrell. 2003. Effect of iron limitation on the cadmium to phosphorus ratio of natural phytoplankton assemblages from the Southern Ocean. Limnol. Oceanogr. **48**: 1079–1087. doi:10.4319/lo.2003.48.3.1079

Cullen, J. T., and M. T. Maldonado. 2012. Biogeochemistry of cadmium and its release to the environment. Cadmium from Toxic. to essentiality 31–62.

Cullen, J. T., and R. M. Sherrell. 1999. Techniques for determination of trace metals in small samples of size-fractionated particulate matter: Phytoplankton metals off central California. Mar. Chem. **67**: 233–247. doi:10.1016/S0304-4203(99)00060-2

Cunningham, B. R., and S. G. John. 2017. The effect of iron limitation on cyanobacteria major nutrient and trace element stoichiometry. Limnol. Oceanogr. **62**: 846–858.

Curl, H., and M. N. Hill. 1964. Progress in the Study of the SeasThe Sea: Ideas and Observations on Progress in the Study of the Seas,.

Cutter, G., K. Casciotti, P. Croot, W. Geibert, L.-E. Heimbürger, M. Lohan, H. Planquette, and T. van de Flierdt. 2017. Sampling and Sample-handling Protocols for GEOTRACES Cruises. Version 3, August 2017.

Cutter, G., J. W. Moffett, M. C. Nielsdóttir, and V. Sanial. 2018. Multiple oxidation state trace elements in suboxic waters off Peru: In situ redox processes and advective/diffusive horizontal transport. Mar. Chem. **201**: 77–89. doi:10.1016/j.marchem.2018.01.003

Dale, A. W., L. Nickelsen, F. Scholz, C. Hensen, A. Oschlies, and K. Wallmann. 2015. A revised global estimate of dissolved iron fluxes from marine sediments. Global Biogeochem. Cycles **29**: 691–707. doi:10.1002/2014GB005017

Denamiel, C., W. P. Budgell, and R. Toumi. 2013. The congo river plume: Impact of the forcing on the far-field and near-field dynamics. J. Geophys. Res. Ocean. **118**: 964–989. doi:10.1002/jgrc.20062

Desboeufs, K., F. Fu, M. Bressac, and others. 2022. Wet deposition in the remote western and central Mediterranean as a source of trace metals to surface seawater. Atmos. Chem. Phys. **22**: 2309–2332. doi:10.5194/acp-22-2309-2022

Dittmar, T., and M. Birkicht. 2001. Regeneration of nutrients in the northern Benguela upwelling and the Angola-Benguela front areas. S. Afr. J. Sci. **97**: 239–246.

Doi, T., T. Tozuka, H. Sasaki, Y. Masumoto, and T. Yamagata. 2007. Seasonal and interannual variations of oceanic conditions in the Angola Dome. J. Phys. Oceanogr. **37**: 2698–2713. doi:10.1175/2007JPO3552.1

Duce, R. A., G. L. Hoffman, B. J. Ray, and others. 1976. Trace metals in the marine atmosphere:

sources and fluxes. Mar. Pollut. Transf. 77–119.

Dulac, F., P. Buat-mçnard, U. Ezat, S. Melki, and G. Bergametti. 1988. Atmospheric input of trace metals to the western Mediterranean: uncertainties in modelling dry deposition from cascade impactor data. Tellus B Chem. Phys. Meteorol. **40**: 362–378. doi:10.3402/tellusb.v40i3.15094

Dulaquais, G., M. Boye, R. Middag, and others. 2014. Contrasting biogeochemical cycles of cobalt in the surface western Atlantic Ocean. Global Biogeochem. Cycles **28**: 1387–1412. doi:10.1002/2014GB004903

Dunckley, J. F., J. R. Koseff, J. V. Steinbuck, S. G. Monismith, and A. Genin. 2012. Comparison of mixing efficiency and vertical diffusivity models from temperature microstructure. J. Geophys. Res. Ocean. **117**: n/a-n/a. doi:10.1029/2012JC007967

Dunne, J. P., R. A. Armstrong, A. Gnnadesikan, and J. L. Sarmiento. 2005. Empirical and mechanistic models for the particle export ratio. Global Biogeochem. Cycles **19**: 1–16. doi:10.1029/2004GB002390

Echegoyen, Y., E. A. Boyle, J. M. Lee, T. Gamo, H. Obata, and K. Norisuye. 2014. Recent distribution of lead in the Indian Ocean reflects the impact of regional emissions. Proc. Natl. Acad. Sci. U. S. A. **111**: 15328–15331. doi:10.1073/pnas.1417370111

Eisma, D., and A. J. Van Bennekom. 1978. The Zaire river and estuary and the Zaire outflow in the Atlantic Ocean. Netherlands J. Sea Res.

Elderfield, H., A. Hepworth, P. N. Edwards, and L. M. Holliday. 1979. Zinc in the Conwy River and estuary. Estuar. Coast. Mar. Sci. **9**: 403–422. doi:10.1016/0302-3524(79)90014-8

Ellwood, M. J., and K. A. Hunter. 2000. The incorporation of zinc and iron into the frustule of the marine diatom Thalassiosira pseudonana. Limnol. Oceanogr. **45**: 1517–1524.

Elrod, V. A., W. M. Berelson, K. H. Coale, and K. S. Johnson. 2004. The flux of iron from continental shelf sediments: A missing source for global budgets. Geophys. Res. Lett. **31**: n/a-n/a. doi:10.1029/2004GL020216

Eltayeb, M. A. H., R. E. Van Grieken, W. Maenhaut, and H. J. Annegarn. 1993. Aerosol-soil fractionation for Namib Desert samples. Atmos. Environ. Part A, Gen. Top. **27**: 669–678. doi:10.1016/0960-1686(93)90185-2

Engel, A., H. Wagner, F. A. C. Le Moigne, and S. T. Wilson. 2017. Particle export fluxes to the oxygen minimum zone of the eastern tropical North Atlantic. Biogeosciences **14**: 1825–1838.

Fairall, C. W., E. F. Bradley, J. E. Hare, A. A. Grachev, and J. B. Edson. 2003. Bulk parameterization of air–sea fluxes: Updates and verification for the COARE algorithm. J. Clim. **16**: 571–591.

Falkowski, P., R. J. Scholes, E. E. A. Boyle, and others. 2000. The global carbon cycle: a test of our knowledge of earth as a system. Science (80-. ). **290**: 291–296.

Figuères, G., J. M. Martin, and M. Meybeck. 1978. Iron behaviour in the Zaire estuary. Netherlands J. Sea Res. **12**: 329–337. doi:10.1016/0077-7579(78)90035-2

Flynn, R. F., J. Granger, J. A. Veitch, S. Siedlecki, J. M. Burger, K. Pillay, and S. E. Fawcett. 2020. On-Shelf Nutrient Trapping Enhances the Fertility of the Southern Benguela

Upwelling System. J. Geophys. Res. Ocean. **125**: 1–24. doi:10.1029/2019JC015948

Frank, M., E. Achterberg, L. Bristow, and others. 2014. METEOR -Berichte Trace Metal Chemistry in the Water Column of the Angola Basin - A Contribution to the International GEOTRACES Program.

Freund, M. 2020. Dispersion of a Tracer in the Eastern Tropical South Pacific - an Investigation of Interactions from the Benthic Boundary Layer to the Ocean Interior. Dr. Diss.

Frew, R. D., and K. A. Hunter. 1992. Influence of Southern Ocean waters on the cadmium–phosphate properties of the global ocean. Nature **360**: 144–146.

Garzoli, S. L., and A. L. Gordon. 1996. Origins and variability of the Benguela Current. J. Geophys. Res. Ocean. **101**: 897–906. doi:10.1029/95JC03221

van Genuchten, C. M., M. J. Hopwood, T. Liu, J. Krause, E. P. Achterberg, M. T. Rosing, and L. Meire. 2022. Solid-phase Mn speciation in suspended particles along meltwater-influenced fjords of West Greenland. Geochim. Cosmochim. Acta **326**: 180–198. doi:10.1016/j.gca.2022.04.003

GEOTRACES Intermediate Data Product Group. 2021. The GEOTRACES Intermediate Data Product 2021 (IDP2021). NERC EDS British Oceanographic Data Centre NOC.

German, C. R., and W. E. Seyfried. 2013. Hydrothermal Processes, 2nd ed. Elsevier Ltd.

Gill, A. E., and E. Adrian. 1982. Atmosphere-ocean dynamics, Academic press.

Glass, J. B., and C. L. Dupont. 2017. Oceanic nickel biogeochemistry and the evolution of nickel use. Biol. Chem. Nickel 12–26.

Gledhill, M., and K. N. Buck. 2012. The organic complexation of iron in the marine environment: a review. Front. Microbiol. **3**: 1–17. doi:10.3389/fmicb.2012.00069

Gledhill, M., A. Hollister, M. Seidel, K. Zhu, E. P. Achterberg, T. Dittmar, and A. Koschinsky. 2022. Trace metal stoichiometry of dissolved organic matter in the Amazon Plume. Sci. Adv. **2249**: 1–11.

Global Gas Flaring Reduction Partnership. 2020. Global Gas Flaring Tracker Report.

Glover, D. M., W. J. Jenkins, and S. C. Doney. 2011. Modeling Methods for Marine Science, Cambridge University Press.

Goldberg, E. D. 1954. Marine geochemistry 1. Chemical scavengers of the sea. J. Geol. **62**: 249–265.

González-Santana, D., H. Planquette, M. Cheize, and others. 2020. Processes driving iron and manganese dispersal from the TAG hydrothermal plume (Mid-Atlantic Ridge): results from a GEOTRACES process study. Front. Mar. Sci. **7**: 568.

Graedel, T. E., D. van Beers, M. Bertram, and others. 2005. The multilevel cycle of anthropogenic zinc. J. Ind. Ecol. **9**: 67–90.

Grasshoff, K., K. Kremling, and M. Ehrhardt. 1999. Methods of Seawater Analysis, K. Grasshoff, K. Kremling, and M. Ehrhardt [eds.]. Wiley.

Guieu, C., F. D'Ortenzio, F. Dulac, and others. 2020. Introduction: Process studies at the air–sea interface after atmospheric deposition in the Mediterranean Sea – objectives and strategy of the PEACETIME oceanographic campaign (May–June 2017). Biogeosciences **17**: 5563–

5585. doi:10.5194/bg-17-5563-2020

Guieu, C., J. M. Martin, A. J. Thomas, and F. Elbaz-Poulichet. 1991. Atmospheric versus river inputs of metals to the Gulf of Lions. Mar. Pollut. Bull. **22**: 176–183. doi:10.1016/0025-326X(91)90467-7

Hassler, C., and M. Ellwood. 2019. Nutrient concentration in seawater samples, collected from the underway supply, CTD and trace metal rosettes in the Southern Ocean during the austral summer of 2016/2017, on board the Antarctic Circumnavigation Expedition (ACE).doi:10.5281/ZENODO.2616606

Hatta, M., C. I. Measures, J. Wu, S. Roshan, J. N. Fitzsimmons, P. Sedwick, and P. Morton. 2015. An overview of dissolved Fe and Mn distributions during the 2010–2011 U.S. GEOTRACES north Atlantic cruises: GEOTRACES GA03. Deep Sea Res. Part II Top. Stud. Oceanogr. **116**: 117–129. doi:10.1016/J.DSR2.2014.07.005

Hawco, N. J., P. J. Lam, J. M. Lee, D. C. Ohnemus, A. E. Noble, N. J. Wyatt, M. C. Lohan, and M. A. Saito. 2018. Cobalt scavenging in the mesopelagic ocean and its influence on global mass balance: Synthesizing water column and sedimentary fluxes. Mar. Chem. **201**: 151–166. doi:10.1016/j.marchem.2017.09.001

Hawco, N. J., D. C. Ohnemus, J. A. Resing, B. S. Twining, and M. A. Saito. 2016. A dissolved cobalt plume in the oxygen minimum zone of the eastern tropical South Pacific. Biogeosciences **13**: 5697–5717. doi:10.5194/bg-13-5697-2016

Heggie, D., G. Klinkhammer, and D. Cullen. 1987. Manganese and copper fluxes from continental margin sediments. Geochim. Cosmochim. Acta **51**: 1059–1070. doi:10.1016/0016-7037(87)90200-6

Heggie, D., and T. Lewis. 1984. Cobalt in pore waters of marine sediments. Nature **311**: 453–455. doi:10.1038/311453a0

Heller, M. I., and P. L. Croot. 2015. Copper speciation and distribution in the Atlantic sector of the Southern Ocean. Mar. Chem. **173**: 253–268. doi:10.1016/j.marchem.2014.09.017

Heller, M. I., P. J. Lam, J. W. Moffett, C. P. Till, J.-M. Lee, B. M. Toner, and M. A. Marcus. 2017. Accumulation of Fe oxyhydroxides in the Peruvian oxygen deficient zone implies non-oxygen dependent Fe oxidation. Geochim. Cosmochim. Acta **211**: 174–193.

Henderson, G. M., E. P. Achterberg, and L. Bopp. 2018. Changing Trace Element Cycles in the 21st Century Ocean. Elements **14**: 409–413. doi:10.2138/gselements.14.6.409

Ho, T.-Y. 2013. Nickel limitation of nitrogen fixation in Trichodesmium. Limnol. Oceanogr. **58**: 112–120.

Ho, T. Y., A. Quigg, Z. V. Finkel, A. J. Milligan, K. Wyman, P. G. Falkowski, and F. M. M. Morel. 2003. The elemental composition of some marine phytoplankton. J. Phycol. **39**: 1145–1159. doi:10.1111/j.0022-3646.2003.03-090.x

Hollister, A. P., M. Leon, J. Scholten, M. Gledhill, and A. Koschinsky. 2022. Distribution and Flux of Trace Metals (Al, Mn, Fe, Co, Ni, Cu, Zn, Cd, Pb and U) in the Amazon and Pará River Estuary and Mixing Plume. Authorea Prepr.

Homoky, W. B., T. M. Conway, S. G. John, D. König, F. Deng, A. Tagliabue, and R. A. Mills. 2021. Iron colloids dominate sedimentary supply to the ocean interior. Proc. Natl. Acad.

Sci. **118**: e2016078118. doi:10.1073/pnas.2016078118

Homoky, W. B., S. G. John, T. M. Conway, and R. A. Mills. 2013. Distinct iron isotopic signatures and supply from marine sediment dissolution. Nat. Commun. **4**: 2143. doi:10.1038/ncomms3143

Homoky, W. B., S. Severmann, J. McManus, W. M. Berelson, T. E. Riedel, P. J. Statham, and R. A. Mills. 2012. Dissolved oxygen and suspended particles regulate the benthic flux of iron from continental margins. Mar. Chem. **134**–**135**: 59–70. doi:10.1016/j.marchem.2012.03.003

Homoky, W. B., T. Weber, W. M. Berelson, and others. 2016. Quantifying trace element and isotope fluxes at the ocean-sediment boundary: A review,.

Hopkins, J., M. Lucas, C. Dufau, M. Sutton, J. Stum, O. Lauret, and C. Channelliere. 2013. Detection and variability of the Congo River plume from satellite derived sea surface temperature, salinity, ocean colour and sea level. Remote Sens. Environ. **139**: 365–385. doi:10.1016/j.rse.2013.08.015

Hopwood, M. J., A. J. Birchill, M. Gledhill, E. P. Achterberg, J. K. Klar, and A. Milne. 2017. A Comparison between Four Analytical Methods for the Measurement of Fe(II) at Nanomolar Concentrations in Coastal Seawater. Front. Mar. Sci. **4**: 1–14. doi:10.3389/fmars.2017.00192

Hopwood, M. J., C. Santana-González, J. Gallego-Urrea, and others. 2020. Fe (II) stability in coastal seawater during experiments in Patagonia, Svalbard, and Gran Canaria. Biogeosciences **17**: 1327–1342.

Hsieh, Y.-T., W. Geibert, E. M. S. Woodward, N. J. Wyatt, M. C. Lohan, E. P. Achterberg, and G. M. Henderson. 2021. Radium-228-derived ocean mixing and trace element inputs in the South Atlantic. Biogeosciences **18**: 1645–1671. doi:10.5194/bg-18-1645-2021

Huffman, G. J., D. T. Bolvin, E. J. Nelkin, and R. F. Adler. 2016. TRMM (TMPA) Precipitation L3 1 Day 0.25 Degree× 0.25 Degree V7. Goddard Earth Sciences Data and Information Services Center (GES DISC ….

Huffman, G. J., E. F. Stocker, D. T. Bolvin, E. J. Nelkin, and J. Tan. 2019. GPM IMERG Early precipitation L3 half hourly 0.1 degree x 0.1 degree V06. Goddard Earth Sci. Data Inf. Serv. Cent. (GES DISC) Greenbelt, MD, USA. doi:10.5067/GPM/IMERG/3B-HH/06

Hunt, H. R., B. A. Summers, M. Sieber, S. Krisch, A. Al-Hashem, M. Hopwood, E. P. Achterberg, and T. M. Conway. 2022. Distinguishing the influence of sediments, the Congo River, and water-mass mixing on the distribution of iron and its isotopes in the Southeast Atlantic Ocean. Mar. Chem. 104181.

Hutchings, L., C. D. van der Lingen, L. J. Shannon, and others. 2009. The Benguela Current: An ecosystem of four components. Prog. Oceanogr. **83**: 15–32. doi:10.1016/j.pocean.2009.07.046

Hutchins, D. A., and K. W. Bruland. 1998. Iron-limited diatom growth and Si:N uptake ratios in a coastal upwelling regime. Nature **393**: 561–564. doi:10.1038/31203

Ighalo, J. O., A. G. Adeniyi, J. A. Adeniran, and S. Ogunniyi. 2021. A systematic literature analysis of the nature and regional distribution of water pollution sources in Nigeria. J. Clean. Prod. **283**: 124566. doi:10.1016/j.jclepro.2020.124566

Inthorn, M., T. Wagner, G. Scheeder, and M. Zabel. 2006. Lateral transport controls distribution, quality, and burial of organic matter along continental slopes in high-productivity areas. Geology **34**: 205. doi:10.1130/G22153.1

Jacquot, J. E., and J. W. Moffett. 2015. Copper distribution and speciation across the International GEOTRACES Section GA03. Deep Sea Res. Part II Top. Stud. Oceanogr. **116**: 187–207. doi:10.1016/J.DSR2.2014.11.013

Janssen, D. J., T. M. Conway, S. G. John, J. R. Christian, D. I. Kramer, T. F. Pedersen, and J. T. Cullen. 2014. Undocumented water column sink for cadmium in open ocean oxygen-deficient zones. Proc. Natl. Acad. Sci. **111**: 6888–6893. doi:10.1073/pnas.1402388111

Janssen, D. J., M. Sieber, M. J. Ellwood, and others. 2020. Dissolved trace metal (Fe, Ni, Cu, Zn, Cd, Pb) concentrations in the Indian and Pacific sectors of the Southern Ocean from the Antarctic Circumnavigation Expedition (2016-2017).doi:10.5281/ZENODO.3634411

Jarre, A., L. Hutchings, S. P. Kirkman, and others. 2015. Synthesis: Climate effects on biodiversity, abundance and distribution of marine organisms in the Benguela. Fish. Oceanogr. **24**: 122–149. doi:10.1111/fog.12086

Jeandel, C., and E. H. Oelkers. 2015. The influence of terrigenous particulate material dissolution on ocean chemistry and global element cycles. Chem. Geol. **395**: 50–66. doi:10.1016/J.CHEMGEO.2014.12.001

Jeandel, C., M. Rutgers van der Loeff, P. J. Lam, M. Roy-Barman, R. M. Sherrell, S. Kretschmer, C. German, and F. Dehairs. 2015. What did we learn about ocean particle dynamics in the GEOSECS-JGOFS era? Prog. Oceanogr. **133**: 6–16. doi:10.1016/j.pocean.2014.12.018

Jensen, L. T., P. Morton, B. S. Twining, and others. 2020. A comparison of marine Fe and Mn cycling: US GEOTRACES GN01 Western Arctic case study. Geochim. Cosmochim. Acta **288**: 138–160.

Jickells, T. D. 1995. Atmospheric inputs of metals and nutrients to the oceans: their magnitude and effects. Mar. Chem. **48**: 199–214. doi:10.1016/0304-4203(95)92784-P

Jickells, T. D. 1999. The inputs of dust derived elements to the Sargasso Sea; a synthesis. Mar. Chem. **68**: 5–14. doi:10.1016/S0304-4203(99)00061-4

Jickells, T. D., Z. S. An, K. K. Andersen, and others. 2005. Global Iron Connections Between Desert Dust, Ocean Biogeochemistry, and Climate. Science (80-. ). **308**: 67–71. doi:10.1126/science.1105959

Jickells, T. D., A. R. Baker, and R. Chance. 2016. Atmospheric transport of trace elements and nutrients to the oceans. Philos. Trans. R. Soc. A Math. Phys. Eng. Sci. **374**: 20150286. doi:10.1098/rsta.2015.0286

Jickells, T. D., A. H. Knap, and T. M. Church. 1984. Trace metals in Bermuda rainwater. J. Geophys. Res. **89**: 1423. doi:10.1029/JD089iD01p01423

Jochum, K. P., U. Nohl, K. Herwig, E. Lammel, B. Stoll, and A. W. Hofmann. 2005. GeoReM: A New Geochemical Database for Reference Materials and Isotopic Standards. Geostand. Geoanalytical Res. **29**: 333–338. doi:https://doi.org/10.1111/j.1751-908X.2005.tb00904.x

John, S. G., and T. M. Conway. 2014. A role for scavenging in the marine biogeochemical

cycling of zinc and zinc isotopes. Earth Planet. Sci. Lett. **394**: 159–167. doi:10.1016/J.EPSL.2014.02.053

John, S. G., J. Helgoe, E. Townsend, and others. 2018. Biogeochemical cycling of Fe and Fe stable isotopes in the Eastern Tropical South Pacific. Mar. Chem. **201**: 66–76. doi:10.1016/j.marchem.2017.06.003

John, S. G., R. L. Kelly, X. Bian, and others. 2022. The biogeochemical balance of oceanic nickel cycling. Nat. Geosci. doi:10.1038/s41561-022-01045-7

Johnson, K. S. Chemical Sensors • MBARI.

Johnson, K. S., F. P. Chavez, and G. E. Friederich. 1999. Continental-shelf sediment as a primary source of iron for coastal phytoplankton. Nature **398**: 697–700. doi:10.1038/19511

Johnson, K. S., R. M. Gordon, and K. H. Coale. 1997. What controls dissolved iron concentrations in the world ocean? Mar. Chem. **57**: 137–161. doi:10.1016/S0304-4203(97)00043-1

Johnson, N. M., C. T. Driscoll, J. S. Eaton, G. E. Likens, and W. H. McDowell. 1981. 'Acid rain', dissolved aluminum and chemical weathering at the Hubbard Brook Experimental Forest, New Hampshire. Geochim. Cosmochim. Acta **45**: 1421–1437. doi:10.1016/0016-7037(81)90276-3

De Jong, J., V. Schoemann, D. Lannuzel, P. Croot, H. De Baar, and J. L. Tison. 2012. Natural iron fertilization of the Atlantic sector of the Southern Ocean by continental shelf sources of the Antarctic Peninsula. J. Geophys. Res. Biogeosciences **117**. doi:10.1029/2011JG001679

de Jong, J., V. Schoemann, D. Lannuzel, J. L. Tison, and N. Mattielli. 2008. High-accuracy determination of iron in seawater by isotope dilution multiple collector inductively coupled plasma mass spectrometry (ID-MC-ICP-MS) using nitrilotriacetic acid chelating resin for pre-concentration and matrix separation. Anal. Chim. Acta **623**: 126–139. doi:10.1016/j.aca.2008.06.013

Jordi, A., G. Basterretxea, A. Tovar-Sánchez, A. Alastuey, and X. Querol. 2012. Copper aerosols inhibit phytoplankton growth in the Mediterranean Sea. Proc. Natl. Acad. Sci. **109**: 21246–21249.

Junker, T., V. Mohrholz, L. Siegfried, and A. van der Plas. 2017. Seasonal to interannual variability of water mass characteristics and currents on the Namibian shelf. J. Mar. Syst. **165**: 36–46. doi:10.1016/J.JMARSYS.2016.09.003

Kadko, D. 1993. An assessment of the effect of chemical scavenging within submarine hydrothermal plumes upon ocean geochemistry. Earth Planet. Sci. Lett. **120**: 361–374.

Karstensen, J., L. Stramma, and M. Visbeck. 2008. Oxygen minimum zones in the eastern tropical Atlantic and Pacific oceans. Prog. Oceanogr. **77**: 331–350. doi:10.1016/j.pocean.2007.05.009

Keeling, R. F., A. Körtzinger, and N. Gruber. 2010. Ocean deoxygenation in a warming world. Ann. Rev. Mar. Sci. **2**: 199–229. doi:10.1146/annurev.marine.010908.163855

Kelly, A. E., M. K. Reuer, N. F. Goodkin, and E. A. Boyle. 2009. Lead concentrations and isotopes in corals and water near Bermuda, 1780–2000. Earth Planet. Sci. Lett. **283**: 93–100.

Kieber, R. J. 2003. Temporal variability of rainwater iron speciation at the Bermuda Atlantic Time Series Station. J. Geophys. Res. **108**: 3277. doi:10.1029/2001JC001031

Kieber, R. J., D. R. Hardison, R. F. Whitehead, and J. D. Willey. 2003. Photochemical Production of Fe(II) in Rainwater. Environ. Sci. Technol. **37**: 4610–4616. doi:10.1021/es030345s

Kieber, R. J., S. A. Skrabal, B. J. Smith, and J. D. Willey. 2005. Organic Complexation of Fe(II) and Its Impact on the Redox Cycling of Iron in Rain. Environ. Sci. Technol. **39**: 1576–1583. doi:10.1021/es040439h

Kieber, R. J., K. Williams, J. D. Willey, S. Skrabal, and G. B. Avery. 2001a. Iron speciation in coastal rainwater: concentration and deposition to seawater. Mar. Chem. **73**: 83–95. doi:10.1016/S0304-4203(00)00097-9

Kieber, R. J., K. Williams, J. D. Willey, S. Skrabal, and G. B. Avery. 2001b. Iron speciation in coastal rainwater: concentration and deposition to seawater. Mar. Chem. **73**: 83–95. doi:10.1016/S0304-4203(00)00097-9

Kittu, L. R., A. J. Paul, M. Fernández-Méndez, M. J. Hopwood, and U. Riebesell. 2023. Coastal N2 fixation rates coincide spatially with N loss in the Humboldt Upwelling System off Peru. Global Biogeochem. Cycles e2022GB007578.

Koch, S. E., M. DesJardins, and P. J. Kocin. 1983. An interactive Barnes objective map analysis scheme for use with satellite and conventional data. J. Appl. Meteorol. Climatol. **22**: 1487–1503.

Krauskopf, K. B. 1956. Factors controlling the concentrations of thirteen rare metals in sea-water. Geochim. Cosmochim. Acta **9**: 1-B32.

Krisch, S., O. Huhn, A. Al-Hashem, M. J. Hopwood, P. Lodeiro, and E. P. Achterberg. 2022. Quantifying Ice-Sheet Derived Lead (Pb) Fluxes to the Ocean; A Case Study at Nioghalvfjerdsbræ. Geophys. Res. Lett. **49**: 1–13. doi:10.1029/2022GL100296

Kuhlbrodt, T., A. Griesel, M. Montoya, A. Levermann, M. Hofmann, and S. Rahmstorf. 2007. On the driving processes of the Atlantic meridional overturning circulation. Rev. Geophys. **45**. doi:10.1029/2004RG000166

Laes, A., S. Blain, P. Laan, S. J. Ussher, E. P. Achterberg, P. Tréguer, and H. J. W. De Baar. 2007. Sources and transport of dissolved iron and manganese along the continental margin of the Bay of Biscay. Biogeosciences **4**: 181–194.

Lam, P. J., and J. K. B. Bishop. 2008. The continental margin is a key source of iron to the HNLC North Pacific Ocean. Geophys. Res. Lett. **35**: 1–5. doi:10.1029/2008GL033294

Lam, P. J., M. I. Heller, P. E. Lerner, J. W. Moffett, and K. N. Buck. 2020. Unexpected Source and Transport of Iron from the Deep Peru Margin. ACS Earth Sp. Chem. **4**: 977–992. doi:10.1021/acsearthspacechem.0c00066

Lam, P. J., J. M. Lee, M. I. Heller, S. Mehic, Y. Xiang, and N. R. Bates. 2018. Size-fractionated distributions of suspended particle concentration and major phase composition from the U.S. GEOTRACES Eastern Pacific Zonal Transect (GP16). Mar. Chem. **201**: 90–107. doi:10.1016/j.marchem.2017.08.013

Landolfi, A., H. Dietze, W. Koeve, and A. Oschlies. 2013. Overlooked runaway feedback in the

marine nitrogen cycle: The vicious cycle. Biogeosciences **10**: 1351–1363. doi:10.5194/bg-10-1351-2013

Laraque, A., J. P. Bricquet, A. Pandi, and J. C. Olivry. 2009. A review of material transport by the Congo River and its tributaries. Hydrol. Process. **23**: 3216–3224. doi:10.1002/hyp.7395

Lass, H. U., and V. Mohrholz. 2008. On the interaction between the subtropical gyre and the Subtropical Cell on the shelf of the SE Atlantic. J. Mar. Syst. **74**: 1–43. doi:10.1016/j.jmarsys.2007.09.008

Lim, B., T. D. Jickells, J. L. Colin, and R. Losno. 1994. Solubilities of Al, Pb, Cu, and Zn in rain sampled in the marine environment over the North Atlantic Ocean and Mediterranean Sea. Global Biogeochem. Cycles **8**: 349–362. doi:10.1029/94GB01267

Lima, D. C. A., P. M. M. Soares, A. Semedo, R. M. Cardoso, W. Cabos, and D. V. Sein. 2019. How Will a Warming Climate Affect the Benguela Coastal Low-Level Wind Jet? J. Geophys. Res. Atmos. **124**: 5010–5028. doi:10.1029/2018JD029574

Little, S. H., D. Vance, C. Walker-Brown, and W. M. Landing. 2014. The oceanic mass balance of copper and zinc isotopes, investigated by analysis of their inputs, and outputs to ferromanganese oxide sediments. Geochim. Cosmochim. Acta **125**: 673–693. doi:10.1016/j.gca.2013.07.046

Liu, M., and T. Tanhua. 2021. Water masses in the Atlantic Ocean: Characteristics and distributions. Ocean Sci. **17**: 463–486. doi:10.5194/os-17-463-2021

Liu, T., S. Krisch, M. J. Hopwood, E. P. Achterberg, and A. Mutzberg. 2022a. Trace metal data from water samples during METEOR cruise M121.doi:10.1594/PANGAEA.947275

Liu, T., S. Krisch, R. C. Xie, M. J. Hopwood, M. Dengler, and E. P. Achterberg. 2022b. Sediment Release in the Benguela Upwelling System Dominates Trace Metal Input to the Shelf and Eastern South Atlantic Ocean. Global Biogeochem. Cycles **36**. doi:10.1029/2022GB007466

Liu, X., and F. J. Millero. 2002. The solubility of iron in seawater. Mar. Chem. **77**: 43–54. doi:10.1016/S0304-4203(01)00074-3

Lohan, M. C., and K. W. Bruland. 2008. Elevated Fe(II) and dissolved Fe in hypoxic shelf waters off Oregon and Washington: An enhanced source of iron to coastal upwelling regimes. Environ. Sci. Technol. **42**: 6462–6468. doi:10.1021/es800144j

Lohan, M. C., P. J. Statham, and D. W. Crawford. 2002. Total dissolved zinc in the upper water column of the subarctic North East Pacific. Deep Sea Res. Part II Top. Stud. Oceanogr. **49**: 5793–5808. doi:10.1016/S0967-0645(02)00215-1

Lorenzato, G., S. Tordo, B. van den Berg, H. M. Howells, and S. Sarmiento-Saher. 2022. Gas Flaring and Methane Emissions Facts and Trends, *In*.

Losno, R., J. L. Colin, N. Le Bris, G. Bergametti, T. Jickells, and B. Lim. 1993. Aluminium solubility in rainwater and molten snow. J. Atmos. Chem. **17**: 29–43. doi:10.1007/BF00699112

Lu, W., Y. Liu, J. Wang, and others. 2020. Global proliferation of offshore gas flaring areas. J. Maps **16**: 396–404.

Luyten, J. R., J. Pedlosky, and H. Stommel. 1983. The ventilated thermocline. J. Phys. Oceanogr.

**13**: 292–309.

Mackey, K. R. M., C.-T. Chien, A. F. Post, M. A. Saito, and A. Paytan. 2015. Rapid and gradual modes of aerosol trace metal dissolution in seawater. Front. Microbiol. **5**. doi:10.3389/fmicb.2014.00794

Mahowald, N., D. S. Ward, S. Kloster, and others. 2011. Aerosol impacts on climate and biogeochemistry. Annu. Rev. Environ. Resour. **36**: 45–74.

Manheim, F. T., and C. M. Lane-Bostwick. 1989. Chemical composition of ferromanganese crusts in the world ocean: a review and comprehensive database. First post.

Martin, J. H., and R. Michael Gordon. 1988. Northeast Pacific iron distributions in relation to phytoplankton productivity. Deep Sea Res. Part A. Oceanogr. Res. Pap. **35**: 177–196. doi:10.1016/0198-0149(88)90035-0

McManus, J., W. M. Berelson, S. Severmann, K. S. Johnson, D. E. Hammond, M. Roy, and K. H. Coale. 2012. Benthic manganese fluxes along the Oregon-California continental shelf and slope. Cont. Shelf Res. **43**: 71–85. doi:10.1016/j.csr.2012.04.016

Measures, C. I., and S. Vink. 2000. On the use of dissolved aluminum in surface waters to estimate dust deposition to the ocean. Global Biogeochem. Cycles **14**: 317–327.

Mercier, H., M. Arhan, and J. R. E. Lutjeharms. 2003. Upper-layer circulation in the eastern Equatorial and South Atlantic Ocean in January–March 1995. Deep Sea Res. Part I Oceanogr. Res. Pap. **50**: 863–887. doi:10.1016/S0967-0637(03)00071-2

Middag, R., H. J. W. Baar, and K. W. Bruland. 2019. The Relationships Between Dissolved Zinc and Major Nutrients Phosphate and Silicate Along the GEOTRACES GA02 Transect in the West Atlantic Ocean. Global Biogeochem. Cycles **33**: 63–84. doi:10.1029/2018GB006034

Middag, R., H. J. W. de Baar, K. W. Bruland, and S. M. A. C. van Heuven. 2020. The Distribution of Nickel in the West-Atlantic Ocean, Its Relationship With Phosphate and a Comparison to Cadmium and Zinc. Front. Mar. Sci. **7**: 1–17. doi:10.3389/fmars.2020.00105

Middag, R., S. M. A. C. van Heuven, K. W. Bruland, and H. J. W. de Baar. 2018. The relationship between cadmium and phosphate in the Atlantic Ocean unravelled. Earth Planet. Sci. Lett. **492**: 79–88. doi:10.1016/j.epsl.2018.03.046

Middag, R., J. M. Rolison, E. George, L. J. A. Gerringa, M. J. A. Rijkenberg, and C. H. Stirling. 2022. Basin scale distributions of dissolved manganese, nickel, zinc and cadmium in the Mediterranean Sea. Mar. Chem. **238**: 104063. doi:10.1016/J.MARCHEM.2021.104063

Millero, F. J., S. Sotolongo, and M. Izaguirre. 1987. The oxidation kinetics of Fe(II) in seawater. Geochim. Cosmochim. Acta **51**: 793–801. doi:10.1016/0016-7037(87)90093-7

Milne, A., C. Schlosser, B. D. Wake, E. P. Achterberg, R. Chance, A. R. Baker, A. Forryan, and M. C. Lohan. 2017. Particulate phases are key in controlling dissolved iron concentrations in the (sub)tropical North Atlantic. Geophys. Res. Lett. **44**: 2377–2387. doi:10.1002/2016GL072314

Moffett, J. W., and J. Ho. 1996. Oxidation of cobalt and manganese in seawater via a common microbially catalyzed pathway. Geochim. Cosmochim. Acta **60**: 3415–3424. doi:10.1016/0016-7037(96)00176-7

Mohrholz, V., C. H. Bartholomae, A. K. van der Plas, and H. U. Lass. 2008. The seasonal

variability of the northern Benguela undercurrent and its relation to the oxygen budget on the shelf. Cont. Shelf Res. **28**: 424–441. doi:10.1016/j.csr.2007.10.001

Mohrholz, V., A. Eggert, T. Junker, G. Nausch, T. Ohde, and M. Schmidt. 2014. Cross shelf hydrographic and hydrochemical conditions and their short term variability at the northern Benguela during a normal upwelling season. J. Mar. Syst. **140**: 92–110. doi:10.1016/J.JMARSYS.2014.04.019

Le Moigne, F. A. C., M. Boye, A. Masson, R. Corvaisier, E. Grossteffan, A. Guéneugues, and P. Pondaven. 2013. Description of the biogeochemical features of the subtropical southeastern Atlantic and the Southern Ocean south of South Africa during the austral summer of the International Polar Year. Biogeosciences **10**: 281–295.

Monteiro, P. M. S., and A. K. van der Plas. 2006. 5 Low oxygen water (LOW) variability in the Benguela system: Key processes and forcing scales relevant to forecasting, p. 71–90. *In* Large Marine Ecosystems. Elsevier.

Monterey, G. I., and L. M. DeWitt. 2000. Seasonal variability of global mixed layer depth from WOD98 temperature and salinity profiles. NOAA Tech. Memo. NMFS.

Moore, C. M. 2016a. Diagnosing oceanic nutrient deficiency. Philos. Trans. R. Soc. A Math. Phys. Eng. Sci. **374**: 20150290. doi:10.1098/rsta.2015.0290

Moore, C. M. 2016b. Diagnosing oceanic nutrient deficiency. Philos. Trans. R. Soc. A Math. Phys. Eng. Sci. **374**: 20150290. doi:10.1098/rsta.2015.0290

Moore, C. M., M. M. Mills, K. R. Arrigo, and others. 2013. Processes and patterns of oceanic nutrient limitation. Nat. Geosci. **6**: 701–710. doi:10.1038/ngeo1765

Moore, R. M., J. D. Burton, P. J. L. Williams, and M. L. Young. 1979. The behaviour of dissolved organic material, iron and manganese in estuarine mixing. Geochim. Cosmochim. Acta **43**: 919–926. doi:10.1016/0016-7037(79)90229-1

Moran, S. B., and R. M. Moore. 1991. The potential source of dissolved aluminum from resuspended sediments to the North Atlantic Deep Water. Geochim. Cosmochim. Acta **55**: 2745–2751. doi:10.1016/0016-7037(91)90441-7

Morel, F. M. M. 2003. The Biogeochemical Cycles of Trace Metals in the Oceans. Science (80-. ). **300**: 944–947. doi:10.1126/science.1083545

Morel, F. M. M., P. J. Lam, and M. A. Saito. 2020. Trace metal substitution in marine phytoplankton. Annu. Rev. Earth Planet. Sci. **48**: 491–517.

Morel, F. M. M., J. R. Reinfelder, S. B. Roberts, C. P. Chamberlain, J. G. Lee, and D. Yee. 1994. Zinc and carbon co-limitation of marine phytoplankton. Nature **369**: 740–742. doi:10.1038/369740a0

Mosley, L. M., and P. S. Liss. 2020. Particle aggregation, pH changes and metal behaviour during estuarine mixing: Review and integration. Mar. Freshw. Res. **71**: 300–310. doi:10.1071/MF19195

Nelson, L. V. S., R. Bay, C. Town, and others. 1996. The Benguela: Large Scale Features and Processes and System Variability. South Atl. 163–210. doi:10.1007/978-3-642-80353-6_9

Nickovic, S., A. Vukovic, and M. Vujadinovic. 2013. Atmospheric processing of iron carried by mineral dust. Atmos. Chem. Phys. **13**: 9169–9181.

Nishioka, J., and H. Obata. 2017. Dissolved iron distribution in the western and central subarctic Pacific: HNLC water formation and biogeochemical processes. Limnol. Oceanogr. **62**: 2004–2022.

NOAA NMFS SWFSC ERD (National Oceanic and Administration, National Marine Fisheries Service, Southwest Fisheries Science Center, E. R. D. Primary Productivity, Aqua MODIS, NPP, Global, 2003-present, EXPERIMENTAL (Monthly Composite) - Datasets - NOAA Data Catalog.

Noble, A. E., Y. Echegoyen-Sanz, E. A. Boyle, and others. 2015. Dynamic variability of dissolved Pb and Pb isotope composition from the US North Atlantic GEOTRACES transect. Deep Sea Res. Part II Top. Stud. Oceanogr. **116**: 208–225.

Noble, A. E., C. H. Lamborg, D. C. Ohnemus, and others. 2012. Basin-scale inputs of cobalt, iron, and manganese from the Benguela-Angola front to the South Atlantic Ocean. Limnol. Oceanogr. **57**: 989–1010. doi:10.4319/lo.2012.57.4.0989

Noble, A. E., D. C. Ohnemus, N. J. Hawco, P. J. Lam, and M. A. Saito. 2017. Coastal sources, sinks and strong organic complexation of dissolved cobalt within the US North Atlantic GEOTRACES transect GA03. Biogeosciences **14**: 2715–2739. doi:10.5194/bg-14-2715-2017

Noffke, A., C. Hensen, S. Sommer, F. Scholz, L. Bohlen, T. Mosch, M. Graco, and K. Wallmann. 2012. Benthic iron and phosphorus fluxes across the Peruvian oxygen minimum zone. Limnol. Oceanogr. **57**: 851–867. doi:10.4319/lo.2012.57.3.0851

NRIAGU, J. O. 1979. Global inventory of natural and anthropogenic emissions of trace metals to the atmosphere. Nature **279**: 409–411. doi:10.1038/279409a0

Ohnemus, D. C., M. E. Auro, R. M. Sherrell, M. Lagerström, P. L. Morton, B. S. Twining, S. Rauschenberg, and P. J. Lam. 2014. Laboratory intercomparison of marine particulate digestions including Piranha: a novel chemical method for dissolution of polyethersulfone filters. Limnol. Oceanogr. Methods **12**: 530–547. doi:10.4319/lom.2014.12.530

Okubo, A. 1971. Oceanic diffusion diagrams. Deep. Res. Oceanogr. Abstr. **18**: 789–802. doi:10.1016/0011-7471(71)90046-5

Olivelli, A., K. Murphy, L. Bridgestock, and others. 2023. Decline of anthropogenic lead in South Atlantic Ocean surface waters from 1990 to 2011: New constraints from concentration and isotope data. Mar. Pollut. Bull. **189**: 114798.

Orians, K. J., and K. W. Bruland. 1985. Dissolved aluminium in the central North Pacific. Nature **316**: 427–429. doi:10.1038/316427a0

Pacyna, J. M., and E. G. Pacyna. 2001. An assessment of global and regional emissions of trace metals to the atmosphere from anthropogenic sources worldwide. Environ. Rev. **9**: 269–298. doi:10.1139/a01-012

Paerl, H. W., J. D. Willey, M. Go, B. L. Peierls, J. L. Pinckney, and M. L. Fogel. 1999. Rainfall stimulation of primary production in western Atlantic Ocean waters: roles of different nitrogen sources and co-limiting nutrients. Mar. Ecol. Prog. Ser. **176**: 205–214. doi:10.3354/meps176205

Pakhomova, S. V., P. O. J. Hall, M. Y. Kononets, A. G. Rozanov, A. Tengberg, and A. V. Vershinin. 2007. Fluxes of iron and manganese across the sediment-water interface under

various redox conditions. Mar. Chem. **107**: 319–331. doi:10.1016/j.marchem.2007.06.001

Pardo, P. C., X. A. Padín, M. Gilcoto, L. Farina-Busto, and F. F. Pérez. 2011. Evolution of upwelling systems coupled to the long-term variability in sea surface temperature and Ekman transport. Clim. Res. **48**: 231–246. doi:10.3354/cr00989

Parker, D. L., T. Morita, M. L. Mozafarzadeh, R. Verity, J. K. McCarthy, and B. M. Tebo. 2007. Inter-relationships of MnO2 precipitation, siderophore–Mn(III) complex formation, siderophore degradation, and iron limitation in Mn(II)-oxidizing bacterial cultures. Geochim. Cosmochim. Acta **71**: 5672–5683. doi:10.1016/J.GCA.2007.03.042

Patey, M. D., M. J. A. A. Rijkenberg, P. J. Statham, M. C. Stinchcombe, E. P. Achterberg, and M. Mowlem. 2008. Determination of nitrate and phosphate in seawater at nanomolar concentrations. TrAC Trends Anal. Chem. **27**: 169–182. doi:10.1016/j.trac.2007.12.006

Peterson, R. G., and L. Stramma. 1991. Upper-level circulation in the South Atlantic Ocean. Prog. Oceanogr. **26**: 1–73. doi:10.1016/0079-6611(91)90006-8

Pilson, M. E. Q. 2012. An Introduction to the Chemistry of the Sea, cambridge university press.

Plass, A., A. W. Dale, and F. Scholz. 2021. Sedimentary cycling and benthic fluxes of manganese, cobalt, nickel, copper, zinc and cadmium in the Peruvian oxygen minimum zone. Mar. Chem. 103982. doi:10.1016/j.marchem.2021.103982

Plass, A., C. Schlosser, S. Sommer, A. W. Dale, E. P. Achterberg, and F. Scholz. 2020. The control of hydrogen sulfide on benthic iron and cadmium fluxes in the oxygen minimum zone off Peru. Biogeosciences **17**: 3685–3704. doi:10.5194/bg-17-3685-2020

Pohl, C., P. L. Croot, U. Hennings, T. Daberkow, G. Budeus, and M. R. v.d. Loeff. 2011. Synoptic transects on the distribution of trace elements (Hg, Pb, Cd, Cu, Ni, Zn, Co, Mn, Fe, and Al) in surface waters of the Northern- and Southern East Atlantic. J. Mar. Syst. **84**: 28–41. doi:10.1016/J.JMARSYS.2010.08.003

Rae, C. D. 2005. A demonstration of the hydrographic partition of the Benguela upwelling ecosystem at 26°40'S. African J. Mar. Sci. **27**: 617–628. doi:10.2989/18142320509504122

Rahlf, P., G. Laukert, E. C. Hathorne, L. H. Vieira, and M. Frank. 2021. Dissolved neodymium and hafnium isotopes and rare earth elements in the Congo River Plume: Tracing and quantifying continental inputs into the southeast Atlantic. Geochim. Cosmochim. Acta **294**: 192–214. doi:10.1016/j.gca.2020.11.017

Rapp, I., C. Schlosser, T. J. Browning, F. Wolf, F. A. C. Le Moigne, M. Gledhill, and E. P. Achterberg. 2020. El Niño-Driven Oxygenation Impacts Peruvian Shelf Iron Supply to the South Pacific Ocean. Geophys. Res. Lett. **47**. doi:10.1029/2019GL086631

Rapp, I., C. Schlosser, J.-L. Menzel Barraqueta, and others. 2019. Controls on redox-sensitive trace metals in the Mauritanian oxygen minimum zone. Biogeosciences **16**: 4157–4182. doi:10.5194/bg-16-4157-2019

Rapp, I., C. Schlosser, D. Rusiecka, M. Gledhill, and E. P. Achterberg. 2017. Automated preconcentration of Fe, Zn, Cu, Ni, Cd, Pb, Co, and Mn in seawater with analysis using high-resolution sector field inductively-coupled plasma mass spectrometry. Anal. Chim. Acta **976**: 1–13. doi:10.1016/j.aca.2017.05.008

Raven, J. A., M. C. W. Evans, and R. E. Korb. 1999. The role of trace metals in photosynthetic

electron transport in O 2-evolving organisms. Photosynth. Res. **60**: 111–150.

Raven, M. R., R. G. Keil, and S. M. Webb. 2021. Microbial sulfate reduction and organic sulfur formation in sinking marine particles. Science (80-. ). **371**: 178–181.

Resing, J. A., P. N. Sedwick, C. R. German, W. J. Jenkins, J. W. Moffett, B. M. Sohst, and A. Tagliabue. 2015. Basin-scale transport of hydrothermal dissolved metals across the South Pacific Ocean. Nature **523**: 200–203. doi:10.1038/nature14577

Reza, R., and G. Singh. 2010. Heavy metal contamination and its indexing approach for river water. Int. J. Environ. Sci. Technol. **7**: 785–792.

Rickes, E. L., N. G. Brink, F. R. Koniuszy, T. R. Wood, and K. Folkers. 1948. Vitamin B12, a cobalt complex. Science (80-. ). **108**: 134.

Roshan, S., T. DeVries, J. Wu, and G. Chen. 2018. The Internal Cycling of Zinc in the Ocean. Global Biogeochem. Cycles **32**: 1833–1849. doi:10.1029/2018GB006045

Roshan, S., and J. Wu. 2015a. Cadmium regeneration within the North Atlantic. Global Biogeochem. Cycles **29**: 2082–2094. doi:10.1002/2015GB005215

Roshan, S., and J. Wu. 2015b. The distribution of dissolved copper in the tropical-subtropical north Atlantic across the GEOTRACES GA03 transect. Mar. Chem. **176**: 189–198. doi:10.1016/j.marchem.2015.09.006

Roshan, S., J. Wu, and T. DeVries. 2017. Controls on the Cadmium-Phosphate Relationship in the Tropical South Pacific. Global Biogeochem. Cycles **31**: 1516–1527. doi:10.1002/2016GB005556

Roshan, S., J. Wu, and W. J. Jenkins. 2016. Long-range transport of hydrothermal dissolved Zn in the tropical South Pacific. Mar. Chem. **183**: 25–32.

Rudnick, R. L., and S. Gao. 2014. Composition of the Continental Crust, p. 1–51. *In* Treatise on Geochemistry. Elsevier.

Rusiecka, D., M. Gledhill, A. Milne, and others. 2018. Anthropogenic signatures of lead in the Northeast Atlantic. Geophys. Res. Lett. **45**: 2734–2743.

Ryan-Keogh, T. J., A. I. Macey, M. C. Nielsdóttir, and others. 2013. Spatial and temporal development of phytoplankton iron stress in relation to bloom dynamics in the high-latitude North Atlantic Ocean. Limnol. Oceanogr. **58**: 533–545. doi:10.4319/lo.2013.58.2.0533

Saito, M. A., J. W. Moffett, S. W. Chisholm, and J. B. Waterbury. 2002. Cobalt limitation and uptake in Prochlorococcus. Limnol. Oceanogr. **47**: 1629–1636. doi:10.4319/lo.2002.47.6.1629

Saito, M. A., G. Rocap, and J. W. Moffett. 2005. Production of cobalt binding ligands in a Synechococcus feature at the Costa Rica upwelling dome. Limnol. Oceanogr. **50**: 279–290. doi:10.4319/lo.2005.50.1.0279

Samanta, S., and T. K. Dalai. 2018. Massive production of heavy metals in the Ganga (Hooghly) River estuary, India: Global importance of solute-particle interaction and enhanced metal fluxes to the oceans. Geochim. Cosmochim. Acta **228**: 243–258.

Sanial, V., L. E. Kipp, P. B. Henderson, and others. 2018. Radium-228 as a tracer of dissolved trace element inputs from the Peruvian continental margin. Mar. Chem. **201**: 20–34. doi:10.1016/j.marchem.2017.05.008

Schlitzer, R. 2020. Ocean Data View. http://odv.awi.de.

Schlosser, C., J. Karstensen, and E. M. S. Woodward. 2019. Distribution of dissolved and leachable particulate Pb in the water column along the GEOTRACES section GA10 in the South Atlantic. Deep. Res. Part I Oceanogr. Res. Pap. **148**: 132–142. doi:10.1016/j.dsr.2019.05.001

Schlosser, C., J. K. Klar, B. D. Wake, and others. 2014. Seasonal ITCZ migration dynamically controls the location of the (sub)tropical Atlantic biogeochemical divide. Proc. Natl. Acad. Sci. U. S. A. **111**: 1438–1442. doi:10.1073/pnas.1318670111

Schmidt, S. B., P. E. Jensen, and S. Husted. 2016. Manganese Deficiency in Plants: The Impact on Photosystem II. Trends Plant Sci. **21**: 622–632. doi:10.1016/J.TPLANTS.2016.03.001

Schneider, T., T. Bischoff, and G. H. Haug. 2014. Migrations and dynamics of the intertropical convergence zone. Nature **513**: 45–53. doi:10.1038/nature13636

Scholz, F., C. R. Löscher, A. Fiskal, and others. 2016. Nitrate-dependent iron oxidation limits iron transport in anoxic ocean regions. Earth Planet. Sci. Lett. **454**: 272–281. doi:10.1016/j.epsl.2016.09.025

Scholz, F., J. Mcmanus, A. C. Mix, C. Hensen, and R. R. Schneider. 2014. The impact of ocean deoxygenation on iron release from continental margin sediments. Nat. Geosci. **7**: 433–437. doi:10.1038/ngeo2162

Schroller-Lomnitz, U., C. Hensen, A. W. Dale, F. Scholz, D. Clemens, S. Sommer, A. Noffke, and K. Wallmann. 2019. Dissolved benthic phosphate, iron and carbon fluxes in the Mauritanian upwelling system and implications for ongoing deoxygenation. Deep Sea Res. Part I Oceanogr. Res. Pap. **143**: 70–84. doi:10.1016/j.dsr.2018.11.008

Sedwick, P. N., E. R. Sholkovitz, and T. M. Church. 2007. Impact of anthropogenic combustion emissions on the fractional solubility of aerosol iron: Evidence from the Sargasso Sea. Geochemistry, Geophys. Geosystems **8**.

Severmann, S., J. McManus, W. M. Berelson, and D. E. Hammond. 2010. The continental shelf benthic iron flux and its isotope composition. Geochim. Cosmochim. Acta **74**: 3984–4004. doi:10.1016/J.GCA.2010.04.022

Shannon, L. V, and A. J. B. G. B. Brundrie. 1986. On the existence of an EI Nifto-type phenomenon in the Benguela System. J. Mar. Res. **44**: 495–520.

Shaw, T. J., J. M. Gieskes, and R. A. Jahnke. 1990. Early diagenesis in differing depositional environments: The response of transition metals in pore water. Geochim. Cosmochim. Acta **54**: 1233–1246. doi:10.1016/0016-7037(90)90149-F

Shelley, R. U., M. Roca-Martí, M. Castrillejo, and others. 2017. Quantification of trace element atmospheric deposition fluxes to the Atlantic Ocean ( > 40°N; GEOVIDE, GEOTRACES GA01) during spring 2014. Deep Sea Res. Part I Oceanogr. Res. Pap. **119**: 34–49. doi:10.1016/j.dsr.2016.11.010

Sherrell, R. M., E. A. Boyle, and B. Hamelin. 1992. Isotopic equilibration between dissolved and suspended particulate lead in the Atlantic Ocean: Evidence from 210Pb and stable Pb isotopes. J. Geophys. Res. Ocean. **97**: 11257–11268.

Shi, Z., M. D. Krom, T. D. Jickells, S. Bonneville, K. S. Carslaw, N. Mihalopoulos, A. R. Baker,

and L. G. Benning. 2012. Impacts on iron solubility in the mineral dust by processes in the source region and the atmosphere: A review. Aeolian Res. **5**: 21–42. doi:10.1016/J.AEOLIA.2012.03.001

Shillington, F. A., C. J. C. Reason, C. M. Duncombe Rae, P. Florenchie, and P. Penven. 2006. 4 Large scale physical variability of the Benguela Current Large Marine Ecosystem (BCLME), p. 49–70. *In* Large Marine Ecosystems.

Sholkovitz, E. R. 1978. The flocculation of dissolved Fe, Mn, Al, Cu, NI, Co and Cd during estuarine mixing. Earth Planet. Sci. Lett. **41**: 77–86.

Siedlecki, S. A., A. Mahadevan, and D. E. Archer. 2012. Mechanism for export of sediment-derived iron in an upwelling regime. Geophys. Res. Lett. **39**. doi:10.1029/2011GL050366

de Souza, G. F., D. Vance, M. Sieber, T. M. Conway, and S. H. Little. 2022. Re-assessing the influence of particle-hosted sulphide precipitation on the marine cadmium cycle. Geochim. Cosmochim. Acta **322**: 274–296. doi:10.1016/J.GCA.2022.02.009

Stein, A. F., R. R. Draxler, G. D. Rolph, B. J. B. Stunder, M. D. Cohen, and F. Ngan. 2015. NOAA's HYSPLIT atmospheric transport and dispersion modeling system. Bull. Am. Meteorol. Soc. **96**: 2059–2077.

Steinfeldt, R., J. Sültenfuß, M. Dengler, T. Fischer, and M. Rhein. 2015. Coastal upwelling off Peru and Mauritania inferred from helium isotope disequilibrium. Biogeosciences **12**: 7519–7533. doi:10.5194/bg-12-7519-2015

Stichel, T., S. Kretschmer, W. Geibert, M. Lambelet, Y. Plancherel, M. Rutgers van der Loeff, and T. van de Flierdt. 2020. Particle–Seawater Interaction of Neodymium in the North Atlantic. ACS Earth Sp. Chem. **4**: 1700–1717. doi:10.1021/acsearthspacechem.0c00034

Stramma, L., and Mathew England. 1999. On the water masses and mean circulation of the South Atlantic Ocean. J. Geophys. Res. **104**: 20,863-20,883.

Sunda, W. G., and S. A. Huntsman. 1994. Photoreduction of manganese oxides in seawater. Mar. Chem. **46**: 133–152. doi:10.1016/0304-4203(94)90051-5

Sunda, W. G., S. Huntsman, and G. Harvey. 1983. Photoreduction of manganese oxides in seawater and its geochemical and biological implications. Nature **301**: 234–236. doi:10.1038/301234a0

Tagliabue, A., O. Aumont, and L. Bopp. 2014. The impact of different external sources of iron on the global carbon cycle. Geophys. Res. Lett. **41**: 920–926. doi:10.1002/2013GL059059

Tagliabue, A., A. R. Bowie, T. DeVries, and others. 2019. The interplay between regeneration and scavenging fluxes drives ocean iron cycling. Nat. Commun. **10**: 1–8. doi:10.1038/s41467-019-12775-5

Tagliabue, A., N. J. Hawco, R. M. Bundy, W. M. Landing, A. Milne, P. L. Morton, and M. A. Saito. 2018. The Role of External Inputs and Internal Cycling in Shaping the Global Ocean Cobalt Distribution: Insights From the First Cobalt Biogeochemical Model. Global Biogeochem. Cycles **32**: 594–616. doi:10.1002/2017GB005830

Takata, H., T. Aono, K. Tagami, and S. Uchida. 2010. Processes controlling cobalt distribution in two temperate estuaries, Sagami Bay and Wakasa Bay, Japan. Estuar. Coast. Shelf Sci. **89**: 294–305. doi:10.1016/J.ECSS.2010.08.003

Thuróczy, C.-E., M. Boye, and R. Losno. 2010. Dissolution of cobalt and zinc from natural and anthropogenic dusts in seawater. Biogeosciences **7**: 1927–1936. doi:10.5194/bg-7-1927-2010

Timmermans, K. R., W. Stolte, and H. J. W. De Baar. 1994. Iron-mediated effects on nitrate reductase in marine phytoplankton. Mar. Biol. **121**: 389–396.

Twining, B. S., and S. B. Baines. 2013. The trace metal composition of marine phytoplankton. Ann. Rev. Mar. Sci. **5**: 191–215. doi:10.1146/annurev-marine-121211-172322

Twining, B. S., S. Rauschenberg, P. L. Morton, and S. Vogt. 2015. Metal contents of phytoplankton and labile particulate material in the North Atlantic Ocean. Prog. Oceanogr. **137**: 261–283. doi:10.1016/J.POCEAN.2015.07.001

Uzoekwe, S. A., Sylvester, C. Izah, Ayobami, and O. Aigberua. 2021. Environmental and human health risk of heavy metals in atmospheric particulate matter (PM10) around gas flaring vicinity in Bayelsa State, Nigeria. **13**: 323–335. doi:10.1007/s13530-021-00085-7

Vangriesheim, A., C. Pierre, A. Aminot, N. Metzl, F. Baurand, and J. C. Caprais. 2009. The influence of Congo River discharges in the surface and deep layers of the Gulf of Guinea. Deep. Res. Part II Top. Stud. Oceanogr. **56**: 2183–2196. doi:10.1016/j.dsr2.2009.04.002

Veitch, J., P. Penven, and F. Shillington. 2010. Modeling equilibrium dynamics of the Benguela current system. J. Phys. Oceanogr. **40**: 1942–1964. doi:10.1175/2010JPO4382.1

Ventura, A., E. F. C. Simões, A. S. Almeida, R. Martins, A. C. Duarte, S. Loureiro, and R. M. B. O. Duarte. 2021. Deposition of Aerosols onto Upper Ocean and Their Impacts on Marine Biota. Atmosphere (Basel). **12**: 684. doi:10.3390/atmos12060684

Verhoef, A., M. Portabella, and A. Stoffelen. 2012. High-resolution ASCAT scatterometer winds near the coast. IEEE Trans. Geosci. Remote Sens. **50**: 2481–2487.

Vieira, L. H., S. Krisch, M. J. Hopwood, A. J. Beck, J. Scholten, V. Liebetrau, and E. P. Achterberg. 2020. Unprecedented Fe delivery from the Congo River margin to the South Atlantic Gyre. Nat. Commun. **11**: 556. doi:10.1038/s41467-019-14255-2

Vohra, K., E. A. Marais, W. J. Bloss, J. Schwartz, L. J. Mickley, M. Van Damme, L. Clarisse, and P.-F. Coheur. 2022. Rapid rise in premature mortality due to anthropogenic air pollution in fast-growing tropical cities from 2005 to 2018. Sci. Adv. **8**: eabm4435.

Wallmann, K., Y. S. José, M. J. Hopwood, C. J. Somes, A. W. Dale, F. Scholz, E. P. Achterberg, and A. Oschlies. 2022. Biogeochemical feedbacks may amplify ongoing and future ocean deoxygenation: a case study from the Peruvian oxygen minimum zone. Biogeochemistry. doi:10.1007/s10533-022-00908-w

White, W. M., and E. M. Klein. 2013. Composition of the Oceanic Crust, 2nd ed. Elsevier Ltd.

Wilke, R. J., and R. Dayal. 1982. The behavior of iron, manganese and silicon in the Peconic River estuary, New York. Estuar. Coast. Shelf Sci. **15**: 577–586.

Willey, J. D., R. J. Kieber, J. J. Humphreys, B. C. Rice, M. J. Hopwood, G. B. Avery, and R. N. Mead. 2015. The role of fossil fuel combustion on the stability of dissolved iron in rainwater. Atmos. Environ. **107**: 187–193. doi:10.1016/J.ATMOSENV.2015.02.033

Wu, B., D. Y. Zhao, H. Y. Jia, Y. Zhang, X. X. Zhang, and S. P. Cheng. 2009. Preliminary risk assessment of trace metal pollution in surface water from Yangtze River in Nanjing Section,

China. Bull. Environ. Contam. Toxicol. **82**: 405–409.

Wu, J., and E. A. Boyle. 1997. Lead in the western North Atlantic Ocean: Completed response to leaded gasoline phaseout. Geochim. Cosmochim. Acta **61**: 3279–3283. doi:10.1016/S0016-7037(97)89711-6

Wu, M., J. S. P. McCain, E. Rowland, R. Middag, M. Sandgren, A. E. Allen, and E. M. Bertrand. 2019. Manganese and iron deficiency in Southern Ocean Phaeocystis antarctica populations revealed through taxon-specific protein indicators. Nat. Commun. **10**: 1–10. doi:10.1038/s41467-019-11426-z

Wuttig, K., A. T. Townsend, P. van der Merwe, and others. 2019. Critical evaluation of a seaFAST system for the analysis of trace metals in marine samples. Talanta **197**: 653–668. doi:10.1016/j.talanta.2019.01.047

Wuttig, K., T. Wagener, M. Bressac, A. Dammshäuser, P. Streu, C. Guieu, and P. L. Croot. 2013. Impacts of dust deposition on dissolved trace metal concentrations (Mn, Al and Fe) during a mesocosm experiment. Biogeosciences **10**: 2583–2600. doi:10.5194/bg-10-2583-2013

Wyatt, N. J., A. Milne, E. M. S. Woodward, A. P. Rees, T. J. Browning, H. A. Bouman, P. J. Worsfold, and M. C. Lohan. 2014. Biogeochemical cycling of dissolved zinc along the GEOTRACES South Atlantic transect GA10 at 40 S. Global Biogeochem. Cycles **28**: 44–56.

Xiang, Y., and P. J. Lam. 2020. Size-Fractionated Compositions of Marine Suspended Particles in the Western Arctic Ocean: Lateral and Vertical Sources. J. Geophys. Res. Ocean. **125**: 1–9. doi:10.1029/2020JC016144

Xie, R. C., S. J. G. Galer, W. Abouchami, M. J. A. Rijkenberg, J. De Jong, H. J. W. De Baar, and M. O. Andreae. 2015. The cadmium-phosphate relationship in the western South Atlantic - The importance of mode and intermediate waters on the global systematics. Mar. Chem. **177**: 110–123. doi:10.1016/j.marchem.2015.06.011

Xie, R. C., M. Rehkämper, P. Grasse, T. van de Flierdt, M. Frank, and Z. Xue. 2019. Isotopic evidence for complex biogeochemical cycling of Cd in the eastern tropical South Pacific. Earth Planet. Sci. Lett. **512**: 134–146. doi:10.1016/j.epsl.2019.02.001

Yee, D., and F. M. M. Morel. 1996. In vivo substitution of zinc by cobalt in carbonic anhydrase of a marine diatom. Limnol. Oceanogr. **41**: 573–577. doi:https://doi.org/10.4319/lo.1996.41.3.0573

Zeller, D., M. L. D. Palomares, A. Tavakolie, and others. 2016. Still catching attention: Sea Around Us reconstructed global catch data, their spatial expression and public accessibility. Mar. Policy **70**: 145–152. doi:10.1016/J.MARPOL.2016.04.046

Zhang, Z., Y. Yu, E. C. Hathorne, L. H. Vieira, P. Grasse, C. Siebert, P. Ralf, and M. Frank. Decoupling of Barium and Silicon at the Congo River-dominated Southeast Atlantic Margin: Insights from Combined Barium and Silicon isotopes (under review). Global Biogeochem. Cycles.

Zhu, K., M. J. Hopwood, J. E. Groenenberg, A. Engel, E. P. Achterberg, and M. Gledhill. 2021. Influence of pH and Dissolved Organic Matter on Iron Speciation and Apparent Iron Solubility in the Peruvian Shelf and Slope Region. Environ. Sci. Technol.

doi:10.1021/acs.est.1c02477

Zitoun, R., E. P. Achterberg, T. J. Browning, L. J. Hoffmann, S. Krisch, S. G. Sander, and A. Koschinsky. 2021. The complex provenance of Cu-binding ligands in the South-East Atlantic. Mar. Chem. **237**: 104047. doi:10.1016/j.marchem.2021.104047

Achterberg, E. P., and C. M. G. Van Den Berg. 1997. Chemical speciation of chromium and nickel in the western Mediterranean. Deep Sea Res. Part II Top. Stud. Oceanogr. **44**: 693–720. doi:10.1016/S0967-0645(96)00086-0

Achterberg, E. P., S. Steigenberger, J. K. Klar, and others. 2020. Trace element biogeochemistry in the high latitude North Atlantic Ocean: seasonal variations and volcanic inputs. Global Biogeochem. Cycles 0–3. doi:10.1016/B978-0-08-095975-7.00602-1

Al-Hashem, A. A., A. Beck, and E. P. Achterberg. 2022. Labile, Refractory, and Total Particulate Trace Metal Concentrations from the GEOTRACES GA08 Shelf section and 3-degree Latitudinal transect.doi:10.1594/PANGAEA.945498

Al-Hashem, A. A., A. J. Beck, S. Krisch, J.-L. Menzel Barraqueta, T. Steffens, and E. P. Achterberg. 2022. Particulate Trace Metal Sources, Cycling, and Distributions on the Southwest African Shelf. Global Biogeochem. Cycles **36**. doi:10.1029/2022GB007453

Alsdorf, D., E. Beighley, A. Laraque, and others. 2016. Opportunities for hydrologic research in the Congo Basin. Rev. Geophys. **54**: 378–409. doi:10.1002/2016RG000517

Amante, C., and B. W. Eakins. 2009. ETOPO1 arc-minute global relief model: procedures, data sources and analysis.

Annegarn, H. ., R. . Van Grieken, D. . Bibby, and F. Von Blottnitz. 1983. Background aerosol composition in the namib desert, South West Africa (Namibia). Atmos. Environ. **17**: 2045–2053. doi:10.1016/0004-6981(83)90361-X

Arrigo, K. R. 2005. Marine microorganisms and global nutrient cycles. Nature **437**: 349–355.

De Baar, H. J. W. 2001. Distributions, sources and sinks of iron in seawater. Biogeochem. iron seawater.

Baars, O., W. Abouchami, S. J. G. Galer, M. Boye, and P. L. Croot. 2014. Dissolved cadmium in the Southern Ocean: Distribution, speciation, and relation to phosphate. Limnol. Oceanogr. **59**: 385–399. doi:10.4319/lo.2014.59.2.0385

Bacon, M. P., D. W. Spencer, and P. G. Brewer. 1976. 210Pb/226Ra and 210Po/210Pb disequilibria in seawater and suspended particulate matter. Earth Planet. Sci. Lett. **32**: 277–296.

Baker, A. R., C. Adams, T. G. Bell, T. D. Jickells, and L. Ganzeveld. 2013. Estimation of atmospheric nutrient inputs to the Atlantic Ocean from 50°N to 50°S based on large-scale field sampling: Iron and other dust-associated elements. Global Biogeochem. Cycles **27**: 755–767. doi:10.1002/gbc.20062

Baker, A. R., and P. L. Croot. 2010. Atmospheric and marine controls on aerosol iron solubility in seawater. Mar. Chem. **120**: 4–13. doi:10.1016/j.marchem.2008.09.003

Baker, A. R., T. D. Jickells, M. Witt, and K. L. Linge. 2006. Trends in the solubility of iron, aluminium, manganese and phosphorus in aerosol collected over the Atlantic Ocean. Mar. Chem. **98**: 43–58. doi:10.1016/j.marchem.2005.06.004

Balls, P. W. 1989. The partition of trace metals between dissolved and particulate phases in european coastal waters: A compilation of field data and comparison with laboratory studies. Netherlands J. Sea Res. **23**: 7–14. doi:10.1016/0077-7579(89)90037-9

Balzano, S., P. J. Statham, R. D. Pancost, and J. R. Lloyd. 2009. Role of microbial populations in the release of reduced iron to the water column from marine aggregates. Aquat. Microb. Ecol. **54**: 291–303.

Barraqueta, J. L. M., J. Klar, M. Gledhill, and others. 2019. Atmospheric deposition fluxes over the Atlantic Ocean: A GEOTRACES case study. Biogeosciences **16**: 1525–1542. doi:10.5194/bg-16-1525-2019

Barraqueta, J. L. M., C. Schlosser, H. Planquette, and others. 2018. Aluminium in the North Atlantic Ocean and the Labrador Sea (GEOTRACES GA01 section): roles of continental inputs and biogenic particle removal. Biogeosciences **15**: 5271–5286.

Barrett, P. M., J. A. Resing, N. J. Buck, C. S. Buck, W. M. Landing, and C. I. Measures. 2012. The trace element composition of suspended particulate matter in the upper 1000 m of the eastern North Atlantic Ocean: A16N. Mar. Chem. **142**–**144**: 41–53. doi:10.1016/J.MARCHEM.2012.07.006

Berger, C. J. M., S. M. Lippiatt, M. G. Lawrence, and K. W. Bruland. 2008. Application of a chemical leach technique for estimating labile particulate aluminum, iron, and manganese in the Columbia River plume and coastal waters off Oregon and Washington. J. Geophys. Res. **113**: 1–16. doi:10.1029/2007jc004703

Bergquist, B. A., and E. A. Boyle. 2006. Dissolved iron in the tropical and subtropical Atlantic Ocean. Global Biogeochem. Cycles **20**: 1–14. doi:10.1029/2005GB002505

Berman-Frank, I., A. Quigg, Z. V Finkel, A. J. Irwin, and L. Haramaty. 2007. Nitrogen-fixation strategies and Fe requirements in cyanobacteria. Limnol. Oceanogr. **52**: 2260–2269.

Best, J. 2019. Anthropogenic stresses on the world's big rivers. Nat. Geosci. **12**: 7–21. doi:10.1038/s41561-018-0262-x

Biller, D. V., and K. W. Bruland. 2013. Sources and distributions of Mn, Fe, Co, Ni, Cu, Zn, and Cd relative to macronutrients along the central California coast during the spring and summer upwelling season. Mar. Chem. **155**: 50–70. doi:10.1016/j.marchem.2013.06.003

Biscéré, T., C. Ferrier-Pagès, R. Grover, A. Gilbert, C. Rottier, A. Wright, C. Payri, and F. Houlbrèque. 2018. Enhancement of coral calcification via the interplay of nickel and urease. Aquat. Toxicol. **200**: 247–256.

Black, E. E., P. J. Lam, J. -M. Lee, and K. O. Buesseler. 2019. Insights From the 238 U- 234 Th Method Into the Coupling of Biological Export and the Cycling of Cadmium, Cobalt, and Manganese in the Southeast Pacific Ocean. Global Biogeochem. Cycles **33**: 15–36. doi:10.1029/2018GB005985

Bonfils, C. J. W., B. D. Santer, J. C. Fyfe, K. Marvel, T. J. Phillips, and S. R. H. Zimmerman. 2020. Human influence on joint changes in temperature, rainfall and continental aridity. Nat. Clim. Chang. **10**: 726–731. doi:10.1038/s41558-020-0821-1

Bonnet, S., and C. Guieu. 2006. Atmospheric forcing on the annual iron cycle in the western Mediterranean Sea: A 1-year survey. J. Geophys. Res. Ocean. **111**.

Borchers, S. L., B. Schnetger, P. Böning, and H.-J. J. Brumsack. 2005. Geochemical signatures of the Namibian diatom belt: Perennial upwelling and intermittent anoxia. Geochemistry, Geophys. Geosystems **6**: 6006. doi:10.1029/2004GC000886

Bordbar, M. H., V. Mohrholz, and M. Schmidt. 2021. The relation of wind-driven coastal and offshore upwelling in the Benguela Upwelling System. J. Phys. Oceanogr. **51**: 3117–3133. doi:10.1175/JPO-D-20-0297.1

Bown, J., M. Boye, A. Baker, and others. 2011. The biogeochemical cycle of dissolved cobalt in the Atlantic and the Southern Ocean south off the coast of South Africa. Mar. Chem. **126**: 193–206. doi:10.1016/j.marchem.2011.03.008

Boyd, P. W., and M. J. Ellwood. 2010. The biogeochemical cycle of iron in the ocean. Nat. Geosci. **3**: 675–682. doi:10.1038/ngeo964

Boyd, P. W., M. J. Ellwood, A. Tagliabue, and B. S. Twining. 2017. Biotic and abiotic retention, recycling and remineralization of metals in the ocean. Nat. Geosci. **10**: 167–173. doi:10.1038/ngeo2876

Boyd, P. W., E. Ibisanmi, S. G. Sander, K. A. Hunter, and G. A. Jackson. 2010. Remineralization of upper ocean particles: Implications for iron biogeochemistry. Limnol. Oceanogr. **55**: 1271–1288. doi:10.4319/lo.2010.55.3.1271

Boyd, P. W., T. Jickells, C. S. Law, and others. 2007. Mesoscale iron enrichment experiments 1993-2005: Synthesis and future directions. Science (80-. ). **315**: 612–617. doi:10.1126/science.1131669

Boyd, P. W., C. S. Law, D. A. Hutchins, and others. 2005. FeCycle: Attempting an iron biogeochemical budget from a mesoscale SF 6 tracer experiment in unperturbed low iron waters. Global Biogeochem. Cycles **19**: n/a-n/a. doi:10.1029/2005GB002494

Boye, M., B. D. Wake, P. Lopez Garcia, J. Bown, A. R. Baker, and E. P. Achterberg. 2012. Distributions of dissolved trace metals (Cd, Cu, Mn, Pb, Ag) in the southeastern Atlantic and the Southern Ocean. Biogeosciences **9**: 3231–3246. doi:10.5194/bg-9-3231-2012

Boyle, E. A. 1988. Cadmium: Chemical tracer of deepwater paleoceanography. Paleoceanography **3**: 471–489.

Boyle, E. A., S. D. Chapnick, G. T. Shen, and M. P. Bacon. 1986. Temporal variability of lead in the western North Atlantic. J. Geophys. Res. **91**: 8573. doi:10.1029/JC091iC07p08573

Boyle, E. A., J. M. Edmond, and E. R. Sholkovitz. 1977. The mechanism of iron removal in estuaries. Geochim. Cosmochim. Acta **41**: 1313–1324. doi:10.1016/0016-7037(77)90075-8

Boyle, E. A., R. M. Sherrell, and M. P. Bacon. 1994. Lead variability in the western North Atlantic Ocean and central Greenland ice: Implications for the search for decadal trends in anthropogenic emissions. Geochim. Cosmochim. Acta **58**: 3227–3238. doi:10.1016/0016-7037(94)90050-7

Braga, E. ., C. Andrié, B. Bourlès, A. Vangriesheim, F. Baurand, and R. Chuchla. 2004. Congo River signature and deep circulation in the eastern Guinea Basin. Deep Sea Res. Part I Oceanogr. Res. Pap. **51**: 1057–1073. doi:10.1016/j.dsr.2004.03.005

Brandt, P., H. W. Bange, D. Banyte, and others. 2015. On the role of circulation and mixing in the ventilation of oxygen minimum zones with a focus on the eastern tropical North

Atlantic. Biogeosciences **12**: 489–512. doi:10.5194/bg-12-489-2015

Braungardt, C. B., E. P. Achterberg, F. Elbaz-Poulichet, and N. H. Morley. 2003. Metal geochemistry in a mine-polluted estuarine system in Spain. Appl. Geochemistry **18**: 1757–1771. doi:10.1016/S0883-2927(03)00079-9

Bremner, J. M. 1980. Physical parameters of the diatomaceous mud belt off South West Africa. Mar. Geol. **34**: 67–76. doi:10.1016/0025-3227(80)90064-X

Bridgestock, L., T. Van De Flierdt, M. Rehkämper, and others. 2016. Return of naturally sourced Pb to Atlantic surface waters. Nat. Commun. **7**: 12921.

Bridgestock, L., M. Rehkämper, T. van de Flierdt, M. Paul, A. Milne, M. C. Lohan, and E. P. Achterberg. 2018. The distribution of lead concentrations and isotope compositions in the eastern Tropical Atlantic Ocean. Geochim. Cosmochim. Acta **225**: 36–51. doi:10.1016/J.GCA.2018.01.018

Broecker, W. S., and T.-H. Peng. 1982. Tracers in the Sea, Lamont-Doherty Geological Observatory, Columbia University Palisades, New York.

Broecker, W. S., and T. Takahashi. 1981. Hydrography of the central Atlantic—IV. Intermediate waters of antarctic origin. Deep Sea Res. Part A. Oceanogr. Res. Pap. **28**: 177–193. doi:10.1016/0198-0149(81)90061-3

Browning, T. J., E. P. Achterberg, A. Engel, and E. Mawji. 2021. Manganese co-limitation of phytoplankton growth and major nutrient drawdown in the Southern Ocean. Nat. Commun. **12**: 884. doi:10.1038/s41467-021-21122-6

Browning, T. J., E. P. Achterberg, I. Rapp, A. Engel, E. M. Bertrand, A. Tagliabue, and C. M. Moore. 2017. Nutrient co-limitation at the boundary of an oceanic gyre. Nature **551**: 242–246. doi:10.1038/nature24063

Browning, T. J., H. A. Bouman, C. M. Moore, C. Schlosser, G. A. Tarran, E. M. S. Woodward, and G. M. Henderson. 2014. Nutrient regimes control phytoplankton ecophysiology in the South Atlantic. Biogeosciences **11**: 463–479.

Browning, T. J., I. Rapp, C. Schlosser, M. Gledhill, E. P. Achterberg, A. Bracher, and F. A. C. Le Moigne. 2018. Influence of Iron, Cobalt, and Vitamin B 12 Supply on Phytoplankton Growth in the Tropical East Pacific During the 2015 El Niño. Geophys. Res. Lett. doi:10.1029/2018GL077972

Bruland, K. W. 1980. Oceanographic distributions of cadmium, zinc, nickel, and copper in the North Pacific. Earth Planet. Sci. Lett. **47**: 176–198. doi:10.1016/0012-821X(80)90035-7

Bruland, K. W., and R. P. Franks. 1983. Mn, Ni, Cu, Zn and Cd in the Western North Atlantic, p. 395–414. *In* Trace Metals in Sea Water. Springer US.

Bruland, K. W., R. Middag, and M. C. Lohan. 2014. Controls of Trace Metals in Seawater, p. 19–51. *In* Treatise on Geochemistry. Elsevier.

Bruland, K. W., K. J. Orians, and J. P. Cowen. 1994. Reactive trace metals in the stratified central North Pacific. Geochim. Cosmochim. Acta **58**: 3171–3182. doi:10.1016/0016-7037(94)90044-2

Bruland, K. W., E. L. Rue, G. J. Smith, and G. R. DiTullio. 2005. Iron, macronutrients and diatom blooms in the Peru upwelling regime: brown and blue waters of Peru. Mar. Chem.

**93**: 81–103. doi:10.1016/j.marchem.2004.06.011

Buck, K. N., M. C. Lohan, C. J. M. Berger, and K. W. Bruland. 2007. Dissolved iron speciation in two distinct river plumes and an estuary: Implications for riverine iron supply. Limnol. Oceanogr. **52**: 843–855. doi:10.4319/lo.2007.52.2.0843

Bultot, F. 1971. Atlas climatique du bassin congolais, Institut National pour l'étude agronomique du Congo.

Carr, M.-E. 2001. Estimation of potential productivity in Eastern Boundary Currents using remote sensing. Deep Sea Res. Part II Top. Stud. Oceanogr. **49**: 59–80. doi:10.1016/S0967-0645(01)00094-7

Chance, R., T. D. Jickells, and A. R. Baker. 2015. Atmospheric trace metal concentrations, solubility and deposition fluxes in remote marine air over the south-east Atlantic. Mar. Chem. **177**: 45–56. doi:10.1016/j.marchem.2015.06.028

Chao, Y., J. D. Farrara, G. Schumann, K. M. Andreadis, and D. Moller. 2015. Sea surface salinity variability in response to the Congo river discharge. Cont. Shelf Res. **99**: 35–45. doi:10.1016/j.csr.2015.03.005

Charette, M. A., P. J. Lam, M. C. Lohan, and others. 2016. Coastal ocean and shelf-sea biogeochemical cycling of trace elements and isotopes: lessons learned from GEOTRACES. Philos. Trans. R. Soc. A Math. Phys. Eng. Sci. **374**: 20160076. doi:10.1098/rsta.2016.0076

Chavez, F. P., and M. Messié. 2009. A comparison of Eastern Boundary Upwelling Ecosystems. Prog. Oceanogr. **83**: 80–96. doi:10.1016/j.pocean.2009.07.032

Chelton, D. B., R. A. DeSzoeke, M. G. Schlax, K. El Naggar, N. Siwertz, and C. D. B. D. R. A. S. M. G. E. N. K. S. Nicolas. 1998. Geographical variability of the first baroclinic Rossby radius of deformation. J. Phys. Oceanogr. **28**: 433–460. doi:https://doi.org/10.1175/1520-0485(1998)028%3C0433:GVOTFB%3E2.0.CO;2

Chen, M., G. Carrasco, N. Zhao, and others. 2023. Boundary exchange completes the marine Pb cycle jigsaw. Proc. Natl. Acad. Sci. **120**: 2017. doi:10.1073/pnas.2213163120

Chester, R. 2009. Marine geochemistry, John Wiley & Sons.

Christensen, J. N., A. N. Halliday, L. V Godfrey, J. R. Hein, and D. K. Rea. 1997. Climate and ocean dynamics and the lead isotopic records in Pacific ferromanganese crusts. Science (80-. ). **277**: 913–918.

Coale, K. H., and K. W. Bruland. 1990. Spatial and temporal variability in copper complexation in the North Pacific. Deep Sea Res. Part A, Oceanogr. Res. Pap. **37**: 317–336. doi:10.1016/0198-0149(90)90130-N

Collier, R., and J. Edmond. 1984. The trace element geochemistry of marine biogenic particulate matter. Prog. Oceanogr. **13**: 113–199. doi:https://doi.org/10.1016/0079-6611(84)90008-9

Colombo, M., J. Li, B. Rogalla, S. E. Allen, and M. T. Maldonado. 2022. Particulate trace element distributions along the Canadian Arctic GEOTRACES section: shelf-water interactions, advective transport and contrasting biological production. Geochim. Cosmochim. Acta **323**: 183–201. doi:10.1016/j.gca.2022.02.013

Conway, T. M., and S. G. John. 2014. Global Biogeochemical Cycles isotopes in the North

Atlantic Ocean. Glob. Biogeochem. Cycles Res. 1111–1128. doi:10.1002/2014GB004862.Received

Conway, T. M., and S. G. John. 2015. The cycling of iron, zinc and cadmium in the North East Pacific Ocean – Insights from stable isotopes. Geochim. Cosmochim. Acta **164**: 262–283. doi:10.1016/j.gca.2015.05.023

Cowen, J. P., and K. W. Bruland. 1985. Metal deposits associated with bacteria: implications for Fe and Mn marine biogeochemistry. Deep Sea Res. Part A, Oceanogr. Res. Pap. **32**: 253–272. doi:10.1016/0198-0149(85)90078-0

Croot, P. L., and P. Laan. 2002. Continuous shipboard determination of Fe(II) in polar waters using flow injection analysis with chemiluminescence detection. Anal. Chim. Acta **466**: 261–273. doi:10.1016/S0003-2670(02)00596-2

Cullen, J. T., Z. Chase, K. H. Coale, S. E. Fitzwater, and R. M. Sherrell. 2003. Effect of iron limitation on the cadmium to phosphorus ratio of natural phytoplankton assemblages from the Southern Ocean. Limnol. Oceanogr. **48**: 1079–1087. doi:10.4319/lo.2003.48.3.1079

Cullen, J. T., and M. T. Maldonado. 2012. Biogeochemistry of cadmium and its release to the environment. Cadmium from Toxic. to essentiality 31–62.

Cullen, J. T., and R. M. Sherrell. 1999. Techniques for determination of trace metals in small samples of size-fractionated particulate matter: Phytoplankton metals off central California. Mar. Chem. **67**: 233–247. doi:10.1016/S0304-4203(99)00060-2

Cunningham, B. R., and S. G. John. 2017. The effect of iron limitation on cyanobacteria major nutrient and trace element stoichiometry. Limnol. Oceanogr. **62**: 846–858.

Curl, H., and M. N. Hill. 1964. Progress in the Study of the SeasThe Sea: Ideas and Observations on Progress in the Study of the Seas,.

Cutter, G., K. Casciotti, P. Croot, W. Geibert, L.-E. Heimbürger, M. Lohan, H. Planquette, and T. van de Flierdt. 2017. Sampling and Sample-handling Protocols for GEOTRACES Cruises. Version 3, August 2017.

Cutter, G., J. W. Moffett, M. C. Nielsdóttir, and V. Sanial. 2018. Multiple oxidation state trace elements in suboxic waters off Peru: In situ redox processes and advective/diffusive horizontal transport. Mar. Chem. **201**: 77–89. doi:10.1016/j.marchem.2018.01.003

Dale, A. W., L. Nickelsen, F. Scholz, C. Hensen, A. Oschlies, and K. Wallmann. 2015. A revised global estimate of dissolved iron fluxes from marine sediments. Global Biogeochem. Cycles **29**: 691–707. doi:10.1002/2014GB005017

Denamiel, C., W. P. Budgell, and R. Toumi. 2013. The congo river plume: Impact of the forcing on the far-field and near-field dynamics. J. Geophys. Res. Ocean. **118**: 964–989. doi:10.1002/jgrc.20062

Desboeufs, K., F. Fu, M. Bressac, and others. 2022. Wet deposition in the remote western and central Mediterranean as a source of trace metals to surface seawater. Atmos. Chem. Phys. **22**: 2309–2332. doi:10.5194/acp-22-2309-2022

Dittmar, T., and M. Birkicht. 2001. Regeneration of nutrients in the northern Benguela upwelling and the Angola-Benguela front areas. S. Afr. J. Sci. **97**: 239–246.

Doi, T., T. Tozuka, H. Sasaki, Y. Masumoto, and T. Yamagata. 2007. Seasonal and interannual

variations of oceanic conditions in the Angola Dome. J. Phys. Oceanogr. **37**: 2698–2713. doi:10.1175/2007JPO3552.1

Duce, R. A., G. L. Hoffman, B. J. Ray, and others. 1976. Trace metals in the marine atmosphere: sources and fluxes. Mar. Pollut. Transf. 77–119.

Dulac, F., P. Buat-mçnard, U. Ezat, S. Melki, and G. Bergametti. 1988. Atmospheric input of trace metals to the western Mediterranean: uncertainties in modelling dry deposition from cascade impactor data. Tellus B Chem. Phys. Meteorol. **40**: 362–378. doi:10.3402/tellusb.v40i3.15094

Dulaquais, G., M. Boye, R. Middag, and others. 2014. Contrasting biogeochemical cycles of cobalt in the surface western Atlantic Ocean. Global Biogeochem. Cycles **28**: 1387–1412. doi:10.1002/2014GB004903

Dunckley, J. F., J. R. Koseff, J. V. Steinbuck, S. G. Monismith, and A. Genin. 2012. Comparison of mixing efficiency and vertical diffusivity models from temperature microstructure. J. Geophys. Res. Ocean. **117**: n/a-n/a. doi:10.1029/2012JC007967

Dunne, J. P., R. A. Armstrong, A. Gnnadesikan, and J. L. Sarmiento. 2005. Empirical and mechanistic models for the particle export ratio. Global Biogeochem. Cycles **19**: 1–16. doi:10.1029/2004GB002390

Echegoyen, Y., E. A. Boyle, J. M. Lee, T. Gamo, H. Obata, and K. Norisuye. 2014. Recent distribution of lead in the Indian Ocean reflects the impact of regional emissions. Proc. Natl. Acad. Sci. U. S. A. **111**: 15328–15331. doi:10.1073/pnas.1417370111

Eisma, D., and A. J. Van Bennekom. 1978. The Zaire river and estuary and the Zaire outflow in the Atlantic Ocean. Netherlands J. Sea Res.

Elderfield, H., A. Hepworth, P. N. Edwards, and L. M. Holliday. 1979. Zinc in the Conwy River and estuary. Estuar. Coast. Mar. Sci. **9**: 403–422. doi:10.1016/0302-3524(79)90014-8

Ellwood, M. J., and K. A. Hunter. 2000. The incorporation of zinc and iron into the frustule of the marine diatom Thalassiosira pseudonana. Limnol. Oceanogr. **45**: 1517–1524.

Elrod, V. A., W. M. Berelson, K. H. Coale, and K. S. Johnson. 2004. The flux of iron from continental shelf sediments: A missing source for global budgets. Geophys. Res. Lett. **31**: n/a-n/a. doi:10.1029/2004GL020216

Eltayeb, M. A. H., R. E. Van Grieken, W. Maenhaut, and H. J. Annegarn. 1993. Aerosol-soil fractionation for Namib Desert samples. Atmos. Environ. Part A, Gen. Top. **27**: 669–678. doi:10.1016/0960-1686(93)90185-2

Engel, A., H. Wagner, F. A. C. Le Moigne, and S. T. Wilson. 2017. Particle export fluxes to the oxygen minimum zone of the eastern tropical North Atlantic. Biogeosciences **14**: 1825–1838.

Fairall, C. W., E. F. Bradley, J. E. Hare, A. A. Grachev, and J. B. Edson. 2003. Bulk parameterization of air–sea fluxes: Updates and verification for the COARE algorithm. J. Clim. **16**: 571–591.

Falkowski, P., R. J. Scholes, E. E. A. Boyle, and others. 2000. The global carbon cycle: a test of our knowledge of earth as a system. Science (80-. ). **290**: 291–296.

Figuères, G., J. M. Martin, and M. Meybeck. 1978. Iron behaviour in the Zaire estuary.

Netherlands J. Sea Res. **12**: 329–337. doi:10.1016/0077-7579(78)90035-2

Flynn, R. F., J. Granger, J. A. Veitch, S. Siedlecki, J. M. Burger, K. Pillay, and S. E. Fawcett. 2020. On-Shelf Nutrient Trapping Enhances the Fertility of the Southern Benguela Upwelling System. J. Geophys. Res. Ocean. **125**: 1–24. doi:10.1029/2019JC015948

Frank, M., E. Achterberg, L. Bristow, and others. 2014. METEOR -Berichte Trace Metal Chemistry in the Water Column of the Angola Basin - A Contribution to the International GEOTRACES Program.

Freund, M. 2020. Dispersion of a Tracer in the Eastern Tropical South Pacific - an Investigation of Interactions from the Benthic Boundary Layer to the Ocean Interior. Dr. Diss.

Frew, R. D., and K. A. Hunter. 1992. Influence of Southern Ocean waters on the cadmium–phosphate properties of the global ocean. Nature **360**: 144–146.

Garzoli, S. L., and A. L. Gordon. 1996. Origins and variability of the Benguela Current. J. Geophys. Res. Ocean. **101**: 897–906. doi:10.1029/95JC03221

van Genuchten, C. M., M. J. Hopwood, T. Liu, J. Krause, E. P. Achterberg, M. T. Rosing, and L. Meire. 2022. Solid-phase Mn speciation in suspended particles along meltwater-influenced fjords of West Greenland. Geochim. Cosmochim. Acta **326**: 180–198. doi:10.1016/j.gca.2022.04.003

GEOTRACES Intermediate Data Product Group. 2021. The GEOTRACES Intermediate Data Product 2021 (IDP2021). NERC EDS British Oceanographic Data Centre NOC.

German, C. R., and W. E. Seyfried. 2013. Hydrothermal Processes, 2nd ed. Elsevier Ltd.

Gill, A. E., and E. Adrian. 1982. Atmosphere-ocean dynamics, Academic press.

Glass, J. B., and C. L. Dupont. 2017. Oceanic nickel biogeochemistry and the evolution of nickel use. Biol. Chem. Nickel 12–26.

Gledhill, M., and K. N. Buck. 2012. The organic complexation of iron in the marine environment: a review. Front. Microbiol. **3**: 1–17. doi:10.3389/fmicb.2012.00069

Gledhill, M., A. Hollister, M. Seidel, K. Zhu, E. P. Achterberg, T. Dittmar, and A. Koschinsky. 2022. Trace metal stoichiometry of dissolved organic matter in the Amazon Plume. Sci. Adv. **2249**: 1–11.

Global Gas Flaring Reduction Partnership. 2020. Global Gas Flaring Tracker Report.

Glover, D. M., W. J. Jenkins, and S. C. Doney. 2011. Modeling Methods for Marine Science, Cambridge University Press.

Goldberg, E. D. 1954. Marine geochemistry 1. Chemical scavengers of the sea. J. Geol. **62**: 249–265.

González-Santana, D., H. Planquette, M. Cheize, and others. 2020. Processes driving iron and manganese dispersal from the TAG hydrothermal plume (Mid-Atlantic Ridge): results from a GEOTRACES process study. Front. Mar. Sci. **7**: 568.

Graedel, T. E., D. van Beers, M. Bertram, and others. 2005. The multilevel cycle of anthropogenic zinc. J. Ind. Ecol. **9**: 67–90.

Grasshoff, K., K. Kremling, and M. Ehrhardt. 1999. Methods of Seawater Analysis, K. Grasshoff, K. Kremling, and M. Ehrhardt [eds.]. Wiley.

Guieu, C., F. D'Ortenzio, F. Dulac, and others. 2020. Introduction: Process studies at the air–sea interface after atmospheric deposition in the Mediterranean Sea – objectives and strategy of the PEACETIME oceanographic campaign (May–June 2017). Biogeosciences **17**: 5563–5585. doi:10.5194/bg-17-5563-2020

Guieu, C., J. M. Martin, A. J. Thomas, and F. Elbaz-Poulichet. 1991. Atmospheric versus river inputs of metals to the Gulf of Lions. Mar. Pollut. Bull. **22**: 176–183. doi:10.1016/0025-326X(91)90467-7

Hassler, C., and M. Ellwood. 2019. Nutrient concentration in seawater samples, collected from the underway supply, CTD and trace metal rosettes in the Southern Ocean during the austral summer of 2016/2017, on board the Antarctic Circumnavigation Expedition (ACE).doi:10.5281/ZENODO.2616606

Hatta, M., C. I. Measures, J. Wu, S. Roshan, J. N. Fitzsimmons, P. Sedwick, and P. Morton. 2015. An overview of dissolved Fe and Mn distributions during the 2010–2011 U.S. GEOTRACES north Atlantic cruises: GEOTRACES GA03. Deep Sea Res. Part II Top. Stud. Oceanogr. **116**: 117–129. doi:10.1016/J.DSR2.2014.07.005

Hawco, N. J., P. J. Lam, J. M. Lee, D. C. Ohnemus, A. E. Noble, N. J. Wyatt, M. C. Lohan, and M. A. Saito. 2018. Cobalt scavenging in the mesopelagic ocean and its influence on global mass balance: Synthesizing water column and sedimentary fluxes. Mar. Chem. **201**: 151–166. doi:10.1016/j.marchem.2017.09.001

Hawco, N. J., D. C. Ohnemus, J. A. Resing, B. S. Twining, and M. A. Saito. 2016. A dissolved cobalt plume in the oxygen minimum zone of the eastern tropical South Pacific. Biogeosciences **13**: 5697–5717. doi:10.5194/bg-13-5697-2016

Heggie, D., G. Klinkhammer, and D. Cullen. 1987. Manganese and copper fluxes from continental margin sediments. Geochim. Cosmochim. Acta **51**: 1059–1070. doi:10.1016/0016-7037(87)90200-6

Heggie, D., and T. Lewis. 1984. Cobalt in pore waters of marine sediments. Nature **311**: 453–455. doi:10.1038/311453a0

Heller, M. I., and P. L. Croot. 2015. Copper speciation and distribution in the Atlantic sector of the Southern Ocean. Mar. Chem. **173**: 253–268. doi:10.1016/j.marchem.2014.09.017

Heller, M. I., P. J. Lam, J. W. Moffett, C. P. Till, J.-M. Lee, B. M. Toner, and M. A. Marcus. 2017. Accumulation of Fe oxyhydroxides in the Peruvian oxygen deficient zone implies non-oxygen dependent Fe oxidation. Geochim. Cosmochim. Acta **211**: 174–193.

Henderson, G. M., E. P. Achterberg, and L. Bopp. 2018. Changing Trace Element Cycles in the 21st Century Ocean. Elements **14**: 409–413. doi:10.2138/gselements.14.6.409

Ho, T.-Y. 2013. Nickel limitation of nitrogen fixation in Trichodesmium. Limnol. Oceanogr. **58**: 112–120.

Ho, T. Y., A. Quigg, Z. V. Finkel, A. J. Milligan, K. Wyman, P. G. Falkowski, and F. M. M. Morel. 2003. The elemental composition of some marine phytoplankton. J. Phycol. **39**: 1145–1159. doi:10.1111/j.0022-3646.2003.03-090.x

Hollister, A. P., M. Leon, J. Scholten, M. Gledhill, and A. Koschinsky. 2022. Distribution and Flux of Trace Metals (Al, Mn, Fe, Co, Ni, Cu, Zn, Cd, Pb and U) in the Amazon and Pará River Estuary and Mixing Plume. Authorea Prepr.

Homoky, W. B., T. M. Conway, S. G. John, D. König, F. Deng, A. Tagliabue, and R. A. Mills. 2021. Iron colloids dominate sedimentary supply to the ocean interior. Proc. Natl. Acad. Sci. **118**: e2016078118. doi:10.1073/pnas.2016078118

Homoky, W. B., S. G. John, T. M. Conway, and R. A. Mills. 2013. Distinct iron isotopic signatures and supply from marine sediment dissolution. Nat. Commun. **4**: 2143. doi:10.1038/ncomms3143

Homoky, W. B., S. Severmann, J. McManus, W. M. Berelson, T. E. Riedel, P. J. Statham, and R. A. Mills. 2012. Dissolved oxygen and suspended particles regulate the benthic flux of iron from continental margins. Mar. Chem. **134**–**135**: 59–70. doi:10.1016/j.marchem.2012.03.003

Homoky, W. B., T. Weber, W. M. Berelson, and others. 2016. Quantifying trace element and isotope fluxes at the ocean-sediment boundary: A review,.

Hopkins, J., M. Lucas, C. Dufau, M. Sutton, J. Stum, O. Lauret, and C. Channelliere. 2013. Detection and variability of the Congo River plume from satellite derived sea surface temperature, salinity, ocean colour and sea level. Remote Sens. Environ. **139**: 365–385. doi:10.1016/j.rse.2013.08.015

Hopwood, M. J., A. J. Birchill, M. Gledhill, E. P. Achterberg, J. K. Klar, and A. Milne. 2017. A Comparison between Four Analytical Methods for the Measurement of Fe(II) at Nanomolar Concentrations in Coastal Seawater. Front. Mar. Sci. **4**: 1–14. doi:10.3389/fmars.2017.00192

Hopwood, M. J., C. Santana-González, J. Gallego-Urrea, and others. 2020. Fe (II) stability in coastal seawater during experiments in Patagonia, Svalbard, and Gran Canaria. Biogeosciences **17**: 1327–1342.

Hsieh, Y.-T., W. Geibert, E. M. S. Woodward, N. J. Wyatt, M. C. Lohan, E. P. Achterberg, and G. M. Henderson. 2021. Radium-228-derived ocean mixing and trace element inputs in the South Atlantic. Biogeosciences **18**: 1645–1671. doi:10.5194/bg-18-1645-2021

Huffman, G. J., D. T. Bolvin, E. J. Nelkin, and R. F. Adler. 2016. TRMM (TMPA) Precipitation L3 1 Day 0.25 Degree× 0.25 Degree V7. Goddard Earth Sciences Data and Information Services Center (GES DISC ….

Huffman, G. J., E. F. Stocker, D. T. Bolvin, E. J. Nelkin, and J. Tan. 2019. GPM IMERG Early precipitation L3 half hourly 0.1 degree x 0.1 degree V06. Goddard Earth Sci. Data Inf. Serv. Cent. (GES DISC) Greenbelt, MD, USA. doi:10.5067/GPM/IMERG/3B-HH/06

Hunt, H. R., B. A. Summers, M. Sieber, S. Krisch, A. Al-Hashem, M. Hopwood, E. P. Achterberg, and T. M. Conway. 2022. Distinguishing the influence of sediments, the Congo River, and water-mass mixing on the distribution of iron and its isotopes in the Southeast Atlantic Ocean. Mar. Chem. 104181.

Hutchings, L., C. D. van der Lingen, L. J. Shannon, and others. 2009. The Benguela Current: An ecosystem of four components. Prog. Oceanogr. **83**: 15–32. doi:10.1016/j.pocean.2009.07.046

Hutchins, D. A., and K. W. Bruland. 1998. Iron-limited diatom growth and Si:N uptake ratios in a coastal upwelling regime. Nature **393**: 561–564. doi:10.1038/31203

Ighalo, J. O., A. G. Adeniyi, J. A. Adeniran, and S. Ogunniyi. 2021. A systematic literature

analysis of the nature and regional distribution of water pollution sources in Nigeria. J. Clean. Prod. **283**: 124566. doi:10.1016/j.jclepro.2020.124566

Inthorn, M., T. Wagner, G. Scheeder, and M. Zabel. 2006. Lateral transport controls distribution, quality, and burial of organic matter along continental slopes in high-productivity areas. Geology **34**: 205. doi:10.1130/G22153.1

Jacquot, J. E., and J. W. Moffett. 2015. Copper distribution and speciation across the International GEOTRACES Section GA03. Deep Sea Res. Part II Top. Stud. Oceanogr. **116**: 187–207. doi:10.1016/J.DSR2.2014.11.013

Janssen, D. J., T. M. Conway, S. G. John, J. R. Christian, D. I. Kramer, T. F. Pedersen, and J. T. Cullen. 2014. Undocumented water column sink for cadmium in open ocean oxygen-deficient zones. Proc. Natl. Acad. Sci. **111**: 6888–6893. doi:10.1073/pnas.1402388111

Janssen, D. J., M. Sieber, M. J. Ellwood, and others. 2020. Dissolved trace metal (Fe, Ni, Cu, Zn, Cd, Pb) concentrations in the Indian and Pacific sectors of the Southern Ocean from the Antarctic Circumnavigation Expedition (2016-2017).doi:10.5281/ZENODO.3634411

Jarre, A., L. Hutchings, S. P. Kirkman, and others. 2015. Synthesis: Climate effects on biodiversity, abundance and distribution of marine organisms in the Benguela. Fish. Oceanogr. **24**: 122–149. doi:10.1111/fog.12086

Jeandel, C., and E. H. Oelkers. 2015. The influence of terrigenous particulate material dissolution on ocean chemistry and global element cycles. Chem. Geol. **395**: 50–66. doi:10.1016/J.CHEMGEO.2014.12.001

Jeandel, C., M. Rutgers van der Loeff, P. J. Lam, M. Roy-Barman, R. M. Sherrell, S. Kretschmer, C. German, and F. Dehairs. 2015. What did we learn about ocean particle dynamics in the GEOSECS-JGOFS era? Prog. Oceanogr. **133**: 6–16. doi:10.1016/j.pocean.2014.12.018

Jensen, L. T., P. Morton, B. S. Twining, and others. 2020. A comparison of marine Fe and Mn cycling: US GEOTRACES GN01 Western Arctic case study. Geochim. Cosmochim. Acta **288**: 138–160.

Jickells, T. D. 1995. Atmospheric inputs of metals and nutrients to the oceans: their magnitude and effects. Mar. Chem. **48**: 199–214. doi:10.1016/0304-4203(95)92784-P

Jickells, T. D. 1999. The inputs of dust derived elements to the Sargasso Sea; a synthesis. Mar. Chem. **68**: 5–14. doi:10.1016/S0304-4203(99)00061-4

Jickells, T. D., Z. S. An, K. K. Andersen, and others. 2005. Global Iron Connections Between Desert Dust, Ocean Biogeochemistry, and Climate. Science (80-. ). **308**: 67–71. doi:10.1126/science.1105959

Jickells, T. D., A. R. Baker, and R. Chance. 2016. Atmospheric transport of trace elements and nutrients to the oceans. Philos. Trans. R. Soc. A Math. Phys. Eng. Sci. **374**: 20150286. doi:10.1098/rsta.2015.0286

Jickells, T. D., A. H. Knap, and T. M. Church. 1984. Trace metals in Bermuda rainwater. J. Geophys. Res. **89**: 1423. doi:10.1029/JD089iD01p01423

Jochum, K. P., U. Nohl, K. Herwig, E. Lammel, B. Stoll, and A. W. Hofmann. 2005. GeoReM: A New Geochemical Database for Reference Materials and Isotopic Standards. Geostand.

Geoanalytical Res. **29**: 333–338. doi:https://doi.org/10.1111/j.1751-908X.2005.tb00904.x

John, S. G., and T. M. Conway. 2014. A role for scavenging in the marine biogeochemical cycling of zinc and zinc isotopes. Earth Planet. Sci. Lett. **394**: 159–167. doi:10.1016/J.EPSL.2014.02.053

John, S. G., J. Helgoe, E. Townsend, and others. 2018. Biogeochemical cycling of Fe and Fe stable isotopes in the Eastern Tropical South Pacific. Mar. Chem. **201**: 66–76. doi:10.1016/j.marchem.2017.06.003

John, S. G., R. L. Kelly, X. Bian, and others. 2022. The biogeochemical balance of oceanic nickel cycling. Nat. Geosci. doi:10.1038/s41561-022-01045-7

Johnson, K. S. Chemical Sensors • MBARI.

Johnson, K. S., F. P. Chavez, and G. E. Friederich. 1999. Continental-shelf sediment as a primary source of iron for coastal phytoplankton. Nature **398**: 697–700. doi:10.1038/19511

Johnson, K. S., R. M. Gordon, and K. H. Coale. 1997. What controls dissolved iron concentrations in the world ocean? Mar. Chem. **57**: 137–161. doi:10.1016/S0304-4203(97)00043-1

Johnson, N. M., C. T. Driscoll, J. S. Eaton, G. E. Likens, and W. H. McDowell. 1981. 'Acid rain', dissolved aluminum and chemical weathering at the Hubbard Brook Experimental Forest, New Hampshire. Geochim. Cosmochim. Acta **45**: 1421–1437. doi:10.1016/0016-7037(81)90276-3

De Jong, J., V. Schoemann, D. Lannuzel, P. Croot, H. De Baar, and J. L. Tison. 2012. Natural iron fertilization of the Atlantic sector of the Southern Ocean by continental shelf sources of the Antarctic Peninsula. J. Geophys. Res. Biogeosciences **117**. doi:10.1029/2011JG001679

de Jong, J., V. Schoemann, D. Lannuzel, J. L. Tison, and N. Mattielli. 2008. High-accuracy determination of iron in seawater by isotope dilution multiple collector inductively coupled plasma mass spectrometry (ID-MC-ICP-MS) using nitrilotriacetic acid chelating resin for pre-concentration and matrix separation. Anal. Chim. Acta **623**: 126–139. doi:10.1016/j.aca.2008.06.013

Jordi, A., G. Basterretxea, A. Tovar-Sánchez, A. Alastuey, and X. Querol. 2012. Copper aerosols inhibit phytoplankton growth in the Mediterranean Sea. Proc. Natl. Acad. Sci. **109**: 21246–21249.

Junker, T., V. Mohrholz, L. Siegfried, and A. van der Plas. 2017. Seasonal to interannual variability of water mass characteristics and currents on the Namibian shelf. J. Mar. Syst. **165**: 36–46. doi:10.1016/J.JMARSYS.2016.09.003

Kadko, D. 1993. An assessment of the effect of chemical scavenging within submarine hydrothermal plumes upon ocean geochemistry. Earth Planet. Sci. Lett. **120**: 361–374.

Karstensen, J., L. Stramma, and M. Visbeck. 2008. Oxygen minimum zones in the eastern tropical Atlantic and Pacific oceans. Prog. Oceanogr. **77**: 331–350. doi:10.1016/j.pocean.2007.05.009

Keeling, R. F., A. Körtzinger, and N. Gruber. 2010. Ocean deoxygenation in a warming world. Ann. Rev. Mar. Sci. **2**: 199–229. doi:10.1146/annurev.marine.010908.163855

Kelly, A. E., M. K. Reuer, N. F. Goodkin, and E. A. Boyle. 2009. Lead concentrations and

isotopes in corals and water near Bermuda, 1780–2000. Earth Planet. Sci. Lett. **283**: 93–100.

Kieber, R. J. 2003. Temporal variability of rainwater iron speciation at the Bermuda Atlantic Time Series Station. J. Geophys. Res. **108**: 3277. doi:10.1029/2001JC001031

Kieber, R. J., D. R. Hardison, R. F. Whitehead, and J. D. Willey. 2003. Photochemical Production of Fe(II) in Rainwater. Environ. Sci. Technol. **37**: 4610–4616. doi:10.1021/es030345s

Kieber, R. J., S. A. Skrabal, B. J. Smith, and J. D. Willey. 2005. Organic Complexation of Fe(II) and Its Impact on the Redox Cycling of Iron in Rain. Environ. Sci. Technol. **39**: 1576–1583. doi:10.1021/es040439h

Kieber, R. J., K. Williams, J. D. Willey, S. Skrabal, and G. B. Avery. 2001a. Iron speciation in coastal rainwater: concentration and deposition to seawater. Mar. Chem. **73**: 83–95. doi:10.1016/S0304-4203(00)00097-9

Kieber, R. J., K. Williams, J. D. Willey, S. Skrabal, and G. B. Avery. 2001b. Iron speciation in coastal rainwater: concentration and deposition to seawater. Mar. Chem. **73**: 83–95. doi:10.1016/S0304-4203(00)00097-9

Kittu, L. R., A. J. Paul, M. Fernández-Méndez, M. J. Hopwood, and U. Riebesell. 2023. Coastal N2 fixation rates coincide spatially with N loss in the Humboldt Upwelling System off Peru. Global Biogeochem. Cycles e2022GB007578.

Koch, S. E., M. DesJardins, and P. J. Kocin. 1983. An interactive Barnes objective map analysis scheme for use with satellite and conventional data. J. Appl. Meteorol. Climatol. **22**: 1487–1503.

Krauskopf, K. B. 1956. Factors controlling the concentrations of thirteen rare metals in sea-water. Geochim. Cosmochim. Acta **9**: 1-B32.

Krisch, S., O. Huhn, A. Al-Hashem, M. J. Hopwood, P. Lodeiro, and E. P. Achterberg. 2022. Quantifying Ice-Sheet Derived Lead (Pb) Fluxes to the Ocean; A Case Study at Nioghalvfjerdsbræ. Geophys. Res. Lett. **49**: 1–13. doi:10.1029/2022GL100296

Kuhlbrodt, T., A. Griesel, M. Montoya, A. Levermann, M. Hofmann, and S. Rahmstorf. 2007. On the driving processes of the Atlantic meridional overturning circulation. Rev. Geophys. **45**. doi:10.1029/2004RG000166

Laes, A., S. Blain, P. Laan, S. J. Ussher, E. P. Achterberg, P. Tréguer, and H. J. W. De Baar. 2007. Sources and transport of dissolved iron and manganese along the continental margin of the Bay of Biscay. Biogeosciences **4**: 181–194.

Lam, P. J., and J. K. B. Bishop. 2008. The continental margin is a key source of iron to the HNLC North Pacific Ocean. Geophys. Res. Lett. **35**: 1–5. doi:10.1029/2008GL033294

Lam, P. J., M. I. Heller, P. E. Lerner, J. W. Moffett, and K. N. Buck. 2020. Unexpected Source and Transport of Iron from the Deep Peru Margin. ACS Earth Sp. Chem. **4**: 977–992. doi:10.1021/acsearthspacechem.0c00066

Lam, P. J., J. M. Lee, M. I. Heller, S. Mehic, Y. Xiang, and N. R. Bates. 2018. Size-fractionated distributions of suspended particle concentration and major phase composition from the U.S. GEOTRACES Eastern Pacific Zonal Transect (GP16). Mar. Chem. **201**: 90–107.

doi:10.1016/j.marchem.2017.08.013

Landolfi, A., H. Dietze, W. Koeve, and A. Oschlies. 2013. Overlooked runaway feedback in the marine nitrogen cycle: The vicious cycle. Biogeosciences **10**: 1351–1363. doi:10.5194/bg-10-1351-2013

Laraque, A., J. P. Bricquet, A. Pandi, and J. C. Olivry. 2009. A review of material transport by the Congo River and its tributaries. Hydrol. Process. **23**: 3216–3224. doi:10.1002/hyp.7395

Lass, H. U., and V. Mohrholz. 2008. On the interaction between the subtropical gyre and the Subtropical Cell on the shelf of the SE Atlantic. J. Mar. Syst. **74**: 1–43. doi:10.1016/j.jmarsys.2007.09.008

Lim, B., T. D. Jickells, J. L. Colin, and R. Losno. 1994. Solubilities of Al, Pb, Cu, and Zn in rain sampled in the marine environment over the North Atlantic Ocean and Mediterranean Sea. Global Biogeochem. Cycles **8**: 349–362. doi:10.1029/94GB01267

Lima, D. C. A., P. M. M. Soares, A. Semedo, R. M. Cardoso, W. Cabos, and D. V. Sein. 2019. How Will a Warming Climate Affect the Benguela Coastal Low-Level Wind Jet? J. Geophys. Res. Atmos. **124**: 5010–5028. doi:10.1029/2018JD029574

Little, S. H., D. Vance, C. Walker-Brown, and W. M. Landing. 2014. The oceanic mass balance of copper and zinc isotopes, investigated by analysis of their inputs, and outputs to ferromanganese oxide sediments. Geochim. Cosmochim. Acta **125**: 673–693. doi:10.1016/j.gca.2013.07.046

Liu, M., and T. Tanhua. 2021. Water masses in the Atlantic Ocean: Characteristics and distributions. Ocean Sci. **17**: 463–486. doi:10.5194/os-17-463-2021

Liu, T., S. Krisch, M. J. Hopwood, E. P. Achterberg, and A. Mutzberg. 2022a. Trace metal data from water samples during METEOR cruise M121.doi:10.1594/PANGAEA.947275

Liu, T., S. Krisch, R. C. Xie, M. J. Hopwood, M. Dengler, and E. P. Achterberg. 2022b. Sediment Release in the Benguela Upwelling System Dominates Trace Metal Input to the Shelf and Eastern South Atlantic Ocean. Global Biogeochem. Cycles **36**. doi:10.1029/2022GB007466

Liu, X., and F. J. Millero. 2002. The solubility of iron in seawater. Mar. Chem. **77**: 43–54. doi:10.1016/S0304-4203(01)00074-3

Lohan, M. C., and K. W. Bruland. 2008. Elevated Fe(II) and dissolved Fe in hypoxic shelf waters off Oregon and Washington: An enhanced source of iron to coastal upwelling regimes. Environ. Sci. Technol. **42**: 6462–6468. doi:10.1021/es800144j

Lohan, M. C., P. J. Statham, and D. W. Crawford. 2002. Total dissolved zinc in the upper water column of the subarctic North East Pacific. Deep Sea Res. Part II Top. Stud. Oceanogr. **49**: 5793–5808. doi:10.1016/S0967-0645(02)00215-1

Lorenzato, G., S. Tordo, B. van den Berg, H. M. Howells, and S. Sarmiento-Saher. 2022. Gas Flaring and Methane Emissions Facts and Trends, *In*.

Losno, R., J. L. Colin, N. Le Bris, G. Bergametti, T. Jickells, and B. Lim. 1993. Aluminium solubility in rainwater and molten snow. J. Atmos. Chem. **17**: 29–43. doi:10.1007/BF00699112

Lu, W., Y. Liu, J. Wang, and others. 2020. Global proliferation of offshore gas flaring areas. J.

Maps **16**: 396–404.

Luyten, J. R., J. Pedlosky, and H. Stommel. 1983. The ventilated thermocline. J. Phys. Oceanogr. **13**: 292–309.

Mackey, K. R. M., C.-T. Chien, A. F. Post, M. A. Saito, and A. Paytan. 2015. Rapid and gradual modes of aerosol trace metal dissolution in seawater. Front. Microbiol. **5**. doi:10.3389/fmicb.2014.00794

Mahowald, N., D. S. Ward, S. Kloster, and others. 2011. Aerosol impacts on climate and biogeochemistry. Annu. Rev. Environ. Resour. **36**: 45–74.

Manheim, F. T., and C. M. Lane-Bostwick. 1989. Chemical composition of ferromanganese crusts in the world ocean: a review and comprehensive database. First post.

Martin, J. H., and R. Michael Gordon. 1988. Northeast Pacific iron distributions in relation to phytoplankton productivity. Deep Sea Res. Part A. Oceanogr. Res. Pap. **35**: 177–196. doi:10.1016/0198-0149(88)90035-0

McManus, J., W. M. Berelson, S. Severmann, K. S. Johnson, D. E. Hammond, M. Roy, and K. H. Coale. 2012. Benthic manganese fluxes along the Oregon-California continental shelf and slope. Cont. Shelf Res. **43**: 71–85. doi:10.1016/j.csr.2012.04.016

Measures, C. I., and S. Vink. 2000. On the use of dissolved aluminum in surface waters to estimate dust deposition to the ocean. Global Biogeochem. Cycles **14**: 317–327.

Mercier, H., M. Arhan, and J. R. E. Lutjeharms. 2003. Upper-layer circulation in the eastern Equatorial and South Atlantic Ocean in January–March 1995. Deep Sea Res. Part I Oceanogr. Res. Pap. **50**: 863–887. doi:10.1016/S0967-0637(03)00071-2

Middag, R., H. J. W. Baar, and K. W. Bruland. 2019. The Relationships Between Dissolved Zinc and Major Nutrients Phosphate and Silicate Along the GEOTRACES GA02 Transect in the West Atlantic Ocean. Global Biogeochem. Cycles **33**: 63–84. doi:10.1029/2018GB006034

Middag, R., H. J. W. de Baar, K. W. Bruland, and S. M. A. C. van Heuven. 2020. The Distribution of Nickel in the West-Atlantic Ocean, Its Relationship With Phosphate and a Comparison to Cadmium and Zinc. Front. Mar. Sci. **7**: 1–17. doi:10.3389/fmars.2020.00105

Middag, R., S. M. A. C. van Heuven, K. W. Bruland, and H. J. W. de Baar. 2018. The relationship between cadmium and phosphate in the Atlantic Ocean unravelled. Earth Planet. Sci. Lett. **492**: 79–88. doi:10.1016/j.epsl.2018.03.046

Middag, R., J. M. Rolison, E. George, L. J. A. Gerringa, M. J. A. Rijkenberg, and C. H. Stirling. 2022. Basin scale distributions of dissolved manganese, nickel, zinc and cadmium in the Mediterranean Sea. Mar. Chem. **238**: 104063. doi:10.1016/J.MARCHEM.2021.104063

Millero, F. J., S. Sotolongo, and M. Izaguirre. 1987. The oxidation kinetics of Fe(II) in seawater. Geochim. Cosmochim. Acta **51**: 793–801. doi:10.1016/0016-7037(87)90093-7

Milne, A., C. Schlosser, B. D. Wake, E. P. Achterberg, R. Chance, A. R. Baker, A. Forryan, and M. C. Lohan. 2017. Particulate phases are key in controlling dissolved iron concentrations in the (sub)tropical North Atlantic. Geophys. Res. Lett. **44**: 2377–2387. doi:10.1002/2016GL072314

Moffett, J. W., and J. Ho. 1996. Oxidation of cobalt and manganese in seawater via a common microbially catalyzed pathway. Geochim. Cosmochim. Acta **60**: 3415–3424.

doi:10.1016/0016-7037(96)00176-7

Mohrholz, V., C. H. Bartholomae, A. K. van der Plas, and H. U. Lass. 2008. The seasonal variability of the northern Benguela undercurrent and its relation to the oxygen budget on the shelf. Cont. Shelf Res. **28**: 424–441. doi:10.1016/j.csr.2007.10.001

Mohrholz, V., A. Eggert, T. Junker, G. Nausch, T. Ohde, and M. Schmidt. 2014. Cross shelf hydrographic and hydrochemical conditions and their short term variability at the northern Benguela during a normal upwelling season. J. Mar. Syst. **140**: 92–110. doi:10.1016/J.JMARSYS.2014.04.019

Le Moigne, F. A. C., M. Boye, A. Masson, R. Corvaisier, E. Grossteffan, A. Guéneugues, and P. Pondaven. 2013. Description of the biogeochemical features of the subtropical southeastern Atlantic and the Southern Ocean south of South Africa during the austral summer of the International Polar Year. Biogeosciences **10**: 281–295.

Monteiro, P. M. S., and A. K. van der Plas. 2006. 5 Low oxygen water (LOW) variability in the Benguela system: Key processes and forcing scales relevant to forecasting, p. 71–90. *In* Large Marine Ecosystems. Elsevier.

Monterey, G. I., and L. M. DeWitt. 2000. Seasonal variability of global mixed layer depth from WOD98 temperature and salinity profiles. NOAA Tech. Memo. NMFS.

Moore, C. M. 2016a. Diagnosing oceanic nutrient deficiency. Philos. Trans. R. Soc. A Math. Phys. Eng. Sci. **374**: 20150290. doi:10.1098/rsta.2015.0290

Moore, C. M. 2016b. Diagnosing oceanic nutrient deficiency. Philos. Trans. R. Soc. A Math. Phys. Eng. Sci. **374**: 20150290. doi:10.1098/rsta.2015.0290

Moore, C. M., M. M. Mills, K. R. Arrigo, and others. 2013. Processes and patterns of oceanic nutrient limitation. Nat. Geosci. **6**: 701–710. doi:10.1038/ngeo1765

Moore, R. M., J. D. Burton, P. J. L. Williams, and M. L. Young. 1979. The behaviour of dissolved organic material, iron and manganese in estuarine mixing. Geochim. Cosmochim. Acta **43**: 919–926. doi:10.1016/0016-7037(79)90229-1

Moran, S. B., and R. M. Moore. 1991. The potential source of dissolved aluminum from resuspended sediments to the North Atlantic Deep Water. Geochim. Cosmochim. Acta **55**: 2745–2751. doi:10.1016/0016-7037(91)90441-7

Morel, F. M. M. 2003. The Biogeochemical Cycles of Trace Metals in the Oceans. Science (80-. ). **300**: 944–947. doi:10.1126/science.1083545

Morel, F. M. M., P. J. Lam, and M. A. Saito. 2020. Trace metal substitution in marine phytoplankton. Annu. Rev. Earth Planet. Sci. **48**: 491–517.

Morel, F. M. M., J. R. Reinfelder, S. B. Roberts, C. P. Chamberlain, J. G. Lee, and D. Yee. 1994. Zinc and carbon co-limitation of marine phytoplankton. Nature **369**: 740–742. doi:10.1038/369740a0

Mosley, L. M., and P. S. Liss. 2020. Particle aggregation, pH changes and metal behaviour during estuarine mixing: Review and integration. Mar. Freshw. Res. **71**: 300–310. doi:10.1071/MF19195

Nelson, L. V. S., R. Bay, C. Town, and others. 1996. The Benguela: Large Scale Features and Processes and System Variability. South Atl. 163–210. doi:10.1007/978-3-642-80353-6_9

Nickovic, S., A. Vukovic, and M. Vujadinovic. 2013. Atmospheric processing of iron carried by mineral dust. Atmos. Chem. Phys. **13**: 9169–9181.

Nishioka, J., and H. Obata. 2017. Dissolved iron distribution in the western and central subarctic Pacific: HNLC water formation and biogeochemical processes. Limnol. Oceanogr. **62**: 2004–2022.

NOAA NMFS SWFSC ERD (National Oceanic and Administration, National Marine Fisheries Service, Southwest Fisheries Science Center, E. R. D. Primary Productivity, Aqua MODIS, NPP, Global, 2003-present, EXPERIMENTAL (Monthly Composite) - Datasets - NOAA Data Catalog.

Noble, A. E., Y. Echegoyen-Sanz, E. A. Boyle, and others. 2015. Dynamic variability of dissolved Pb and Pb isotope composition from the US North Atlantic GEOTRACES transect. Deep Sea Res. Part II Top. Stud. Oceanogr. **116**: 208–225.

Noble, A. E., C. H. Lamborg, D. C. Ohnemus, and others. 2012. Basin-scale inputs of cobalt, iron, and manganese from the Benguela-Angola front to the South Atlantic Ocean. Limnol. Oceanogr. **57**: 989–1010. doi:10.4319/lo.2012.57.4.0989

Noble, A. E., D. C. Ohnemus, N. J. Hawco, P. J. Lam, and M. A. Saito. 2017. Coastal sources, sinks and strong organic complexation of dissolved cobalt within the US North Atlantic GEOTRACES transect GA03. Biogeosciences **14**: 2715–2739. doi:10.5194/bg-14-2715-2017

Noffke, A., C. Hensen, S. Sommer, F. Scholz, L. Bohlen, T. Mosch, M. Graco, and K. Wallmann. 2012. Benthic iron and phosphorus fluxes across the Peruvian oxygen minimum zone. Limnol. Oceanogr. **57**: 851–867. doi:10.4319/lo.2012.57.3.0851

NRIAGU, J. O. 1979. Global inventory of natural and anthropogenic emissions of trace metals to the atmosphere. Nature **279**: 409–411. doi:10.1038/279409a0

Ohnemus, D. C., M. E. Auro, R. M. Sherrell, M. Lagerström, P. L. Morton, B. S. Twining, S. Rauschenberg, and P. J. Lam. 2014. Laboratory intercomparison of marine particulate digestions including Piranha: a novel chemical method for dissolution of polyethersulfone filters. Limnol. Oceanogr. Methods **12**: 530–547. doi:10.4319/lom.2014.12.530

Okubo, A. 1971. Oceanic diffusion diagrams. Deep. Res. Oceanogr. Abstr. **18**: 789–802. doi:10.1016/0011-7471(71)90046-5

Olivelli, A., K. Murphy, L. Bridgestock, and others. 2023. Decline of anthropogenic lead in South Atlantic Ocean surface waters from 1990 to 2011: New constraints from concentration and isotope data. Mar. Pollut. Bull. **189**: 114798.

Orians, K. J., and K. W. Bruland. 1985. Dissolved aluminium in the central North Pacific. Nature **316**: 427–429. doi:10.1038/316427a0

Pacyna, J. M., and E. G. Pacyna. 2001. An assessment of global and regional emissions of trace metals to the atmosphere from anthropogenic sources worldwide. Environ. Rev. **9**: 269–298. doi:10.1139/a01-012

Paerl, H. W., J. D. Willey, M. Go, B. L. Peierls, J. L. Pinckney, and M. L. Fogel. 1999. Rainfall stimulation of primary production in western Atlantic Ocean waters: roles of different nitrogen sources and co-limiting nutrients. Mar. Ecol. Prog. Ser. **176**: 205–214. doi:10.3354/meps176205

Pakhomova, S. V., P. O. J. Hall, M. Y. Kononets, A. G. Rozanov, A. Tengberg, and A. V. Vershinin. 2007. Fluxes of iron and manganese across the sediment-water interface under various redox conditions. Mar. Chem. **107**: 319–331. doi:10.1016/j.marchem.2007.06.001

Pardo, P. C., X. A. Padín, M. Gilcoto, L. Farina-Busto, and F. F. Pérez. 2011. Evolution of upwelling systems coupled to the long-term variability in sea surface temperature and Ekman transport. Clim. Res. **48**: 231–246. doi:10.3354/cr00989

Parker, D. L., T. Morita, M. L. Mozafarzadeh, R. Verity, J. K. McCarthy, and B. M. Tebo. 2007. Inter-relationships of MnO2 precipitation, siderophore–Mn(III) complex formation, siderophore degradation, and iron limitation in Mn(II)-oxidizing bacterial cultures. Geochim. Cosmochim. Acta **71**: 5672–5683. doi:10.1016/J.GCA.2007.03.042

Patey, M. D., M. J. A. A. Rijkenberg, P. J. Statham, M. C. Stinchcombe, E. P. Achterberg, and M. Mowlem. 2008. Determination of nitrate and phosphate in seawater at nanomolar concentrations. TrAC Trends Anal. Chem. **27**: 169–182. doi:10.1016/j.trac.2007.12.006

Peterson, R. G., and L. Stramma. 1991. Upper-level circulation in the South Atlantic Ocean. Prog. Oceanogr. **26**: 1–73. doi:10.1016/0079-6611(91)90006-8

Pilson, M. E. Q. 2012. An Introduction to the Chemistry of the Sea, cambridge university press.

Plass, A., A. W. Dale, and F. Scholz. 2021. Sedimentary cycling and benthic fluxes of manganese, cobalt, nickel, copper, zinc and cadmium in the Peruvian oxygen minimum zone. Mar. Chem. 103982. doi:10.1016/j.marchem.2021.103982

Plass, A., C. Schlosser, S. Sommer, A. W. Dale, E. P. Achterberg, and F. Scholz. 2020. The control of hydrogen sulfide on benthic iron and cadmium fluxes in the oxygen minimum zone off Peru. Biogeosciences **17**: 3685–3704. doi:10.5194/bg-17-3685-2020

Pohl, C., P. L. Croot, U. Hennings, T. Daberkow, G. Budeus, and M. R. v.d. Loeff. 2011. Synoptic transects on the distribution of trace elements (Hg, Pb, Cd, Cu, Ni, Zn, Co, Mn, Fe, and Al) in surface waters of the Northern- and Southern East Atlantic. J. Mar. Syst. **84**: 28–41. doi:10.1016/J.JMARSYS.2010.08.003

Rae, C. D. 2005. A demonstration of the hydrographic partition of the Benguela upwelling ecosystem at 26°40’S. African J. Mar. Sci. **27**: 617–628. doi:10.2989/18142320509504122

Rahlf, P., G. Laukert, E. C. Hathorne, L. H. Vieira, and M. Frank. 2021. Dissolved neodymium and hafnium isotopes and rare earth elements in the Congo River Plume: Tracing and quantifying continental inputs into the southeast Atlantic. Geochim. Cosmochim. Acta **294**: 192–214. doi:10.1016/j.gca.2020.11.017

Rapp, I., C. Schlosser, T. J. Browning, F. Wolf, F. A. C. Le Moigne, M. Gledhill, and E. P. Achterberg. 2020. El Niño-Driven Oxygenation Impacts Peruvian Shelf Iron Supply to the South Pacific Ocean. Geophys. Res. Lett. **47**. doi:10.1029/2019GL086631

Rapp, I., C. Schlosser, J.-L. Menzel Barraqueta, and others. 2019. Controls on redox-sensitive trace metals in the Mauritanian oxygen minimum zone. Biogeosciences **16**: 4157–4182. doi:10.5194/bg-16-4157-2019

Rapp, I., C. Schlosser, D. Rusiecka, M. Gledhill, and E. P. Achterberg. 2017. Automated preconcentration of Fe, Zn, Cu, Ni, Cd, Pb, Co, and Mn in seawater with analysis using high-resolution sector field inductively-coupled plasma mass spectrometry. Anal. Chim. Acta **976**: 1–13. doi:10.1016/j.aca.2017.05.008

Raven, J. A., M. C. W. Evans, and R. E. Korb. 1999. The role of trace metals in photosynthetic electron transport in O 2-evolving organisms. Photosynth. Res. **60**: 111–150.

Raven, M. R., R. G. Keil, and S. M. Webb. 2021. Microbial sulfate reduction and organic sulfur formation in sinking marine particles. Science (80-. ). **371**: 178–181.

Resing, J. A., P. N. Sedwick, C. R. German, W. J. Jenkins, J. W. Moffett, B. M. Sohst, and A. Tagliabue. 2015. Basin-scale transport of hydrothermal dissolved metals across the South Pacific Ocean. Nature **523**: 200–203. doi:10.1038/nature14577

Reza, R., and G. Singh. 2010. Heavy metal contamination and its indexing approach for river water. Int. J. Environ. Sci. Technol. **7**: 785–792.

Rickes, E. L., N. G. Brink, F. R. Koniuszy, T. R. Wood, and K. Folkers. 1948. Vitamin B12, a cobalt complex. Science (80-. ). **108**: 134.

Roshan, S., T. DeVries, J. Wu, and G. Chen. 2018. The Internal Cycling of Zinc in the Ocean. Global Biogeochem. Cycles **32**: 1833–1849. doi:10.1029/2018GB006045

Roshan, S., and J. Wu. 2015a. Cadmium regeneration within the North Atlantic. Global Biogeochem. Cycles **29**: 2082–2094. doi:10.1002/2015GB005215

Roshan, S., and J. Wu. 2015b. The distribution of dissolved copper in the tropical-subtropical north Atlantic across the GEOTRACES GA03 transect. Mar. Chem. **176**: 189–198. doi:10.1016/j.marchem.2015.09.006

Roshan, S., J. Wu, and T. DeVries. 2017. Controls on the Cadmium-Phosphate Relationship in the Tropical South Pacific. Global Biogeochem. Cycles **31**: 1516–1527. doi:10.1002/2016GB005556

Roshan, S., J. Wu, and W. J. Jenkins. 2016. Long-range transport of hydrothermal dissolved Zn in the tropical South Pacific. Mar. Chem. **183**: 25–32.

Rudnick, R. L., and S. Gao. 2014. Composition of the Continental Crust, p. 1–51. *In* Treatise on Geochemistry. Elsevier.

Rusiecka, D., M. Gledhill, A. Milne, and others. 2018. Anthropogenic signatures of lead in the Northeast Atlantic. Geophys. Res. Lett. **45**: 2734–2743.

Ryan-Keogh, T. J., A. I. Macey, M. C. Nielsdóttir, and others. 2013. Spatial and temporal development of phytoplankton iron stress in relation to bloom dynamics in the high-latitude North Atlantic Ocean. Limnol. Oceanogr. **58**: 533–545. doi:10.4319/lo.2013.58.2.0533

Saito, M. A., J. W. Moffett, S. W. Chisholm, and J. B. Waterbury. 2002. Cobalt limitation and uptake in Prochlorococcus. Limnol. Oceanogr. **47**: 1629–1636. doi:10.4319/lo.2002.47.6.1629

Saito, M. A., G. Rocap, and J. W. Moffett. 2005. Production of cobalt binding ligands in a Synechococcus feature at the Costa Rica upwelling dome. Limnol. Oceanogr. **50**: 279–290. doi:10.4319/lo.2005.50.1.0279

Samanta, S., and T. K. Dalai. 2018. Massive production of heavy metals in the Ganga (Hooghly) River estuary, India: Global importance of solute-particle interaction and enhanced metal fluxes to the oceans. Geochim. Cosmochim. Acta **228**: 243–258.

Sanial, V., L. E. Kipp, P. B. Henderson, and others. 2018. Radium-228 as a tracer of dissolved trace element inputs from the Peruvian continental margin. Mar. Chem. **201**: 20–34.

doi:10.1016/j.marchem.2017.05.008

Schlitzer, R. 2020. Ocean Data View. http://odv.awi.de.

Schlosser, C., J. Karstensen, and E. M. S. Woodward. 2019. Distribution of dissolved and leachable particulate Pb in the water column along the GEOTRACES section GA10 in the South Atlantic. Deep. Res. Part I Oceanogr. Res. Pap. **148**: 132–142. doi:10.1016/j.dsr.2019.05.001

Schlosser, C., J. K. Klar, B. D. Wake, and others. 2014. Seasonal ITCZ migration dynamically controls the location of the (sub)tropical Atlantic biogeochemical divide. Proc. Natl. Acad. Sci. U. S. A. **111**: 1438–1442. doi:10.1073/pnas.1318670111

Schmidt, S. B., P. E. Jensen, and S. Husted. 2016. Manganese Deficiency in Plants: The Impact on Photosystem II. Trends Plant Sci. **21**: 622–632. doi:10.1016/J.TPLANTS.2016.03.001

Schneider, T., T. Bischoff, and G. H. Haug. 2014. Migrations and dynamics of the intertropical convergence zone. Nature **513**: 45–53. doi:10.1038/nature13636

Scholz, F., C. R. Löscher, A. Fiskal, and others. 2016. Nitrate-dependent iron oxidation limits iron transport in anoxic ocean regions. Earth Planet. Sci. Lett. **454**: 272–281. doi:10.1016/j.epsl.2016.09.025

Scholz, F., J. Mcmanus, A. C. Mix, C. Hensen, and R. R. Schneider. 2014. The impact of ocean deoxygenation on iron release from continental margin sediments. Nat. Geosci. **7**: 433–437. doi:10.1038/ngeo2162

Schroller-Lomnitz, U., C. Hensen, A. W. Dale, F. Scholz, D. Clemens, S. Sommer, A. Noffke, and K. Wallmann. 2019. Dissolved benthic phosphate, iron and carbon fluxes in the Mauritanian upwelling system and implications for ongoing deoxygenation. Deep Sea Res. Part I Oceanogr. Res. Pap. **143**: 70–84. doi:10.1016/j.dsr.2018.11.008

Sedwick, P. N., E. R. Sholkovitz, and T. M. Church. 2007. Impact of anthropogenic combustion emissions on the fractional solubility of aerosol iron: Evidence from the Sargasso Sea. Geochemistry, Geophys. Geosystems **8**.

Severmann, S., J. McManus, W. M. Berelson, and D. E. Hammond. 2010. The continental shelf benthic iron flux and its isotope composition. Geochim. Cosmochim. Acta **74**: 3984–4004. doi:10.1016/J.GCA.2010.04.022

Shannon, L. V, and A. J. B. G. B. Brundrie. 1986. On the existence of an EI Nifto-type phenomenon in the Benguela System. J. Mar. Res. **44**: 495–520.

Shaw, T. J., J. M. Gieskes, and R. A. Jahnke. 1990. Early diagenesis in differing depositional environments: The response of transition metals in pore water. Geochim. Cosmochim. Acta **54**: 1233–1246. doi:10.1016/0016-7037(90)90149-F

Shelley, R. U., M. Roca-Martí, M. Castrillejo, and others. 2017. Quantification of trace element atmospheric deposition fluxes to the Atlantic Ocean ( > 40°N; GEOVIDE, GEOTRACES GA01) during spring 2014. Deep Sea Res. Part I Oceanogr. Res. Pap. **119**: 34–49. doi:10.1016/j.dsr.2016.11.010

Sherrell, R. M., E. A. Boyle, and B. Hamelin. 1992. Isotopic equilibration between dissolved and suspended particulate lead in the Atlantic Ocean: Evidence from 210Pb and stable Pb isotopes. J. Geophys. Res. Ocean. **97**: 11257–11268.

Shi, Z., M. D. Krom, T. D. Jickells, S. Bonneville, K. S. Carslaw, N. Mihalopoulos, A. R. Baker, and L. G. Benning. 2012. Impacts on iron solubility in the mineral dust by processes in the source region and the atmosphere: A review. Aeolian Res. **5**: 21–42. doi:10.1016/J.AEOLIA.2012.03.001

Shillington, F. A., C. J. C. Reason, C. M. Duncombe Rae, P. Florenchie, and P. Penven. 2006. 4 Large scale physical variability of the Benguela Current Large Marine Ecosystem (BCLME), p. 49–70. *In* Large Marine Ecosystems.

Sholkovitz, E. R. 1978. The flocculation of dissolved Fe, Mn, Al, Cu, NI, Co and Cd during estuarine mixing. Earth Planet. Sci. Lett. **41**: 77–86.

Siedlecki, S. A., A. Mahadevan, and D. E. Archer. 2012. Mechanism for export of sediment-derived iron in an upwelling regime. Geophys. Res. Lett. **39**. doi:10.1029/2011GL050366

de Souza, G. F., D. Vance, M. Sieber, T. M. Conway, and S. H. Little. 2022. Re-assessing the influence of particle-hosted sulphide precipitation on the marine cadmium cycle. Geochim. Cosmochim. Acta **322**: 274–296. doi:10.1016/J.GCA.2022.02.009

Stein, A. F., R. R. Draxler, G. D. Rolph, B. J. B. Stunder, M. D. Cohen, and F. Ngan. 2015. NOAA's HYSPLIT atmospheric transport and dispersion modeling system. Bull. Am. Meteorol. Soc. **96**: 2059–2077.

Steinfeldt, R., J. Sültenfuß, M. Dengler, T. Fischer, and M. Rhein. 2015. Coastal upwelling off Peru and Mauritania inferred from helium isotope disequilibrium. Biogeosciences **12**: 7519–7533. doi:10.5194/bg-12-7519-2015

Stichel, T., S. Kretschmer, W. Geibert, M. Lambelet, Y. Plancherel, M. Rutgers van der Loeff, and T. van de Flierdt. 2020. Particle–Seawater Interaction of Neodymium in the North Atlantic. ACS Earth Sp. Chem. **4**: 1700–1717. doi:10.1021/acsearthspacechem.0c00034

Stramma, L., and Mathew England. 1999. On the water masses and mean circulation of the South Atlantic Ocean. J. Geophys. Res. **104**: 20,863-20,883.

Sunda, W. G., and S. A. Huntsman. 1994. Photoreduction of manganese oxides in seawater. Mar. Chem. **46**: 133–152. doi:10.1016/0304-4203(94)90051-5

Sunda, W. G., S. Huntsman, and G. Harvey. 1983. Photoreduction of manganese oxides in seawater and its geochemical and biological implications. Nature **301**: 234–236. doi:10.1038/301234a0

Tagliabue, A., O. Aumont, and L. Bopp. 2014. The impact of different external sources of iron on the global carbon cycle. Geophys. Res. Lett. **41**: 920–926. doi:10.1002/2013GL059059

Tagliabue, A., A. R. Bowie, T. DeVries, and others. 2019. The interplay between regeneration and scavenging fluxes drives ocean iron cycling. Nat. Commun. **10**: 1–8. doi:10.1038/s41467-019-12775-5

Tagliabue, A., N. J. Hawco, R. M. Bundy, W. M. Landing, A. Milne, P. L. Morton, and M. A. Saito. 2018. The Role of External Inputs and Internal Cycling in Shaping the Global Ocean Cobalt Distribution: Insights From the First Cobalt Biogeochemical Model. Global Biogeochem. Cycles **32**: 594–616. doi:10.1002/2017GB005830

Takata, H., T. Aono, K. Tagami, and S. Uchida. 2010. Processes controlling cobalt distribution in two temperate estuaries, Sagami Bay and Wakasa Bay, Japan. Estuar. Coast. Shelf Sci.

**89**: 294–305. doi:10.1016/J.ECSS.2010.08.003

Thuróczy, C.-E., M. Boye, and R. Losno. 2010. Dissolution of cobalt and zinc from natural and anthropogenic dusts in seawater. Biogeosciences **7**: 1927–1936. doi:10.5194/bg-7-1927-2010

Timmermans, K. R., W. Stolte, and H. J. W. De Baar. 1994. Iron-mediated effects on nitrate reductase in marine phytoplankton. Mar. Biol. **121**: 389–396.

Twining, B. S., and S. B. Baines. 2013. The trace metal composition of marine phytoplankton. Ann. Rev. Mar. Sci. **5**: 191–215. doi:10.1146/annurev-marine-121211-172322

Twining, B. S., S. Rauschenberg, P. L. Morton, and S. Vogt. 2015. Metal contents of phytoplankton and labile particulate material in the North Atlantic Ocean. Prog. Oceanogr. **137**: 261–283. doi:10.1016/J.POCEAN.2015.07.001

Uzoekwe, S. A., Sylvester, C. Izah, Ayobami, and O. Aigberua. 2021. Environmental and human health risk of heavy metals in atmospheric particulate matter (PM10) around gas flaring vicinity in Bayelsa State, Nigeria. **13**: 323–335. doi:10.1007/s13530-021-00085-7

Vangriesheim, A., C. Pierre, A. Aminot, N. Metzl, F. Baurand, and J. C. Caprais. 2009. The influence of Congo River discharges in the surface and deep layers of the Gulf of Guinea. Deep. Res. Part II Top. Stud. Oceanogr. **56**: 2183–2196. doi:10.1016/j.dsr2.2009.04.002

Veitch, J., P. Penven, and F. Shillington. 2010. Modeling equilibrium dynamics of the Benguela current system. J. Phys. Oceanogr. **40**: 1942–1964. doi:10.1175/2010JPO4382.1

Ventura, A., E. F. C. Simões, A. S. Almeida, R. Martins, A. C. Duarte, S. Loureiro, and R. M. B. O. Duarte. 2021. Deposition of Aerosols onto Upper Ocean and Their Impacts on Marine Biota. Atmosphere (Basel). **12**: 684. doi:10.3390/atmos12060684

Verhoef, A., M. Portabella, and A. Stoffelen. 2012. High-resolution ASCAT scatterometer winds near the coast. IEEE Trans. Geosci. Remote Sens. **50**: 2481–2487.

Vieira, L. H., S. Krisch, M. J. Hopwood, A. J. Beck, J. Scholten, V. Liebetrau, and E. P. Achterberg. 2020. Unprecedented Fe delivery from the Congo River margin to the South Atlantic Gyre. Nat. Commun. **11**: 556. doi:10.1038/s41467-019-14255-2

Vohra, K., E. A. Marais, W. J. Bloss, J. Schwartz, L. J. Mickley, M. Van Damme, L. Clarisse, and P.-F. Coheur. 2022. Rapid rise in premature mortality due to anthropogenic air pollution in fast-growing tropical cities from 2005 to 2018. Sci. Adv. **8**: eabm4435.

Wallmann, K., Y. S. José, M. J. Hopwood, C. J. Somes, A. W. Dale, F. Scholz, E. P. Achterberg, and A. Oschlies. 2022. Biogeochemical feedbacks may amplify ongoing and future ocean deoxygenation: a case study from the Peruvian oxygen minimum zone. Biogeochemistry. doi:10.1007/s10533-022-00908-w

White, W. M., and E. M. Klein. 2013. Composition of the Oceanic Crust, 2nd ed. Elsevier Ltd.

Wilke, R. J., and R. Dayal. 1982. The behavior of iron, manganese and silicon in the Peconic River estuary, New York. Estuar. Coast. Shelf Sci. **15**: 577–586.

Willey, J. D., R. J. Kieber, J. J. Humphreys, B. C. Rice, M. J. Hopwood, G. B. Avery, and R. N. Mead. 2015. The role of fossil fuel combustion on the stability of dissolved iron in rainwater. Atmos. Environ. **107**: 187–193. doi:10.1016/J.ATMOSENV.2015.02.033

Wu, B., D. Y. Zhao, H. Y. Jia, Y. Zhang, X. X. Zhang, and S. P. Cheng. 2009. Preliminary risk

assessment of trace metal pollution in surface water from Yangtze River in Nanjing Section, China. Bull. Environ. Contam. Toxicol. **82**: 405–409.

Wu, J., and E. A. Boyle. 1997. Lead in the western North Atlantic Ocean: Completed response to leaded gasoline phaseout. Geochim. Cosmochim. Acta **61**: 3279–3283. doi:10.1016/S0016-7037(97)89711-6

Wu, M., J. S. P. McCain, E. Rowland, R. Middag, M. Sandgren, A. E. Allen, and E. M. Bertrand. 2019. Manganese and iron deficiency in Southern Ocean Phaeocystis antarctica populations revealed through taxon-specific protein indicators. Nat. Commun. **10**: 1–10. doi:10.1038/s41467-019-11426-z

Wuttig, K., A. T. Townsend, P. van der Merwe, and others. 2019. Critical evaluation of a seaFAST system for the analysis of trace metals in marine samples. Talanta **197**: 653–668. doi:10.1016/j.talanta.2019.01.047

Wuttig, K., T. Wagener, M. Bressac, A. Dammshäuser, P. Streu, C. Guieu, and P. L. Croot. 2013. Impacts of dust deposition on dissolved trace metal concentrations (Mn, Al and Fe) during a mesocosm experiment. Biogeosciences **10**: 2583–2600. doi:10.5194/bg-10-2583-2013

Wyatt, N. J., A. Milne, E. M. S. Woodward, A. P. Rees, T. J. Browning, H. A. Bouman, P. J. Worsfold, and M. C. Lohan. 2014. Biogeochemical cycling of dissolved zinc along the GEOTRACES South Atlantic transect GA10 at 40 S. Global Biogeochem. Cycles **28**: 44–56.

Xiang, Y., and P. J. Lam. 2020. Size-Fractionated Compositions of Marine Suspended Particles in the Western Arctic Ocean: Lateral and Vertical Sources. J. Geophys. Res. Ocean. **125**: 1–9. doi:10.1029/2020JC016144

Xie, R. C., S. J. G. Galer, W. Abouchami, M. J. A. Rijkenberg, J. De Jong, H. J. W. De Baar, and M. O. Andreae. 2015. The cadmium-phosphate relationship in the western South Atlantic - The importance of mode and intermediate waters on the global systematics. Mar. Chem. **177**: 110–123. doi:10.1016/j.marchem.2015.06.011

Xie, R. C., M. Rehkämper, P. Grasse, T. van de Flierdt, M. Frank, and Z. Xue. 2019. Isotopic evidence for complex biogeochemical cycling of Cd in the eastern tropical South Pacific. Earth Planet. Sci. Lett. **512**: 134–146. doi:10.1016/j.epsl.2019.02.001

Yee, D., and F. M. M. Morel. 1996. In vivo substitution of zinc by cobalt in carbonic anhydrase of a marine diatom. Limnol. Oceanogr. **41**: 573–577. doi:https://doi.org/10.4319/lo.1996.41.3.0573

Zeller, D., M. L. D. Palomares, A. Tavakolie, and others. 2016. Still catching attention: Sea Around Us reconstructed global catch data, their spatial expression and public accessibility. Mar. Policy **70**: 145–152. doi:10.1016/J.MARPOL.2016.04.046

Zhang, Z., Y. Yu, E. C. Hathorne, L. H. Vieira, P. Grasse, C. Siebert, P. Ralf, and M. Frank. Decoupling of Barium and Silicon at the Congo River-dominated Southeast Atlantic Margin: Insights from Combined Barium and Silicon isotopes (under review). Global Biogeochem. Cycles.

Zhu, K., M. J. Hopwood, J. E. Groenenberg, A. Engel, E. P. Achterberg, and M. Gledhill. 2021. Influence of pH and Dissolved Organic Matter on Iron Speciation and Apparent Iron

Solubility in the Peruvian Shelf and Slope Region. Environ. Sci. Technol. doi:10.1021/acs.est.1c02477

Zitoun, R., E. P. Achterberg, T. J. Browning, L. J. Hoffmann, S. Krisch, S. G. Sander, and A. Koschinsky. 2021. The complex provenance of Cu-binding ligands in the South-East Atlantic. Mar. Chem. **237**: 104047. doi:10.1016/j.marchem.2021.104047

# Statement of declaration

I, Te Liu, hereby declare that I have written the PhD thesis with the title **" Trace Metal Biogeochemical Cycling and Fluxes in the eastern South Atlantic"** independently without improper external assistance and that I have listed all relevant sources. Moreover, I assure that the PhD thesis has been written under compliance of the rules for good scientific practice of the German Research association and that the PhD thesis has not been submitted to an examining body for the conferral of a degree elsewhere, neither in part or as a whole, and that none of my academic degrees has ever been withdrawn. Published or submitted for publication manuscripts are identified at the relevant places.

Te Liu

Kiel, 20.03.2023